# The OLED Emitter $Ir(btp)_2(acac)$ – Photophysical Properties of the Triplet State Studied by Highly-Resolving Spectroscopy

**Dissertation**

zur Erlangung des Doktorgrades der Naturwissenschaften (Dr. rer. nat.)
an der Naturwissenschaftlichen Fakultät IV – Chemie und Pharmazie –
der Universität Regensburg

vorgelegt von
Walter J. Finkenzeller
aus Ingolstadt

Regensburg, 2008

Promotionsgesuch eingereicht am 26.03.2008

Die Arbeit wurde angeleitet von Prof. Dr. H. Yersin am Institut für Physikalische und Theoretische Chemie der Universität Regensburg.

Prüfungsausschuss: Prof. Dr. R. Winter, Vorsitzender
Prof. Dr. H. Yersin, 1. Gutachter
Prof. Dr. B. Dick, 2. Gutachter
Prof. Dr. A. Penzkofer

## Parts of this work are already published:

Bauer, R; Finkenzeller, W.J.; Bogner, U.; Thompson, M.E.; Yersin, H.
*Matrix Influence on the OLED Emitter Ir(btp)$_2$(acac) in Polymeric Host Materials – Studies by Persistent Spectral Hole Burning*
*Organic Electronics* **2008**, in press.

Yersin, H; Finkenzeller, W.J.
In *Highly Efficient OLEDs with Phosphorescent Materials*; Yersin, H., Ed.; Wiley-VCH: Weinheim, 2007, p.1.

Finkenzeller, W.J.; Thompson, M.E., Yersin, H.
*Phosphorescence Dynamics and Spin-Lattice Relaxation of the OLED Emitter Ir(btp)$_2$(acac)*
*Chemical Physics Letters* **2007**, *444*, 273.

Finkenzeller, W.J.; Hofbeck, T.; Thompson, M.E., Yersin, H.
*Triplet State Properties of the OLED Emitter Ir(btp)$_2$(acac) – Characterization by Site-Selective Spectroscopy and Application of High Magnetic Fields*
*Inorganic Chemistry* **2007**, *46*, 5076.

# Contents

# Introduction

Since many years, organo-transition metal complexes are known to show great potential for a variety of applications in chemistry, physics and engineering. Examples are chemo- and biosensors [1–6], photo-catalyzers in preparative chemistry [7–10], and photo-sensitizers for singlet oxygen [11] or dye sensitized solar cells [12–17]. Because of these fascinating possibilities, organo-transition metal complexes have been under scientific research for a fairly long time and complexes such as, for example, $Ru(bpy)_3^{2+}$ [1][18–23] have been under investigation in applied as well as in fundamental research fields.

It is not so long, since a new application for organo-transition metal complexes has attracted attention. Organic light-emitting devices (OLEDs) (see, e.g. [24–29] utilize the light emission that can, under certain conditions, occur in organic materials upon application of an electric field. This so-called (organic) *electroluminescence* was discovered by Pope et al. already in 1963 in a crystalline layer of anthracene.[30] However, the onset of electroluminescence was observed at comparatively high voltages and it took more than 20 years, until Tang and van Slyke could demonstrate that organic electroluminescence is also possible to be observed at lower voltages (below 10 V).[31] This was the beginning of a rapid development of the OLED technology.

Organic light emitting devices are attractive for display technology and lighting and open up new possibilities for both. Thus it will not only be possible to fabricate flat panel displays with a maximum in viewing quality in scalable size and at low cost, but even flexible and transparent displays will become realizable. The applications in focus range from large television screens and displays for advertising to mobile applications such as small displays for cellular phones, PDAs,[2] digital cameras and camcorders, and portable media players. For some applications, OLED technology has already entered the commercial market. Especially in portable audio players and cellular phones, OLED displays already replace the conventional liquid-crystal display (LCD) technology to a growing extent. More exotic applica-

[1] bpy=2,2'-bipyridine

[2] PDA=**P**ersonal **D**igital **A**ssistant

tions like transparent displays applicable as car head-up displays or flexible displays to be used, for example, as rollout displays, are under development.

For many of these applications, the key requirement is a minimized power consumption. In this regard, OLEDs offer certain advantages compared to other technologies (see Sects. 1.2 and 2.1) Among other reasons, this renders the OLED technology also extremely attractive in solid-state lighting, where it is ascribed a great potential to deliver highest power efficiencies at very low production costs. By replacing conventional lighting systems such as incandescent light bulbs, the United States alone speculate to accumulate energy savings until 2025 of more than $100 billion and therefore could defer the construction of forty 1 GW power plants.[32, 33]

It has already been demonstrated that OLEDs can reach an energy efficacy of 100 lm/W or more, which is comparable to the best inorganic LEDs or even better.[34–36] Interestingly, these high efficiencies can only be obtained by using phosphorescent emitter materials.[34–39] Application of these materials allows the utilization of both singlet and triplet excited states of the emitter, which are usually involved in the operation of an OLED due to *spin statistics* (Sect. 2.1).This so called *triplet harvesting* can provide up to fourfold electroluminescence quantum efficiencies of phosphorescent emitters compared to fluorescent ones. Therefore it is not surprising that a great deal of interest has been dedicated to organo-transition metal complexes to be employed as emitter materials in OLEDs. These complexes can exhibit a phosphorescence of very high efficiency up to nearly 100% and moreover, can be adapted to meet further requirements due to their chemical versatility concerning the central-metal ion and the choice of ligands (see Sects. 2.3 and 2.4). Especially iridium complexes seem to be exceedingly suited for OLEDs and, therefore, are usually the first choice for fabrication or engineering of high efficiency devices.[34–44] Up to the present, substantial progress has been made in the development of organo-transition metal emitters for OLED application, especially in the green spectral region.[34, 35, 37, 39] In contrast, blue and red emitter complexes still have to be enhanced with respect to stability and luminescence efficiency – especially in view of lighting applications. This can possibly be achieved by a controlled chemical tuning of organo-transition metal complexes on the basis of a detailed understanding of emission properties and their relation to chemical characteristics. Usually, the electroluminescence in an OLED originates from the very same excited state which also governs the emission after optical excitation (photoluminescence). Therefore, optical spectroscopy can be a powerful means to study a complex also with respect to its suitability for application in OLEDs. The

photophysics of organo-transition-metal complexes such as Platinum or Ruthenium complexes has been discussed extensively in the literature.[45–47] However, iridium complexes, and especially those which have been shown to be well-suited as OLED emitters, are not characterized to a sufficient degree.

Very recently, a few spectroscopic [48–50] and theoretical [51, 52] investigations on OLED relevant iridium complexes have been reported. Nevertheless, it is not known so far, why precisely iridium complexes exhibit emission properties that make them perform so well when employed in OLED devices although, regarding a further development of the complexes, this information would be highly desirable.

In the presented report, this issue is addressed by theoretical considerations and spectroscopic investigations of the red emitter $Ir(btp)_2(acac)$[3], a well-known representative of the group of iridium complexes. $Ir(btp)_2(acac)$ was an important milestone towards efficient OLED emitters with a saturated red emission and replaced the formerly used PtOEP[4] due to its higher emission quantum yield and its lower emission decay time. (See Sect. 3.1 and Ref. [40].) Spectroscopic approaches to characterize iridium complexes are comparatively challenging, since the octahedral coordination of these complexes makes it difficult to find suitable matrices for investigations. In this report, the first detailed highly resolved spectroscopic studies of an OLED relevant emitter complex are presented on the example of $Ir(btp)_2(acac)$.

The complex was investigated by use of site-selective excitation and emission spectroscopy in a $CH_2Cl_2$ matrix at cryogenic temperatures. Measurements under variation of temperature and magnetic field strength as well as time resolved and emission decay time measurements were applied to characterize the emitting triplet state $\mathbf{T_1}$ of $Ir(btp)_2(acac)$. Chapter 3 motivates the investigation of $Ir(btp)_2(acac)$ and gives a spectroscopic introduction. In Chapter 4, the three substates of the emitting triplet state $\mathbf{T_1}$ are identified and an energy level diagram is worked out. In the Chapters 5 and 6, the emission decay and spin-lattice relaxation dynamics of $Ir(btp)_2(acac)$, and the vibrational satellite structure, respectively, are studied. Based on the investigations and in the context of previous work in this field, a classification of the emitting state $\mathbf{T_1}$ of $Ir(btp)_2(acac)$ is accomplished and a criterion is presented to assess the potential of a complex to be a good OLED emitter. Moreover, as the matrices used for emitter complexes in OLEDs usually are amorphous, comparative investigations were carried out on thin films of $Ir(btp)_2(acac)$ in the polymers PVB, PVK, and PFO[5]. Therefore the technique of persistent spectral

[3] bis(2-(2'-benzothienyl)-pyridinato-*N*,$C^{3'}$)iridium(acetylacetonate)

[4] Pt(II) Octaethylporphine

[5] For chemical notations, see Sect. 7.1

hole burning (PSHB) was applied and adapted to the discussed class of materials (Chapter 7). The results are discussed with respect to the OLED performance of the complex (Sect. 7.7). The report begins with two introductory chapters, of which the first presents an overview of the OLED technology. The second introduces fundamental properties of organo-transition metal complexes. This chapter also points out peculiarities of octahedral complexes which might be responsible for a superior OLED performance of these complexes.

# 1 OLEDs – An Introduction

*This chapter gives an introduction into the field of organic light-emitting devices (OLEDs). It addresses the basic working principle of OLEDs, specifies important efficiency variables, and summarizes basic strategies to optimize device efficiencies. Examples of typical device structures and of commonly applied materials are presented. The chapter concludes with an overview of the current status of the technology.*

## 1.1 Basic working principle

The principle setup of an OLED is illustrated in Figure 1. The device consists of an organic layer or a system of organic layers sandwiched between two electrodes. The layers are built up on top of a glass substrate typically in the sequence anode - organic layer(s) - cathode with a thickness of the organic layer(s) in the order of 100 nm. The anode most often consists of a non-stoichiometric composite of $SnO_2$ (10-20%) and $In_2O_3$ (80-90%) called 'indium tin oxide' (ITO) which is applied by sputtering and is transparent. The cathode is usually a low-work function metal such as Al or Ca, which is evaporated. Between these electrodes, a voltage of typically between 2 and 20 V is applied and leads to the emission of light within the organic layer(s). In a typical bottom emitting device as given in Figure 1, the generated light is transmitted through the glass substrate. Structures, in which the light is coupled out in the opposite direction, are also possible. The working principle of such an OLED device is described in Fig. 2. In this illustration, the HOMO and LUMO[6] level of the organic layer as well as the Fermi-levels of the anode and of the cathode are given. To drive the device, a voltage is applied between the electrodes. Upon operation, electrons are injected from the cathode into the organic layer and likewise, holes[7] are injected into the organic layer from the anode. Due

[6] HOMO=**H**ighest **O**ccupied **M**olecular **O**rbital, LUMO=**L**owest **U**noccupied **M**olecular **O**rbital

[7] Note that a 'hole' represents a model particle. The HOMO of a neutral organic molecule is usually populated by two electrons. If one electron is extracted, for example, by transferring it to the

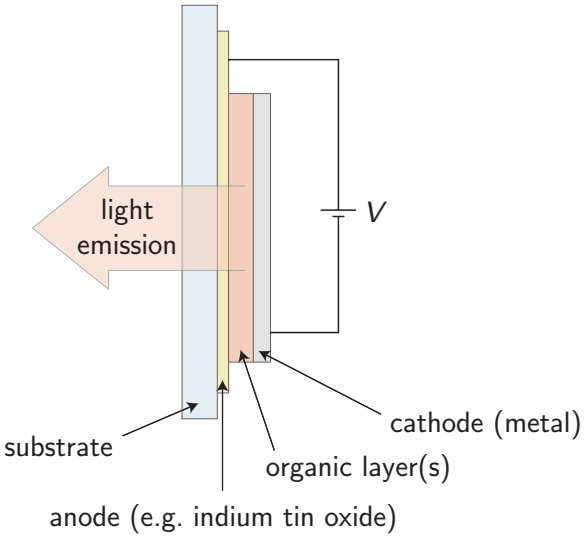


**Figure 1** Principal setup of an organic light-emitting diode (OLED). In a real device, usually several organic layers are necessary for efficient operation. Improved device structures and examples of materials are presented in Sects. 1.3 and 1.5, respectively.

to the applied electrical field, these carriers migrate towards each other and form a bound state, which is often referred to as an exciton state. This state corresponds to an excited state of an emitter molecule in the organic layer. The exciton, finally, can decay under emission of a photon. As, usually, the cathode is a reflective metal, and the anode is a transparent layer of ITO, the light that is generated this way, leaves the device through the anode and the substrate. Detailed descriptions addressing the processes of exciton formation and the mechanisms of exciton decay will be given in Sects. 2.1 and 2.3, respectively.

Although the concept of a device with only one single organic layer is quite oversimplified, the four important steps of operation are illustrated: charge injection, charge transport, exciton formation, and radiative exciton decay. Regarding these processes, the choice of materials used in the device is crucial for its efficiency. Usually, a single organic material cannot unite all required properties such as, for example, a high mobility for electrons and holes. Thus, almost in all real devices

anode, a positively charged molecule is left. Such a 'hole' has properties of a particle. It carries a positive charge, a spin (the one of the residual electron) and it can move from HOMO to HOMO with a specific hole mobility by hopping. This hopping corresponds to a hopping of the residual electrons in the HOMOs in the opposite direction

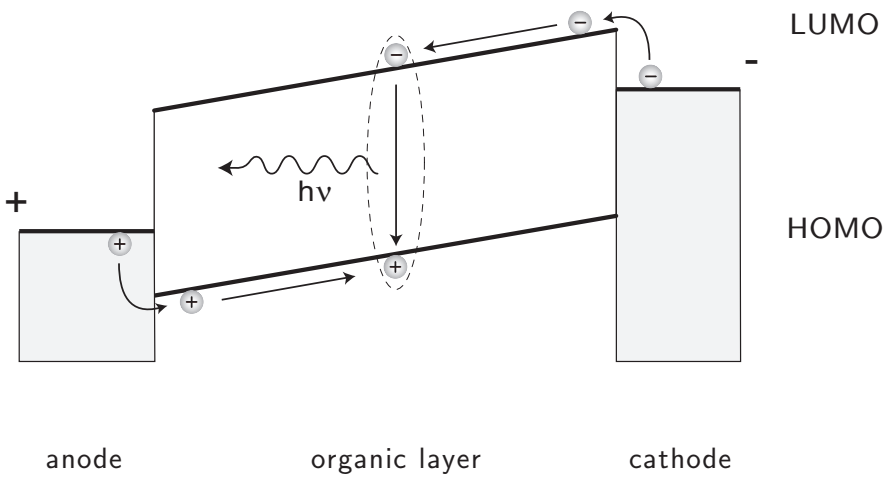


**Figure 2** Working principle of an OLED. The four basic steps of operation are: charge injection, charge transport, exciton formation, and radiative exciton decay. The latter two processes are discussed in detail in Sects. 2.1 and 2.3. Note that the picture of well-defined HOMO and LUMO levels in the organic layer is strongly idealized. Also level bending at the interfaces is neglected.

several organic layers are implemented, each of which is optimized with respect to a specific functionality. Corresponding multi layer device architectures are presented in Sect. 1.3, where approaches of optimizing efficiency and the respective material requirements are addressed. Examples of applied materials are given in Sect. 1.5.

In general, even in multi-layer devices, the system of organic layers is thin and usually does not exceed a thickness of $\approx 200\,\mu m$. The reason is, to allow for high electric field strengths which are necessary to drive a current in the otherwise insulating organic materials. Charge carrier mobilities of organic materials usually lie in the order of $10^{-4}\,cm^2/Vs$ or below and thus are several orders of magnitude smaller than for inorganic semiconductors. Therefore, the transport mechanism in organics is usually charge hopping and involves polaronic states.

The fabrication of a device can proceed in different ways. In almost any case, the ITO anode is applied to the substrate by sputtering and the cathode is finally evaporated on top of the structure. In contrast, several methods are available to apply the organic layers. As a matter of principle, solution processing or vacuum deposition can be applied. Which method to choose is, among others, determined by the organic materials. These are represented by two classes – small organic molecules and polymers (see Sect. 1.5). For OLEDs, it is usually desired to have

amorphous organic layers in order to gain smooth surfaces and thus good contact at the interfaces. Therefore small molecular organic materials usually have to be applied by vacuum deposition to avoid crystallization. Polymer materials, in contrast, can be applied by methods of solution processing, such as spin-coating or inkjet-printing. The cost-effectiveness of solution processing and the possibility of large area applications represent important advantages over inorganic LEDs, which are single-crystalline and expensive to produce. However, highly efficient OLEDs are usually fabricated by evaporation, as with this method sophisticated organic structures can be realized layer by layer. Examples of both types are presented below.

## 1.2 Efficiency

To develop an understanding of the parameters which govern the efficiency of an OLED, a definition of commonly used efficiency expressions is helpful. The internal quantum efficiency (QE) $\eta_{\text{int}}$ is defined as the number of photons generated in the device in relation to the number of electrons that have been injected into the device.

$$\eta_{\text{int}} = \beta \cdot \gamma \cdot \phi_{\text{PL}} \tag{1}$$

It is determined by three parameters: $\beta$ is the fraction of injected electrons, which finally forms exciton states that can decay radiatively. Interestingly, this factor limits the maximum quantum efficiency obtainable with fluorescent emitters to 25% and it is the reason for the importance of triplet emitters for OLEDs (see Sect. 2.1). $\gamma$ is a charge balance factor which is determined by the ratio of the numbers of injected holes and electrons. $\phi_{\text{PL}}$ is the photoluminescence quantum yield of the emitter material. An additional factor $\eta_{\text{OC}}$ determines the fraction of the generated light that is coupled out of the device. This results in the external quantum efficiency of the device, i.e. the ratio of extracted photons to injected electrons.

$$\eta_{\text{ext}} = \eta_{\text{int}} \cdot \eta_{\text{OC}} \tag{2}$$

Based on $\eta_{\text{ext}}$, the important power conversion efficiency (PCE) is obtained.

$$\eta_{\text{PCE}} = \eta_{\text{ext}} \cdot \frac{h\nu}{eV} \tag{3}$$

This expression additionally relates the energy of a generated photon to the electrical energy, which has been necessary for its creation. Therefore $\eta_{\text{PCE}}$ represents the

power consumption of an OLED – a parameter which is crucial, for example, for mobile display applications or lighting. It is usually given in the dimension $\mathrm{lmW}^{-1}$ [8] According to these definitions, it becomes obvious, what the important factors for efficient OLED operation are:

- Application of triplet emitters.
- High photoluminescence quantum yield of the emitter material.
- Balanced injection and transport of electrons and holes.
- High out-coupling efficiency.
- Low operation voltage.

To address these issues, an optimized device architecture and an adequate choice of materials is necessary. In the next section, an idealized layer composition and desired material properties are discussed. Examples of real devices are given in Sect. 1.3 as well and an overview of materials is presented in Sect. 1.5.

## 1.3 Device optimization

### Device architecture

A straightforward approach of improving the power efficiency of OLED devices is to introduce additional organic layers and materials, each of which is optimized for a specific functionality. If all steps of operation, such as charge injection and charge transport, are addressed, one ends up with a multilayer structure that may easily consist of seven organic layers. A corresponding idealized device structure is depicted in Fig. 3. Again, the HOMO and the LUMO levels of the organic layers are given together with the Fermi levels of the anode and the cathode. Most importantly, separate charge-transport layers for electrons and holes are employed. This is especially crucial, as organic materials usually exhibit strongly different electron- and hole-mobilities. Therefore, an electron-transport layer (ETL) consisting of an organic material with high electron mobility is placed between the cathode and the emission layer (EML). Similarly, a hole-transport layer (HTL) employing an organic material with high hole mobility is placed between the anode and the emission layer. The transport layers reduce ohmic losses and provide a balanced current

[8] lm =[luminous flux]

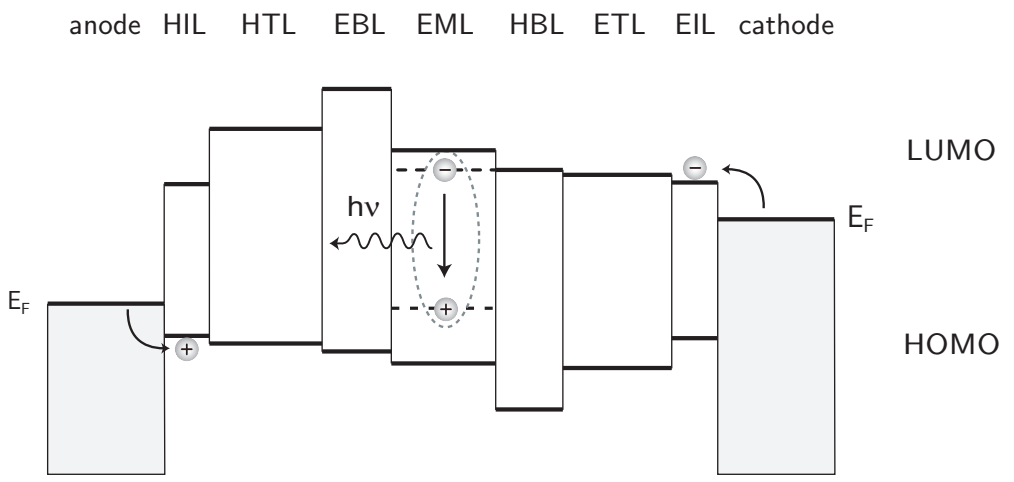


**Figure 3** HOMO-LUMO diagram of an idealized OLED with multiple layers. ETL/HTL=electron/hole transport layer, EIL/HIL=electron/hole injection layer, EBL/HBL=electron/hole blocking layer, EML=emission layer

(compare the $\gamma$-factor in Sect. 1.2). Thus the operation voltage is lowered and the buildup of space charges is prevented.

To facilitate efficient charge injection into these transport layers, usually an injection layer for electrons (EIL) and holes (HIL), respectively, is applied between the transport layers and their adjacent electrode. For example, it has been shown that a very thin layer of LiF or CsF (0.5 to 1 nm) considerably reduces the work function of the metal surface at the cathode and also protects the ETL from chemical reaction with the cathode material.[53, 54]

The emission layer itself in nearly any case is not a pure layer of the emitter material, but is comprised of a matrix material, which is doped with an emitter material at a level of 1-15%, typically 3-8%, weight. In highly efficient devices usually organo-transition metal complexes are employed as emitter dopants. Due to their phosphorescent nature, these complexes can exhibit drastically higher quantum yields of electroluminescence than fluorescent materials do. (See Sect. 2.1.) This is due to the fact that, from a statistical point of view, 75% of all excitons created in the device are triplet excitons (compare the $\beta$-factor in Sect. 1.2), which cannot decay radiatively, if fluorescent emitters are used. A detailed discussion of this behavior is given in Sects 2.1 and 2.4. The matrix prevents (or at least reduces) the interaction of emitter molecules, i.e. the quenching of excited states of emitter molecules by energy transfer processes. This is especially important, as

phosphorescent emitters exhibit a relatively long excited state lifetime compared to fluorescent ones. The matrix material ideally is 'conductive' for both electrons and holes. Otherwise, exciton recombination and emission take place at an interface between the EML and a transport layer and not in the bulk material.

To prevent electrons/holes from crossing the EML and leaving the device through the anode/cathode without having formed excitons, additionally often electron- (EBL) and hole-blocking layers (HBL) are applied adjacent to the EML. An EBL, for example, should feature a high LUMO energy compared to the EML and it should be conductive for holes. This helps to reduce ohmic losses and to confine the exciton formation zone to the EML, also counteracting the undesired formation of exciplexes at the interfaces of the EML. However, such blocking layers may lead to the buildup of high charge densities at the interfaces, with unfavorable consequences for the device lifetime.[55] In real devices, the EBL is in many cases obsolete, as electrons are easily trapped in the LUMOs of the emitter dopant, which usually lie at significantly lower energy than the LUMOs of the matrix molecules.

Generally, comparing the HOMO levels or the LUMO levels of the different layers in Fig. 3, it becomes obvious that energy barriers are present at the interfaces respectively between two layers. In order to reduce the operation voltage of an OLED, these barriers have to be minimized by alignment of HOMOs/LUMOs using an adequate combination of materials. In this context, it has to be pointed out that HOMO and LUMO levels of amorphous organic materials are not as well defined as, for comparison, band edges of inorganic semiconductors. They are rather distributed over a certain energy range due to the strong disorder in these media. Thus, depicted energy levels are only to be taken as indicative. The HOMO level of the emitter dopant should preferably lie at a higher energy than the one of the matrix to promote the trapping of the hole at the emitter. In this case, the exciton formation can occur at the emitter molecule itself rather than on a host molecule. The latter would require a subsequent energy transfer to the emitter, which imposes additional conditions on the electrical excitation process.

Note that the layer composition as discussed in this section is given to illustrate principle strategies. Real devices as presented below will usually deviate from this structure, since often an applied material can serve more than one purpose. Thus, for example, a hole transport material can simultaneously act as an electron blocker. This way, the number of layers can be reduced and, as will be seen below in this section, high internal quantum efficiencies can be already attained with a three-layer device. Obviously, a smaller number of layers is advantageous for fabrication-related reasons. Thus, even devices comprising only two solution-

processed layers are investigated and can achieve comparatively high efficiencies, when blends of electron- and hole-transport materials with the matrix-emitter moiety are employed.[44, 56] In contrast, also additional layers, which are not depicted in Fig. 3 may be favorable, such as a second emission layer in a device reported by He et al. [57], a double-blocking layer [58], or a double interfacial layer [59].

To make use of the internally generated light of an OLED, the outcoupling also has to be optimized. This is important, as the outcoupling efficiency $\eta_{\mathrm{OC}}$ (see Sect. 1.2) is usually limited to only $\approx$ 20% for typical OLEDs, if no special measures are taken.[60] Different methods have been demonstrated to enhance the $\eta_{\mathrm{OC}}$ factor. Thus, one can apply cavities to make use of interference effects [61, 62], or insert thin layers of very low refractive index such as silica aerogel [63] to minimize total reflectance. Moreover, periodic structures in the optical layer of an OLED can enhance the outcoupling by Bragg scattering of otherwise waveguided modes out of the device.[64–66] Similarly, diffusors like sandblasted glass or holographic diffusors have been shown to improve outcoupling.[62] Further, organic capping layers on top emitting devices [67] and lens optics [68] have also proven to inrease the outcoupling efficiency. However, some of these methods also introduce undesired characteristics such as an angular dependence of the emission intensity or/and of the emission spectrum.

## Doping

Beyond the structural considerations in conjunction with the proper choice of materials presented above, an interesting and intensely studied approach of enhancing the performance of an OLED device is controlled chemical doping of organic materials. A comprehensive review on chemical doping in organic devices is given in Ref. [69]. By controlled n-doping of the electron transport material and p-doping of the hole transport material, the conductivity can be raised several orders of magnitude above the intrinsic conductivity of the respective pure material. The resulting device structure is often referred to as a p-i-n device, as it consists of an intrinsic emission layer and of p- and n-doped hole- and electron-transport layers, respectively. The principle of doping is to provide additional mobile charge carriers by adding constituents, which either donate electrons to the LUMO states (n-type doping) or remove electrons from the HOMO states (p-type doping).[69] This is illustrated in Fig. 4. Examples of materials are given in Sect. 1.5. The primary advantage of doping is the reduction of the Ohmic resistance of the transport layers. Thus, the voltage drop across these layers can be kept to a minimum and the oper-

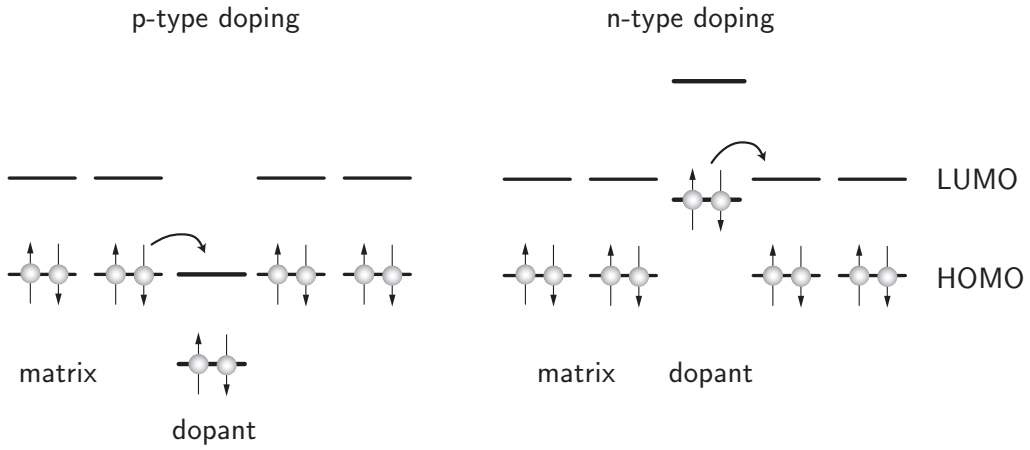


**Figure 4** Principles of molecular doping of organic materials. In p-type doping, the molecular dopant introduces additional acceptor states to energy range of the matrix HOMO levels. In n-type doping, an electron donor provides additional electrons to the matrix LUMOs

ation voltage of a device can be close to the photon energy of the emitted light.[69] But doping offers at least a few more advantages (see Ref. [69]): (i) Due to the high conductivity of the doped transport layers and the respective low voltage drop, these layers can be made thicker than realizable with undoped materials. In this case, the probability of shortcuts is reduced, a higher stability during the preparation process is allowed for and a tuning of the optical micro-cavity towards a higher outcoupling efficiency is possible. (ii) Doped transport layers in contact with the electrodes facilitate efficient charge injection. Due to their high conductivity, space charge regions in the organic layers at the contact, which usually counteract efficient injection, are very narrow and can be tunneled through by the carriers. (iii) Further, a balanced transport of electrons and holes may be more easily attained in doped layers, as the conductivity of each of these layers can be tuned over a wide range by the doping.

All these factors principally result in a higher power conversion efficiency of an OLED due to a reduction of the operation voltage. Thus, for example, by the Leo group a doped device has been demonstrated, which exhibits an efficiency of $\eta_{\mathrm{PCE}} = 77\,\mathrm{lmW^{-1}}$ at $100\,\mathrm{cd\,m^{-2}}$ and an operation voltage of 2.6 V, which is close to the photon energy of the emitted green light of $\sim 2.4\,\mathrm{eV}$.[57] However, it is pointed out that doping and the associated reduction in driving voltage only affects the power conversion efficiency of an OLED and not the internal quantum efficiency. Already

undoped devices, can achieve $\eta_{\text{int}}$ values near 100%, as will be demonstrated in the following.

## 1.4 Examples

Figure 5 illustrates a device reported by the Forrest and Thompson groups already in 2001.[41] This device is based on small-molecule, vacuum depositable materials and applies an organo-transition metal complex as emitter dopant. The Figure depicts the corresponding HOMO and LUMO levels[9] of the applied materials in the absence of an electrical bias and neglecting level-bending at the interfaces. The chemical structures are given in Sect. 1.5 (Fig. 7). It is clearly seen that there are remaining energy barriers at the interfaces and, thus, hopping of electrons downward in energy and of holes upward do not seem to be favored, although this would be advantageous. The energy barriers, however can be overcome be level-shifts due to the electric field, and additionally by thermal activation processes. Interestingly, the HOMO levels of the hole-transport material and of the emitter dopant are well aligned, while the matrix HOMO lies at significantly lower energy. Hence, hole trapping and subsequent exciton-formation are probable to occur on the dopant rather than in the bulk of the matrix material. This is the favorable situation in general.[70, 71] Moreover, it is seen that HTL and ETL also may act as blocking layers for electrons and holes, respectively.

Thus, although consisting only of three organic layers, the depicted device reaches a high internal quantum efficiency of 87% and a relatively high power efficiency of $60\,\text{lmW}^{-1}$. However, these values were obtained only at low current densities. With increasing current, the efficiency gradually decreases due to a growing influence of different quenching effects, of which triplet-triplet annihilation is regarded to be of particular importance.[41, 71, 72]

Alternatively, an approach of achieving efficient electroluminescence with a solution-processed device is illustrated in Fig. 6. Materials structures are again given in Sect. 1.5. The depicted device structure has been reported by Neher et al. [44] and consists of only two organic layers. Note that, usually, it is not easily possible to create multi-layer devices by solution processing, as the materials of adjacent layers would have to be soluble in different solvents, which makes high additional demands on material engineering. Nevertheless, an exception is given by the ex-

[9] Note that, in a strict sense, the corresponding energy values are negative. Here, they are given as absolute values only for simplicity.

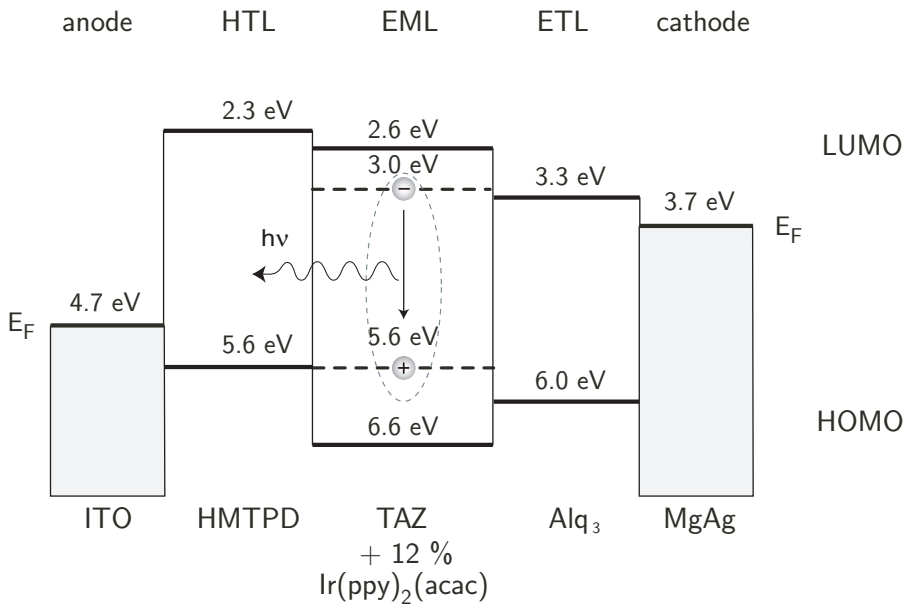


**Figure 5** Layer structure of an OLED device reported by Thompson and Forrest [41]. The HOMO/LUMO values are given relative to the vacuum level, and are negative therefore. For the emission layer (EML), the oxidation and reduction potentials are given for the host (solid line) and the emitter (dashed line). Material-structures are given in Sect. 1.5.

ample of Fig. 6. PEDOT:PSS, which is a hole-injection and transport material, is water soluble and is not affected by the application of further organic materials such as PVK that are soluble in organic solvents. PEDOT:PSS considerably reduces the energy barrier for hole-injection and additionally provides a smooth interface and thus a good contact to the subsequent organic emission layer. The emission layer is comprised of a matrix material, which is doped by an organometallic emitter compound, similarly as described above. To these materials, however, additionally a hole-transport and an electron-transport material are blended at a suitable concentration, to circumvent the problem of low and for both types different mobilities of the charge carriers. The material blend is applied, for example by spin-coating, from a combined solution.

In this blended device, it is still important that the HOMO level of the emitter lies higher in energy than the HOMO level of any of the other materials to allow for efficient hole-trapping at the emitter. The device, despite its relatively simple structure, reaches a power conversion efficiency of 24 $\mathrm{lm\,W^{-1}}$ at 4.4 V with a brightness

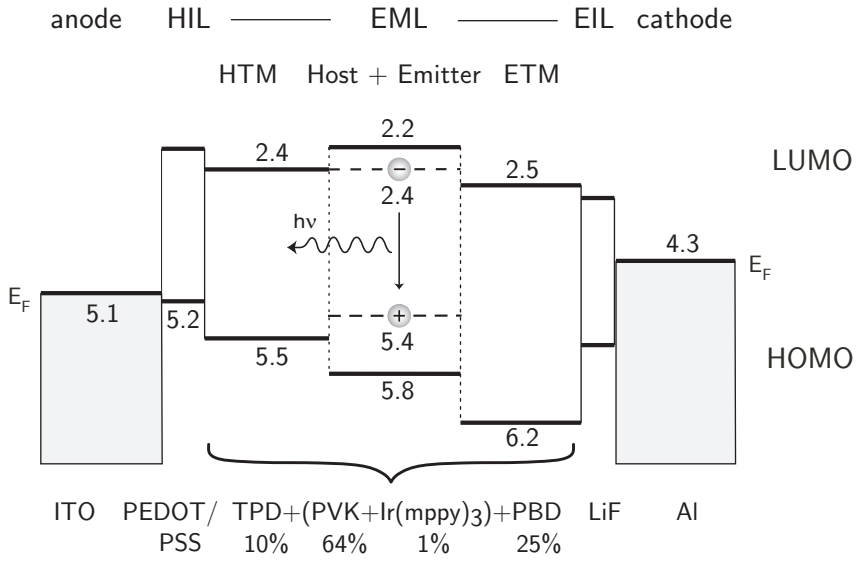


**Figure 6** Layer structure of an OLED device reported by Neher [44]. In this device, the emission layer (EML) consists of a blend of electron- and hole-transporting material, matrix material, and emitter dopant. The respective HOMO and LUMO levels are given as absolute values in eV. The dashed lines represent the HOMO/LUMO levels of the emitter complex. Material-structures are given in Sect. 1.5.

of 136 cd m$^{-2}$ and a quantum efficiency of more than 10%.[44]

## 1.5 Materials and fabrication

As already mentioned in Sect. 1.1, organic LEDs can be classified into two categories, which differ first of all by their methods of preparation. Vacuum deposited OLEDs are processed by sublimation of the organic materials in an ultra-high vacuum chamber which then deposit onto the substrate. On the other hand, OLEDs can also be prepared from solution by use of different techniques. Among these are, for example, spin-coating, dip-coating, rubber-stamping, doctor-blading[10] or even inkjet-printing. Vacuum deposited OLEDs are usually comprised of small molecular organic materials, as the materials have to be sublimable. Therefore, the respective devices are often referred to as *small-molecule OLEDs (sm-OLEDs)*. For

[10]Preparation method, where a polymer is cast on the substrate and, subsequently, excess material is removed by use of a sharp-edged blade.

solution-processed OLEDs, primarily polymeric materials are used. This is crucial to prevent the organic layers from crystallizing. Such devices are often called *polymer OLEDs* or *PLEDs*. Note that crystallization is believed to be a major lifetime limiting process for OLEDs, because it roughens the surface which may result in contact delamination.[73] In modern solution processed OLEDs, usually composite materials are used which consist of a polymeric matrix, and blended small molecular transport materials (see previous section).

In general, sophisticated device architectures are more easily realized by vacuum deposition, since it allows for a consecutive deposition of multiple layers. Therefore, this method is suitable to fabricate highly efficient devices and the possibility of well-defined structuring through shadow masks allows, for example, to produce high definition displays up to a certain scale. On the other hand, solution-processing is predestined for large area and low-cost applications.

The materials used for an OLED must fulfill a series of requirements such as suitability for the specific fabrication procedure, good film forming properties, sufficiently high glass transition temperature to avoid crystallization within the desired lifetime of the device, and chemical and photochemical stability. The anode and the cathode material should feature a high electron affinity and a low work function, respectively. For the organic layers, HOMO/LUMO levels are desired to match those of the adjacent layer to keep energy barriers low. Further, for electron-injection, electron-transport and hole-blocking layer, a high electron-mobility is required. Correspondingly, the layers which adjoin to the anode should have high hole-transport mobilities. Also the purity of the organic materials is of high importance, since unintentional impurities can introduce trap states, which may affect charge transport or lead to emission quenching. In this concern, vacuum deposition offers the interesting possibility of additional purification by special sublimation techniques.[11]

Figure 7 depicts the structures of some basic often applied materials including those materials used for the devices illustrated in Figs. 5 and 6. The materials are given under their commonly used trivial name. $\alpha$-NPD, for example, is a hole transport material with a hole mobility of $10^{-3}\,\mathrm{cm\,V^{-1}s^{-1}}$ which is comparatively high for an organic material. Molecules applied as electron-transporters usually exhibit lower mobilities than hole-transporters. PEDOT:PSS is a hole-conductive material which is often spin-cast on top of ITO anode layers. It reduces the injection barrier for holes significantly by lowering the work function of ITO and creates a smooth

[11] Vacuum gradient sublimation (see Ref. [69]).

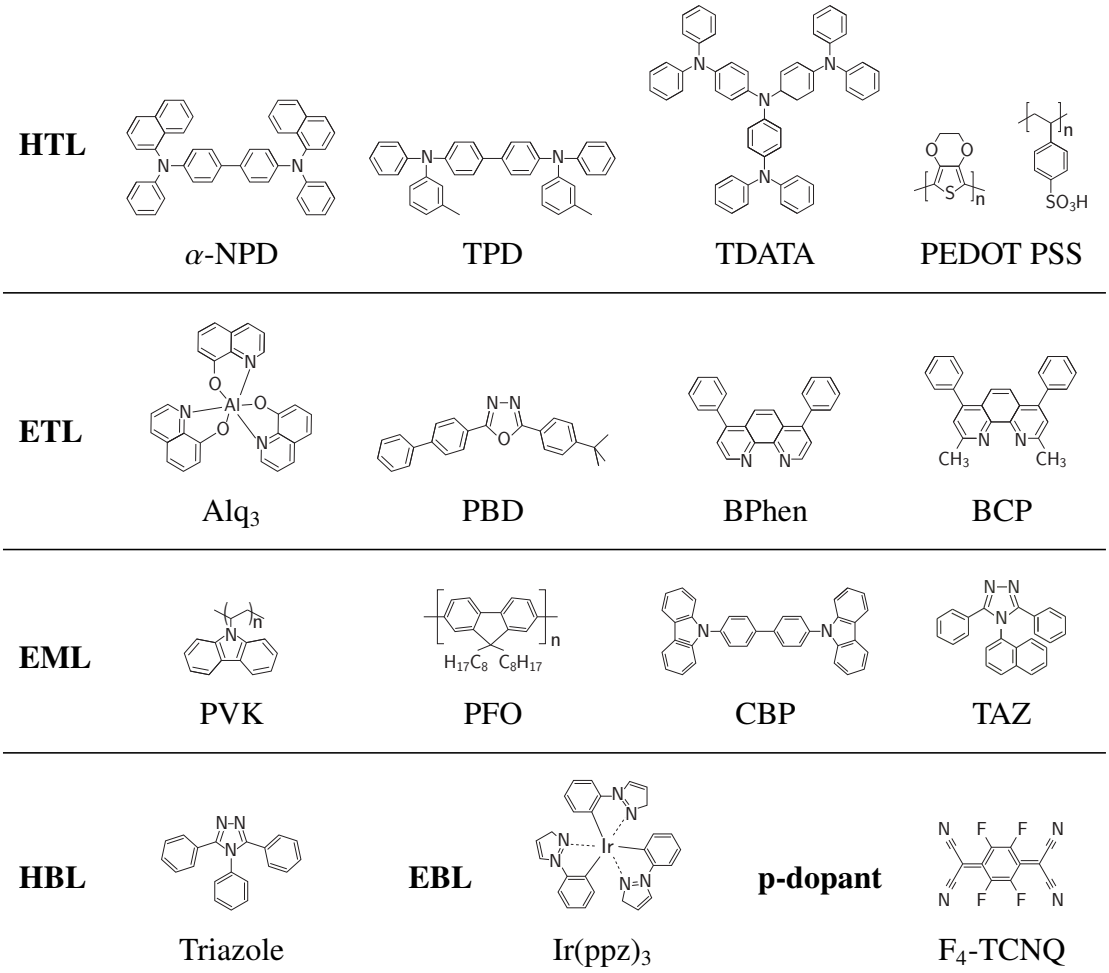


**Figure 7** Structures of some often applied OLED materials. HTL/ETL=hole/electron-transport layer, HBL/EBL=hole/electron-blocking layer, EML=emission layer

interface to the subsequent layers. Moreover it can be used to replace ITO as an anode material.[69] $Alq_3$ is a well-known electron transporter and has also been applied as fluorescent green emitter in early OLEDs. BCP and BPhen are a hole-transport materials which are often utilized as hole-blockers due to their low-lying HOMO level. The materials assigned to the EML are matrix materials applied to host emitter dopants. Emitter materials are given separately in Fig. 8. The polymeric materials PVK and PFO are also used as matrices for spectroscopic investigations below in this work (Sect. 7). CBP is a very common host material often used

with the green emitter $Ir(ppy)_3$. $Ir(ppz)_3$ is a blue emitter with a high-lying LUMO level and is therefore also used as electron-blocking material, whereas triazoles are used as hole-blockers. $F_4$-TCNQ is a p-type dopant, which can be used with a variety of hole-transport materials, such as TDATA or MeO-TPD (a TPD derivative with an attached methoxy group).[69] n-type doping is achieved, for example, by use of alkali metals such as Li, by molecular compounds with extremely high-lying HOMOs, or with cationic salts. For a comprehensive discussion and examples, see the review [69].

Emitter dopants also have to fulfill certain requirements to be suitable for OLEDs. Thus, for these materials it is as well important to be chemically and photochemically stable. Further, they have to be processable, i.e. they must be either sublimable or soluble. The HOMO level of the emitter should lie at higher energy than that of the matrix to allow for direct hole trapping at the emitter, and the triplet energy of the emitter should be smaller compared to the one of the matrix material to prevent an energy transfer from the emitter to the matrix. Concerning reabsorption, the emitter should also feature a large energy difference between its emission and intense absorption bands. This is always fulfilled to a sufficient degree, as far as organo-transition metal complexes are used. Emission wavelength and spectral width are important to gain the color and color purity desired for a certain application. A high photoluminescence quantum yield $\phi_{\mathrm{PL}}$ and a large $\beta$-factor (see Sect. 1.2) are required to attain a high efficiency of the OLED. Note that $\phi_{\mathrm{PL}}$ can be very high also for purely organic dyes, but the electroluminescence quantum yield $\phi_{\mathrm{EL}}$ is limited to $1/4$ of $\phi_{\mathrm{PL}}$ as, for statistical reasons, $3/4$ of all excitons end up as triplet excited states, which cannot decay radiatively in these compounds (see Sect. 2.1). Therefore, triplet emitters have to be used, if high efficiencies are required. Finally, the emission decay time of the emitter must be short to avoid saturation effects, which cause an efficiency roll-off at high current density or accelerated degradation of the device. This is especially important for high brightness applications.

Examples of phosphorescent organo-transition metal emitter dopants are given in Fig. 8. The figure includes some prominent emitter complexes, which are most commonly used in OLED laboratories. Blue emitting complexes are still rare and for a long time FIr(pic) and FIr6 were the only complexes with high efficiencies in photoluminescence and electroluminescence. For example, the $\phi_{\mathrm{PL}}$ of FIr(pic) is close to 100%, when doped into a high triplet energy host.[74] However, the emission color of FIr(pic) is not a pure blue, neither is that of FIr6. The perception of these complexes' emissions by the human eye can rather be described as a sky-blue color. Efficient deep blue complexes are still under development, but structures such

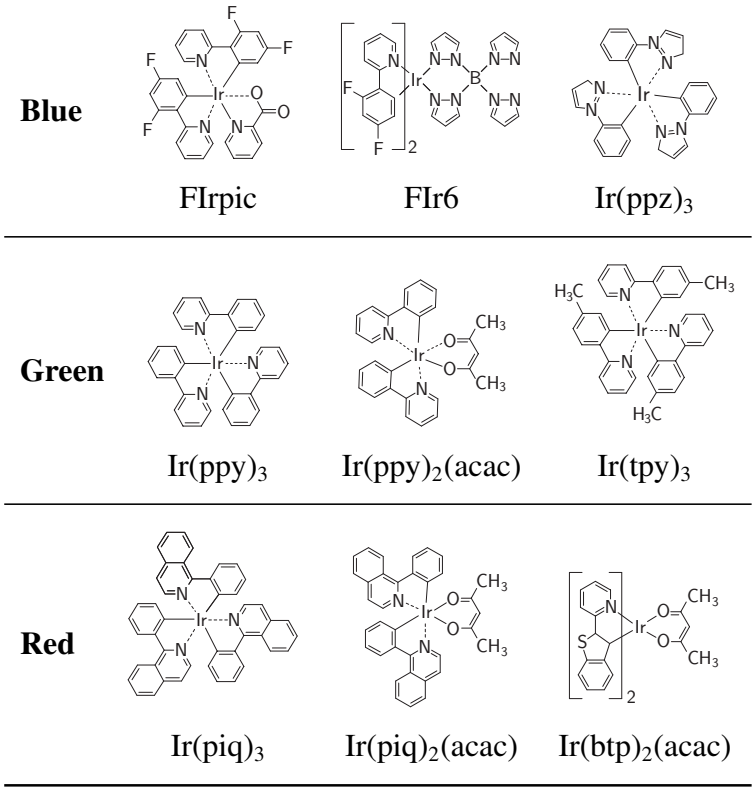


**Figure 8** Structures of phosphorescent emitter dopants commonly used for OLEDs

as, e.g., of $Ir(ppz)_3$ with N-pyrazolyl- type carbene ligands seem promising.[75, 76] In contrast, the green emitters $Ir(ppy)_3$ and its derivatives are mature highly efficient emitters. $Ir(ppy)_3$ features a pure green emission peaking at around 512 nm , a PL efficiency of nearly 100% and a short emission decay time of $\approx$2 µs in a CBP matrix [74], and has been applied in a variety of devices (e.g., see Refs. [35, 77–79]). $Ir(piq)_3$ and $Ir(btp)_2(acac)$ are well-known and efficient red emitters. For $Ir(btp)_2$-(acac) in a solid CBP film, for example, a PL efficiency in the order of 50% and an emission decay time of $< 10$ µs has been reported.[74] The complex is investigated spectroscopically in detail later in this report. (See Chapters 3 to 7.)

Other classes of complexes have also been investigated. For example, recently a Pt-metalloporphyrin infrared emitter with an emission maximum at 765 nm and $\phi_{\mathrm{PL}} \approx 0.7$ has been reported in [80]. Moreover dendrimers with Ir-complex cores have been developed [81–83] and complexes with functionalized ligands [84, 85] have been investigated as well as polymers with conjugated or non-conjugated link-

age of an emitter complex [86–88]. Ru-complexes [23, 24, 89, 90], Re-complexes [24, 91–93], Os-complexes [24, 90, 94–96], Pt-complexes [24, 97–100] and rare-earth complexes [24, 101, 102] have been synthesized and tested as OLED emitters. Nevertheless, the complexes given in Fig. 8 represent the most frequently used triplet emitters.

## 1.6 State of the art

OLED research is already at an advanced stage and modern laboratory prototypes reach excellent performance data. Thus, for example, a green OLED device has been demonstrated, which reaches a power conversion efficiency of 133 lm $W^{-1}$ and an external quantum efficiency of 29% with a luminance of 100 cd $m^{-2}$ and at an operation voltage of 2.5 V. The device employs a novel electron-transport material and $Ir(ppy)_3$ as a phosphorescent emitter.[34] Also based on $Ir(ppy)_3$, a top-emitting device with doped transport layers has been published, which utilizes silver for both the cathode and the anode, a double emission layer, and enhanced outcoupling due to an organic capping layer. It reaches a PCE of 69 lm $W^{-1}$ and $\eta_{ext} \approx 18\%$ at 1000 cd $m^{-2}$ and 2.85 V.[103] Similarly, for a green bottom-emitting device it was demonstrated that a silver anode modified by $CF_4$ plasma treatment to improve outcoupling and hole-injection can lead to about twice the efficiency of a reference ITO based device. With a microcavity structure for enhanced outcoupling, a PCE of 79 lm$W^{-1}$ and an external QE of 18% at 100 cd $m^{-2}$ was obtained.[79]

Efficient sky-blue devices using FIr(pic) as emitter and high triplet energy materials as host and transport materials have been reported to gain 39 lm $W^{-1}$ and 21% external QE at 100 cd $m^{-2}$.[39] A saturated blue emission has been obtained with FIr(pic) by adjusting the emission spectrum with a microcavity structure.[62] In this device the angular dependence of the emission has been corrected by application of scattering media to obtain a lambertian characteristic. Researchers from Sanyo have fabricated a green fluorescent device, which attains an external QE of 10% and 32 lm $W^{-1}$ at 740 cd $m^{-2}$ and maintains the high quantum efficiency up to $10^5$ cd $m^{-2}$.[104]

Solution processed phosphorescent single-layer OLEDs have been fabricated which exhibit 36 lm $W^{-1}$ at 100 cd $m^{-2}$.[105] Moreover, even flexible OLEDs with amorphous In Zn oxide (IZO) as anode have been realized and show a high power efficiency of 33 lm $W^{-1}$ and $\eta_{ext} \approx 14\%$.[106]

White OLEDs for solid state lighting applications are intensely studied as well.

The white emission in these devices is, for example, created by color mixing of red, green, and blue emission by blending of different dopants in one emission layer or by stacking different emission layers. Thus, General Electric showcased in 2004 a 24 x 24 inch lighting panel prototype that produced 1200 lm with an efficiency of 15 lm $W^{-1}$.[107] Recently, researchers of Konica Minolta demonstrated a white phosphorescent OLED with extremely high PCE of 64 lm $W^{-1}$ and a device lifetime of 10 000 h at a luminance of 1000 cd $m^{-2}$.[108] A similar efficiency was achieved with a'multi-unit OLED' reported in [38], which features multiple vertically stacked emissive layers and a light outcoupling film attached to the glass substrate. Moreover, to reduce costs, which is very crucial in lighting, low-cost vacuum-free production methods such as roll-to-roll lamination techniques are successfully investigated.

Red and green phosphorescent OLEDs have reached a device lifetime at 1000 cd $m^{-2}$ of 300 000 h and 250 000 h, respectively.[109] This is suitable for most applications. However, the operation life of phosphorescent blue OLEDs is still too short with about 6000 h.[109] In RGB devices, this differential aging additionally leads to undesired color changes over the device lifetime. For lighting, a minimum of 10 000 h is required,[110] and the design goal of the European OLLA project is to achieve this lifetime at 1000 cd $m^{-2}$ and at 50 lm $W^{-1}$. The long term research goal of the U.S. department of energy is even 160 lm $W^{-1}$. For comparison, a standard incandescent bulb exhibits about 15 lm $W^{-1}$ and a lifetime of 1000 h. Fluorescent lamps feature initial PCEs of 60 – 80 lm $W^{-1}$ and a lifetime of 15 000-20 000 h. Thus, OLEDs seem to be not far from commercialization and leading lighting companies like General Electric consider a commercialization within the next three years possible.

OLED displays even have entered the market already starting with small displays, for example for cellular phones, PDAs, and portable media players, which make little demands on operation lifetime. Larger displays have been demonstrated. At the Consumer Electronics Show (CES) 2008 in Las Vegas Sony presented two OLED panels – one 10 mm thick panel with 27" screen diagonal and 1920 × 1080 pixels and a 3 mm thick 11" panel with 1024 × 768 pixels.[111] Both exhibit an enormous contrast ratio of 1 000 000 : 1 and an operation lifetime of 30 000 h. Samsung even demonstrated a 31" panel.[111] However a cost-effective and profitable mass production is not possible thus far.

# 2 Organometallic Triplet Emitters

*This chapter highlights the connection between OLED efficiency and phosphorescence. The situation of energy states in organometallic complexes and the origin of phosphorescence is explained. An approach for the classification of emitter complexes according to their photophysical properties is also presented. Moreover, theoretical considerations are employed to explain the outstanding OLED suitability of octahedral complexes.*

## 2.1 Why use phosphorescent emitters in OLEDs – Spin-effects and triplet harvesting

In Sect. 1.1 it has been pointed out that, upon operation of an OLED, electrons and holes that have been injected from the cathode and from the anode, respectively, pairwise form bound states. These bound states are referred to as excitons and, in their final stage, represent electronically excited states of an emitter molecule (emitter dopant). Since electron and hole both carry a spin, for the exciton a total spin has to be considered. The spin quantum number of electron and hole of $s = 1/2$ can result in the quantum numbers $S = 0$ or $S = 1$ of the total spin of the exciton. $S = 0$ corresponds to the singlet state described by an antisymmetric spin wavefunction. $S = 1$ is related to a triplet state represented by a symmetric spin wavefunction. The triplet state consists of three triplet substates with the magnetic spin quantum numbers $M_S = 1, 0, -1$. Thus, electron and hole can combine in a total of four spin combinations. For simple statistical reasons, $1/4$ of all excitons will combine as singlet excitons, while $3/4$ will combine as triplet excitons. If fluorescent emitters are used, only the 25% singlet excitons can decay radiatively. The triplet excitons, on the other hand, are desactivated radiationless in this case and therefore are lost.[12] To circumvent this problem, usually triplet emitters are used.

[12] For purely organic (fluorescent) molecules, radiative decay times of phosphorescence are long and can be in the order of several ms or more. Thus, a phosphorescence is usually not observable at ambient temperature for such compounds.

Nevertheless, there has been a controversial discussion in the literature, whether the exact formation ratio of singlet and triplet excitons can deviate from 1:3 (see, e.g. Refs. [112–114]).

On account of this, the process of exciton formation is investigated in some more detail in the following: For this purpose, it is assumed that the exciton formation process directly leads to an excited state of an emitter molecule. A corresponding model is illustrated in Figure 9. Note that exciton formation at a host molecule with subsequent energy transfer to an emitter molecule is also possible, but is regarded unfavorable, as the energy transfer process implicates supplementary requirements (see, e.g. Ref. [70]).[13] As a starting point, it is assumed that a hole is already trapped at an emitter molecule and a nearby electron resides at the LUMO of a host molecule. It has been proposed specifically for efficient devices containing Ir(III) emitter complexes [41, 97, 116], but also for PtOEP [117], that the hole is trapped on the emitter molecule first. Such a situation is strongly favored, if the HOMO energy of the emitter complex well matches the one of the hole-transport material and the HOMO energy of the matrix material lies at significantly lower energy (compare Fig. 5 and Ref. [41]). This avoids the electrical excitation of the host and also eliminates energy back transfer from guest to host.[118]

As seen in Fig. 9, the electron – or more exactly, the negatively charged polaron[14] – migrates by hopping in the EML towards the anode. This occurs due to the external potential $V$, but usually also requires thermal activation energy to overcome energy sinks caused by inhomogeneities and polaronic effects. As long as the electron is far from the trapped hole, the particles are neither bound nor correlated (Fig. 9 left). However, when the electron comes into the vicinity of the hole, it experiences a Coulomb attraction to the hole. When the Coulomb binding energy $\Delta E(\mathrm{e}-\mathrm{h})$ is larger than the thermal energy $k_\mathrm{B}T$, the electron-hole pair can be regarded as bound and thus can already be termed as *exciton*. The critical electron-hole separation is given by

$$\Delta E(\mathrm{e}-\mathrm{h}) = \frac{e^2}{4\pi\epsilon_0\epsilon R_\mathrm{c}} = k_\mathrm{B}T \quad , \tag{4}$$

wherein $e$ is the electron charge and $\epsilon_0$ and $\epsilon$ represent the dielectric constants of the vacuum and the host material, respectively. Assuming $\epsilon = 3$, a value of $R_\mathrm{c} \approx 180\,\text{Å}$ is obtained for $T = 300\,\mathrm{K}$. Obviously, a binding of electron and hole occurs already at a comparatively large spatial separation of the particles, when still a large number

[13] However, devices applying this principle have also been demonstrated.[115]

[14] Electron (or hole) hopping is normally connected with a polarization of the matrix. The charged particle coupled to its matrix distortions represents a polaron. (See, e.g., Ref. [121].)

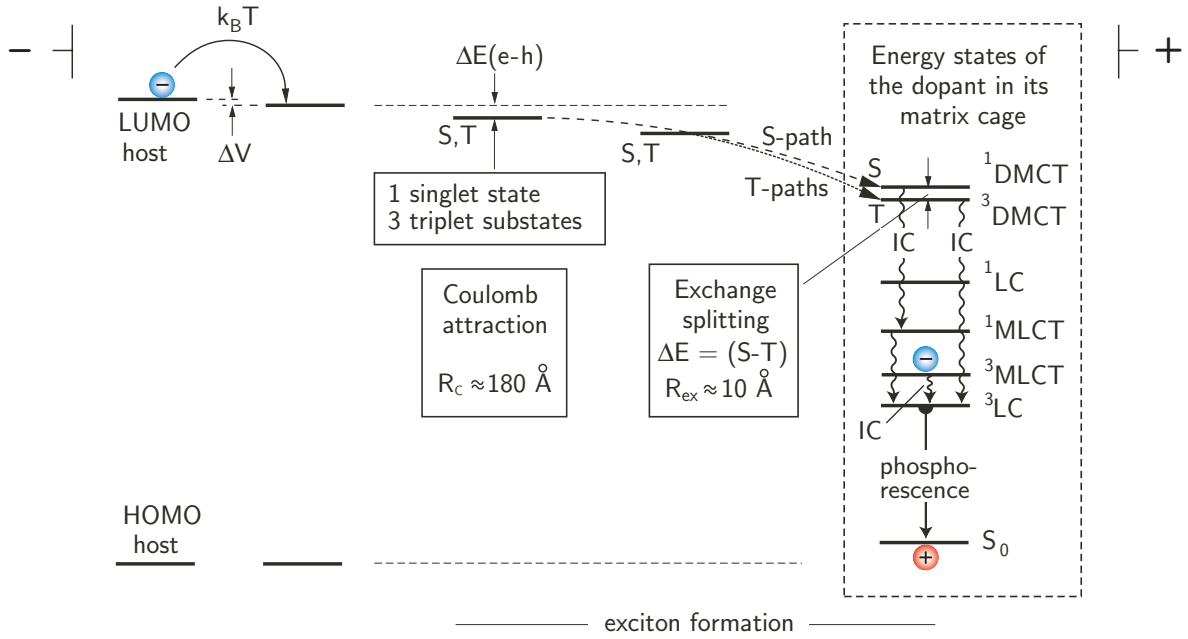


**Figure 9** Process of exciton formation. In this model, the exciton formation is induced by Coulomb attraction between electron and hole and starts already at a separation of 150 Å to 180 Å. The exciton trapping at the emitter complex, which is doped into a host material, occurs via dopant-to-matrix charge transfer states ($^{1,3}$**DMCT** states) [119, 120]. It finally results in a population of the lowest excited triplet state of the emitter molecule via internal conversion (IC) and intersystem crossing (ISC). The lower-lying states depicted in the dashed frame represent electronic states of the emitter molecule itself. However, this energy level diagram is strongly simplified.

of host molecules lies in between them. Since one can already speak of an exciton, from this point on the total spin has to be included into further considerations. The exciton can be found in the singlet state **S** or in the triplet state **T** (i.e. in a triplet substate). However, at this point those states are still quasi-degenerate (see Fig. 9) and thus, the probability of formation of a singlet or a triplet, respectively, is supposed to be just the same. Regarding many excitons, a *population ratio of one to three* of singlet to triplet substates will be obtained.

When, driven by the Coulomb attraction, the electron approaches the hole further, at a distance of 10 to 15 Å, the wavefunctions of electron and hole begin to overlap [119, 122]. At this point, the exchange interaction takes effect and splits the singlet state **S** and the triplet state **T** by about twice the exchange integral. In

this situation of small wavefunction overlap, the splitting $\Delta E(\mathrm{S}-\mathrm{T})$ is expected to be much smaller than typically found for singlet-triplet splittings in molecules. It depends approximately exponentially on the electron-hole separation $R$ according to

$$\Delta E(\mathrm{S}-\mathrm{T}) \propto \exp(-aR) \quad , \tag{5}$$

where $a$ is a constant which depends on the individual wavefunctions of the emitter dopant and the nearest neighbor host molecules. It is important to note that the singlet-triplet splitting due to exchange interaction emerges long after the electron-hole pair is already coulombically bound. Therefore, a deviation from the statistical ratio of the formation of singlet and triplet excitons-precursors is unlikely. Further, it has been shown in Ref. [123] that these exciton precursors do not undergo interconversion between singlet and triplet configurations. Thus the total spin is conserved until both electron and hole finally reside at a triplet emitter molecule and intramolecular spin-orbit coupling takes effect.

At a further stage, the electron will be located at a host molecule in the nearest neighborhood (first coordination sphere) of the hole. This can also be considered from a different point of view. Such a situation corresponds to a charge transfer excitation. The corresponding states represent dopant-to-matrix charge transfer (DMCT) states.[119, 124] Regarding the spin of the remaining electron in the HOMO of the dopant and the spin of the electron in the LUMO of the matrix molecule, $^{1}$**DMCT** and $^{3}$**DMCT** states are obtained. These states and a number of lower-lying states which are largely confined to the (triplet emitter) dopant itself, such as $^{1,3}\pi\pi^{*}$ or $^{1,3}$**MLCT** states are illustrated in the dashed frame of Fig. 9.

On the basis of the presented energy level scheme, also the relaxation paths from the $^{1,3}$**DMCT** to the low-lying states of the emitter become apparent. The relaxation from the $^{3}$**DMCT** will be faster within the system of triplet states rather than making a prior spin-flip. This is due to the fact that spin-orbit coupling (SOC) in organic host molecules is relatively small and, thus, intersystem crossing (ISC) is not favored. As a consequence, fast processes of internal conversion (IC) populate the lowest triplet state $\mathbf{T_1}$. Similarly, a fast IC from the $^{1}$**DMCT** will lead to the population of the lowest singlet state $\mathbf{S_1}$. As ISC is effective in triplet emitter dopants, a subsequent ISC from the lowest singlet $\mathbf{S_1}$ finally leads to population of the lowest triplet state $\mathbf{T_1}$. The relaxation times within the singlet or triplet manifold, respectively, are of the order of 1 ps or faster, while the ISC processes can be slower or of similar time, depending on the importance of SOC and the resulting perturbation of the lowest triplet by singlet admixtures. In a favorable situation, which is usually

found for organo-transition metal triplet emitters, the intersystem crossing rate is very high (order of $10^{12}$ to $10^{13}$ $s^{-1}$).[45, 125, 126] Hence, relaxation processes to the lowest triplet state mostly yield an efficiency near 100%. This means that all excitons originally formed as singlet (25%) or triplet (75%) excitons finally end up in the lowest triplet state $\mathbf{T_1}$ of the emitter molecule. If the triplet state decays radiatively with a high quantum yield, this phenomenon is called *triplet harvesting*. It allows in principle the fourfold electroluminescence efficiency to be obtained with triplet emitters compared with purely organic singlet emitters.

## 2.2 Energy states of typical OLED emitters

The electroluminescence (EL) spectrum of a properly-built OLED usually resembles the photoluminescence (PL) spectrum of the applied emitter material. This is the basis of the spectroscopic investigations of the organometallic phosphorescent complex $Ir(btp)_2(acac)$ presented in the Chapters. 3 to 7. The photoluminescence behavior of a compound is determined by the properties of its emitting state which, in organo-transition metal complexes, is the triplet state $\mathbf{T_1}$, and its ground state. Specifically, the emission properties are closely related to the molecular orbitals (MOs) responsible for the $\mathbf{T_1}$ state and for the electronic ground state. As seen in the following, in organo-transition metal complexes several of those so-called "frontier orbitals" have to be considered.

Basically, there are the $\pi$- and the excited $\pi^*$-orbitals of the organic ligands and the d- and excited $d^*$-orbitals of the central metal atom.[15] To obtain a simple model for the situation of the complexes low-lying energy states, it is first of all sufficient to take into account only one HOMO and one LUMO regarding each, the $\pi$- and the d-orbitals. These four frontier orbitals HOMO, HOMO-1, and LUMO, LUMO+1 are illustrated on the example of Fig. 10a. For most molecules, which are interesting for application in OLEDs, the HOMOs are occupied by two electrons and the compound is diamagnetic.

Already in this simple model, four excitations are possible: first of all, a ligand-centered (LC) excitation, in this case of $\pi$-$\pi^*$ character, and a metal-to-ligand charge transfer (MLCT) excitation of d-$\pi^*$ character. These are of essential importance for typical OLED emitters and, for example, dominate the emission properties of the complex $Ir(btp)_2(acac)$ in the focus of this report. In Fig. 10b, an interim model of

[15] The degeneracy of the d-orbitals, which would apply to the free atom, is in part lifted due to the lowered symmetry caused by the ligand-field. (Compare Sect. 2.5 and Fig. 13.)

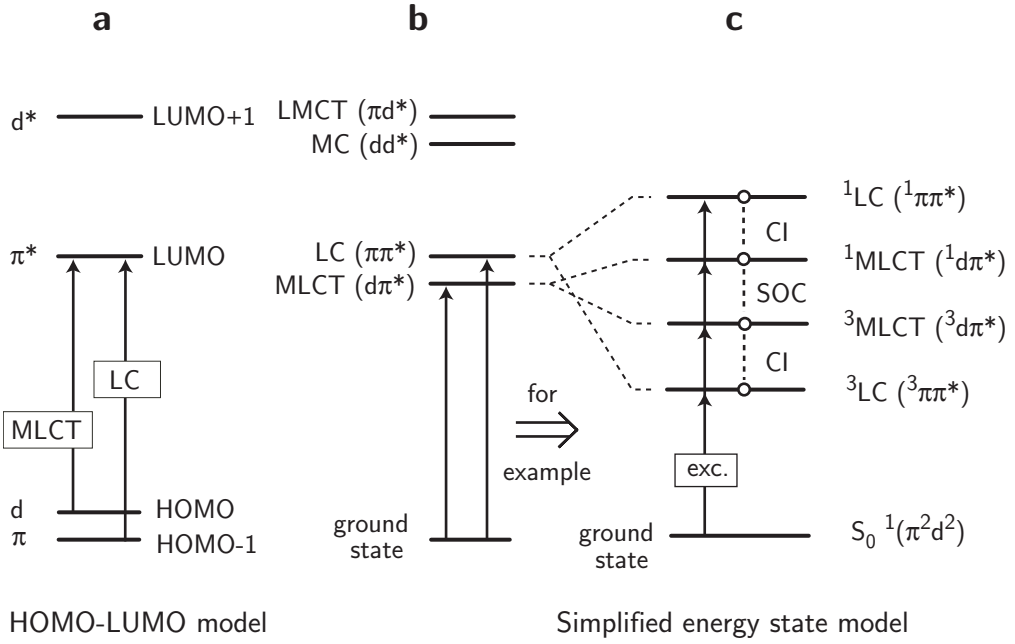


**Figure 10** (a) Example of simple MO model for a compound with single $\pi$-, d-, and $\pi^*$-orbitals and the respective transitions. It is assumed that the d$^*$-orbital lies at a significantly higher energy so that it does not lead to low-lying energy states. (b) Interim model of energy states resulting from (a). (c) Energy state model including the exchange splitting into singlet and triplet states. The states can experience mixings due to configuration interaction (CI) and spin-orbit coupling (SOC). Note that the sequence of states can differ from the given situation.

states resulting from the described transitions is given. Secondly, in principle also a metal-centered (MC) transition of d-d$^*$ character and a ligand-to-metal charge transfer (LMCT) transition of $\pi$-d$^*$ character can occur. However, these excitations are not important, if the d$^*$-orbital(s) lie(s) at high energies. Since the presence of low-lying d$^*$-orbitals can lead to emission quenching at ambient temperature, [120] OLED emitters are usually chosen to have d$^*$-orbitals, which lie at sufficiently high energy. Therefore these LMCT and MC excitations are not included in the further discussion.

It is important to note that the model schematically given in Fig. 10b is a very crude one. To approximate a more realistic model of energy states, electron-electron interactions have to be taken into account, i.e. the Coulomb and the exchange interaction between the electron in the excited state and the remaining electron in

the ground state. This leads to a splitting into singlet and triplet of the **LC** state ($^1$**LC** ($^1\boldsymbol{\pi\pi^*}$) and $^3$**LC** ($^3\boldsymbol{\pi\pi^*}$)) and of the **MLCT** state ($^1$**MLCT** ($^1\mathbf{d\pi^*}$) and $^3$**MLCT** ($^3\mathbf{d\pi^*}$))(compare Fig. 10c). The magnitude of splitting is determined by the exchange integral which, for example for the **LC** state, is given by

$$K = \text{const} \times \left\langle \pi(r_1)\pi^*(r_2) \left| \frac{1}{r_{12}} \right| \pi(r_2)\pi^*(r_1) \right\rangle \quad . \tag{6}$$

$\pi$ and $\pi^*$ are the HOMO and LUMO wavefunctions, $r_1$ and $r_2$ represent the electron coordinates, and $r_{12}$ the separation between the two electrons (compare, e.g. , Ref. [127], p. 174).

On closer inspection of the exchange integral, an important consequence becomes obvious: With an increasing conjugation length of the $\pi$ and $\pi^*$ orbitals, the exchange integral becomes smaller. This is found in purely organic molecules where, for example, from benzene to anthracene, the singlet-triplet splitting $\Delta E(^1\pi\pi^*\text{-}^3\pi\pi^*)$ decreases from $\approx 18000\,\text{cm}^{-1}$ to $\approx 10500\,\text{cm}^{-1}$ [128]. To organo-transition metal complexes, a corresponding trend applies. For **MLCT** states, the spatial extension of the wavefunctions is usually significantly larger than for **LC** states. Hence, the singlet-triplet splitting can be significantly smaller for **MLCT** states (or **LC** states with **MLCT** admixtures) than it is for (pure) **LC** states.[45] This difference is expressed also in Fig. 10c.

Due to the fact that the singlet-triplet splitting can be quite different for the lowest states **LC** and **MLCT**, it is not possible to predict the sequence of the lowest energy states as seen in Fig. 10c simply from the relative positions of the involved molecular orbitals given in Fig. 10a. Thus the situation illustrated in Fig. 10c represents only an example, which but is typical for a large number of complexes. (Compare Fig. 11, next Section.)

However, for the emission properties of a complex, the character of the lowest state regarding its LC/MLCT parentage is crucial. Spin-orbit coupling (SOC) to higher-lying singlet states, which can provide allowedness to the radiative transition from the lowest triplet state $\mathbf{T_1}$ to the ground state $\mathbf{0}$, is only effective, if this $\mathbf{T_1}$ state is of significant MLCT parentage. This is not necessarily the case only for pure **M**LCT states. Also **L**C states can exhibit significant MLCT parentage due to mixing with higher lying **M**LCT states. Different mixings can occur by electron-electron interaction between the different configurations (MLCT, LC, configuration interaction) and by SOC, and are indicated as well in Fig. 10c. Details about these mixings are discussed in Sect. 2.5.

Although the energy state diagram of Fig. 10c is quite illustrative, the real situation is considerably more complex. In particular, the number of energy states is far from being realistic. If more frontier orbitals are included in the considerations, the number of resulting energy states is drastically increased. Thus, for example, a model in which eight frontier orbitals are taken into account and which is applied to $Ir(ppy)_3$, has been published in Ref. [120] (p. 20 ff.). Regarding all possible transitions between the in part degenerate frontier orbitals in $C_3$ symmetry, a total number of 108 MLCT/LC states is obtained, 36 of which are doubly degenerate. If the $C_3$ symmetry is not obeyed strictly, the latter states split and a total number of even 144 states is obtained. Interestingly, also a theoretical investigation carried out by Nozaki [52] involves a large number of states, of which 70 states are found to lie within $8000\,cm^{-1}$ (1 eV) above the lowest triplet state $\mathbf{T_1}$. Accordingly, the density of states in the lower energy range is quite high and it is again pointed out that these states are, in part, quantum-mechanically mixed. This will be addressed in the following sections.

## 2.3 Origin of phosphorescence – Spin-orbit coupling

As substantiated in Sect. 2.1, triplet excitons need to be utilized in OLEDs in order to achieve high efficiencies. Harvesting of triplet excitons is possible by applying emitter dopants which emit due to a transition from an excited triplet state to a singlet ground state. Such a phosphorescence is in principle forbidden by reason of spin selection rules. It only gains allowedness, in case the emitting triplet state does not represent a 'pure' triplet, but also contains singlet contributions. This is often given in organo-transition metal complexes, in which singlet and triplet states may be partially mixed due to (indirect or direct) spin-orbit coupling (SOC, compare Sect. 2.2). SOC may strongly affect the emitting triplet state $\mathbf{T_1}$ of such a complex and, hence, determines important photophysical properties. In the following, important effects of SOC are introduced in more detail. Especially the splitting of the $\mathbf{T_1}$ state into substates and the radiative rates of the transitions from these substates to the electronic ground state $\mathbf{S_0}$ are addressed.

A quantum mechanical description of SOC can be given by perturbation theory using the spin-orbit Hamiltonian $\hat{H}_{SO}$ for the many electron states. It is given as a

sum of one-electron operators $\hat{h}_{\mathrm{SO}}$.

$$\hat{H}_{\mathrm{SO}} = \sum_i \hat{h}_{\mathrm{SO},i} \tag{7}$$

An operator $h_{\mathrm{SO},i}$, in turn, represents (approximately) a sum of contributions of each atom A of the complex

$$\hat{h}_{\mathrm{SO},i} = \sum_A \hat{h}_{\mathrm{SO}}(A) \quad , \tag{8}$$

where $\hat{h}_{\mathrm{SO}}(A)$ represents the SOC Hamiltonian of electron $i$ regarding its orbital angular momentum with respect to atom A. It is of the form

$$\hat{h}_{\mathrm{SO}}(A) = \xi_{\mathrm{A}}(r) \cdot \hat{\mathbf{l}}(A) \cdot \hat{\mathbf{s}} \quad , \tag{9}$$

wherein $\hat{\mathbf{l}}(A)$ is the operator of the orbital angular momentum with respect to atom A and $\hat{\mathbf{s}}$ is the operator of the spin momentum of an electron, respectively. $\xi_{\mathrm{A}}(r)$ is a one-electron spin-orbit coupling constant, which increases with an effective nuclear charge of atom A and depending on the distance to atom A. $\xi_{\mathrm{A}}(r)$ is large particularly for third row transition metals and, for example, for Ir this constant is assumed to be by a factor of more than 100 larger than for C.[129] Thus, the contributions of all other nuclei in the molecule can be neglected and the sum of Eq. 8 reduces to $\hat{h}_{\mathrm{SO}}(M)$, with $M$ being the heavy central-metal. The many-electron SOC Hamiltonian then can be written as

$$\hat{H}_{\mathrm{SO}} \approx \sum_i \xi_M(r_i) \cdot \hat{\mathbf{l}}_i(M) \cdot \hat{\mathbf{s}}_{\mathbf{i}} \quad . \tag{10}$$

This operator can be used to express the energies of the triplet substates in second order spin-orbit perturbation theory. The zero-order wavefunctions $\phi_{\mathrm{S_n}}$ and $\phi_{\mathrm{T_n}}$ and the energies $E_{\mathrm{S_n}}$ and $E_{\mathrm{T_n}}$ of the singlet and triplet states are considered as known. They are, for example, determined by DFT calculations.[52, 130, 131] The energies $E$(i) of the resulting (perturbed) triplet substates of $\mathbf{T_1}$, with i = I, II, III can be expressed by [120, 132]

$$E(\mathrm{i}) = E_{\mathrm{T_1}} + \sum_{\substack{n \\ \text{singlets}}} \frac{\left|\left\langle \phi_{\mathrm{S_n}} \left| \hat{\mathrm{H}}_{\mathrm{SO}} \right| \phi_{\mathrm{T_{1(i)}}} \right\rangle\right|^2}{E_{\mathrm{T_1}} - E_{\mathrm{S_n}}} + \sum_{\substack{n \\ \text{triplets}}} \frac{\left|\left\langle \phi_{\mathrm{T_{n(j)}}} \left| \hat{\mathrm{H}}_{\mathrm{SO}} \right| \phi_{\mathrm{T_{1(i)}}} \right\rangle\right|^2}{E_{\mathrm{T_1}} - E_{\mathrm{T_n}}} \quad . \tag{11}$$

The matrix elements are non-zero, if the mixing states have the same symmetry

representation.[120] This is due to the fact that $\hat{H}_{SO}$ is totally symmetric. Due to the mixing, an energetic stabilization of the substates **I**, **II**, and **III** results. Since this stabilization occurs individually for each substate, depending on the respective matrix elements, a separation of the substates results which is referred to as zero-field splitting (ZFS) of the $\mathbf{T_1}$ state. The ZFS of organo-transition metal complexes due to SOC can be by a factor of 2000 higher than the typical splitting in purely organic molecules, which is mainly due to spin-spin interactions. (See Ref. [120] and Fig. 11.) The magnitude of ZFS is an important parameter for an assessment of photophysical properties of a complex and its applicability as OLED emitters. This will be discussed in Sects. 2.5 and 4.5.

As already mentioned above, SOC also influences the allowedness of an optical transition from the $\mathbf{T_1}$ state to the electronic ground state $\mathbf{S_0}$. The rate constant $k^r(\mathrm{i})$ of a transition from the triplet substate i, with i = I, II, III, to the electronic ground state can be expressed by use of perturbation theory as [133, 134]

$$k^r(\mathrm{i}) = \mathrm{const} \times \bar{\nu}^3 \times \left| \sum_{S_n} \frac{\left\langle \phi_{S_n} \left| \hat{H}_{SO} \right| \phi_{T_{1(i)}} \right\rangle}{E_{T_1} - E_{S_n}} \times \left\langle \phi_{S_0} \left| e\hat{\mathbf{r}} \right| \phi_{S_n} \right\rangle \right|^2 \quad , \qquad (12)$$

where $\bar{\nu}$ is the transition energy in $\mathrm{cm}^{-1}$ and $e\hat{\mathbf{r}}$ is the electric dipole operator. The transition from $\mathbf{T_1}$ to $\mathbf{S_0}$ gains allowedness from the mixing of singlet states, for which the transition to the ground state is spin-allowed, to the triplet $\mathbf{T_1}$. In Sect. 2.2 it has been shown that a large number of excited states is available in an adjacent small energy range and can in principle contribute. Thus, radiative rates may be greatly enhanced in organo-transition metal complexes compared to purely organic molecules. Emission decay times can be shortened by several orders of magnitude, for example from s for the free ligand to a few µs for the complex. Note that, depending on the matrix elements of Eq. 12, the resulting decay times of the individual substates can be quite different. For example, it has been found for a large number of complexes that the radiative transition $\mathbf{I} \rightarrow \mathbf{0}$ from the lowest substate to the ground state is largely forbidden, while transition $\mathbf{III} \rightarrow \mathbf{0}$ is significantly allowed.[48, 120, 135] For $Ir(btp)_2(acac)$, for example, the corresponding rates vary by a factor of more than 50 (see Chapt. 5), for $Ir(ppy)_3$ this factor is even as large as $\approx 200$ [48]. Thus, for these complexes, the lowest substate represents an almost pure triplet, while states **II** and **III** contain significant admixtures of singlet character. For $Ir(ppy)_3$, the described situation has been substantiated theoretically in Ref. [52]. Nozaki calculated singlet contributions to the substates **II** and **III** of

2% and 1%, respectively, and no singlet contributions to substate **I**.

An increase of the radiative rates usually will also bring about an increase of the photoluminescence quantum yield $\phi_{\mathrm{PL}}$, if the non-radiative rates (constant $k^{\mathrm{nr}}$) are assumed to stay the same, according to

$$\phi_{\mathrm{PL}} = \frac{k^{\mathrm{r}}}{k^{\mathrm{r}} + k^{\mathrm{nr}}} \quad . \tag{13}$$

## 2.4 Zero-field splitting and MLCT perturbation

In the previous section, it has been shown that spin-orbit coupling of the $\mathbf{T_1}$ state to higher lying singlets is crucial for gaining those photophysical properties of a compound which render it attractive for application in OLEDs. Spin-orbit coupling, however, is only effective, if $^{1,3}$**MLCT** ($^{1,3}\mathbf{d\pi^*}$) contributions are present in the mixing wavefunctions. This is easily seen by a closer inspection of a coupling matrix element as given in Eqs. 11 and 12. If the electronic wavefunction is written as a product of spatial orbitals $\chi$ and spin parts $\theta$, according to

$$\phi = \chi \cdot \theta \quad \text{with} \quad \theta = \uparrow, \downarrow \quad , \tag{14}$$

a matrix element of the single electron SOC Hamiltonian (with coupling by the central metal M) can be explicated using Eq. 9 as

$$\left\langle \phi_1 \left| \hat{\mathrm{h}}_{\mathrm{SO}}(\mathrm{M}) \right| \phi_2 \right\rangle = \xi_{\mathrm{M}}(\mathrm{r}) \left\langle \chi_1 \left| \hat{\mathbf{l}}(\mathrm{A}) \right| \chi_2 \right\rangle \cdot \langle \theta_1 \left| \hat{\mathbf{s}} \right| \theta_2 \rangle \quad . \tag{15}$$

Obviously, the first matrix element on the right-hand side will only not vanish, if both spatial wavefunctions carry orbital angular momentum with respect to the same center (M). Only in this case, the orbital angular momentum operator may couple the spatial wavefunctions.[132] If the center is a heavy metal ion such as Ir(III) or Pt(II), spin-orbit coupling may be significant. For typical organo-transition metal complexes like Ir(III) or Pt(II) emitters, d-orbital character has to be involved in both coupling wavefunctions. This is fulfilled in case the coupling states each result from an MLCT (d-$\pi^*$) excitation. (See the theoretical elaboration in Ref. [132].) Conclusively, SOC couples only those states effectively which contain sufficient MLCT contributions, such as $^{1,3}$**MLCT** states. In contrast, coupling between largely ligand-centered ($^{1,3}$**LC**) states or between $^{1,3}$**LC** and $^{1,3}$**MLCT** states will not be effective. If, in a typical situation (see Fig. 10), the lowest excited state is a $^3$**LC** state, direct coupling to higher-lying states will correspondingly not occur.

However, indirect coupling can occur, if the lowest-lying state **$^3$LC** is mixed with a nearby MLCT state such as a **$^3$MLCT** state by configuration interaction (CI). Then, the MLCT parentage enables SOC to higher-lying singlet and triplet MLCT states. Hence, in organo-transition metal complexes, a presence of effects of spin-orbit coupling indicates an MLCT perturbation of the emitting **$^3$LC** state.

Interestingly, this circumstance can even be applied to assess the extent/degree of MLCT perturbation of the **$^3$LC** state. As discussed in the previous section, state mixing by spin-orbit coupling – among others – results in a zero-field splitting of the lowest triplet state. Assuming that a **$^3$LC** state is the lowest excited state, its ZFS reflects the extent of MLCT admixtures to this state. The magnitude of ZFS may therefore by used for a classification of complexes according to the MLCT parentage of their emitting states. Thus, complexes with a small ZFS, for example below 1 $cm^{-1}$, are regarded to emit from only slightly perturbed ligand-centered **$^3$LC** states. Representatives of this class are, for example, $Pd(2\text{-thpy})_2$ [45, 136] (thpy=(2-thienyl)pyridinate), $Pdq_2$ (q=8-hydroxyquinoline) [137] and $Ptq_2$ [46, 125] and $[Rh(bpy)_3]^{3+}$ (bpy=2,2'-bipyridine) [22, 138] and $[Pt(bpy)_2]^{2+}$ [46, 138, 139] as well as the heteroleptic $Ir(ppy)_2(CO)(Cl)$ [135, 140]. In contrast, in complexes featuring a large ZFS, the emitting state is dominated by MLCT parentage. This is the case for the well-known $Ir(ppy)_3$, for which we previously demonstrated a large zero-field splitting of more than 80 $cm^{-1}$ (see Ref. [48]). Evidence for the high MLCT character has also been given in theoretical investigations of Hay [51] and Nozaki [52]. Other examples of emitters with strong MLCT components are $[Ru(bpy)_3]^{2+}$ and $[Os(bpy)_3]^{2+}$ with zero-field splittings of the lowest triplet state of 60 [46, 138, 141] and 210 $cm^{-1}$ [46, 141], respectively. If the emitting triplet of a complex exhibits a ZFS-value in the intermediate range, this state is classified as mixed **$^3$LC/$^3$MLCT** state or as **$^3$LC** state with significant MLCT-perturbations. To this class, complexes such as $Pt(2\text{-thpy})_2$ and $Pt(2\text{-ppy})_2$, with 16 [45, 46, 141] and 32 $cm^{-1}$ [46, 141], respectively, are assigned. $Pt(Me_4salen)$ (salen=*N,N'*-bis(salicylidene)) is another representative of this group featuring a splitting of 17 $cm^{-1}$.[142] In the chapters below (Chapts. 4 and 7), an assessment of ZFS is presented for the frequently applied OLED emitter $Ir(btp)_2(acac)$. The referred investigations have been carried out in different matrices and yield moderate ZFS values between 15 and 27 $cm^{-1}$. An interpretation is given in Sect.4.5. For a systematic assessment of MLCT parentage of the emitting states $\mathbf{T_1}$ in different complexes, an ordering scheme has been developed by Yersin [45, 46, 119, 120, 138, 141, 143] which is given in Fig. 11. This scheme brings the discussed ZFS and MLCT parentage in relation for a large number of complexes.

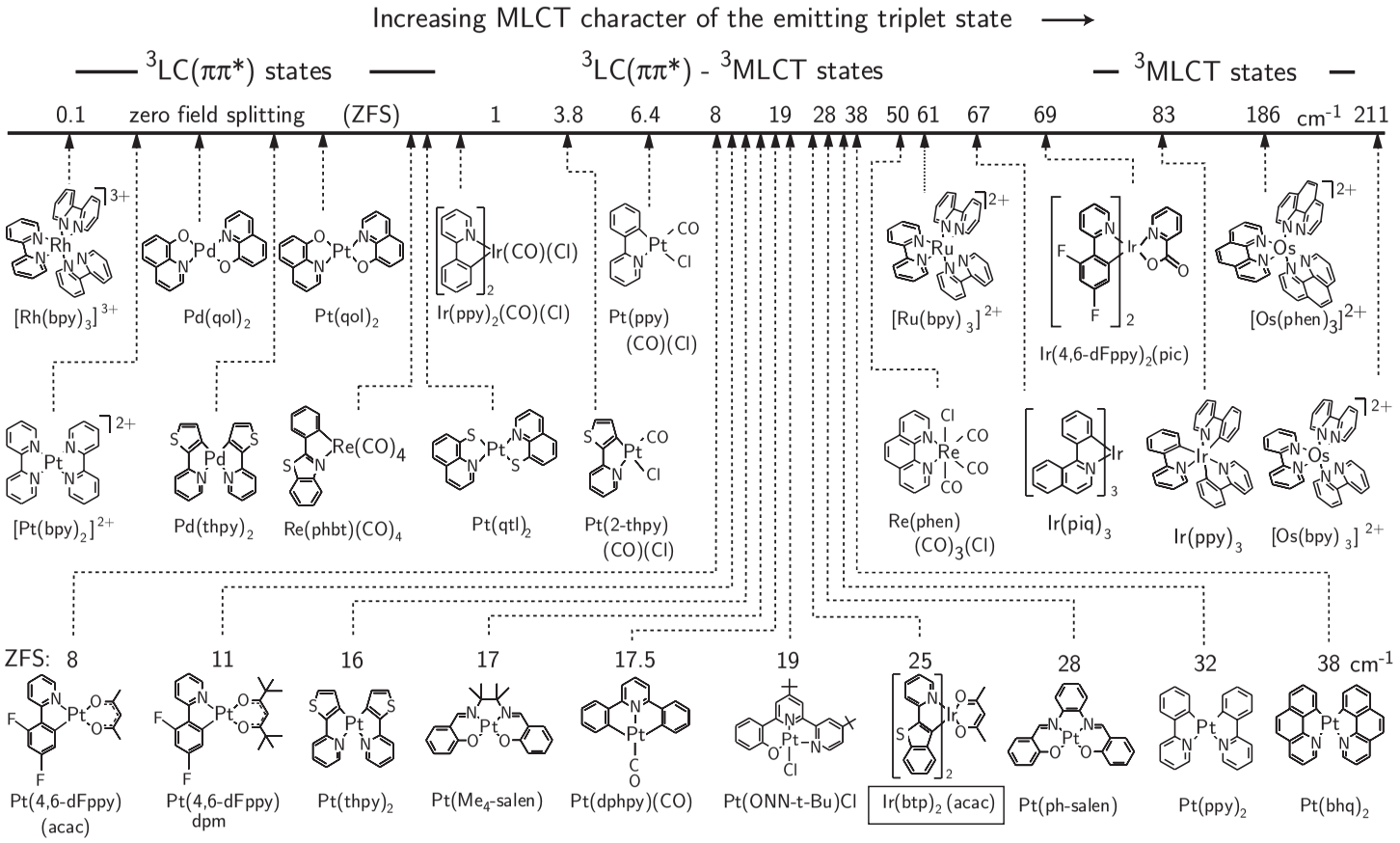


**Figure 11** Ordering scheme for organo-transition metal complexes with respect to the MLCT parentage of the emitting state $\mathbf{T_1}$, developed by Yersin et al. (compare, e.g., the Refs. [45, 46, 119, 120, 138, 141, 143]). The MLCT parentage is closely related to the zero-field splitting (ZFS) of the $\mathbf{T_1}$ state and determines important photophysical properties of the complexes, such as the radiative rates, intersystem crossing times, and luminescence quantum yields.

An assessment of the MLCT character is of great importance, as this is responsible not only for the ZFS of the lowest triplet, but also for many other properties which govern the photophysics of a compound. Thus, for example, with increasing MLCT character, the *singlet-triplet splitting* $\Delta E(S_1 - T_1)$ becomes smaller. For purely organic molecules of the size of the ligands used and exhibiting $\pi$-$\pi^*$ transitions, the splitting is typically of the order of $10^4\,\mathrm{cm}^{-1}$. On the other hand, in organo-transition metal complexes splittings as small as $3000\,\mathrm{cm}^{-1}$ may easily be found. (Compare Ref. [45].) MLCT perturbed wavefunctions have a larger spatial extension and therefore experience weaker electron-electron interactions. Moreover, a larger MLCT parentage of the emitting state strongly affects the *intersystem crossing (ISC)* between the $\mathbf{S_1}$ state and the $\mathbf{T_1}$ state. In organic $\pi\pi^*$-emitter molecules the corresponding rate is comparatively small. The characteristic time is usually notedly longer than the radiative decay time of the $\mathbf{S_1}$ state and can be in the order of 100 ns or even more. In contrast, in organo-transition metal complexes the ISC is drastically reduced due to singlet-triplet mixing induced by SOC. For $Pt(thpy)_2$ with a high MLCT perturbation, for example, the ISC time is as short as ≈50 fs.[45] ISC therefore effectively quenches the fluorescence and populates the lowest triplet $\mathbf{T_1}$. This represents an important factor for the OLED application of organo-transition metal complexes, as not only the 75% triplet excitons, but also the 25% singlet excitons are supposed to be harvested (see Sect. 2.1). The most important trend is, however, that the *radiative rates* of phosphorescence (transition $\mathbf{T_1} \rightarrow \mathbf{S_0}$) increase drastically with the MLCT perturbation of the emitting state. Singlet admixtures to $\mathbf{T_1}$ substates as described in the previous section can, for example, reduce the *radiative decay time* from ≈1 s, as typical for organic $\pi\pi^*$-emitter compounds, to only a few µs in organometallic complexes with significant MLCT character. To give an example, for $Ir(ppy)_3$ in THF (tetrahydrofurane) solution a decay time of substate **III** of ≈750 ns has been demonstrated.[48] A short emission decay time is quite important for emitters in OLEDs, to reduce saturation effects and bimolecular emission quenching at high current densities, and also to improve the chemical stability of the emitter. Along with a shorter emission decay time of an emitter comes usually also a higher *emission quantum yield* $\phi_{PL}$, if the non-radiative rates are not altered as well. (Compare Eqs. 1 and 13.) The essential importance of high $\phi_{PL}$ values for OLEDs has been pointed out in Sect. 1.2. Organo-transition metal complexes can exhibit very high values of $\phi_{PL}$ which can come close to 100%, as is the case, for example, for $Ir(ppy)_3$ in CBP matrix.[74] Beside the described important trends, also the vibrational satellite structure of the emission is altered. With increasing MLCT character, metal-ligand vibrations are

stronger involved in the emission process. As a consequence, corresponding low energy vibrational satellites, observed in the energy range up to about 600 $cm^{-1}$ from the electronic origin, become more important.[144] This phenomenon, which can lead to a smearing out of the emission spectrum, will be discussed for $Ir(btp)_2$-(acac) in Chapt. 6.

To summarize, desired properties of an organo-transition metal complex to be applicable as OLED emitter are closely related to the MLCT parentage of the emitting triplet state. In this regard, extensive investigations are necessary to be able to relate the MLCT parentage with chemical peculiarities of a complex to be able to systematically improve or design new complexes.

## 2.5 Spin-orbit coupling routes – Why octahedral complexes may be better

On closer inspection of the ordering scheme given in Fig. 11 , an interesting trend strikes the attention. Complexes with a large zero-field splitting above 40 $cm^{-1}$ and correspondingly high MLCT parentage of the $\mathbf{T_1}$ state, systematically seem to feature (quasi-)octahedral coordination. In particular, one finds Ir(III), Os(II), Ru(II), and Re(I) compounds with a $d^6$ electron configuration. For quasi-square planar compounds such as Pt ($d^8$ electron configuration) in contrast, comparatively high ZFS values, larger than 40 $cm^{-1}$, have not yet been observed. To understand this phenomenon, the routes of spin-orbit coupling have to be compared for those two classes of compounds.

As seen in Sect. 2.2, a large number of adjacent higher lying states is available for mixing with the $\mathbf{T_1}$ state by spin-orbit interaction. Nonetheless, only a comparatively small number of mixing matrix-elements contributes significantly.[52, 132] These are to be identified. First of all, in Sect. 2.4 it has been shown that the mixing matrix-elements are $\neq 0$, only if d-orbital contributions are contained in both the respective wavefunctions. This is the case for states containing MLCT parentage. But this rule can be further refined: In Ref. [132] it is pointed out that a coupling even of two MLCT states, if they involve the same *same $\pi^*$-orbital*, is only effective, in case *different d-orbitals* are involved in these coupling states. This is illustrated in Fig. 12, showing a situation in which two MLCT states interact simply by being coupled by a one-electron operation between different d-orbitals.

With this important message, the differences of quasi-square planar and quasi-octahedral compounds can be identified. Ligand-field theory tells us, how the d-

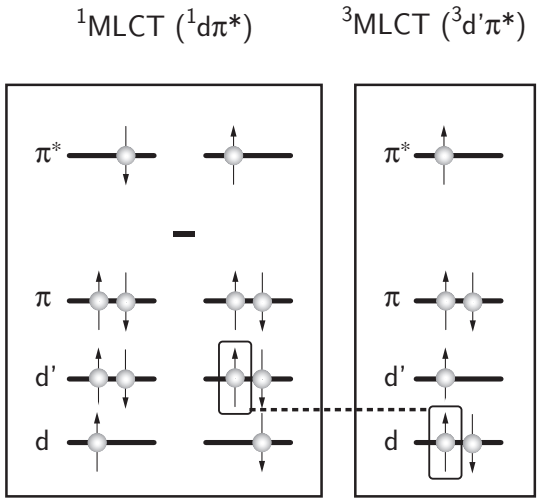


**Figure 12** SOC between a **$^1$MLCT ($^1$d$\pi^*$)** and a **$^3$MLCT ($^3$d′$\pi^*$)** state. The states differ only in the occupation of one orbital. According to [132] and the therein given coupling rules, SOC may only be effective, if in the concerned states different d-orbits are involved (here d and d'). (Illustration adapted from Ref. [132].)

orbitals of the central metal split, when going from the spherical symmetry of the free atom to the reduced symmetry in an octahedral ($O_h$ symmetry) or a planar ($D_{4h}$ symmetry) situation. The splittings for both classes are given in Fig. 13 according to Ref. [145]. In $O_h$ symmetry, the six d-electrons will occupy the lowest (degenerate) orbitals $d_{xy}$, $d_{yz}$, and $d_{xz}$. If the symmetry of the complex is distorted, the degeneracy of these orbitals will be lifted and a splitting will occur (not depicted). If the distortion is weak, the corresponding splitting will be small. Therefore, in case of a $d-\pi^*$ excitation from one of those d-orbitals (e.g. $d_{xy}$), a second d-orbital (d', e.g. $d_{yz}$) will be close enough to allow for a mixing of states according to Fig. 12. The presence of at least one d'-orbital close to the d-orbital involved in the excitation renders strong SOC possible. The smaller the energy denominator $\Delta E$(d−d') (compare Eqs. 11 and 12) of the mixing matrix element is, the more effective the mixing may be. Due to the energy proximity of the three lowest d-orbitals in the quasi-octahedral situation, corresponding complexes often exhibit strong effects of SOC. For exactly the same reason, however, the mixing conditions in the quasi-square planar case are distinctly different. A strict square planar coordination is characterized by a lower symmetry than given in case of an octahedral coordination. Therefore, additional splittings occur. The situation is given on the right hand side

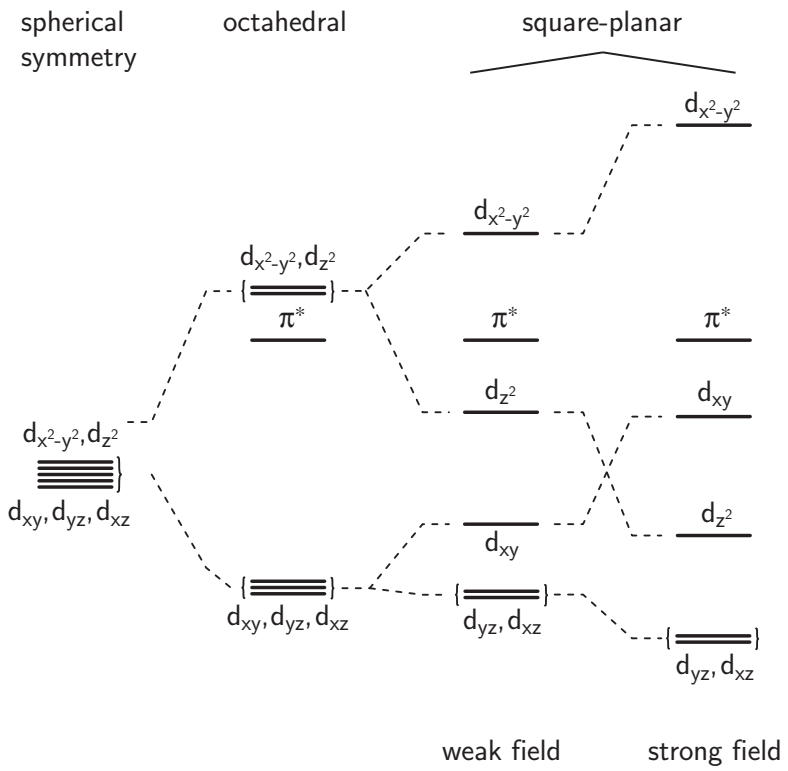


**Figure 13** Splitting of the d-orbitals under the influence of an octahedral ligand field (a) and a square planar ligand field (b). The splitting pattern in the square planar case can be derived from the octahedral one assuming a distortion, which removes the two ligands in z-dimension. The square planar case is given for a weak and a strong ligand field, respectively. (Illustration adapted from Ref. [145] p. 69)

of Fig. 13 for a strong ligand field. The splitting can be derived from the octahedral situation assuming a distortion, which removes the two ligands in z-dimension (see e.g. Ref. [145] p. 58 ff and p. 69). In the ground state, the eight d-electrons will occupy the orbitals $d_{xy}$, $d_{yz}$, $d_{xz}$, and $d_{z^2}$. In case of a strong ligand field, the HOMO ($d_{xy}$, d) and the HOMO-1 ($d_{z^2}$, d') level exhibit a large energy separation. This is also the case if, in a more realistic view, the square planar symmetry is regarded to be distorted. Hence, due to the larger energy denominator $\Delta E(\mathrm{d} - \mathrm{d}')$, mixing of the two lowest lying MLCT states is less favored for quasi-square planar complexes as compared to quasi-octahedral ones. This represents an approach to a general explanation of why stronger MLCT character is possible with an octahedral coordination.

Having in mind the splitting patterns of Fig. 13, one might also come to a different conclusion. For the quasi-square planar case, weaker ligands may exist which lead to an intermediate d-orbital splitting with the $d_{z^2}$ and the $d_{xy}$ orbital coming very close. SOC could be of similar strength as found for effective octahedral emitters then. However, such a situation has not been found so far and, in practice, ligands are used which cause a high ligand field strength ('strong ligands'). This is necessary to shift the unoccupied d-orbitals to sufficiently high energies, since low lying d-states quench the emission effectively.

On the other hand, even for complexes with $d^6$ electron configuration, the octahedral symmetry might be seriously distorted, leading to a situation, which is not much better than the one in quasi-square planar complexes.

## 2.6 Summary

In this chapter, it has been shown that important photophysical properties of organo-transition-metal complexes are closely related to the metal-to-ligand charge transfer (MLCT) character of the emitting triplet state $\mathbf{T_1}$. According to the ordering scheme given in Sect. 2.4 (Fig. 11), there is a trend which indicates that those complexes exhibiting a high MLCT character and, thus, effective spin-orbit coupling are in the majority of cases (quasi-)octahedral ones. Nevertheless, (quasi-)octahedral complexes with only little MLCT perturbation of the $\mathbf{T_1}$ state exist as well. (Compare Fig. 11 and, e.g., Ref. [135].) This depends, for example, on the type of ligands and the ligand-field strength.[120] In particular, it is not unlikely that the matrix environment which, in some form, is always present when applying or investigating a complex, might play an important role as well. The role of the environment, however, has not been specifically investigated up to now by high resolution spectroscopic means, since most of the spectroscopy on organo-transition metal complexes so far has been carried out in Shpol'skii matrices.[45, 46, 146] Shpol'skii matrices are frozen (polycrystalline) n-alkanes which are relatively inert and often allow to register highly resolved spectra due to weak inhomogeneous and homogeneous broadening in these matrices. However, this does not necessarily also apply to other matrices, e.g. matrices which are oftentimes used in OLEDs. In general, a significant influence of the environment on the emission properties of a complex rather seems likely. In the following chapters it is intended to find evidence of matrix effects on the $\mathbf{T_1}$ state of an organo-transition metal complex on the example of $Ir(btp)_2(acac)$, which is investigated spectroscopically in different host materials.

# 3 Ir(btp)$_2$(acac) – A Red OLED Emitter

## 3.1 Motivation

The importance of the metal-to-ligand charge transfer (MLCT) character of the emitting triplet state $\mathbf{T_1}$ of organo-transition metal complexes has been pointed out in the preceding chapter. Photophysical properties, such as a short emission decay time and a high emission quantum yield are related to a large MLCT character of the $\mathbf{T_1}$ state. The degree of MLCT character is characterized by the magnitude of zero-field splitting (ZFS) of the $\mathbf{T_1}$ state into substates.

Interestingly, the importance of the ZFS is attracting more and more attention among material developers and device scientists, and an increasing number of experimental and theoretical investigations addresses the ZFS and MLCT character of OLED related complexes.[52, 147–149] However, the number of OLED-relevant complexes which have been investigated hitherto in this respect is quite low, whereas extensive investigations are necessary, for example, for synthetic chemists to be able to include the MLCT character into chemical considerations, when designing new complexes. Presumably, for complexes to be successfully applicable in OLEDs, there is a minimum value the ZFS should not fall below. Such a limit has not been defined so far in the literature, although it could represent an important design goal for organo-transition metal complexes to be applied in OLED.

The investigations on Ir(btp)$_2$(acac) (bis(2-(2'-benzothienyl)-pyridinato-*N*,C$^{3'}$)-iridium(acetylacetonate), see Fig. 14) described in the following chapters are aimed to lead towards a better understanding of the photophysical characteristics of Ir-complexes, in particular, those important for OLED applications.

Ir(btp)$_2$(acac) is a well-known representative of the group of organo-transition metal triplet emitters. Several properties render it highly attractive for application in OLEDs. The complex exhibits a saturated red emission peaking at about 612 nm,[40, 42, 150] which is close to the NTSC[16] standard recommended for video display. Moreover, the emitter features a high photoluminescence quantum yield of,

[16]NTSC= National Television System Commitee.

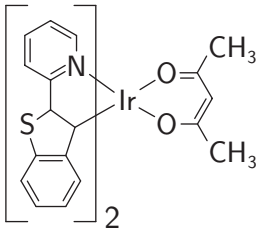


$Ir(btp)_2(acac)$

**Figure 14** Chemical structure of the red triplet emitter $Ir(btp)_2(acac)$, which is frequently used in OLEDs.

e.g., 21% in solution with a decay time of 5.8 µs.[150] In a CBP[17] film, a $\phi_{PL}$ value of even 50% has been reported.[74] A high $\phi_{PL}$ value is retained even at high doping levels, e.g. 90% of the maximum $\phi_{PL}$ value is found at 33 wt% doping.[74] Further, the higher solubility compared to the one of the related tris-cyclometalated compound $Ir(btp)_3$ [151] renders $Ir(btp)_2(acac)$ also suitable for solution processing.

$Ir(btp)_2(acac)$ has already been investigated as emitter in different types of devices. For example, efficient red emitting OLEDs have been built with this molecule both by vacuum deposition [40, 150, 152] and by solution processing [42, 151, 153, 154]. Polymeric devices with conjugated or non-conjugated linkage of the emitter to a polymer host have been under study.[87, 88, 155] In addition to OLEDs incorporating $Ir(btp)_2(acac)$, electrogenerated chemiluminescence (ECL) has been demonstrated with the complex.[156–159] Moreover, the feasibility of producing OLEDs on float glass [160] as well as by deposition of the emission layer by spray coating [161, 162] has been studied using $Ir(btp)_2(acac)$. Further, several physical investigations, such as UPS and X-ray absorption spectroscopy,[163] and studies of charge transport properties of $Ir(btp)_2(acac)$ neat films and $Ir(btp)_2(acac)$ doped into a CBP matrix,[164] have also been carried out.

These extensive investigations demonstrate the high interest in $Ir(btp)_2(acac)$. Obviously, it is an attractive candidate for detailed spectroscopic investigations of its emission properties. First assignments were already presented in Ref. [150]. Mainly on the basis of ambient temperature broad band emission and absorption spectra of $Ir(btp)_2(acac)$ dissolved in Me-THF (2-methyltetrahydrofuran), the emitting triplet has been assigned to be of ligand-centered $\pi\pi^*$ character with MLCT admixtures. This is confirmed in the present report by high-resolution emission

[17] CBP=(4,4'-bis(carbazol-9-yl)biphenyl); for the structure, see Fig. 7

and excitation spectroscopic studies. The extent of MLCT character is assessed on the basis of the ZFS of the $\mathbf{T_1}$ state by high-resolution spectroscopy at low temperatures. Measurements under variation of temperature and magnetic field strength are applied as supporting experiments. The ZFS, in particular, is studied for different environments of the complex by site-selecting techniques (Chapt. 4) and by the newly applied method of spectral hole burning (Chapt. 7). Moreover, the relaxation properties within the system of $\mathbf{T_1}$ substates **I**, **II**, and **III** (Chapt. 5) and from these substates to the $\mathbf{S_1}$ ground state are studied at different temperatures by site-selective emission decay time measurements. Further, the vibrational satellite structure of the emission is discussed (Chapt. 6) on the basis of site-selected emission spectra recorded under variation of temperature or magnetic field strength, or using a time-resolving technique. The results are discussed with respect to the suitability of complexes as emitters in OLEDs.

## 3.2 Synthesis

$Ir(btp)_2(acac)$ was synthesized in the group of Prof. Mark E. Thompson (University of Southern California, Los Angeles, CA) according to the procedure described in Ref. [150], starting with a chloro-bridged dimer complex. The synthesis was carried out in inert gas atmosphere. The $Ir(btp)_2(acac)$ product is air stable and was characterized by elemental analysis (C, H, N), high-resolution mass spectroscopy, and NMR spectroscopy.

$Ir(btp)_2(acac)$ is assumed to feature an octahedral coordination geometry around Ir with *cis*-C,C *trans*-N,N chelate disposition (see Fig. 15). A corresponding structure has been proven for other complexes of the form $Ir(C\wedge N)_2(LX)$, for example, for $Ir(ppy)_2(acac)$ and $Ir(tpy)_2(acac)$.[165]

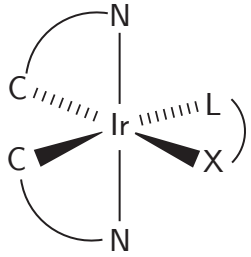


**Figure 15** Coordination geometry of $Ir(C\wedge N)_2(LX)$ complexes as given in Ref. [165].

## 3.3 Spectroscopic introduction

Figure 16 shows the absorption and the emission spectrum of $Ir(btp)_2(acac)$ measured under ambient conditions. The observed transitions are assigned in accordance with the literature [150] and in analogy to the assignments of the recently investigated compounds $Ir(ppy)_3$ [48] and $Ir(ppy)_2(CO)(Cl)$ [135].

Strong transitions in the wavelength region below ≈350 nm (28570 $cm^{-1}$) are assigned to be largely of LC (ligand-centered) (btp)$\pi\pi^*$ character. Maxima are observed at 284 nm (35210 $cm^{-1}$, $\epsilon_{max}$ = 33000 l $mol^{-1}cm^{-1}$), 327 nm (30580 $cm^{-1}$, $\epsilon_{max}$ = 22250 l $mol^{-1}cm^{-1}$), and 339 nm (29500 cm, $\epsilon_{max}$ = 22350 l $mol^{-1}cm^{-1}$). The absorption between 410 nm and 535 nm, with its maximum at 484 nm (20660 $cm^{-1}$, $\epsilon_{max}$ = 6300 l $mol^{-1}cm^{-1}$) is assigned to transitions from the singlet ground state to states with strong MLCT (Ir5d-(btp)$\pi^*$) contributions. This interpretation is based on the fact that for the pure (btp) ligand no significant absorptions are found in this energy range and **LMCT** states lie at higher energies. d-d$^*$ and $\pi$-$\pi^*$ transitions, on the other hand, exhibit significantly lower $\epsilon$ values than those observed between 410 nm and 535 nm. Weak transitions in the long wavelength region of the absorption are scaled by a factor of 100 in Fig. 16 (dashed line). Two weak bands at 552 nm (18115 cm, $\epsilon_{max}$ estimated to 60 l $mol^{-1}cm^{-1}$) and 598 nm (16720 $cm^{-1}$, $\epsilon_{max} \approx$ 80 l $mol^{-1}cm^{-1}$) represent absorptions both related to a triplet state, which turns out to be the lowest and emitting state $\mathbf{T_1}$, as described below. In the corresponding excitation, the (btp) ligand is expected to be predominantly involved, as the triplet levels of the (acac) ligand lie well above those of (btp).[150] Due to the resonance between absorption and emission, the peak at 598 nm corresponds to the electronic origins of the $\mathbf{T_1}$ state (for details, see Sect. 4.2). The shoulder at 552 nm exhibits an energy separation to the peak at 598 nm of ≈1400 $cm^{-1}$. Therefore, it might correspond to vibrational satellites. Indeed, the structure of the 300 K emission spectrum shows an equivalent band , which can safely be assigned to (several overlapping) vibrational satellites of ≈1400 $cm^{-1}$ energy difference relative to the corresponding electronic origins (see below). The fact that the absorption into the lowest triplet state $\mathbf{T_1}$ is observed is remarkable. It indicates an MLCT admixture to this state, since absorptions into largely pure triplet states exhibit substantially lower $\epsilon$-values and are usually not observed.

An excitation spectrum recorded at 77 K (Fig. 17) shows a structure quite similar to the absorption spectrum at 300 K, but a slight narrowing of the bands is observed. Thus, a more detailed structure is revealed in the regions of the ligand-centered transitions between 315 nm and 410 nm. Especially, an additional shoulder

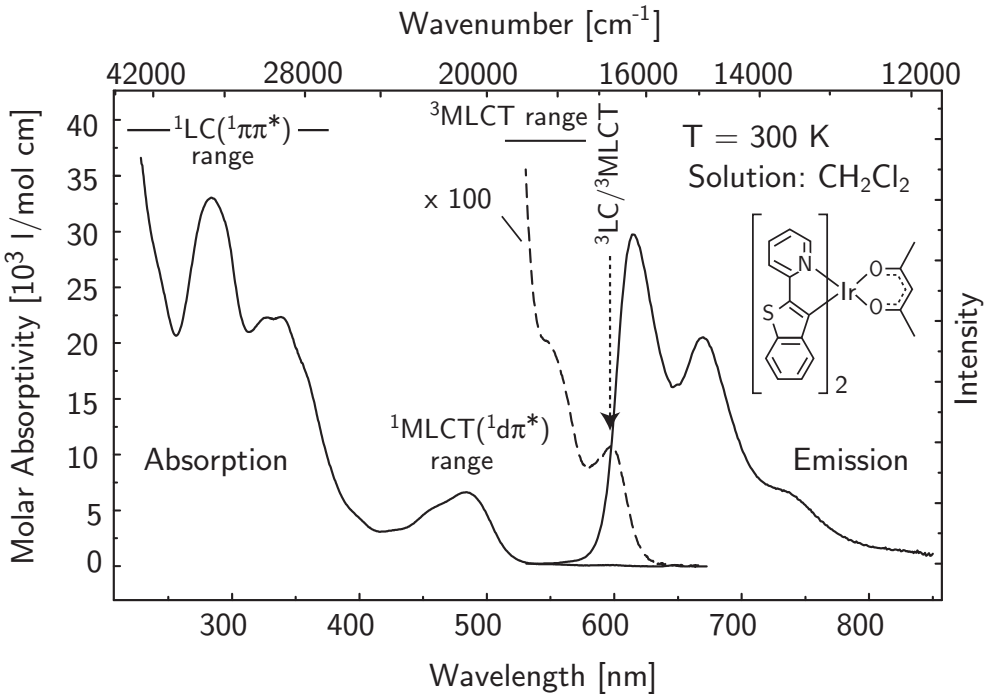


**Figure 16** Absorption and emission spectrum of $Ir(btp)_2(acac)$ in $CH_2Cl_2$ under ambient conditions. The dashed line shows the absorption in the region of the lowest excited states scaled by a factor of 100. The emission spectrum was measured at a concentration of about $10^{-5}$ mol/l under cw-excitation at 480 nm. The assignments given should not be taken too strictly, i.e., states designated as $^{1,3}$**LC** and $^{1,3}$**MLCT** contain also contributions of $d\pi^*$ and $\pi\pi^*$ character, respectively.

at 517 nm (19340 $cm^{-1}$) is recognized, with a significant molar extinction of roughly 1200 l $mol^{-1}cm^{-1}$. This value is by a factor of 15 larger than the one found for the band at 598 nm. Therefore, the shoulder is tentatively assigned to a higher lying state featuring a markedly larger MLCT contribution than the $\mathbf{T_1}$ state. This assignment is in agreement with the interpretation given for $Ir(ppy)_3$ which shows a similar structure in the region of the $^{1}$**MLCT**/$^{3}$**MLCT** $\leftrightarrow \mathbf{S_0}$ transitions.[135, 166, 167] In this context, it is important to note that, due to mixing of states by spin-orbit coupling, an assignment as either singlet or triplet is not strictly adequate and, therefore, should only by taken as a guideline.

The emission spectrum of $Ir(btp)_2(acac)$ measured in $CH_2Cl_2$ at 300 K and at 77 K, respectively, is depicted as well in Fig. 16 and Fig. 17. Both spectra are comprised of four broad bands. The spectrum recorded at 300 K has its maxi-

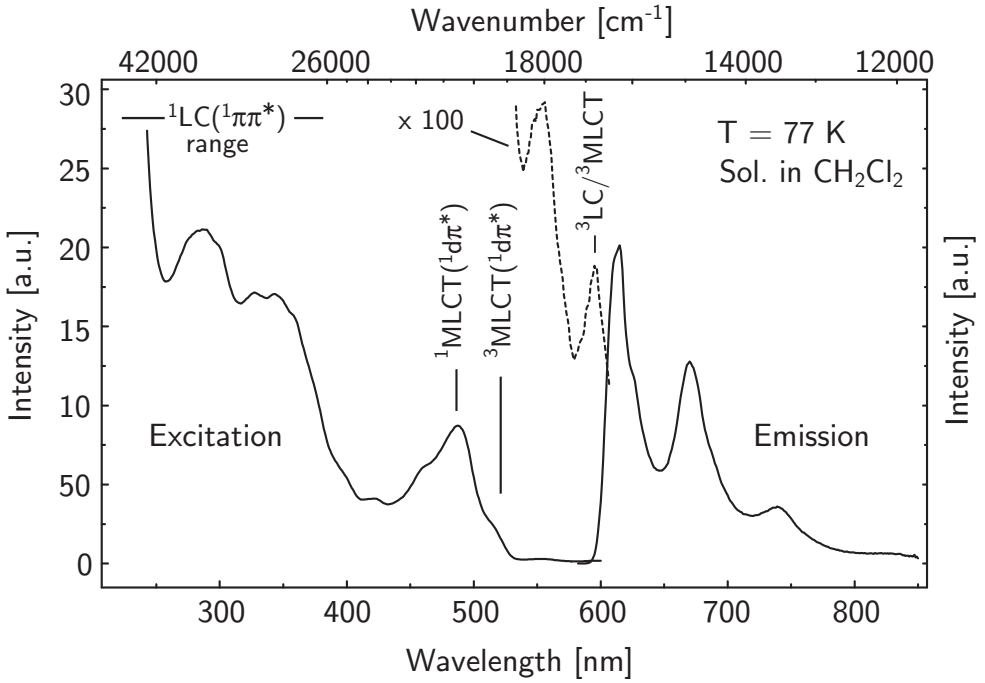


**Figure 17** Excitation ($\lambda_{det}$ = 614 nm) and emission spectrum of $Ir(btp)_2(acac)$ in $CH_2Cl_2$ at 77 K. The dotted structure shows the excitation in the region of the lowest excited states scaled by a factor of 100. The emission spectrum was measured at a concentration of about $10^{-5}$ mol/l under cw-excitation at 480 nm.

mum at 615 nm (16260 $cm^{-1}$). This band is related to the electronic origin transitions broadened inhomogeneously and homogeneously. Further peaks are found at 670 nm (14925 $cm^{-1}$), 738 nm (13550 $cm^{-1}$) and a weak one 825 nm (12120 $cm^{-1}$). These are ascribed to overlapping vibrational satellites which form a progression-like structure. Indeed, at low temperature ($T$ <10 K), a progression of ≈1400 $cm^{-1}$ is observed (see Sect. 6.4). With cooling from 300 K to 77 K, the emission spectrum experiences a band narrowing, presumably due to a decrease of the homogeneous broadening by electron-phonon interactions. The discussed progression-like structure is pronounced and an additional shoulder on the low energy side of the first band is revealed at 626 nm (15985 $cm^{-1}$). This shoulder probably represents overlapping vibrational satellites corresponding to low energy vibrational modes. In particular, in resolved low temperature emission spectra (see Chapt. 6) a strong satellite corresponding to a 288 $cm^{-1}$ vibrational mode is identified. This energy closely matches the energy separation of the discussed shoulder from the emission

maximum at 615 nm (16260 $cm^{-1}$). The occurrence of intense satellites in the energy region below 500 $cm^{-1}$ fits to an MLCT admixture to the emitting state. This is due to the fact that MLCT transitions usually involve metal-ligand vibrational modes the energies of which lie predominantly in this range.

# 4 Emission Spectra of $Ir(btp)_2(acac)$ – Electronic Origins

## 4.1 Low-temperature spectra and site distribution

Figure 18a shows the emission spectrum of $Ir(btp)_2(acac)$ in $CH_2Cl_2$ recorded at 4.2 K in comparison to the spectrum measured at 77 K. Both spectra were recorded using UV excitation ($\lambda_{exc}$ = 363.8 nm).

While at 77 K, the spectrum is constituted only of broad bands of halfwidths of about 500 $cm^{-1}$, cooling to 4.2 K reveals a manifold of narrow lines of halfwidths of only a few $cm^{-1}$ and a broad background. Both the narrow lines as well as the background of the 4.2 K spectrum can be explained taking into account that the $Ir(btp)_2(acac)$ dopant molecules can experience dissimilar interactions with their respective environment in the host matrix. Different orientations of the dopants within the matrix (host) cage and/or a different number of host molecules that are being replaced cause dissimilar shifts of the electronic states, splittings, and couplings to the matrix. For a large number of molecules, a broad inhomogeneous distribution of transition energies results and one observes unresolved emission. The broad background of the 4.2 K emission spectrum in Fig. 18 is explained in these terms. On the other hand, a specific doping situation (site) may exist for guest molecules in the host matrix, which is energetically favorable. Such a specific *site* can be realized by a large number of guest molecules which, therefore, all experience similar interactions with their host environment. Correspondingly, narrow lines can occur in the spectra. The spectrum depicted in Fig. 18a and enlarged in Fig. 18b shows a number of such lines. Each is related to one specific and discrete site.

Most of the narrow lines in the 4.2 K emission spectrum represent electronic **0**-**0** transitions from a substate of the lowest triplet state $\mathbf{T_1}$ to the ground state $\mathbf{S_0}$. This is indicated by the fact that at the corresponding energies the respective molecules can be excited resonantly and selectively. In particular, these narrow lines represent transitions from triplet substate **II** to the ground state (for details, see below). The distribution of sites found for $Ir(btp)_2(acac)$ doped into $CH_2Cl_2$ spans a width of

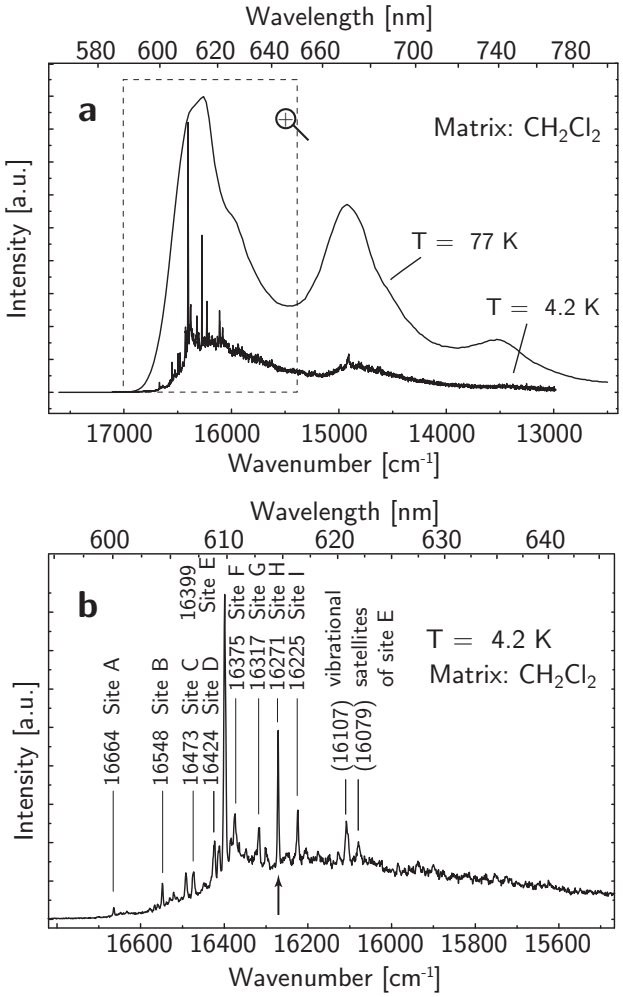


**Figure 18** Comparison of the emission spectra of $Ir(btp)_2(acac)$ in $CH_2Cl_2$ ($10^{-5}$ mol/l) recorded at 77 K and 4.2 K, respectively, excited at 363.8 nm. At 77 K, the spectrum is still unresolved due to inhomogeneous broadening and homogeneous broadening by electron-phonon coupling. The 4.2 K spectrum shows a site structure consisting mainly of highly resolved electronic 0-0 lines and an intense inhomogeneous background. (b) Magnified region of the 4.2 K emission framed in (a). All lines labeled with capital letters represent electronic origins ($\mathbf{T_1}$ substate **II** → ground state $\mathbf{S_0}$) of different sites. In particular, site **H** at 16271 $cm^{-1}$ (arrow in (b)) will be subject to detailed investigations in the following sections.

about 450 $cm^{-1}$. The different sites are labeled with capitals in Fig. 18. The main site is located at 16399 $cm^{-1}$ (site **E**). Weaker sites are found blue-shifted to the

main site at least up to 16664 $cm^{-1}$ and red-shifted at least down to 16220 $cm^{-1}$. Data on the different sites of $Ir(btp)_2(acac)$ in $CH_2Cl_2$, including the energies of the three triplet substates, zero-field splitting values, and relative intensities, are summarized below in Sect. 4.4 (Table 1). The corresponding data are also given for the main site found in n-octane and in single crystals of $Ir(btp)_2(acac)$.

For completeness, the question is addressed of why the resolution is lost as the temperature is increased from 4.2 K to 77 K (Fig. 18a). This is due to temperature dependent (homogeneous) broadening caused by electron-phonon interaction[18]: Low-energy vibrations of the dopant in its lattice cage (pseudo-local phonons) couple to the purely electronic and the vibronic transitions. This leads to the appearance of phonon sidebands (satellites), which accompany the zero-phonon (phonon 0-0) lines and which are spectrally much broader than these.[168] With temperature increase, the phonon-sidebands gain intensity at the expense of the intensities of the zero-phonon lines. Moreover, the zero-phonon lines themselves (electronic origins and vibrational satellites) are broadened with temperature increase due to thermally activated phonon 1-1 transitions, 2-2 transitions, etc. which have slightly different energies than the 0-0 transitions due to the differences of the force constants in the electronic ground state as compared to the triplet state. At 77 K, for example, the spectral features of the discrete sites have become too broad to be distinguished from the inhomogeneous background and additionally overlap for the different sites (compare Fig. 18a). Hence, an unresolved spectrum results, which finally approximates the shape of the inhomogeneous background of the 4.2 K spectrum.

## 4.2 Electronic origins and energy level diagram

Using a tunable laser, a specific site can be studied individually by selective excitation, i.e. by resonantly exciting the corresponding molecules. One specific site exhibiting an electronic origin at 16271 $cm^{-1}$ (site **H**) is the most suitable one for this investigation. It is located in the longer wavelength region of the distribution which prevents the unintentional excitation of other sites. Furthermore, due to the high relative intensity of site **H**, its emission is well detectable. Figure 19 shows a selected excitation spectrum measured at $T = 4.2$ K and emission spectra in the range of the 0-0 transitions for different temperatures.

[18] For detailed information on homogeneous broadening by electron-phonon coupling, compare the reviews [120] and [168].

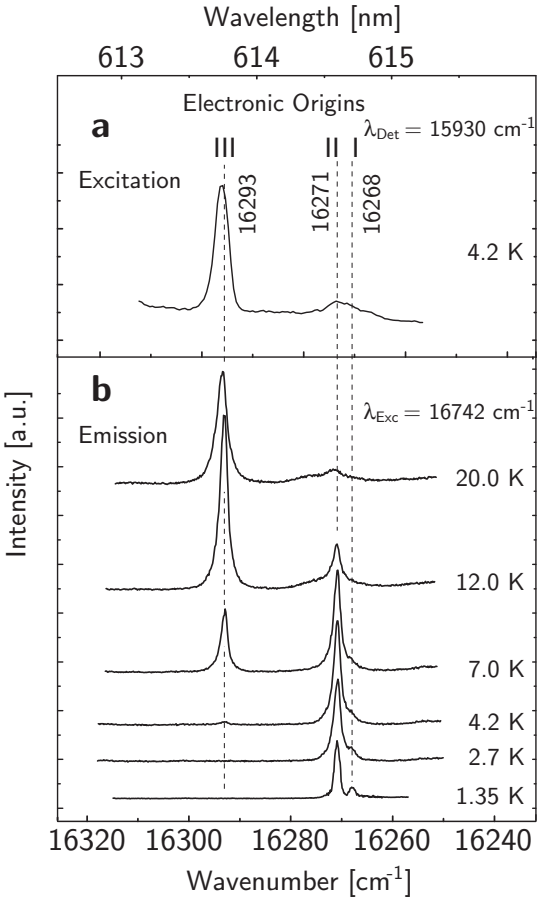


**Figure 19** (a) Site-selective excitation spectrum in the region of the electronic origins recorded at 4.2 K. The emission is detected on a vibrational satellite of the **II** $\rightarrow$ **0** transition at 15930 $cm^{-1}$ (341 $cm^{-1}$ vibration). (b) Site-selective emission in the region of the electronic origins recorded at different temperatures under excitation into a vibrational satellite of the **0** $\rightarrow$ **III** transition at 16742 $cm^{-1}$ (449 $cm^{-1}$ vibration). The intensities of the different spectra are comparable. The spectrum at 1.35 K was recorded with higher resolution to obtain the energy difference $\Delta E_{\mathrm{II-I}}$ between substates **I** and **II**. The energy values given in (a) are rounded to the corresponding accuracy of the absolute wavenumber of $\pm 1\,cm^{-1}$. The relative accuracy is as high as $\pm 0.2\,cm^{-1}$.

Three lines are observed. It will be shown below that they represent purely electronic 0-0 transitions between the $\mathbf{T_1}$ substates **I**, **II** and **III**, and the ground state **0** ($\mathbf{S_0}$). The purely electronic nature is substantiated by the fact that the transitions exhibit the same energy in excitation and emission. Moreover, experiments carried out

under application of high magnetic fields demonstrate that these three lines belong to the same triplet parent term (see Sect. 4.3). The spectra reveal that the substates **I** and **II** are separated by $(2.9 \pm 0.2)\,\mathrm{cm}^{-1}$, whereas the splitting of substates **I** and **III**, which represents the total zero-field splitting, amounts to $(25.0 \pm 0.5)\,\mathrm{cm}^{-1}$. According to the extensive investigations by Yersin et al. [45, 119, 120] and the ordering scheme which correlates ZFS values and MLCT character (compare Sect. 2.4), this value of $\Delta E_{\mathrm{III-I}}$ shows that the $\mathbf{T_1}$ state does not represent a $^3$**LC** state. It is significantly perturbed by MLCT admixtures.

Figure 19b shows emission spectra of $Ir(btp)_2(acac)$ in the region of the electronic origins, recorded at temperatures between 1.35 K and 20 K. These spectra of site **H** are selectively excited at $16742\,\mathrm{cm}^{-1}$. This energy corresponds to a vibrational satellite of $\bar{\nu} = 449\,\mathrm{cm}^{-1}$ to the **0** → **III** transition. The spectrum at 1.35 K clearly shows two close-lying lines at $16271\,\mathrm{cm}^{-1}$ and at $16268\,\mathrm{cm}^{-1}$ corresponding to the transitions **II** → **0** and **I** → **0**, respectively. With temperature increase, emission **I** → **0** becomes weaker and is not detectable above 10 K, while the line originating from state **II** gains intensity up to about 5 K. Near 5 K, a third line appears at $16293\,\mathrm{cm}^{-1}$. This line assigned to the 0-0 transition **III** → **0**. With further temperature increase up to 20 K, the intensity of this line **III** increases drastically, while the line at $16271\,\mathrm{cm}^{-1}$ corresponding to transition **II** → **0** looses intensity. Heating up to higher temperatures, e.g. to 50 K, does not reveal any higher lying state. Figure 20 summarizes the intensity ratios of the electronic origin lines in a Boltzmann plot.

The experimental data can be fit by the equation

$$\ln\left(\frac{I_{\mathrm{III}}}{I_{\mathrm{I+II}}}\right) = \mathrm{const} + \frac{-\Delta E_{\mathrm{III-I/II}}}{k_{\mathrm{B}} T} \quad , \tag{16}$$

wherein $I_{\mathrm{III}}$ and $I_{\mathrm{I+II}}$ represent the intensities of the origin line III (**III** → **0** (0-0)) and the sum of the intensities of the lines I and II (**I**/**II** → **0** (0-0)), respectively. The sum is used as the resolution of the measured spectra for $T \geq 2$ K does not allow to treat the corresponding lines I and II separately with sufficient accuracy. $\Delta E_{\mathrm{III-II/I}}$ is the energy separation between the substates **I**/**II** and **III** and $k_B$ is the Boltzmann constant. The fit gives an energy separation of $(22.7 \pm 0.5)\,\mathrm{cm}^{-1}$. This value reproduces the average of the splittings $\Delta E_{\mathrm{III-I}}$ and $\Delta E_{\mathrm{III-II}}$ which was determined independently by high resolution experiments (see Fig. 19). The result obtained is of particular interest. Application of Eq. 16 is only allowed if the thermal equilibration between state **III** and the states **I**/**II** is fast.[139, 169–171] Obviously, this is fulfilled for pro-

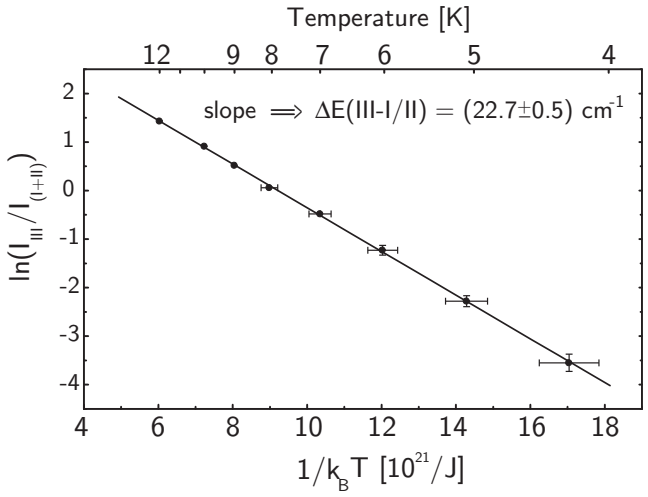


**Figure 20** Logarithmic plot of the intensity ratio of the electronic origin line III relative to the sum of the intensities of lines I and II versus $1/k_BT$. The slope of the linear fit reveals an energy separation of $(22.7 \pm 0.5)\,\mathrm{cm}^{-1}$.

cesses **III** $\leftrightarrow$ **I** and **III** $\leftrightarrow$ **II**. Therefore, it can be concluded that the lines observed in Fig. 19 result from states which belong to one single site and are intrinsic to the molecules of this ensemble. An alternative interpretation in which the three lines would be assigned to different sites would not hold, since at concentrations of $10^{-5}$ mol/l fast processes of energy transfer between states of different sites are not expected to occur. The conclusion that the three states belong to the same molecule follows also from the investigations under high magnetic fields (see Sect. 4.3). For completeness, it is remarked that the equilibration between the substates **I** and **II** is very slow at low temperature. For example at 1.5 K, the corresponding spin-lattice relaxation (SLR) time is as long as 22 µs (see Sect. 5.3). As a consequence, the emission from substate **II** cannot be frozen out. (Compare also review [139].)

The excitation spectrum presented in 19a demonstrates that transition **0** $\rightarrow$ **III** exhibits the highest oscillator strength, while transition **0** $\rightarrow$ **II** shows a significantly lower intensity. Transition **0** $\rightarrow$ **I** is very weak. Since the excitation intensities reflect the oscillator strengths and since these are proportional to the radiative rates, one expects a similar trend for the individual decay times of the substates **I**, **II** and **III**. Indeed, they are determined in Sect 5.1 to $\tau_{\mathrm{I}} = (150 \pm 5)\,\mu\mathrm{s}$, $\tau_{\mathrm{II}} = (58 \pm 3)\,\mu\mathrm{s}$, and $\tau_{\mathrm{III}} = (1.5 \pm 0.5)\,\mu\mathrm{s}$, respectively. The long emission decay time $\tau_{\mathrm{I}}$ is an indication of an almost pure triplet character of substate **I**, while the short decay time of state **III** indicates at least a small singlet component mixed in (compare Ref.

[120]). This is in agreement to a recent theoretical investigation by Nozaki.[52] In this study, using a strongly simplified model for $Ir(ppy)_3$, it is shown that substate **I** is largely a pure triplet state, while the substates **II** and **III** contain singlet contributions of the order of 1%. Figure 21 summarizes the data obtained for $Ir(btp)_2(acac)$ in $CH_2Cl_2$ (site **H**) in an energy level diagram.

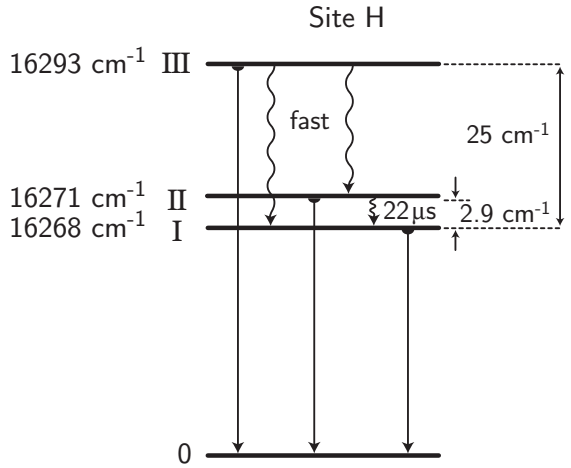


**Figure 21** Energy level diagram and photophysical data for the lowest triplet state $\mathbf{T_1}$ of $Ir(btp)_2(acac)$. The state is classified as $^3$**LC** state which is significantly MLCT perturbed. The values given apply to the specific site under investigation (site **H** in Fig. 18b). Other sites display different values (compare Sect. 4.4, Table 1). After excitation of triplet substate **III**, the relaxation to the lower lying substates (spin-lattice relaxation, SLR) is fast even at 1.2 K. However, the relaxation time between the substates **II** and **I** is comparatively long and amounts to 22 µs at 1.5 K. This value and the individual decay times are determined in Sects. 5.3 and 5.1, respectively, and are given here for completeness. The dashed lines represent vibrational levels, which are usually also involved in the emission processes.

## 4.3 Magnetic field effects

In order to obtain further evidence that the three states **I**, **II**, and **III** represent substates of one triplet term, $Ir(btp)_2(acac)$ is also investigated under high magnetic field. Figure 22 shows the emission lines of $Ir(btp)_2(acac)$ in $CH_2Cl_2$ (site **H**) in the energy range of the electronic origin transitions at different magnetic flux densities between $B = 0$ T and $B = 8$ T. In Fig. 22a, the complete spectral range of all three

electronic origins, measured at $T = 8\,\mathrm{K}$, is depicted. The comparatively high temperature was chosen to provide sufficient population of the higher-lying substate **III**. Figure 22b reproduces the region of the electronic origins **I** → **0** and **II** → **0**. The spectra are monitored at $T = 2.8\,\mathrm{K}$ with a higher resolution. The population of substate **III** is frozen out at this temperature and the resolution is enhanced.

The external magnetic field significantly alters the emission spectrum. With increase of the magnetic field strength, distinct Zeeman shifts of the transition energies are observed. Transition **III** → **0** (0-0) is shifted to higher energy from $16293\,\mathrm{cm}^{-1}$ at $B = 0\,\mathrm{T}$ to $\approx 16295\,\mathrm{cm}^{-1}$ at $B = 8\,\mathrm{T}$, while transition **I** → **0** (0-0) is shifted to lower energy from $16268\,\mathrm{cm}^{-1}$ ($B = 0\,\mathrm{T}$) to $\approx 16265.5\,\mathrm{cm}^{-1}$ ($B = 8\,\mathrm{T}$). The energy of **II** → **0** (0-0) of $16271\,\mathrm{cm}^{-1}$ at $B = 0\,\mathrm{T}$ is only slightly increased by $\approx 0.5\,\mathrm{cm}^{-1}$ up to $B = 8\,\mathrm{T}$. Thus, the splitting between substates **I** and **II**, which amounts to $2.9\,\mathrm{cm}^{-1}$ at $B = 0\,\mathrm{T}$, is increased to $6.0\,\mathrm{cm}^{-1}$ at $B = 8\,\mathrm{T}$. The total splitting $\Delta E_{\mathrm{III-I}}$ is enlarged from $25\,\mathrm{cm}^{-1}$ at 0 T to $29.5\,\mathrm{cm}^{-1}$ at 8 T. In Fig. 23, the magnetic field induced energy shifts of the three electronic origins are summarized.

The Zeeman shifts are not symmetric. At $B = 8\,\mathrm{T}$, the energy separation between the substates **I** and **II** is increased by $3.1\,\mathrm{cm}^{-1}$, whereas the separation between the states **II** and **III** is enhanced only by $1.5\,\mathrm{cm}^{-1}$. These asymmetric Zeeman shifts are qualitatively understood since the B-field induced mixings between the corresponding energy states depend on their energy separations at zero field (energy denominators) which are strongly asymmetric for $\mathrm{Ir(btp)_2(acac)}$. For completeness, it has to be remarked that the Zeeman shifts can be quite different for molecules with different orientations relative to the magnetic field vector. This applies also to polycrystalline samples, as the molecules of one specific site have different orientations for the different micro-crystals. Therefore, the observed Zeeman pattern represents an average for quasi-continuously distributed orientations. A corresponding quantitative analysis is not presented in this case, but has been carried out, for example, for $\mathrm{Pt(thpy)_2}$ (thpy = 2-(2'-thienyl)pyridinato-N,C5') in Ref. [172].

An additional effect of application of the magnetic field becomes apparent in the spectra of Fig. 22. At 0 T, the transition from substate **I** to the ground state **0** is very weak. With increase of the field strength, it gains significant intensity. This effect becomes obvious already for $B < 1\,\mathrm{T}$ (not shown). At 2 T, the intensity stemming from the perturbed state $\mathbf{I_B}$ is almost equal to that of transition $\mathbf{II_B} \rightarrow \mathbf{0}$ which, in return, looses intensity upon increase of the magnetic field strength. At $B = 6\,\mathrm{T}$, for example, the intensity of transition $\mathbf{I_B} \rightarrow \mathbf{0}$ dominates clearly. For an explanation of this effect, three factors are of importance. First, the magnetic field-induced mixing of the wavefunction of substate **I** with the wavefunctions of

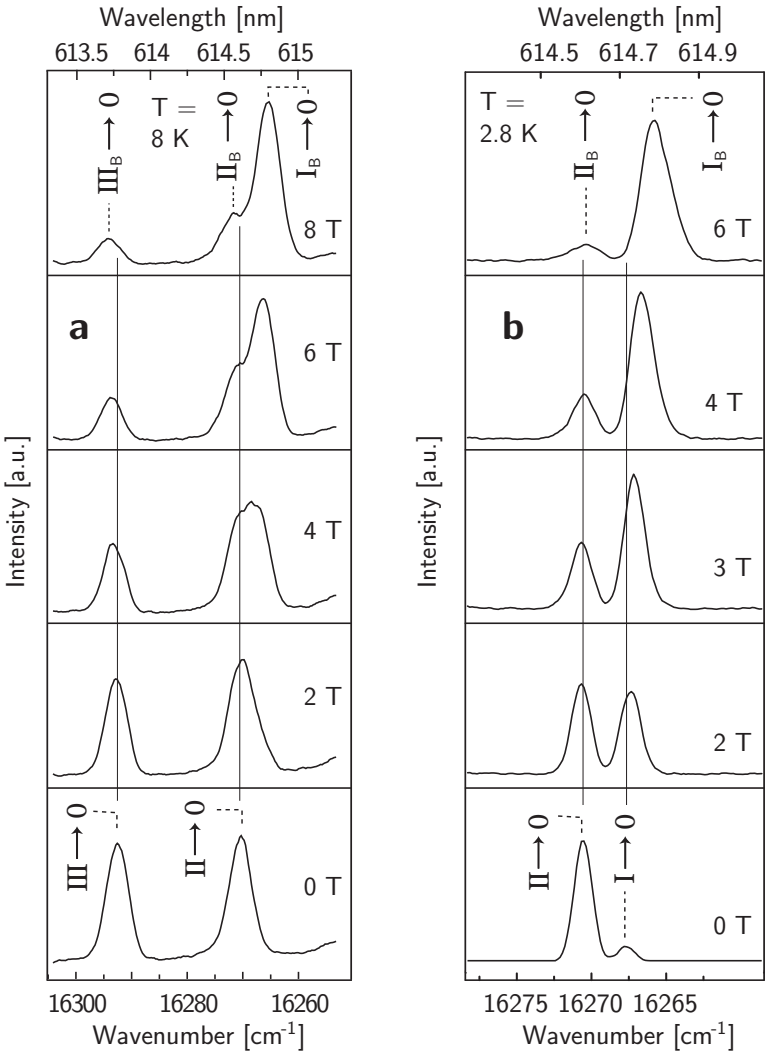


**Figure 22** Emission spectra of site **H** of $Ir(btp)_2(acac)$ in $CH_2Cl_2$ in the region of the electronic origins at different magnetic field strengths. The spectra of (a) were registered at $T = 8\,K$, to obtain sufficient thermal population of substate **III** ($\bar{\nu}_{exc}$ =26810 $cm^{-1}$, non-selective excitation). (b) Emission spectra in the energy range of the electronic origins **I** → **0** and **II** → **0** recorded at 2.8 K with a higher resolution. For these measurements, selective excitation of substate **III** was used. The corresponding excitation energy of 16293 $cm^{-1}$ at $B = 0\,T$ was stepwise shifted to higher energy by ≈0.2 $cm^{-1}$/T to account for the field-induced blue shift of substate **III**. At $B = 8\,T$, the excitation energy was ≈16295 $cm^{-1}$.

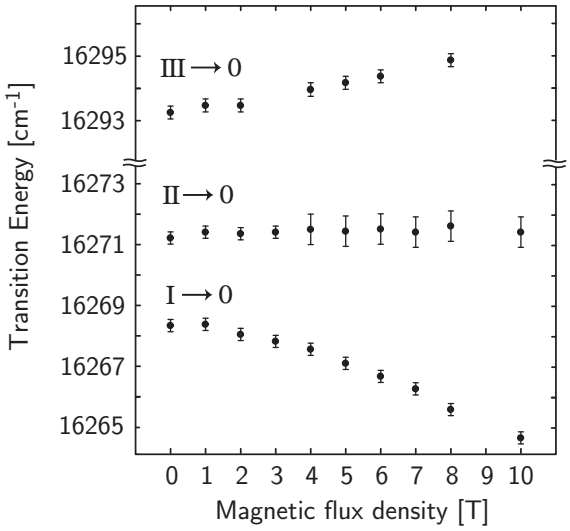


**Figure 23** Magnetic field induced shifts of the $\mathbf{T_1}$ substates **I**, **II**, and **III** of $Ir(btp)_2$-(acac) in $CH_2Cl_2$ (site **H**). The data are extracted from emission spectra recorded at various temperatures in the range from 2.8 K to 14 K. The emission from the magnetically perturbed substate $\mathbf{I_B}$ was measured at $T = 2.8$ K, while the energy of the emission lines corresponding to the transitions $\mathbf{II_B} \rightarrow \mathbf{0}$ and $\mathbf{III_B} \rightarrow \mathbf{0}$ was determined at 8 K and 14 K, respectively. The higher temperature was chosen to provide sufficient population of these states. For recording emission from substates **I** and **II**, substate **III** was excited, while emission from substate **III** was measured under excitation into a vibrational satellite of substate **III** (16742 $cm^{-1}$ at 0 T). Selective excitation was always tuned with increasing magnetic field strength to match the excitation energy of the Zeeman shifted state **III**.

the two higher states renders transition $\mathbf{I_B} \rightarrow \mathbf{0}$ more allowed. Secondly, due to the increased splitting between substates **I** and **II** under magnetic field, the Boltzmann factor for population of state **II** (relative to state **I**) is significantly smaller. Thirdly, spin-lattice relaxation between the triplet substates becomes considerably faster with increasing field-induced energy separation between the corresponding states (compare Refs. [45] and [139]). Accordingly, the Boltzmann distribution is established faster and thus the non-equilibrated fraction of the emission resulting from the higher lying substate $\mathbf{II_B}$ is strongly reduced at $B = 6$ T. The increased allowedness of transition $\mathbf{I_B} \rightarrow \mathbf{0}$ under application of a magnetic field should also be reflected in the emission decay time of substate **I**. In particular, the almost pure and long-lived triplet substate is expected to experience a distinct reduction of the emis-

sion decay time when mixing with shorter-lived substates occurs. Indeed, drastic effects are observed (Fig. 24). At $T = 1.7\,\mathrm{K}$, the emission decay time of substate **I** decreases from $\tau_\mathrm{I} = 133\,\mu\mathrm{s}$ at $B = 0\,\mathrm{T}$ to $20\,\mu\mathrm{s}$ at $B = 10\,\mathrm{T}$. The measurements were carried out with detection at the respective Zeeman shifted electronic origin (for $B = 0\,\mathrm{T}$ at $16268\,\mathrm{cm}^{-1}$ and for $B = 10\,\mathrm{T}$ at $16264.7\,\mathrm{cm}^{-1}$). These data show clearly that a simple approach of taking into account only a mixing of the two lowest strongly interacting substates is not successful – in contrast to the situation found for $Ir(ppy)_3$.[48] This is due to the observation that the decay time of $\mathbf{I_B}$ at $B = 10\,\mathrm{T}$ is with $\tau_\mathrm{B}$ =20 µs much shorter than the decay time of **II** at $B = 0\,\mathrm{T}$ ($\tau_\mathrm{II}$ =58 µs). Therefore, it has to be concluded that the Zeeman mixing occurs between all three substates. In particular, the singlet component of substate **III** is responsible for the drastic shortening of the emission decay time of the lowest substate by the applied high magnetic field.

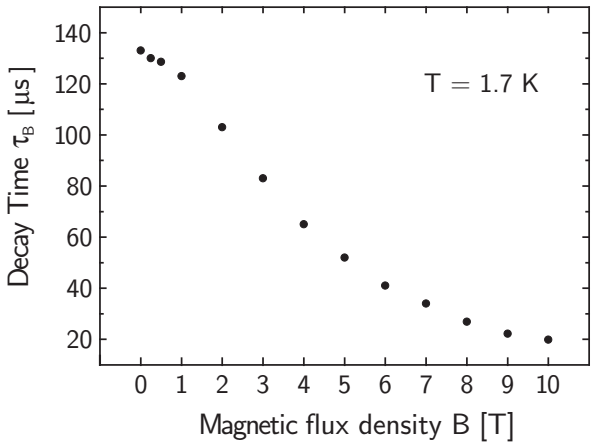


**Figure 24** Emission decay time of triplet substate **I** of $Ir(btp)_2(acac)$ in $CH_2Cl_2$ (site **H**). The decay time is measured for different magnetic flux densities $B$ at 1.7 K and under selective excitation of $\mathbf{T_1}$ substate **III**. The excitation energy of $16293\,\mathrm{cm}^{-1}$ at $B = 0\,\mathrm{T}$ was tuned with increasing magnetic field strength to account for the Zeeman shift of substate **III**. The decay behavior is monoexponential in the whole range.

The Zeeman effects as described above are typical for three substates of one parent $\mathbf{T_1}$ term. Thus, the magnetic field behavior gives direct evidence that the three lines **I**, **II**, and **III** cannot be related to different sites, but represent emissions from one specific site (site **H**).

## 4.4 Variation of zero-field splitting – matrix influence

In the previous sections, spectroscopic properties of the lowest triplet state $\mathbf{T_1}$ of $Ir(btp)_2(acac)$ have been investigated on the example of one specific site (site **H**) of the complex in a polycrystalline $CH_2Cl_2$ matrix. Importantly, the three substates **I**, **II**, and **III** of the $\mathbf{T_1}$ state could be identified and their separations have been determined to $\Delta E_{\mathrm{II-I}}$ =2.9 $cm^{-1}$ and to $\Delta E_{\mathrm{III-I}}$ =25.0 $cm^{-1}$, respectively. However, as seen in Sect. 4.1, in the $CH_2Cl_2$ host several further spectroscopic sites exist. The distribution of their transition energies spans a width of 450 $cm^{-1}$. Such a distribution is due to dissimilar dopant-matrix interactions and is a well-known phenomenon in the spectroscopy of organic molecules doped into Shpol'skii or Shpol'skii-like matrices. For organo-transition metal complexes, this phenomenon is usually found as well, as has been demonstrated, for example, for $Pt(thpy)_2$ [173], $Pd(thpy)_2$ [174], and $[Ru(bpy)_3]^{2+}$ [46, 175] and $[Os(bpy)_3]^{2+}$ [46, 176]. Nevertheless, it is not clear from the first, in how far the results attained for site **H** of $Ir(btp)_2(acac)$ in $CH_2Cl_2$ are representative for this complex, i.e., whether they can be transferred to other sites in $CH_2Cl_2$ or other matrices. Therefore, investigations as described in the previous sections were extended to other sites in $CH_2Cl_2$ and to an *n*-octane matrix, and were carried out also for a single crystal of $Ir(btp)_2(acac)$. Investigation of an individual site was again achieved with the help of emission and excitation spectroscopy under selective excitation and emission, respectively. Additionally, variation of temperature and, in part, of high magnetic fields have been applied to ensure a reliable interpretation of the observed data.

As an example, Figure 25 shows site-selective spectra of the regions of electronic origins for the two sites **E** and **H** (compare Fig. 18). These sites are especially suited for detailed studies due to the high intensities of the corresponding lines compared to the background. Moreover, they are found in the lower energy region of the distribution, which renders the simultaneous excitation of vibrational levels of the excited states of emitters in other sites lying at lower energies unlikely.

The obtained data clearly show that the two sites exhibit distinctly different total zero-field splittings of the $\mathbf{T_1}$ substates. For site **E**, $\Delta E_{\mathrm{III-I}}$ amounts to 14.8 $cm^{-1}$, while for site **H** a splitting of 25.0 $cm^{-1}$ is found. The splitting $\Delta E_{\mathrm{II-I}}$ between the two lower substates of 2.9 $cm^{-1}$ is identical for these specific sites, but - as shown a Table 1 - this is not the general case. A study of the ZFSs of sites **A** to **I** of $Ir(btp)_2$-(acac) in $CH_2Cl_2$ reveals that the total ZFS $\Delta E_{\mathrm{III-I}}$ is distributed from 14.8 $cm^{-1}$ to

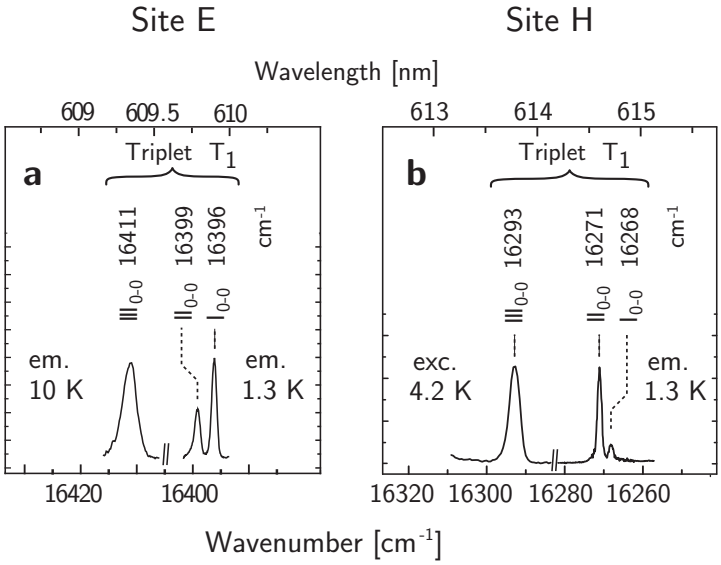


**Figure 25** The region of the electronic origins (0-0 transitions) is displayed for the two major sites **E** (a) and **H** (b) of $Ir(btp)_2(acac)$ in $CH_2Cl_2$. The emission spectra of site **E** were obtained by exciting into the vibrational satellite of substate **III** at 16775 $cm^{-1}$ (16411 $cm^{-1}$ + 364 $cm^{-1}$), while the emission spectrum of site **H** was measured under excitation into the vibrational satellite of substate **III** at 16742 $cm^{-1}$ (16293 $cm^{-1}$ + 449 $cm^{-1}$). The excitation spectrum of site **H** was recorded under detection at substate **II** (16271 $cm^{-1}$). Note that the intensity ratio of the lines $II_{0-0}$ and $I_{0-0}$ is significantly different for the two sites. This is mainly a consequence of different spin-lattice relaxation times found for the relaxation from substate **II** to **I** (see Sect. 5.3).

26.5 $cm^{-1}$. Additional investigations of $Ir(btp)_2(acac)$ in *n*-octane and as a single crystal result in $\Delta E_{III-I}$ values of 25.3 $cm^{-1}$ and 19 $cm^{-1}$, respectively. The splitting $\Delta E_{II-I}$ varies from 2.2 $cm^{-1}$ to 3.7 $cm^{-1}$ for the different sites and matrices. A correlation to the $\Delta E_{III-I}$ variation does not exist. The ZFS values are summarized in Table 1, together with the relative intensities of the lines corresponding to the different sites. The variation of $\Delta E$(ZFS) by almost 100% indicates a strong influence of the host on the $\mathbf{T_1}$ state.

**Table 1** Transition energies and zero-field splittings (ZFS) for various sites of $Ir(btp)_2(acac)$ doped into $CH_2Cl_2$ and *n*-octane, respectively, and for single crystals of $Ir(btp)_2(acac)$. Properties of the sites **E** and **H** are discussed in detail (see text).

| Matrix | Site | Relative Intensity | Spectral position [$cm^{-1}$] | | | ZFS [$cm^{-1}$] | |
|---|---|---|---|---|---|---|---|
| | | | **I** | **II** | **III** | $\Delta E_{II-I}$ | $\Delta E_{III-I}$ |
| $CH_2Cl_2$ | A | 0.03 | - | 16664 | - | - | - |
| | B | 0.09 | - | 16584 | 16566 | - | $\approx 21$ |
| | C | 0.08 | 16470 | 16473 | 16488 | $3.2 \pm 0.5$ | $17.5 \pm 1$ |
| | D | 0.14 | 16422 | 16424 | 16445 | $2.2 \pm 0.5$ | $23.0 \pm 0.5$ |
| | E | 1 | 16396 | 16399 | 16411 | $2.9 \pm 0.2$ | $14.8 \pm 0.5$ |
| | F | 0.12 | - | 16375 | $\approx 16395$ | - | $\approx 23$ |
| | G | 0.12 | 16314 | 16317 | 16333 | $3.7 \pm 1$ | $19 \pm 3$ |
| | H | 0.49 | 16268 | 16271 | 16293 | $2.9 \pm 0.2$ | $25.0 \pm 0.5$ |
| | I | 0.19 | 16221 | 16225 | 16247 | $2.6 \pm 0.3$ | $26.5 \pm 1$ |
| *n*-Octane | A | 0.89 | 16298 | 16201 | 16224 | $2.5 \pm 0.2$ | $25.3 \pm 0.5$ |
| Single Crystal | - | - | 16293 | 16296 | 16312 | $2.4 \pm 0.4$ | $19 \pm 1$ |

## 4.5 Assignment of the emitting state – Conclusions

Based on the spectroscopic results presented in the previous sections, the emitting state $\mathbf{T_1}$ of $Ir(btp)_2(acac)$ can be classified. The three substates **I**, **II**, and **III** of the $\mathbf{T_1}$ state have been identified from emission and excitation spectra at different temperatures. Measurements at high magnetic fields provide additional evidence for the triplet nature of the emitting substates and prove directly that these substates result from a $\mathbf{T_1}$ parent term of one specific site. In Section 2.4, it has been shown that the zero-field splitting of the $\mathbf{T_1}$ state into substates may be regarded as a measure of the MLCT perturbation of the $\mathbf{T_1}$ state. In particular, a large value of $\Delta E_{\mathrm{III-I}}$ corresponds to a strong MLCT perturbation (high MLCT character) of this state. For $Ir(btp)_2(acac)$ in various sites of $CH_2Cl_2$ and in *n*-octane, and $Ir(btp)_2$-(acac) as a single crystal, $\Delta E_{\mathrm{III-I}}$ values have been found to vary in the range from $14.8\,cm^{-1}$ to $26.5\,cm^{-1}$. For an assessment of the MLCT character on the basis of the ZFS, the ordering scheme developed by Yersin et al. and introduced in Sect. 2.4 (compare Fig. 11 and Refs. [45, 46, 119, 120, 138, 141]) has proven useful.

The ZFS of $Ir(btp)_2(acac)$ lies for all sites and matrices in the intermediate range of this ordering scheme. According to this, the emitting triplet $\mathbf{T_1}$ of $Ir(btp)_2(acac)$ is assigned as ligand-centered ($^3$**LC**) (btp) $^3\pi\pi^*$ state with significant admixtures of MLCT character.

The variation of the zero-field splitting found for the different sites of $Ir(btp)_2$-(acac) in $CH_2Cl_2$ and for the different matrices (compare Table 1) proves a significant influence of the host environment on the emitting triplet state. Since the environment is not expected to directly influence the individual substates of one triplet state in significantly different ways, the most likely explanation is a varying MLCT admixture to the $\mathbf{T_1}$ state depending on the interaction with the matrix cage. Most probably, the admixture is modulated by changes in the energy separation between the $\mathbf{T_1}$ state and one or several mixing states, e.g. the next higher lying $^3$**MLCT** state (see Fig. 26). Relative shifts between such states can have different reasons, such as changes of the local solvent polarity or changes of the complex geometry. Concerning the first, it is known that, upon changes of the solvent polarity, MLCT states of organometallic complexes usually experience larger shifts as compared to LC states.[177, 178] This was demonstrated, e.g. for Re(I)-complexes (see Ref. [177]), for which an increase of the solvent polarity leads to a blue shift of the lowest $^1$**MLCT** state and a slight red shift of the $^3$**LC** state. Therefore, the energy separation is increased and the degree of mixing is reduced, resulting in a longer emission decay time.[177] A similar effect may also be present for $Ir(btp)_2(acac)$ in different solvents. For the sites of $Ir(btp)_2(acac)$ in $CH_2Cl_2$, a different degree of mixing of the $^3$**LC** and the lowest $^3$**MLCT** state may be present, if the effective polarity of the matrix molecules experienced by the $Ir(btp)_2(acac)$ dopant varies with the specific site situation. The interaction between the matrix and the dopant is probably large, if the charge density of the dopant in the outer regions and the local polarity/polarizability of adjacent matrix molecules is large. Interestingly, the variation of the zero-field splitting, as given in Table 1, is more pronounced for the $CH_2Cl_2$ host than for the less polar octane host, where it amounts to only $\pm 2\,cm^{-1}$ (not listed).

Alternatively, the influences of the host environment may also be explained in different terms. Thus, the influences may as well be due to specific site dependent distortions of the molecular symmetry/geometry. Such distortions would, in general, alter the ligand field splitting. As discussed in Sect. 2.5, depending on the splitting pattern, a (direct or indirect) mixing of the $\mathbf{T_1}$ state with higher-lying singlets or triplets may be favored more or less. It has been shown that even for small molecules such as pentacene in p-terphenyl crystals significant distortions due to

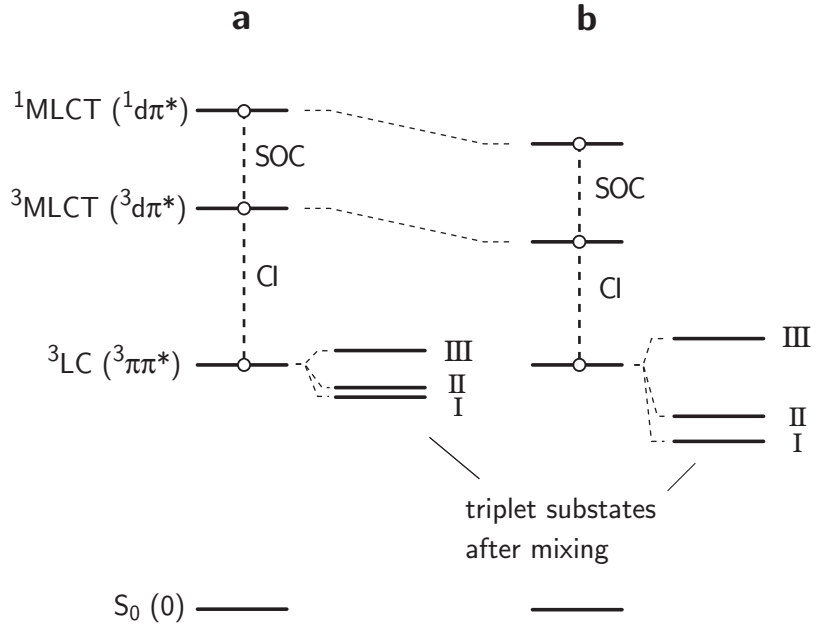


**Figure 26** Mixing of the lowest triplet state $\mathbf{T_1}$ (here $^3$**LC**) of an organo-transition metal complex with higher lying states. ($^3$**MLCT** and $^1$**MLCT**). Here, the situation of indirect mixing of $\mathbf{T_1}$ to the $^1$**MLCT** state via configurational interaction (CI) with the $^3$**MLCT** state is given. Note that the two states $^3$**MLCT** and $^1$**MLCT** are given here as representatives of the triplet and singlet manifolds of MLCT states, respectively. Generally, several of these states may be involved in the mixings to the $\mathbf{T_1}$ state. A change of the energy separations (energy denominators) of the involved states due to influences of the host can have a significant effect on the mixing coefficients and thus on the resulting zero-field splitting of the $\mathbf{T_1}$ state.

static interactions with the host lattice can occur. (Compare the molecular packing calculations given in Ref. [179].) For a complex as large as $Ir(btp)_2(acac)$, such distortions may play an important role. In particular for $Pt(thpy)_2$ in octane, it has been proposed in the literature, that interactions with the matrix cage can lead to different structures of the complex.[120] It cannot be decided in the frame of this report, which of the discussed effects is mainly responsible for the observations. However, possibly Ir-complexes are especially sensitive to both, since for these complexes, higher-lying singlets and triplets seem to be located relatively close in energy to each other and to the $\mathbf{T_1}$ state. This is indicated by DFT calculations carried out for $Ir(ppy)_3$.[52] If the substates of $\mathbf{T_1}$ obtain their (small) singlet character by direct or indirect mixing to one or several of these states, the corresponding energy denom-

inator(s) for mixing will be comparatively small, and thus sensitive to small shifts of the energy states due to distortions caused by the host. Such distortions will be different for different sites or matrices and a distribution of important photophysical properties such as the ZFS, the intersystem crossing rates or the radiative rates may result.

In this context, it has to be remarked that those ensembles of molecules in the distribution with low ZFS and MLCT character may exhibit poor photophysical properties. This results from the correlation of high MLCT character of the emitting state of a complex to favorable photophysical properties such as, for example, a short emission decay time. Therefore, a distribution of ZFS values may indicate an overall limitation to favorable emission properties, especially with regard to an application of the complex as OLED emitter. Note, however, that although higher radiative rates are expected to occur with increasing $\Delta E$(ZFS), nonradiative processes are not considered here. Therefore, a direct correlation between MLCT perturbation and photoluminescence quantum yield is not possible. Yet, the MLCT perturbation can be regarded as a necessary but not sufficient condition for complexes' usability in OLEDs.

In this respect, an important result of the hitherto existing studies of organotransition metal complexes can be pointed out. All good OLED emitters investigated so far, including Ir(btp)$_2$(acac), exhibit zero-field splittings of the parent $\mathbf{T_1}$ term of larger than about $10\,\mathrm{cm}^{-1}$. (Compare Fig. 11.)

# 5 Emission Decay Behavior of $Ir(btp)_2(acac)$

In this chapter, the emission decay behavior of $Ir(btp)_2(acac)$ in $CH_2Cl_2$ is studied. In particular, the decay behavior of the individual substates of the $\mathbf{T_1}$ state is investigated. The decay times of these states **I**, **II**, and **III** found at low temperature govern the emission decay time also at ambient temperature.

High radiative decay rates are crucial for OLEDs in two concerns. First, for emitter materials with higher radiative rates, saturation effects occur at higher current densities. Therefore, a device can be operated at a higher brightness. Secondly, the decay rates indirectly affect the phosphorescence quantum efficiency. This is due to the fact that the competing processes of radiationless decay are less important, if the radiative rates are higher. (Compare Sect. 2.3, Eq. 13.)

The radiative rates of emission from the $\mathbf{T_1}$ state are high, if the transition from this state to the ground state is sufficiently allowed. This allowedness is induced by spin-orbit coupling, which is only effective, if sufficient MLCT character is present in the $\mathbf{T_1}$ state. In the previous chapter it has been shown that the MLCT character of $Ir(btp)_2(acac)$ varies for different ensembles of molecules occupying different sites in a $CH_2Cl_2$ host. Therefore, it is of particular interest, to investigate in how far the variation of the MLCT character in the emitting $\mathbf{T_1}$ state of $Ir(btp)_2(acac)$ in turn affects the emission decay rates. This topic is addressed in the present chapter by a comparison of the relaxation dynamics of the $\mathbf{T_1}$ state of $Ir(btp)_2(acac)$ in the two spectroscopic sites **E** and **H** in $CH_2Cl_2$.

## 5.1 Individual emission decay times of the $T_1$ substates

The individual decay of the three substates cannot be measured directly, since at low temperature, the emission of higher lying states, such as substate **III**, is frozen out, while at higher temperatures, one usually measures a thermalized emission of all three substates. However, the individual decay times of the three $\mathbf{T_1}$ substates

can still be determined from the temperature dependence of the thermalized decay time.[48, 169, 180, 181] For a thermally equilibrated system of three excited states the rate constant for depopulation is given by the expression [48, 139, 169–171, 180]

$$k_{\text{therm}} = \frac{k_{\text{I}} + k_{\text{II}} \cdot \mathrm{e}^{-\Delta E_{\text{II–I}}/k_{\text{B}}T} + k_{\text{III}} \cdot \mathrm{e}^{-\Delta E_{\text{III–I}}/k_{\text{B}}T}}{1 + \mathrm{e}^{-\Delta E_{\text{II–I}}/k_{\text{B}}T} + \mathrm{e}^{-\Delta E_{\text{III–I}}/k_{\text{B}}T}} = \frac{1}{\tau_{\text{therm}}} \quad , \tag{17}$$

wherein $k_{\text{I}}$, $k_{\text{II}}$, and $k_{\text{III}}$ are the total rate constants for depopulation of substate **I**, **II**, and **III**, respectively. $\Delta E_{\text{II–I}}$ and $\Delta E_{\text{III–I}}$ are the energy separations between substates **I** and **II**, and substates **I** and **III**, respectively. $k_{\text{B}}$ is the Boltzmann constant. The rate constant $k_{\text{therm}}$ is the inverse of the measured decay time $\tau_{\text{therm}}$. Figure 27 shows emission decay curves of $Ir(btp)_2(acac)$ in $CH_2Cl_2$ for the example of site **H** at selected temperatures. The curves are registered after pulsed and selective

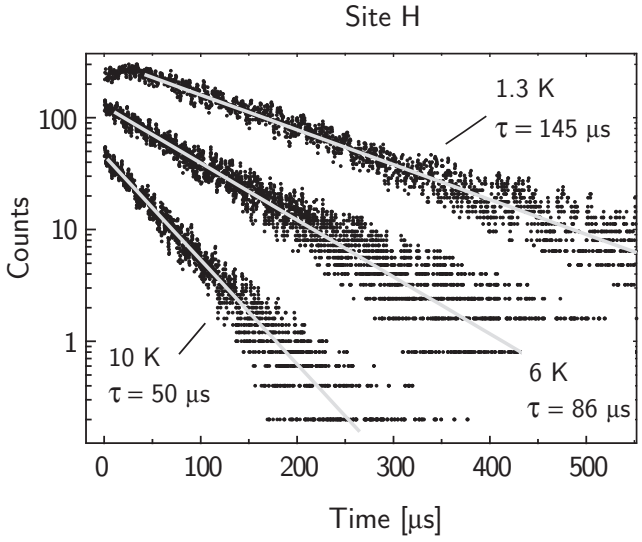


**Figure 27** Emission decay of triplet $\mathbf{T_1}$ substate **I** ($I_{0-0}$, 16268 $cm^{-1}$) of $Ir(btp)_2$-(acac) in $CH_2Cl_2$ (site **H**) measured after selective excitation of substate **III** ($III_{0-0}$, 16293 $cm^{-1}$) at selected temperatures. The curves are monoexponential except for a short rise of the curve recorded at 1.3 K (see Sect. 5.3). Upon temperature increase, the decay time becomes shorter due to thermal population of the higher lying substates **II** and **III**.

excitation from **0** to substate **III** at 16293 $cm^{-1}$ ($III_{0-0}$) and detected at the energy of transition **I** → **0** ($I_{0-0}$, 16268 $cm^{-1}$). At all temperatures, the emission from substate **I** decays monoexponentially, at least for $t \gtrsim 50\,\mu s$. The initial rise of the curve measured at $T = 1.3\,K$ represents an effect of thermalization by spin-

lattice relaxation, which is exceptionally slow. This effect will be explained in Sect. 5.3. The initial process is completed at about 50 µs after the excitation pulse. Thereafter, a monoexponential decay is observed and the system of three substates can be considered to be thermally equilibrated. The corresponding decay time at $T = 1.3$ K amounts to 145 µs. With temperature increase, the decay time becomes shorter and, for example, amounts to 86 µs at $T = 6$ K and to 50 µs at $T = 10$ K. The values of the monoexponential decays at different temperatures are plotted in Fig. 28. These plots can be utilized to determine the individual decay times of

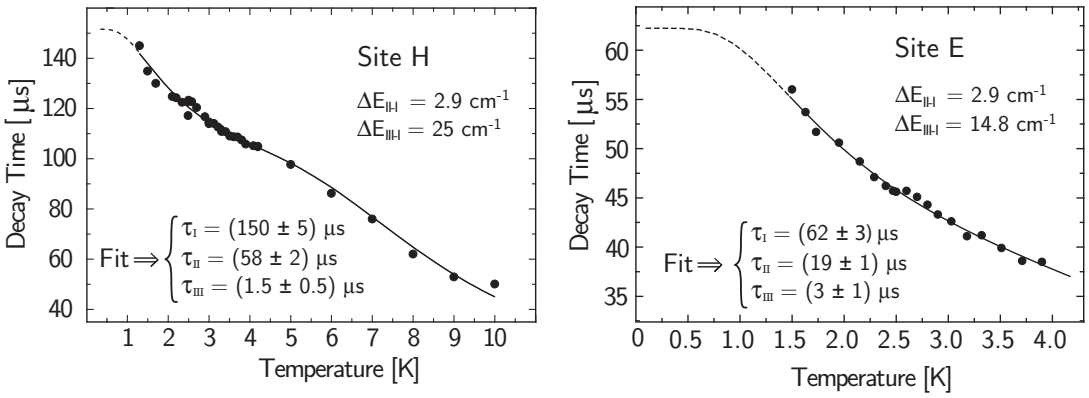


**Figure 28** Emission decay times of $Ir(btp)_2(acac)$ versus temperature for the two major sites **E** and **H** in $CH_2Cl_2$. The emission decay was recorded after excitation of substate **III** and with detection at the energy of transition **I** → **0** of the respective site. A fit of Eq. 17, using the energy separations $\Delta E_{\mathrm{II-I}}$ and $\Delta E_{\mathrm{III-I}}$ obtained from highly resolved spectra allows to determine the decay times of the individual substates.

the substates **I**, **II**, and **III** by fitting of Eq. 17 to the measured decay time data. Corresponding fit curves are given in Fig. 28 for the two sites. The fits are carried out with fixed splitting values $\Delta E_{\mathrm{II-I}}$ and $\Delta E_{\mathrm{III-I}}$ according to the values obtained from highly resolved spectra (see Sect. 4.2). The obtained individual decay times of the $\mathbf{T_1}$ substates of $Ir(btp)_2(acac)$ in $CH_2Cl_2$ are $\tau_{\mathrm{I}} = (62 \pm 3)$ µs, $\tau_{\mathrm{II}} = (19 \pm 1)$ µs, and $\tau_{\mathrm{III}} = (3 \pm 1)$ µs for site **E**, and $\tau_{\mathrm{I}} = (150 \pm 5)$ µs, $\tau_{\mathrm{II}} = (58 \pm 2)$ µs, and $\tau_{\mathrm{III}} = (1.5 \pm 0.5)$ µs for site **H**. Extending the fit curve to lower temperature shows that for both sites a plateau is present, however, only below about $T = 0.6$ K. This result reveals that, for $Ir(btp)_2(acac)$, even the decay times measured at 1.3 K do not represent the individual emission decay time of substate **I**. Even at this temperature, a small effect of thermal repopulation of substate **II**, being only 2.9 $cm^{-1}$ apart, is

present.

Remarkably, the decay times of substates **I** and **II** are significantly shorter for site **E** than for site **H**. The decay time of state **III**, which usually experiences the strongest mixing to higher lying states, in turn, tends to be shorter for site **H** than it is for site **E**. For this behavior, different explanations are possible: On the one hand, the different decay times of $Ir(btp)_2(acac)$ in the two sites may reflect different *radiative* allowednesses of the corresponding transitions. These may be a consequence of different mixing situations of the individual triplet substates with higher lying singlet states, which is possibly connected with the different ZFS and thus MLCT character in the two sites. On the other hand, also different rates of non-radiative deactivation to the ground state may be responsible for the observed differences of the two sites. In this context it is important to note that the determined decay times $\tau_{\mathrm{I}}$, $\tau_{\mathrm{II}}$, and $\tau_{\mathrm{III}}$ reflect the total deactivations of the triplet substates to the ground state by radiative and non-radiative processes. An assessment of the non-radiative rates, however, requires measurements of the emission quantum efficiency, which was not feasible with the available experimental equipment. Therefore, an ultimate interpretation of the different decay times of $Ir(btp)_2(acac)$ in the two sites **E** and **H** in $CH_2Cl_2$ can not be given here.

## 5.2 Processes of spin-lattice relaxation

In Sect. 5.1, the temperature dependence of the thermalized emission decay component has been studied. However, a detailed analysis of the short (rise and decay) components reveals specific relaxation properties between the triplet substates. These effects are based on processes of spin-lattice relaxation (SLR).

SLR from one substate of $\mathbf{T_1}$ to another usually occurs by a transfer of energy to or from the host lattice in form of phonons. Therefore, the relaxation rate depends on the energy separation of the involved triplet substates and on the phonon density of states in the energy range of this separation. The transition in energy can occur by three different processes – the *direct process*, the *Orbach process*, and the *Raman process*. These will be briefly introduced in the following. It has to be remarked that the relaxation between two substates of a triplet state requires a spin-reorientation during the transition. This spin-flip may also be brought about by the interaction of phonons with the triplet substates of a molecule. The phonon modes can cause fluctuations of molecular properties, such as intramolecular distances, and thus can modulate electronic charge distributions, SOC, and mixing coefficients between

different states. A detailed discussion of such mechanisms is not intended in this context, but is given for example, in Refs. [139, 171, 182–190].

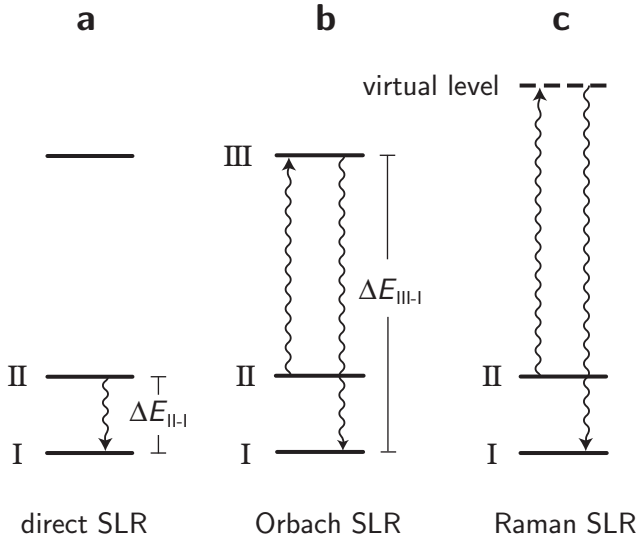


**Figure 29** Illustration of the three different processes of spin-lattice relaxation (SLR). The states **I**, **II**, and **III** represent, for example, triplet substates of organo-transition metal compounds.

## The direct process

The direct process designates the non-radiative transition between two states by emission or absorption of one phonon. For example, upon relaxation from substate **II** to substate **I** (compare Fig. 29a), one phonon of the energy $\Delta E_{\text{II–I}}$ is transmitted to the lattice. At higher temperature, also the inverse process can occur. Hence, the effective rate of $k_{\text{II–I}}^{\text{SLR}}$, which may be measured, represents the net rate of up and down processes. It is given by the expression (e.g., see Refs. [46, 139, 171, 182, 187, 191, 192])

$$k_{\text{II–I}}^{\text{SLR}}(\text{direct}) = \frac{3}{2\pi\hbar^4\rho v^5} \cdot \left|\left\langle \text{II} \left| \hat{\text{V}} \right| \text{I} \right\rangle\right|^2 \cdot (\Delta E_{\text{II–I}})^3 \cdot \coth\left(\Delta E_{\text{II–I}}/2k_{\text{B}}T\right) \quad , \quad (18)$$

wherein $\rho$ is the mass density of the matrix material, $v$ the (average) velocity of sound in the matrix, and $k_{\text{B}}$ the Boltzmann constant. $\hat{V}$ represents the perturbation caused by lattice modes (phonons) which couple the electronic states **I** and **II**. The

direct process usually dominates the other processes of SLR at low temperature and its rate exhibits only a week temperature dependence.

## The Orbach process

At higher temperatures, relaxation between two states may also occur by a two phonon process involving a third energy level (see Fig. 29b). Relaxation from substate **II** to substate **I** by this so-called *Orbach process* proceeds by absorption of one phonon of the energy $\Delta E_{\mathrm{III-II}}$ and the subsequent emission of a phonon of the energy $\Delta E_{\mathrm{III-I}}$. The corresponding up process can also occur. The net rate $k_{\mathrm{II-I}}^{\mathrm{SLR}}$ according to the Orbach process is obtained by the equation [139, 171]

$$k_{\mathrm{II-I}}^{\mathrm{SLR}}(\mathrm{Orbach}) = \frac{C_{\mathrm{III,II}}\, C_{\mathrm{III,I}} \left(\mathrm{e}^{\Delta E_{\mathrm{III-II}}/k_{\mathrm{B}}T} + e^{\Delta E_{\mathrm{III-I}}/k_{\mathrm{B}}T}\right)}{C_{\mathrm{III,I}}\, e^{\Delta E_{\mathrm{III-I}}/k_{\mathrm{B}}T} \left(e^{\Delta E_{\mathrm{III-II}}/k_{\mathrm{B}}T} - 1\right) + C_{\mathrm{III,II}}\, e^{\Delta E_{\mathrm{III-II}}/k_{\mathrm{B}}T} \left(e^{\Delta E_{\mathrm{III-I}}/k_{\mathrm{B}}T} - 1\right)}, \tag{19}$$

with the abbreviations

$$C_{\mathrm{III,I}} = \frac{3}{2\pi\hbar^4\rho v^5} \cdot \left|\left\langle \mathrm{III} \left| \hat{\mathrm{V}} \right| \mathrm{I} \right\rangle\right|^2 \cdot (\Delta E_{\mathrm{III-I}})^3 \tag{20}$$

$$C_{\mathrm{III,II}} = \frac{3}{2\pi\hbar^4\rho v^5} \cdot \left|\left\langle \mathrm{III} \left| \hat{\mathrm{V}} \right| \mathrm{II} \right\rangle\right|^2 \cdot (\Delta E_{\mathrm{III-II}})^3 \quad . \tag{21}$$

The involved parameters and matrix elements correspond to the definitions given above. Under the assumption that the energy separation $\Delta E_{\mathrm{II-I}}$ is small compared to the separation $\Delta E_{\mathrm{III-I}}$, i.e., $\Delta E_{\mathrm{III-I}} \approx \Delta E_{\mathrm{III-II}} = \Delta E$, Equation 19 can be approximated by

$$k_{\mathrm{II-I}}^{\mathrm{SLR}}(\mathrm{Orbach}) \approx \frac{2C_{\mathrm{III,II}}C_{\mathrm{III,I}}}{(C_{\mathrm{III,I}} + C_{\mathrm{III,II}})} \cdot \frac{1}{e^{\Delta E/k_{\mathrm{B}}T} - 1} \quad . \tag{22}$$

An even simpler expression is obtained for sufficiently low temperatures, where $k_{\mathrm{B}}T \ll \Delta E$. In this case, the rate becomes

$$k_{\mathrm{II-I}}^{\mathrm{SLR}}(\mathrm{Orbach}) \approx const \cdot (\Delta E)^3 \cdot e^{-\Delta E/k_{\mathrm{B}}T} \quad . \tag{23}$$

This approximation of the Orbach process will be applied in the next section to fit the temperature dependence of the total SLR rate $k_{\mathrm{II-I}}^{\mathrm{SLR}}$ of $\mathrm{Ir(btp)_2(acac)}$ in $\mathrm{CH_2Cl_2}$ at low temperatures ($T < 4\,\mathrm{K}$).

### The Raman Process

A Raman scattering process can also lead to relaxation between the two states **II** and **I**. This process can be also regarded as a two phonon process, whereby the involved intermediate level is a virtual one (see Fig. 29c). The temperature dependence of the Raman SLR rate is usually approximated by the power law [139, 171, 187, 189, 190]

$$k_{\mathrm{II-I}}^{\mathrm{SLR}}(\mathrm{Raman}) = R \cdot T^n \qquad . \tag{24}$$

$R$ is a constant and $n$ is an empirical parameter equal to 5 or 7 (for non-Kramers compounds) [189]. For organo-transition metal complexes hitherto studied, the $T^5$ dependence describes the experimental observations better than the $T^7$ dependence. [139] The Raman process is usually only important, if no higher lying electronic energy state is present to enable the more effective Orbach process.

## 5.3 Effects of spin-lattice relaxation in Ir(btp)$_2$(acac)

Figure 30 shows emission decay and rise curves measured for site **H** of Ir(btp)$_2$(acac) in $CH_2Cl_2$ at a temperature of 1.5 K. The excitation energy was 16293 cm$^{-1}$, corresponding to transition **0** → **III**. Curve (a) represents the emission decay of substate **II** detected at 16271 cm$^{-1}$ (**II** → **0**, $\mathrm{II}_{0-0}$), while curve (b) shows the emission rise and decay of substate **I** detected at 16268 cm$^{-1}$ (**I** → **0**, $\mathrm{I}_{0-0}$).

Obviously, the emission from substate **II** (Fig. 30a), detected at $\mathrm{II}_{0-0}$ (16271 cm$^{-1}$), decays bi-exponentially with a 16 µs and a 135 µs component. On the other hand, the emission from substate **I**, detected at $\mathrm{I}_{0-0}$ at 16268 cm$^{-1}$ (Fig. 30b), shows an initial rise of about 16 µs and then a monoexponential decay of 135 µs. In both cases, the long component represents the decay time of the thermalized population of the $\mathbf{T_1}$ substates according to Eq. 17 and Fig. 28. Therefore, at a given temperature, the same decay time is found for both electronic origins $\mathrm{I}_{0-0}$ and $\mathrm{II}_{0-0}$, while the short component observed immediately after excitation shows a distinct spectral dependence. The initial decay and rise components are determined by processes of spin-lattice relaxation from substate **II** to substate **I**. Substate **II** decays with 16 µs populating substate **I**, which shows the corresponding emission rise. This rise, however, does not start from zero intensity, since substate **I** is also populated directly by a fast process of SLR from substate **III**. The corresponding SLR time $\tau_{\mathrm{III-I}}^{\mathrm{SLR}}$ is estimated to be shorter than 50 ns (see below in this section). The observation of the

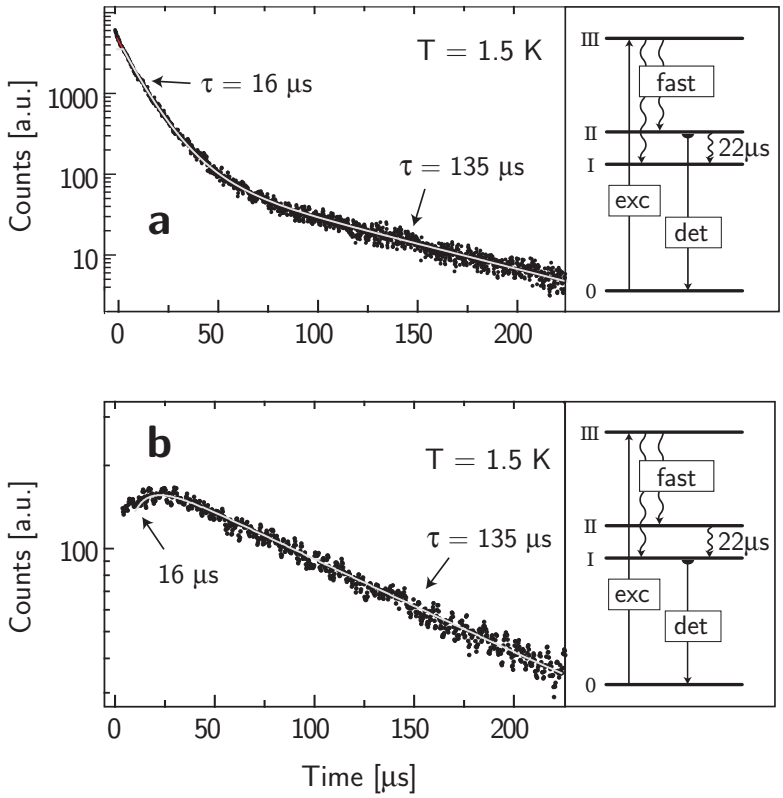


**Figure 30** Emission decay and rise curves of Ir(btp)$_2$(acac) in $CH_2Cl_2$ (site **H**) under excitation into $\mathbf{T_1}$ substate **III** (16293 cm$^{-1}$) at 1.5 K. (a) Detection at the energy of transition **II** $\rightarrow$ **0** (16271 cm$^{-1}$) gives a bi-exponential decay behavior. The short component of 16 µs is given by two deactivation paths, the deactivation from substate **II** to the ground state (**II** $\rightarrow$ **0**) with a time constant of 58 µs (Fig. 4) and the deactivation by SLR from **II** to **I** with 22 µs (see below). The long component reflects the decay after thermal equilibration. The corresponding decay time of 135 µs is shorter than the decay time $\tau_I$ of substate **I** due to slight thermal population of substate **II** even at $T$ = 1.5 K. (b) Detection at the energy of transition **I** $\rightarrow$ **0** (16268 cm$^{-1}$) shows an initial rise of the emission intensity due to population of substate **I** by spin-lattice relaxation from substate **II** to substate **I**. The rise time fits well to the short decay component of 16 µs of (a). Note that substate **I** is not only populated by slow SLR from substate **II**, but also directly by a fast SLR from substate **III** after excitation of this state.

16 µs decay of substate **II** and the same value as rise of the emission from substate **I** represents a direct prove of the occurrence of SLR processes in this time range.

However, the deactivation of substate **II** occurs by competing processes. This

substate is depopulated by SLR with a rate of $k_{\mathrm{II-I}}^{\mathrm{SLR}} = 1/\tau_{\mathrm{II-I}}^{\mathrm{SLR}}$ and by (radiative and possibly also non-radiative) deactivation to the ground state $\mathbf{S_0}$. Thus, the emission decay rate $k_{\mathrm{II}}^{\mathrm{em}}$ corresponding to the measured short component is given by Eq. 25

$$k_{\mathrm{II}}^{\mathrm{em}} = \frac{1}{\tau_{\mathrm{II-I}}^{\mathrm{em}}} = k_{\mathrm{II-I}}^{\mathrm{SLR}} + k_{\mathrm{II}} \tag{25}$$

$\tau_{\mathrm{II}}^{\mathrm{em}}$ is the decay time of the short component observed at the electronic origin $\mathrm{II}_{0-0}$. $k_{\mathrm{II}}$ is the inverse of the decay time $\tau_{\mathrm{II}}$ of substate **II** to the ground state as determined in Sect. 5.1. With $\tau_{\mathrm{II}}^{\mathrm{em}} = 16\,\mu\mathrm{s}$ and $k_{\mathrm{II}} = 1/\tau_{\mathrm{II}} = 1/58\,\mu\mathrm{s}$, one obtains from Eq. 25 $\tau_{\mathrm{II-I}}^{\mathrm{SLR}} = 22\,\mu\mathrm{s}$ (site **H**) at 1.5 K. When the temperature is increased, the SLR time becomes shorter. This is seen in Fig. 31, which depicts emission decay curves for site **H** in the temperature range between 1.5 K and 5 K. The emission is detected at the electronic origin $\mathbf{II} \rightarrow \mathbf{0}$ ($\mathrm{II}_{0-0}$ at 16271 cm$^{-1}$). (Compare also Fig. 30a.) The short decay component is shortened from 16 µs at 1.5 K to 11.5 µs at 2.5 K and to 2.5 µs at 3.5 K and becomes less intense. Above about 5 K, the short component is not observed at all and therefore is shorter than the detection limit of ≈300 ns. Moreover, the long decay component (thermalized decay) becomes shorter as well with temperature increase. This latter behavior has been discussed in Sect. 5.1.

To investigate the temperature dependence of the rate of SLR, the corresponding values $k_{\mathrm{II-I}}^{\mathrm{SLR}}$ are determined according to Eq. 25 and plotted for the temperature range from 1.5 K to 4 K for each of the two sites **E** and **H** (Fig. 32).

The two sites show a distinctly different behavior. This is already seen when comparing the relaxation times at $T = 1.5$ K. For site **E**, $\tau_{\mathrm{II-I}}^{\mathrm{SLR}}$ amounts to only 4 µs, while for site **H** a significantly longer value of 22 µs is obtained. With temperature increase, the SLR rate increases only smoothly up to a certain temperature and then rises rapidly. For site **E**, this rise has its onset near 2.0 K and for site **H** near 2.7 K. Moreover, for site **E** the increase of $k_{\mathrm{II-I}}^{\mathrm{SLR}}$ is steeper than for site **H**. For an interpretation, the different processes of spin-lattice relaxation have to be considered - the *direct process*, the *Orbach process*, and the *Raman process*. According to the details given in Sect. 5.2 an analytical expression for the total spin-lattice relaxation rate $k_{\mathrm{II-I}}^{\mathrm{SLR}}$ of all three processes is given by [139, 171]

$$k_{\mathrm{II-I}}^{\mathrm{SLR}} = \left[c_1 \cdot (\Delta E_{\mathrm{II-I}})^3 \cdot \coth\left(\frac{\Delta E_{\mathrm{II-I}}}{2k_{\mathrm{B}}T}\right)\right]^{\mathrm{direct}} + \left[c_2 \cdot (\Delta E)^3 \cdot \mathrm{e}^{-\Delta E/k_{\mathrm{B}}T}\right]^{\mathrm{Orbach}} + [c_3 \cdot T^n]^{\mathrm{Raman}}. \tag{26}$$

Here, the simplified expression (Eq. 23) is used for the Orbach relaxation rate. The corresponding assumptions $\Delta E_{\mathrm{III-I}} \approx \Delta E_{\mathrm{III-II}} = \Delta E$ and $k_{\mathrm{B}}T \ll \Delta E$ are sufficiently

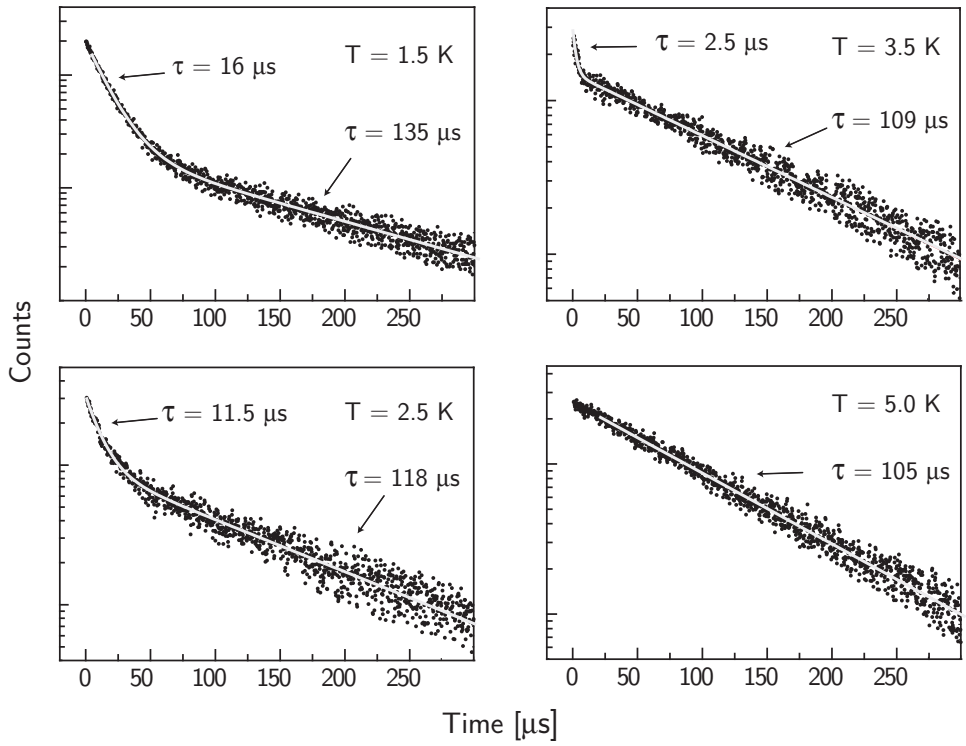


**Figure 31** Emission decay of Ir(btp)$_2$(acac) in $CH_2Cl_2$ (site **H**) under excitation into $\mathbf{T_1}$ substate **III** (16293 cm$^{-1}$) and detection at the energy of transition $\mathrm{II}_{0-0}$ (16271 cm$^{-1}$). The curves are depicted for selected temperatures in the range from 1.5 K to 5.0 K. The short component is strongly shortened upon temperature increase and becomes less intense. This reflects the temperature dependence of spin-lattice relaxation from substate **II** to substate **I**. At about 5 K, the process of thermalization has become fast and the decay time of the short component is below the detection limit, which was ≈300 ns in this experiment. The long component represents the decay of the thermally equilibrated substates (compare Fig. 27 and Eq. 17).

fulfilled for the two sites **E** and **H** of Ir(btp)$_2$(acac) in $CH_2Cl_2$ in the discussed temperature range. Eq. 26 can be used for a fit to the experimental data given in Fig. 32 to obtain information about the involved processes of spin-lattice relaxation. For the fitting procedure, those energy separations $\Delta E_{\mathrm{II-I}}$ and $\Delta E$ ($\Delta E_{\mathrm{III-II}}$) obtained from emission and excitation spectra (compare Sect. 4.2) were applied and kept fixed. When regarding only the *direct process* (first term of Eq. 26), the observed data can be fit from 1.5 K up to about 2 K for site **E** and to about 2.7 K for site **H**

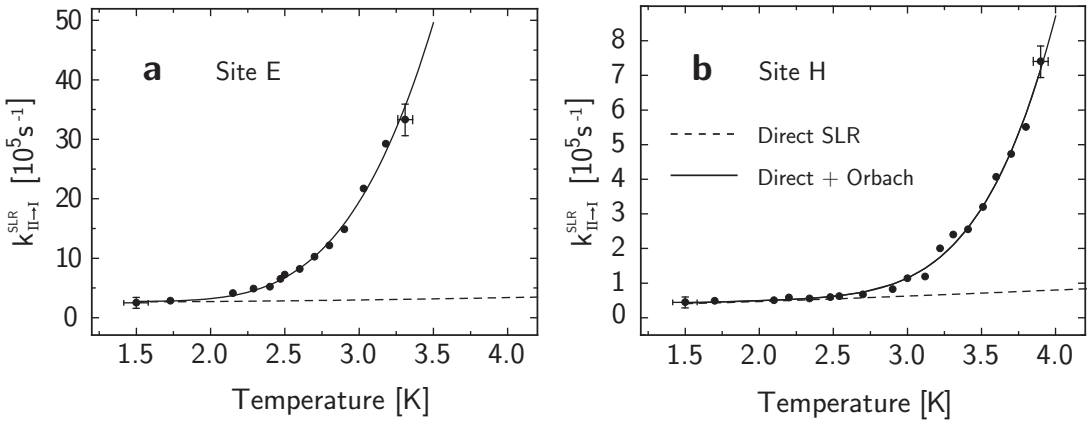


**Figure 32** Rate of spin-lattice relaxation from $\mathbf{T_1}$ substate **II** to substate **I** for site **E** (a) and site **H** (b) of Ir(btp)$_2$(acac) in $CH_2Cl_2$. The solid lines represent fits to the experimental data according to the total rate of direct processes and Orbach processes of SLR (Eq. 26). The temperature behavior is different for both sites, in particular with respect to the rate at 1.5 K and the onset of the Orbach process. The direct process alone (dotted line) cannot explain the observed temperature dependence.

(compare dashed lines in Fig. 32). Hence, in this range the *direct process* clearly dominates. However, at higher temperatures, the observed temperature dependence deviates significantly from the curve predicted for the *direct process* alone. This indicates the participation of further processes of SLR. Indeed, including both the *direct process* and the *Orbach process*, Eq. 26 can be well fit to the experimental data. Thus, the *Orbach process* is responsible for the rapid increase of the SLR rate above 2.0 K (site **E**) and 2.7 K (site **H**), respectively. A significant influence of the *Raman process* is not indicated within the accuracy of the experimental data. This is understandable, since in the presence of a closely higher lying electronic energy level, the *Orbach process* is expected to dominate strongly over the *Raman process* – a situation, which has been found also for other complexes, such as Pt(thpy)$_2$ [139, 171]. The higher importance of the *Orbach process* at low temperature for site **E** as compared to site **H** can be explained by the difference of the energy separation $\Delta E_{\mathrm{III-II}}$ to substate **III** for the two sites. According to Eq. 26, the SLR rate due to the *Orbach* component is higher for a compound with a smaller energy separation $\Delta E$. Thus, for site **E** with a zero-field splitting of $\Delta E \approx \Delta E_{\mathrm{III-II}} = 12\,\mathrm{cm}^{-1}$, the *Orbach process* gains influence already below 2 K, while for site **H** with a splitting $\Delta E \approx \Delta E_{\mathrm{III-II}} = 22\,\mathrm{cm}^{-1}$ its onset is observed at about 2.7 K. Moreover, the rate of the *direct process* of SLR from substate **II** to state **I** at $T = 1.5$ K is different for the

two sites **E** and **H** with a characteristic time of 22 µs for site **H** and of 4 µs for site **E**. This behavior is mainly responsible for the different intensity ratio of the two emission lines $\mathrm{II}_{0-0}$ and $\mathrm{I}_{0-0}$, if compared for the two sites. (Fig. 25) The difference of the rates of the *direct process* of SLR for the two sites cannot be explained by different energy separations $\Delta E_{\mathrm{II-I}}$, since both sites exhibit the same value of 2.9 cm$^{-1}$. For an interpretation, one has to account for the fact that molecules in different sites experience dissimilar matrix environments, where different electron-phonon coupling and/or different sound velocities in the anisotropic $CH_2Cl_2$ take effect. However, in general, the SLR times $\tau^{\mathrm{SLR}}_{\mathrm{II-I}}$ of all sites in $CH_2Cl_2$ will also depend on the energy separation $\Delta E_{\mathrm{II-I}}$. To demonstrate the different situations in all sites of Ir(btp)$_2$(acac) in $CH_2Cl_2$, the available intensity ratios $I_{\mathrm{II}}/I_{\mathrm{I}}$ of the emission lines $\mathrm{II}_{0-0}$ and $\mathrm{I}_{0-0}$ are summarized in Table 2.

**Table 2** Intensity ratio $I_{\mathrm{II}}/I_{\mathrm{I}}$ of the electronic origin lines $\mathrm{II}_{0-0}$ and $\mathrm{I}_{0-0}$ of the emission of Ir(btp)$_2$(acac) in different sites/matrices. The integrated intensities were determined by fit of a Gaussian line shape to the respective lines.

| **Matrix** | **$CH_2Cl_2$** | | | | | **Single Crystal** |
|---|---|---|---|---|---|---|
| **Site** | **C** | **D** | **E** | **H** | **I** | |
| $\Delta E_{\mathrm{II-I}}$ [cm$^{-1}$] | 3.2 | 2.2 | 2.9 | 2.9 | 2.6 | 2.4 |
| $I_{\mathrm{II}}/I_{\mathrm{I}}$ (1.5 K) | 0.5 | 5.2 | 0.5 | 3.5 | 1.4 | 1 |
| $I_{\mathrm{II}}/I_{\mathrm{I}}$ (4.2 K) | 1.1 | 11.5 | 1.7 | 11.9 | 8 | 5.4 |

At 1.5 K and under excitation of a vibrational satellite of substate **III** (site **H**) at 16742 cm$^{-1}$ (449 cm$^{-1}$ vibration), no emission is observed at the energy of the electronic origin of transition **III** $\rightarrow$ **0** at 16293 cm$^{-1}$. This indicates that the times of spin-lattice relaxation $\tau^{\mathrm{SLR}}_{\mathrm{III-I}}$ and $\tau^{\mathrm{SLR}}_{\mathrm{III-II}}$ are significantly shorter than the detection limit of about 50 ns. In fact, a rough estimate of the corresponding rates at $T$ = 1.5 K according to the term for the direct process (Eq. 26) results in a time of spin-lattice relaxation from substate **III** to each of the two lower substates of the order of $\tau^{\mathrm{SLR}}_{\mathrm{III-I/II}}$ (direct) $\approx$ 20 ns for both sites. These values are obtained by use of the known energy separations $\Delta E_{\mathrm{III-I}}$ and $\Delta E_{\mathrm{III-II}}$ and assuming the same electron-phonon coupling as for the substates **I** and **II** (same constants $c_1$ in Eq. 26). As a matter of fact, spin-lattice relaxation processes involving $\mathbf{T_1}$ substate **III** are very effective.

Interestingly, the fast thermalization between the two lower lying substates **I/II** and substate **III** makes it even possible to excite the lower lying substate **II** and to observe the anti-Stokes emission from the higher lying substate **III**. This is demonstrated in Fig. 33 for site **H**. After selective excitation of substate **II** at 16271 $cm^{-1}$, the high energy emission line $III_{0-0}$ at 16293 $cm^{-1}$ corresponding to transition **III** → **0** is observable at temperatures higher than about 5 K. The intensity of this line increases with increasing temperature, according to the thermal population of substate **III**.

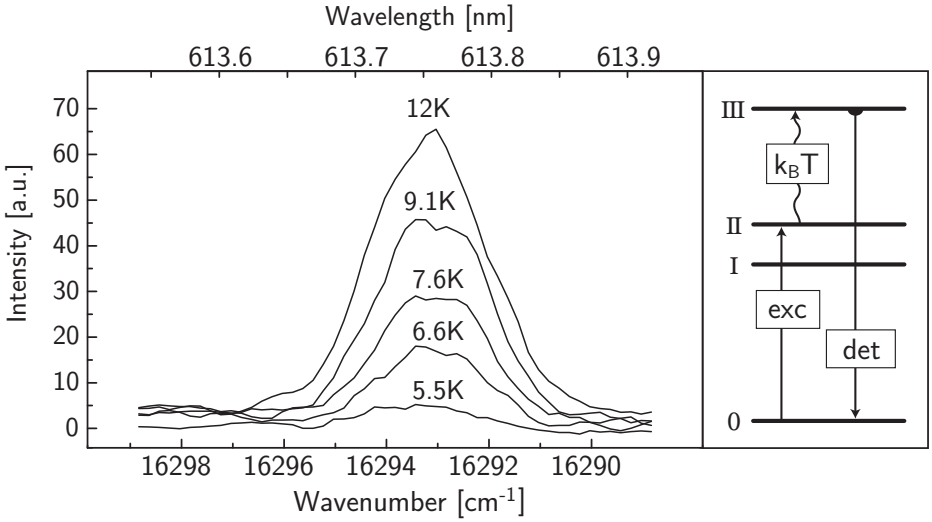


**Figure 33** Anti-Stokes emission of $Ir(btp)_2(acac)$ in $CH_2Cl_2$ (site **H**) at different temperatures. After selective excitation of $\mathbf{T_1}$ substate **II** as depicted in the inset, state **III** is thermally populated and emission from this state is observed at the energy of the electronic origin transition **III** → **0** (0-0) of 16293 $cm^{-1}$.

## 5.4 Emission decay behavior and matrix influence – Conclusions

The emission decay dynamics of $Ir(btp)_2(acac)$ has been investigated in detail for two sites of the complex in a $CH_2Cl_2$ host. Selective decay time measurements of $Ir(btp)_2(acac)$ in each of the two sites **E** and **H** reveal distinctly different properties of these sites. At low temperature, the individual decay times of the substates **I**, **II**, and **III** of $\mathbf{T_1}$ have been determined to $\tau_I$ =62 µs, $\tau_{II}$ =19 µs, and $\tau_{III}$ =3 µs (site **E**),

and to $\tau_{\mathrm{I}}$ =150 µs, $\tau_{\mathrm{II}}$ =58 µs, and $\tau_{\mathrm{III}}$ =1.5 µs (site **H**). These values are summarized in Fig. 34 and in Table 3 which also gives a few further values obtained for $Ir(btp)_2$-(acac) in *n*-octane and as a single crystal.

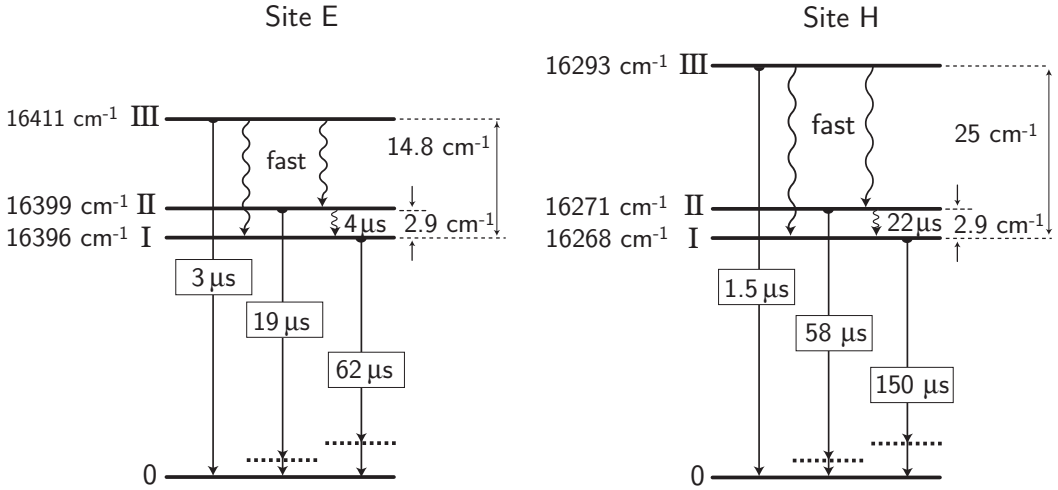


**Figure 34** Energy level diagram of the two sites **E** and **H** of $Ir(btp)_2(acac)$ in $CH_2Cl_2$ including the individual decay times $\tau_{\mathrm{I}}$, $\tau_{\mathrm{II}}$, and $\tau_{\mathrm{III}}$ and the spin-lattice relaxation time $\tau^{\mathrm{SLR}}_{\mathrm{II-I}}$ at $T$ = 1.5 K.

**Table 3** Emission decay times of the triplet substates **I**, **II**, and **III** of $Ir(btp)_2$-(acac) in different sites of $CH_2Cl_2$ and as a single crystal. The time of spin-lattice relaxation from substate **II** to substate **I** at $T$ = 1.5 K is also given, where available.

| **Matrix** | **Site** | $\tau_{\mathrm{I}}$ **[µs ]** | $\tau_{\mathrm{II}}$ **[µs ]** | $\tau_{\mathrm{III}}$ **[µs ]** | $\tau^{\mathrm{SLR}}_{\mathrm{II-I}}$ **[µs ]** |
|---|---|---|---|---|---|
| $CH_2Cl_2$ | E | 62 | 19 | 3 | 4 |
| | H | 150 | 58 | 1.5 | 22 |
| *n*-octane | A | 105 | 51 | - | 57 |
| Single crystal | - | 140 | - | - | - |

Obviously, the host environment of the complex has a significant effect on the decay times $\tau_{\mathrm{I}}$, $\tau_{\mathrm{II}}$, $\tau_{\mathrm{III}}$. A variation of the individual emission decay times of the triplet substates of a complex with the matrix environment also fits to another observation. For $Ir(btp)_2(acac)$ doped into $CH_2Cl_2$ or octane, the emission decay curves are

not monoexponential in case of non-selective excitation. As an example, an emission decay curve of $Ir(btp)_2(acac)$ in $CH_2Cl_2$, registered at 10 K after UV-excitation ($\bar{\nu}_{exc}$ =28169 $cm^{-1}$), is depicted in Fig. 35. Corresponding non-monoexponential decay curves are found in a large temperature range from 1.2 K up to at least 150 K. At very low temperature, e.g. $T < 5$ K this behavior is due to the fact that slow processes of spin-lattice relaxation govern the decay dynamics. At higher temperatures, e.g. $T > 5$ K, the substates emit from a thermal equilibrium and therefore the decay would be expected to occur monoexponentially. It has to be remarked that a decrease of the doping concentration and of the pulse energy of the exciting laser does not lead to a monoexponential behavior as expected. The deviation from a monoexponential decay, however, might be a result of the varying decay time for the different sites. Therefore, the corresponding decay curve might represent a superposition of several monoexponential decay curves of the respective sites.

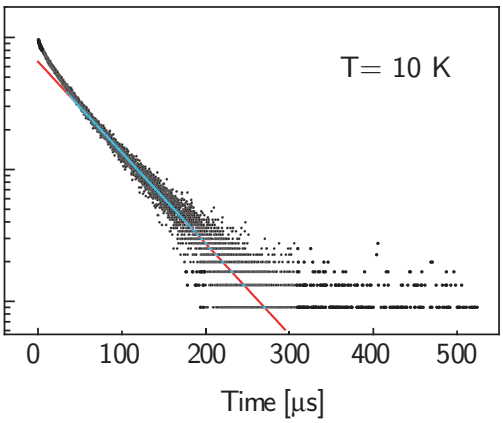


**Figure 35** Decay of the emission from the triplet state $\mathbf{T_1}$ of $Ir(btp)_2(acac)$ in $CH_2Cl_2$ registered at $T = 10$ K. The emission was monitored at an energy of 16400 $cm^{-1}$ after non-selective excitation in the UV ($\bar{\nu}_{exc}$ =28169 $cm^{-1}$). At $T$ = 10 K, the population of the substates **I**, **II**, and **III** is in thermal equilibrium. Nevertheless, the observed decay is not monoexponential.

Interestingly, a monoexponential decay in case of non-selective detection as described for $Ir(btp)_2(acac)$ is not an exception, but rather is typical for the class of Ir-complexes. Non-monoexponential decay at low temperature has been observed as well for $Ir(ppy)_3$ [193], $Ir(piq)_3$ and $Ir(piq)_2(acac)$ [194], and for $Ir(bt)_2(acac)$[19] [195]. On the other hand, many complexes, such as Pt-complexes, a large number of

[19] $Ir(bt)_2(acac)$=bis(2-phenylbenzothiazolato-$N,C^{2'}$)iridium(acetylacetonate)

which has been investigated so far, or Os-complexes, usually exhibit purely mono-exponential decays. Examples are the complexes Pt(dFppy)(dpm)[20] and Pt(dFppy)$_2$, [196] Pt(Me$_4$salen)[21] [142], and [Os(phen)$_2$(dppene)]$^{2+}$ [22] [181, 197] and [Os(phen)$_2$(dpae)]$^{2+}$ [23] [197]. The non-monoexponential decay behavior can have different reasons. At first sight, concentration quenching, additional decay channels, or radiationless processes seem to be responsible. Concentration quenching can probably be excluded: Since for Ir(btp)$_2$(acac), the critical radius of energy transfer (the Förster radius) has been determined to ≈1 nm [198], a quenching at a concentration of ≈ $10^{-5}$ mol/L is unlikely. Moreover, the decay behavior is independent of the pulse energy and repetition rate of the exciting laser and thus is independent of the density of *excited* Ir(btp)$_2$(acac) molecules. Therefore, the decay behavior can indeed be attributed to different properties of different molecules or subsets of molecules, which is consistent with the observed differences for the specific sites of Ir(btp)$_2$(acac) in the $CH_2Cl_2$ host. Additional decay channels, such as an excited state, which lies in a thermally accessible energy range above the $\mathbf{T_1}$ state also have to be considered. However, in highly resolved excitation spectra of Ir(btp)$_2$(acac) in the different sites in $CH_2Cl_2$, the existence of such states is not indicated at least up to ≈500 cm$^{-1}$ above substate **III**. Non-radiative processes, on the other hand, cannot be ruled out that easily from being responsible for a non-monoexponential decay behavior. Possible processes are quenching by oxygen or nonradiative decay to the ground state by transfer of the excitation energy to the host lattice. Indeed, oxygen quenching has been found to be responsible for varying emission decay times of single DiIC$_{18}$[24] molecules in PMMA[25] and polystyrene hosts.[199] In this case, the variation of the $\tau$ values arises due to varying local oxygen concentrations in the hosts. Such a behavior has to be considered also for organo-transition metal complexes. However, it can be stated that the phenomenon of non-monoexponential decay curves is even observed for Ir-complexes with a very high quantum efficiency, such as for example Ir(ppy)$_3$, which exhibits a quantum efficiency in CBP close to 100% [74]. Therefore, radiationless deactivation of the emitting states in general is supposed not to be responsible for the phenomenon of non-exponential decay curves. On the other hand, the radiative rates of an organo-transition metal com-

[20] dFppy=2-(4',6'-difluorophenyl)pyridinato-*N,C*$^{2'}$, dpm=dipivaloylmethanate
[21] salen=*N,N'*-bis(salicylidene)
[22] phen=1,10-phenanthroline, dppene=bis(diphenylphosphino)ethene,
[23] dpae=bis(diphenylarsano)ethan
[24] 1,1'-dioctadecyl-3,3,3',3'-tetramethylindocarbocyanine-5,5'-perchlorate
[25] polymethyl-methacrylate

plex are known to be connected with the MLCT character in the emitting state. As a general trend, this correlation is well established for *different complexes*.[45] Hence, it is reasonable to assume that a similar trend also applies to *one complex, for which the MLCT character varies with the matrix environment*. It is not unlikely that the decay behavior of Ir-complexes such as $Ir(ppy)_3$ is due to different MLCT admixtures to the triplet substates of different molecules/subsets of molecules. The behavior of the $Ir(btp)_2(acac)$ complex, for which a varying MLCT character is indicated by a distribution of ZFS values (compare Chapt. 4), fits well to these considerations. Nevertheless, for this specific complex, it cannot be excluded on the basis of the available data that the differences between the sites/matrices, which are considerably large, result mainly from non-radiative processes. For a stringent interpretation of the decay behavior of $Ir(btp)_2(acac)$ in $CH_2Cl_2$, the contribution of non-radiative deactivation needs to be assessed by measurements of the emission quantum yield at low temperature.

From the emission decay times $\tau_I$, $\tau_{II}$, and $\tau_{III}$ determined at low temperature, the thermalized decay time at higher temperature can be calculated by use of Eq. 17. In this manner, decay times at $T = 77\,K$ of $\approx 8.5\,\mu s$ and $\approx 5.8\,\mu s$ are obtained for site **E** and **H** of $Ir(btp)_2(acac)$ in $CH_2Cl_2$, respectively. For $T = 300\,K$, values of $7.7\,\mu s$ (site **E**) and $4.7\,\mu s$ (site **H**) result. These values are compared in Table 4 with measured decay times of the complex in $CH_2Cl_2$, in octane, and in the three polymeric hosts PVK, PVB and PFO.[26] For comparison, also the decay time at 300 K of $Ir(btp)_2(acac)$ doped into the OLED host CBP (compare Fig. 7) is given.

The calculated decay times at 77 K and 300 K for the two sites **E** and **H** in $CH_2Cl_2$ lie in a similar range as measured for the $Ir(btp)_2(acac)$ complex in $CH_2Cl_2$ or other matrices. The values calculated for site **H**, are only slightly smaller than the ones measured for the complex in $CH_2Cl_2$, while the values obtained for site **E** are larger. The results show that the individual decay times of the triplet substates determined at low temperature are reasonable. However, at $T = 300\,K$, all emission decay curves of $Ir(btp)_2(acac)$ in the different matrices reflect a monoexponential behavior. This is in contrast to the behavior at lower temperatures, in particular below 150 K, and is not fully understood so far. One possible explanation is a dynamic averaging of the observed decay time values at higher temperature.

It has to be remarked that none of the decay times measured at ambient temperature is a purely radiative decay time. The $Ir(btp)_2(acac)$ complex is known to exhibit

[26] PVK=poly-*N*-vinylcarbazol
PVB=polyvinylbutyral
PFO=poly(9,9-dioctylfluoren-2,7-diyl); For structures, see Fig. 47.

**Table 4** Emission decay time of $Ir(btp)_2(acac)$ doped into different matrices. The values given for the two sites **E** and **H** in $CH_2Cl_2$ are calculated (compare Eq. 17) from the decay times of the individual triplet substates obtained by site-selective investigations at low-temperature. All other values represent decay times measured after non-selective excitation. The decay time of the complex in CBP is taken from Ref. [198]. The decay time marked with an asterisk is obtained from Ref. [200].

| **Matrix** | **$CH_2Cl_2$** | | **$CH_2Cl_2$** | **Octane** | **PVK** | **PVB** | **PFO** | **CBP** |
|---|---|---|---|---|---|---|---|---|
| | **Site E** | **Site H** | **Measured** | | | | | |
| $\tau$(77 K) [ µs ] | 8.5 | 5.8 | 6.5 | 7.2 | 6.7 | 8.2 | 8.0 | - |
| $\tau$(300 K) [ µs ] | 7.7 | 4.7 | 5.5* | - | 4.7 | 5.2 | 2.5 | 5.4 |

an emission quantum yield at 300 K of ≈50%, when doped into a CBP matrix.[74] For the complex in $CH_2Cl_2$, the quantum efficiency probably lies in a similar range or even below. Thus, the fact that the calculated decay times lie in the same range as the measured decay times, leads to the assumption that the quantum efficiency of the order of 50% is already contained in the decay times $\tau_I$, $\tau_{II}$, and $\tau_{III}$ determined at low temperature. This fits to investigations described in Ref. [200], which indicate a largely constant quantum efficiency in the temperature range from 5 K to 300 K for $Ir(btp)_2(acac)$ in CBP.

# 6 Emission Spectra of $Ir(btp)_2(acac)$ in $CH_2Cl_2$ – Vibrational Satellite Structures

In this chapter, the vibrational satellite structure of the emission of $Ir(btp)_2(acac)$ is investigated with the complex in the $CH_2Cl_2$ matrix and for comparison also in *n*-octane and as a single crystal. The vibrational satellite structure of organometallic complexes is not only interesting from a scientific point of view, but is important also for OLEDs. This is due to the fact that a limitation for the use of organo-transition metal complexes in display applications is often color purity of their emission. Obviously, emitters in OLEDs intended for the application in displays are required to feature a narrow-band emission spectrum to provide pure fundamental colors blue, green, and red, respectively. However, emission spectra of organo-transition metal complexes are often broad. The width of an emission spectrum is, among others, given by the extension of the vibrational satellite structure of the emission. For emitters, for example, which have their emission maximum in the blue spectral region, the vibrational satellite structure can often extend so far to longer wavelengths to reach into the green spectral region. The perception of the human eye is therefore not a pure blue, but a so-called 'sky-blue' or even turquoise color. On the other hand, the emission of a complex with its maximum in the red may reach into the infrared, therefore sacrificing the device efficiency (perceptible to the human eye).

Clearly, it is very important to study the mechanisms which lead to the occurrence of vibrational satellites, and to understand the corresponding spectral features. This will be addressed in the following.

## 6.1 Emission spectrum under site-selective excitation

Figure 36 shows the emission spectrum of $Ir(btp)_2(acac)$ doped into $CH_2Cl_2$, recorded at different temperatures under non-selective excitation at $\lambda_{exc}$=363.8 nm ((a), (b), and (c)). The spectra (a) and (b), registered at 300 K and at 77 K, respectively,

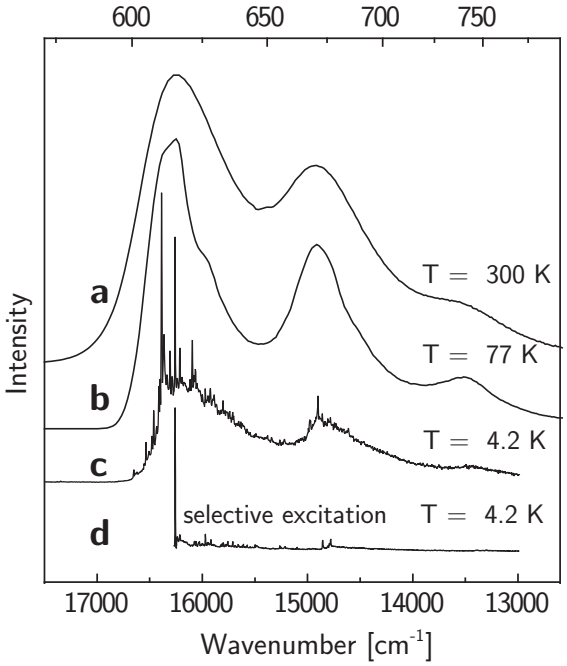


**Figure 36** (a), (b), and (c) Emission spectrum of $Ir(btp)_2(acac)$ in $CH_2Cl_2$ at different temperatures under non-selective excitation ($\lambda_{exc}$=363.8 nm). Even at 77 K, the spectrum is broad and unresolved. At 4.2 K, the homogeneous broadening is significantly reduced and a number of resolved lines due to specific sites is revealed. (d) Resolved emission of a specific site (site **H**) obtained by selective excitation of this site into triplet substate **III** ($\bar{\nu}_{\mathrm{exc}}$ =16293 $\mathrm{cm}^{-1}$)

have already been discussed in Section 3.3. Due to homogeneous and inhomogeneous effects, these spectra are broad and unresolved. The region of the vibrational satellites is given mainly by two broad bands of several overlapping satellites, which form a progression-like structure (compare Sects. 3.3 and 6.4). At 4.2 K, the (homogeneous) line broadening is significantly reduced and a manifold of narrow lines is revealed in addition to a broad background. These lines are ascribed to several discrete sites of the $Ir(btp)_2(acac)$ molecules in the $CH_2Cl_2$ matrix (see Sect. 4.1). The lines in the spectral region between 16700 $\mathrm{cm}^{-1}$ and 16200 $\mathrm{cm}^{-1}$ have been shown in Chapt. 4 to represent electronic origin transitions from $\mathbf{T_1}$ substate **II** to the ground state $\mathbf{S_0}$. Additionally, in the longer wavelength region, a few further narrow lines are observed, for example, at 16110 $\mathrm{cm}^{-1}$, 16080 $\mathrm{cm}^{-1}$, 14990 $\mathrm{cm}^{-1}$, and at 14917 $\mathrm{cm}^{-1}$. These lines represent resolved vibrational satellites of the main site (site **E**) with the electronic origin transition **II** $\rightarrow$ **0** at 16399 $\mathrm{cm}^{-1}$ (compare

Sect. 4.1 and Table 1). Nevertheless, significant details of the vibrational satellite structure are not observed under UV-excitation, due to the overlap of the emission spectra of all sites.

However, the situation becomes more favorable, in case one specific site is excited selectively. This is shown in Fig. 36d on the example of site **H** of $Ir(btp)_2$-(acac) in $CH_2Cl_2$ (compare Fig. 18b). Selective excitation of substate **III** of this site ($\bar{\nu}_{exc}$ =16293 $cm^{-1}$) at $T$ = 4.2 K results in an emission spectrum in which the smearing out due to the simultaneous emission of the molecules in several sites as well as the inhomogeneous background is largely eliminated. Therefore, a well resolved line spectrum is observed. An intense electronic origin occurs at 16271 $cm^{-1}$ resulting from transition **II** $\rightarrow$ **0**, as already discussed in 4.2. Red shifted to this origin line, a rich vibrational satellite structure is also revealed. Although theses satellite lines are rather weak compared to the electronic origin line, it is clearly seen in Fig. 36 that they contribute a substantial part to the total emission intensity. However, the vibrational satellite structure is not easily interpretable as it consists of modes stemming from substate **I** as well as from substate **II**. This is recognized, if the emission spectrum in the region of the vibrational satellites is investigated at different temperatures, magnetic fields, or in different time domains after the excitation pulse, as will be described below. Further, the satellite lines result from different vibrational activities, i.e. from Franck-Condon activity or from Herzberg-Teller (HT) activity. These mechanisms are introduced in the next section.

## 6.2 Franck-Condon and Herzberg-Teller activity

In principle, for a molecular system, the eigenstates are given by the time-independent Schrödinger equation [201]

$$\hat{H}(q,Q)\Psi(q,Q) = \epsilon\,\Psi(q,Q) \qquad , \tag{27}$$

wherein $\Psi(q,Q)$ represents the vibronic wavefunction, and $q$ and $Q$ are electronic and nuclear coordinates, respectively. The Hamiltonian is of the form [201]

$$\hat{H}(q,Q) = \hat{T}(q) + \hat{T}(Q) + \hat{U}(q,Q) \qquad , \tag{28}$$

with the electronic and nuclear kinetic energies, $\hat{T}(q)$ and $\hat{T}(Q)$, respectively. The potential $\hat{U}(q,Q)$ includes the energy of interactions between the electrons, between the electrons and the nuclei, and between the nuclei. This term expresses that the

motion of the electrons and the motion of the nuclei generally are not independent of each other. Thus, $\hat{H}$ does not allow a separation of the variables $q$ and $Q$ and a system of coupled differential equations is obtained, which cannot be solved analytically. However, often approximations can be employed to uncouple these equations. For this purpose, the full molecular wavefunctions are usually expanded in certain basis sets, which allow to introduce specific assumptions in order to achieve nuclear motion separability.

## Born-Oppenheimer approximation and Franck-Condon activity

The Born-Oppenheimer approximation represents one approach to this problem. Therein, when using the so called 'crude adiabatic' basis set (compare Ref. [201]), the wavefunction can be written as simple product of an electronic part $\phi_n(q, Q^0)$ and a vibrational part $\chi_{n,i}(Q)$. $n$ and $i$ number the electronic and the vibrational eigenstates, respectively.

$$\Psi_{n,i}(q, Q) = \phi_n(q, Q^0)\chi_{n,i}(Q) \tag{29}$$

Note that all the $Q$-dependence of the electronic wavefunction is removed, since this wavefunction is defined at one specific nuclear configuration $Q^0$. This decoupling of electronic and nuclear motion is often justified by accounting for the fact that the electron mass is much smaller than nuclear masses. Therefore, the electrons move much more rapidly compared to the nuclei and the system of electrons is assumed to behave like a gas. (See for example Ref. [201].)

With the product wavefunction of Eq. 29, the intensity of a transition from the zero-point vibrational level ($v' = 0$) of an excited state **1** to a vibrational level $v$ of the electronic ground state **0** (regarding a specific normal) mode is approximated by

$$I_{1,0}(v' = 0, v) \propto \left|\left\langle \Psi_1(v') \left|\hat{\mu}\right| \Psi_0(v)\right\rangle\right|^2 = \left|\left\langle \phi_1 \left|\hat{\mu}\right| \phi_0\right\rangle\right|^2 \cdot \left|\left\langle \chi_1(0)\middle|\chi_0(v)\right\rangle\right|^2 \quad , \tag{30}$$

wherein $\hat{\mu}$ is the electric dipole operator. The first term on the right-hand side represents the squared electronic dipole matrix element, and specifies the purely electronic allowedness of the transition. The second term involves the overlap of the vibrational wavefunction in the excited state and in the ground state, and is referred to as *Franck-Condon factor*. It can only be non-zero for totally symmetric modes,

since the vibrational ground state is totally symmetric. The Franck-Condon factor expresses the intensity of a specific vibrational satellite line relative to the purely electronic line. Clearly, it is seen that the intensities of all vibrational satellite lines scale with the allowedness of the purely electronic transition. Importantly, a vibrational satellite structure due to Franck-Condon (FC) activity is only observed for an electronically sufficiently allowed transition. In organo-transition metal complexes, FC-activated satellites often occur with the transition from the $\mathbf{T_1}$ substates **II** and **III** to the ground state.[45, 120]

The Franck-Condon factor regarding a specific normal mode is related to the important *Huang-Rhys parameter* $S$ by

$$\left|\left\langle \chi_1(v=0)\middle|\chi_0(v)\right\rangle\right|^2 = \frac{e^{-S}S^v}{v!} \quad . \tag{31}$$

$S$ is useful as a measure of the relative shift $\Delta Q$ of the equilibrium positions $Q_1^0$ and $Q_0^0$, respectively, of the electronic states **1** and **0** involved in the transition, since it is connected with $\Delta Q$ by

$$S \propto (\Delta Q)^2 = \left(Q_1^0 - Q_0^0\right)^2 \quad . \tag{32}$$

According to Eq. 31, the Huang-Rhys parameter $S$ can directly be determined from highly resolved spectra, if the ratio of the intensities $I_v$ of successive vibrational satellites of a Franck-Condon progression is known.

$$\frac{I_v}{I_{v-1}} = \frac{S}{v} \tag{33}$$

From the equations above, it is seen that a small $S$ corresponds to a small displacement of equilibrium positions between the (electronically) excited state and the ground state. Furthermore, the smaller the Huang-Rhys parameter is, the less of the total intensity will be found in the corresponding progression of vibrational satellites.

## Herzberg-Teller activity

In the spectra of organo-transition metal complexes often vibrational satellites are observed which are not due to Franck-Condon activity, since the corresponding electronic transition is largely forbidden. This can be, for example, the case for the transition from the lowest triplet substate **I** to the ground state, which is of-

ten forbidden. For an explanation, the coupling between the electronic and the nuclear motion – the so called 'vibronic coupling' – can no longer be neglected. This means that the dependence of the electronic wavefunction on the nuclear coordinates, which has been neglected above, has to be reintroduced. A theoretical description was given by Herzberg and Teller already in 1933 [202] and is based on the assumption that the electronic wavefunction $\phi_n$ at any nuclear configuration $Q$ can be expressed in terms of electronic wavefunctions $\phi_m$ at the equilibrium positions $Q^0$ and $Q$-dependent coefficients $a_{n,m}$ [201]

$$\phi_n(q, Q) = \sum_m a_{n,m}(Q)\, \phi_m(q, Q^0) \tag{34}$$

In first order perturbation theory, this wavefunction can be approximated by

$$\phi_n(q, Q) = \phi_n(q, Q^0) + \sum_{m \neq n} a_{n,m}(Q)\, \phi_m(q, Q^0) \quad . \tag{35}$$

The second term on the right-hand side represents the Herzberg-Teller (HT) correction to the adiabatic wavefunction, the electronic part of which is given with the first term (compare Eq. 29). The full HT-corrected wavefunction is then

$$\Psi_{n,i}(q, Q) = \left[\phi_n(q, Q^0) + \sum_{m \neq n} a_{n,m}\phi_m(q, Q^0)\right]\chi_{n,i}(Q) \quad . \tag{36}$$

The index $i$ again represents the quantum number of the nuclear system. The coefficients $a_{n,m}$ contain the coupling matrix elements and, thus, depend on the mechanism of coupling. For purely vibronic coupling they are expressed according to first order perturbation theory as

$$a_{n,m}(Q) = \frac{\left\langle \phi_{\mathrm{m}}(\mathrm{q}, \mathrm{Q}^0) \left| \Delta\hat{\mathrm{H}}(\mathrm{q}, \mathrm{Q}) \right| \phi_{\mathrm{n}}(\mathrm{q}, \mathrm{Q}^0) \right\rangle}{E_n(Q^0) - E_m(Q^0)} \quad , \tag{37}$$

where $E_n(Q^0)$ and $E_m(Q^0)$ are the energies corresponding to the unperturbed wavefunctions $\phi_n(q, Q^0)$ and $\phi_m(q, Q^0)$, respectively. The perturbation operator $\Delta\hat{H}(q, Q)$ is usually obtained from the expansion of $\hat{H}(q, Q)$ as a Taylor series in $Q$ about $Q^0$.

$$\Delta\hat{H}(q, Q) = \hat{H}(q, Q) - \hat{H}(q, Q^0) = \sum_r \left(\frac{\partial\hat{H}(q, Q)}{\partial Q_r}\right)_{Q^0} Q_r + \ldots \quad . \tag{38}$$

According to Eq. 36, the electronic part of the wavefunction contains admixtures of other wavefunctions. The mixing is a consequence of the $Q$-dependence of the Hamiltonian $\Delta\hat{H}(q, Q)$ and is, accordingly, induced by a nuclear displacement corresponding to a vibration altering the (electronic) Hamiltonian. If at least for one of the admixed states the transition to the ground state is dipole allowed, allowedness will also be provided to the transition from the perturbed state to the corresponding vibrational level of the ground state. In other words, the Herzberg-Teller corrections to the adiabatic wavefunction result in additional terms contributing to the transition intensity as given in Eq. 30, which may be $\neq 0$. Thus, Herzberg-Teller vibronic coupling can induce intensity to vibrational satellites (even if the purely electronic transition is dipole forbidden), but not to the corresponding origin.[45]

In organometallic complexes, substate **I** is often a nearly pure triplet, and thus the transition $\mathbf{I} \rightarrow \mathbf{0}$ is largely spin-forbidden. In this case, more specific mechanisms of HT-coupling have to be considered, which induce intensity to corresponding vibrational satellites according to the discussed formalism:

(a) *Spin-vibronic coupling* can cause mixing of two electronic states of different multiplicity due to a change of spin-orbit coupling given by a vibration-induced change of nuclear displacements. Therefore, the Hamiltonian must contain the spin-orbit operator $\hat{H}_{SO}$, as is anyway appropriate for organo-transition metal complexes with a heavy-metal center, i.e. $\hat{H}(q, Q) = \hat{H}_0(q, Q^0) + \hat{H}_{SO}(q, Q^0)$. In correspondence to Eq. 38, one obtains (compare, e.g. Ref. [203])

$$\Delta\hat{H}(q, Q) = \sum_r \left\{ \left( \frac{\partial \hat{H}_0(q, Q)}{\partial Q_r} \right)_{Q^0} + \left( \frac{\partial \hat{H}_{SO}(q, Q)}{\partial Q_r} \right)_{Q^0} \right\} Q_r \ldots \quad . \tag{39}$$

The corresponding mechanism has been proposed from theoretical considerations by Albrecht [203] and demonstrated for the first time experimentally by Yersin et al. [45, 46, 204]. It can particularly be found for metal-ligand vibrational modes. As mainly the central metal ion is responsible for spin-orbit coupling, a displacement of the metal coordinate (due to a vibration) can cause a change of SOC, and therefore a mixing of wavefunctions according to Eq. 35. However, this is valid only for states with sufficient MLCT parentage, since only such states can experience effective SOC (compare Sect. 2.4) and thus vibration-induced changes of SOC.

(b) *Vibronic coupling in the triplet manifold to a spin-orbit coupled state* is a further mechanism, which can be responsible for the occurrence of vibrational satellites with otherwise forbidden transitions. This mechanism is discussed especially for ligand internal vibrations which do not modulate the SOC Hamiltonian, since

the heavy metal center is not involved in these vibrations.[45]

## 6.3 Temperature dependence

For $Ir(btp)_2(acac)$, detailed information on the vibrational satellite structure and, especially, on Franck-Condon (FC) and Herzberg-Teller (HT) activity is obtained by investigation of the emission spectra at different temperatures. In Figure 37, the vibrational satellites as observed in emission are shown for site **H** of $Ir(btp)_2(acac)$ in $CH_2Cl_2$. The spectra are recorded at 1.5 K, 4.2 K, and 10 K, respectively, under excitation of triplet substate **III** at 16293 $cm^{-1}$ (0-0 transition). For each temperature, also the region of the origin transitions is depicted for comparison. These electronic origin spectra were registered under excitation into a vibrational satellite of the **0** $\rightarrow$ **III** transition at 16742 $cm^{-1}$ (compare Fig. 19). The intensities of all spectra are comparable, but note that the spectra in the region of the vibrational satellites are scaled by a factor of 10 relative to the intensities of the electronic origin spectra.

At each temperature, the vibrational satellite structure exhibits a large number of lines. A general classification can be given on the basis of the vibrational energies. Low energy modes occurring up to about 600 $cm^{-1}$ red-shifted to the electronic origin involve vibrations of a large mass, e.g. of the central heavy-atom, and/or low force constants. This has been substantiated, for example, by a comparison of vibrational energies of $Pt(thpy)_2$ to those of $Pd(thpy)_2$.[45] Consequently, most of the corresponding satellites of $Ir(btp)_2(acac)$ are ascribed to metal-ligand (M-L) vibrational modes. Note that satellites with energies lower than $\approx$180 $cm^{-1}$ do not occur in the emission spectra (or are very weak), except for one band which is found at 18 $cm^{-1}$ relative to the origin (not depicted). This sideband to the origin is attributed to overlapping satellites which result from vibrations of the chromophore in its lattice cage. Such satellites, often referred to as (pseudo-local) phonon satellites (see, e.g. Ref. [120]), are typical for the energy range below 100 $cm^{-1}$. Weak sidebands of this type accompany not only the electronic origin but also vibrational satellites at their low-energy side. On the other hand, fundamentals with energies higher than $\approx$600 $cm^{-1}$ represent ligand-internal vibrations.[45, 120] A detailed list of all vibrational energies is given in Table 5 (Appendix B).

Further interpretations are difficult, since the emission spectrum at each temperature does not originate only from one single triplet substate each. Due to the zero-field splitting of $\Delta E_{\mathrm{II-I}}$ =2.9 $cm^{-1}$, even at $T$ = 1.5 K substate **II** is slightly pop-

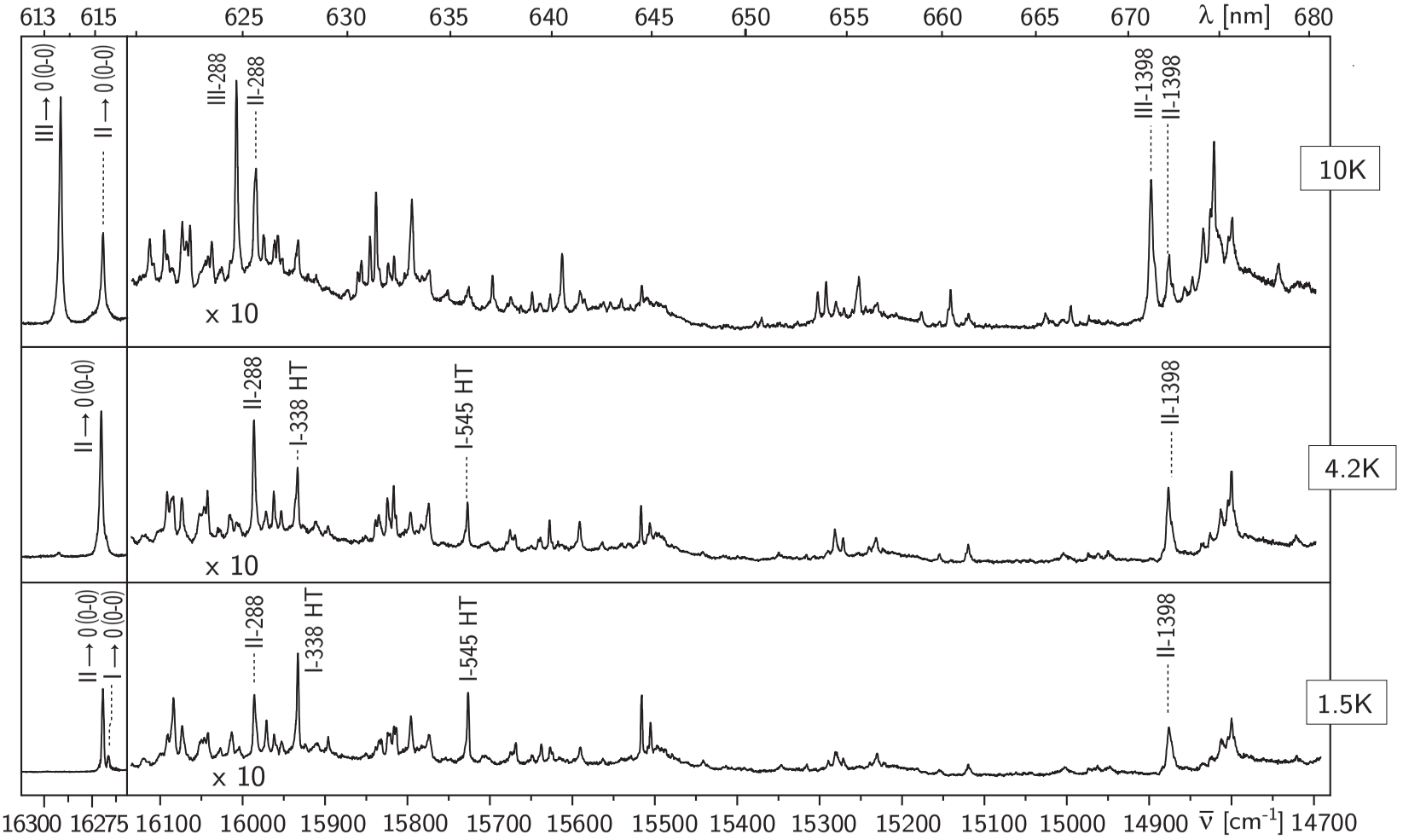


**Figure 37** Emission of $Ir(btp)_2(acac)$ in $CH_2Cl_2$ (site **H**) in the region of the vibrational satellites, recorded at 1.5 K, 4.2 K, and 10 K, respectively. For excitation, the energy of the electronic origin of the **0** → **III** transition ($\bar{\nu}_{exc}$ =16293 $cm^{-1}$) was chosen. The emission spectra in the range of the electronic origin transitions are also given for comparison (compare Fig. 19). The vibrational satellite lines are, in part, labeled according to the respective origins $I_{0-0}$, $II_{0-0}$, and $III_{0-0}$, and tentatively assigned with respect to the Herzberg-Teller (HT) and Franck-Condon (FC) activity (see Sect. 6.5).

ulated thermally (compare Sect. 5.1). Moreover, the spin-lattice relaxation from substate **II** to substate **I** is comparatively slow with $\tau_{\mathrm{II-I}}^{\mathrm{SLR}}$ =22 µs at this temperature (see Sect. 5.3). Thus, as already shown in Sect. 4.2 and further substantiated in Sect. 5.3, both substates **I** and **II** contribute to the emission of $Ir(btp)_2(acac)$ in $CH_2Cl_2$ at 1.5 K. Correspondingly, the vibrational satellite structure at $T$ = 1.5 K is expected to represent a superposition of satellites occurring with the transitions **I** → **0** and **II** → **0**. When the temperature is increased to 4.2 K, substate **II** becomes further populated thermally. This is tellingly demonstrated by the intensity distribution of the electronic origins. As a result, the intensity distribution of the vibrational satellite structure is altered drastically as well. For several satellites, the intensity is enhanced after the temperature increase from 1.5 K to 4.2 K. These can be assigned to result from transition **II** → **0**. Examples are the lines at 15983 $cm^{-1}$ (II-288 $cm^{-1}$) and at 14873 $cm^{-1}$ (II-1398 $cm^{-1}$), respectively. On the other hand, satellites for which the intensity is reduced upon temperature increase are regarded to occur with transition **I** → **0**, such as, for example, the lines at 15930 $cm^{-1}$ (I-338 $cm^{-1}$) and at 15723 $cm^{-1}$ (I-545 $cm^{-1}$). A noteworthy contribution of emission from substate **III** is not indicated at $T$ = 4.2 K. However, increasing the temperature to 10 K leads to thermal population of substate **III**. According to the emission spectra in the region of the electronic origins (Fig. 37 left), at this temperature the emission from substate **III** dominates, but the emission from substate **II** still contributes strongly. Accordingly, the vibrational satellites assigned to occur with transition **II** → **0** are still observed in the emission spectrum. These satellites, though, are observed as doublets, i.e. for each line stemming from substate **II** a complementary line is found at ≈22 $cm^{-1}$ higher in energy. However, this is not easily recognized for all satellites, since a larger number of lines is present in the spectrum recorded at 10 K. The separation of the doublet lines represents the zero-field splitting $\Delta E_{\mathrm{III-II}}$ of the substates **II** and **III**. The intensity ratio of the line-pair within each doublet corresponds to the intensity ratio of the respective electronic origins. For these reasons, the higher-energy lines of the doublets can safely be ascribed to vibrational modes occurring with transition **III** → **0**. Hence, for example, the 288 $cm^{-1}$ and the 1398 $cm^{-1}$ mode are now represented by the lines at 16005 $cm^{-1}$ (III-288 $cm^{-1}$) and 14895 $cm^{-1}$ (III-1398 $cm^{-1}$), respectively.

On the basis of these considerations, each vibrational satellite can be assigned to a specific substate of $\mathbf{T_1}$. However, due to the multitude of satellite lines found in the spectrum, a more systematic approach to carry out this assignment is appropriate. A corresponding method is presented in the following section.

## 6.4 Individual emission spectra from I, II, and III

The observed emission lines of $Ir(btp)_2(acac)$ in $CH_2Cl_2$ (site **H**) can be systematically and thoroughly related to the three individual substates of the $\mathbf{T_1}$ state, from which they originate, by an algebraic calculation. The basis therefore is that the emission spectrum is available at three different temperatures $T_1$, $T_2$, and $T_3$, as given in Fig. 37 for 1.5 K, 4.2 K, and 10 K. The corresponding data can be written as a $3 \times n$-matrix $\boldsymbol{D}$, with $n$ different intensity-values $I_k$ ($k = 1 \ldots \mathrm{n}$) (data points) for each temperature.

$$\boldsymbol{D} = \begin{pmatrix} I_1(\mathrm{T}_1) & \cdots & I_\mathrm{n}(\mathrm{T}_1) \\ I_1(\mathrm{T}_2) & \cdots & I_\mathrm{n}(\mathrm{T}_2) \\ I_1(\mathrm{T}_3) & \cdots & I_\mathrm{n}(\mathrm{T}_3) \end{pmatrix} \tag{40}$$

Each row of the matrix represents the intensity-values (numbers of counts) of the emission spectrum at one specific temperature, $T_1$, $T_2$, or $T_3$. As seen in the previous section, emission from at least two triplet substates contributes to each of the spectra. Each column represents the number of counts at one specific spectral position at the different temperatures. This matrix is to be transformed into another $3 \times \mathrm{n}$-matrix $\boldsymbol{S}$, in which each row represents an emission spectrum from one individual triplet substate, the three spectra being orthogonal.

$$\boldsymbol{S} = \begin{pmatrix} I_1^{\mathrm{I}} & \cdots & I_\mathrm{n}^{\mathrm{I}} \\ I_1^{\mathrm{II}} & \cdots & I_\mathrm{n}^{\mathrm{II}} \\ I_1^{\mathrm{III}} & \cdots & I_\mathrm{n}^{\mathrm{III}} \end{pmatrix} \tag{41}$$

$I_k^i$ ($k = 1 \ldots \mathrm{n}$) represents the contribution of emission from substate $i$ ($i$ =I,II,III) to the intensity at data point $k$. Due to physical reasons, a $3 \times 3$ coefficient matrix $\boldsymbol{K}$ exists, which relates the matrices $\boldsymbol{D}$ and $\boldsymbol{S}$ by

$$\boldsymbol{K} \cdot \boldsymbol{S} = \boldsymbol{D} \quad . \tag{42}$$

The existance of the matrix $\boldsymbol{K}$ can be taken for granted, since obviously the physical law governing the intensity contributions of the emissions from the different substates at a given temperature is the same for all (spectral) data points (columns of the matrix $\boldsymbol{D}$ and $\boldsymbol{S}$, respectively). The matrix $\boldsymbol{K}$ contains the intensity ratios of the emissions from the individual substates at a given temperature, normalized by

the total intensity $I_{\mathrm{tot}}(\mathrm{T})$ at this temperature. Thus the problem writes as

$$\begin{pmatrix} 1/I_{\mathrm{tot}}(\mathrm{T}_1) & \frac{I_{\mathrm{II}}}{I_{\mathrm{I}}}(\mathrm{T}_1)/I_{\mathrm{tot}}(\mathrm{T}_1) & \frac{I_{\mathrm{III}}}{I_{\mathrm{I}}}(\mathrm{T}_1)/I_{\mathrm{tot}}(\mathrm{T}_1) \\ 1/I_{\mathrm{tot}}(\mathrm{T}_2) & \frac{I_{\mathrm{II}}}{I_{\mathrm{I}}}(\mathrm{T}_2)/I_{\mathrm{tot}}(\mathrm{T}_2) & \frac{I_{\mathrm{III}}}{I_{\mathrm{I}}}(\mathrm{T}_2)/I_{\mathrm{tot}}(\mathrm{T}_2) \\ 1/I_{\mathrm{tot}}(\mathrm{T}_3) & \frac{I_{\mathrm{II}}}{I_{\mathrm{I}}}(\mathrm{T}_3)/I_{\mathrm{tot}}(\mathrm{T}_3) & \frac{I_{\mathrm{III}}}{I_{\mathrm{I}}}(\mathrm{T}_3)/I_{\mathrm{tot}}(\mathrm{T}_3) \end{pmatrix} \cdot \begin{pmatrix} I_1^{\mathrm{I}} & \cdots & I_{\mathrm{n}}^{\mathrm{I}} \\ I_1^{\mathrm{II}} & \cdots & I_{\mathrm{n}}^{\mathrm{II}} \\ I_1^{\mathrm{III}} & \cdots & I_{\mathrm{n}}^{\mathrm{III}} \end{pmatrix} = \begin{pmatrix} I_1(\mathrm{T}_1) & \cdots & I_{\mathrm{n}}(\mathrm{T}_1) \\ I_1(\mathrm{T}_2) & \cdots & I_{\mathrm{n}}(\mathrm{T}_2) \\ I_1(\mathrm{T}_3) & \cdots & I_{\mathrm{n}}(\mathrm{T}_3) \end{pmatrix}, \quad (43)$$

with

$$I_{\mathrm{tot}}(\mathrm{T}_1) = 1 + \frac{I_{\mathrm{II}}}{I_{\mathrm{I}}}(\mathrm{T}_1) + \frac{I_{\mathrm{III}}}{I_{\mathrm{I}}}(\mathrm{T}_1) \quad . \quad (44)$$

Expression 43 represents a number of $n$ independent inhomogeneous systems of equations – one for each data point recorded at a certain wavenumber at the three temperatures, i.e., one for each column of the matrices $\boldsymbol{S}$ and $\boldsymbol{D}$. The entries of the coefficient matrix are known and can be expressed with the radiative rate constants $k_i^r$ and the Boltzmann factors for population of the respective higher-lying state (see Appendix A).

$$\frac{I_i}{I_{\mathrm{I}}} = \frac{k_i^r}{k_{\mathrm{I}}^r} \cdot e^{-\frac{\Delta E_{\mathrm{i-I}}}{k_B T}} \quad (45)$$

The rate constant $k_i^r$ is given by the total rate constant $k_i$ of radiative and non-radiative deactivation of triplet substate **I** to the ground state $\mathbf{S_0}$, and the quantum efficiency $\phi_i$ of the radiative transition from i to the ground state according to $k_i^r = \phi_{\mathrm{PL}} \cdot k_i$. (See also Eq. 13.) $\Delta E_{i-\mathrm{I}}$ is the energy difference of the triplet substates $i$ and **I** as given above. Eq. 45 is valid only in case the respective substates of $\mathbf{T_1}$ are in thermal equilibrium for the whole time of the emission. However, this is not the case for site **H** of $Ir(btp)_2(acac)$ in $CH_2Cl_2$ at low temperature. In Sect. 5.3, it was shown, that the thermalization between the substates **II** and **I** by spin-lattice relaxation is comparatively slow. The thermal equilibrium is established sufficiently fast only at $T \geq 5$ K. Hence, the entries $\frac{I_{\mathrm{II}}}{I_{\mathrm{I}}}$ of the coefficient matrix $\boldsymbol{K}$ for 1.5 K and 4.2 K are not fully adequate to describe the intensity distribution between the emissions stemming from the substates **I** and **II**. They rather have to be corrected with respect to SLR from **II** to **I**. The appropriate expression is given by (see Appendix A)

$$\frac{I_{\mathrm{II}}}{I_{\mathrm{I}}} = \frac{k_{\mathrm{II}}^r}{k_{\mathrm{I}}^r} \left[ e^{-\frac{\Delta E_{\mathrm{II-I}}}{k_B T}} + \frac{\left( \frac{n_{\mathrm{II}}^0}{n_{\mathrm{I}}^0} - e^{-\frac{\Delta E_{\mathrm{II-I}}}{k_B T}} \right) \left( k_{\mathrm{I}} + k_{\mathrm{II}}\, e^{-\frac{\Delta E_{\mathrm{II-I}}}{k_B T}} \right)}{\left( \frac{n_{\mathrm{II}}^0}{n_{\mathrm{I}}^0} + 1 \right) k_{\mathrm{II-I}}^{\mathrm{SLR}}(T)} \right] \quad , \quad (46)$$

where $k_{\mathrm{II-I}}^{SLR}$ represents the rate of spin-lattice relaxation from substate **II** to substate

**I**, and $n_{\mathrm{I}}^0$ and $n_{\mathrm{II}}^0$ are the initial population densities of **I** and **II**, respectively. In case of a very fast SLR, as given for all other entries of matrix $\boldsymbol{K}$, the second term on the right hand side of Eq. 46 vanishes and the intensity ratio can be written like already given in Eq. 45. The whole matrix $\boldsymbol{K}$ is then given by

$$\boldsymbol{K} = \begin{pmatrix} \frac{1}{I_{\mathrm{tot}}(\mathrm{T}_1)} & \frac{1}{I_{\mathrm{tot}}(\mathrm{T}_1)} \cdot \frac{k_{\mathrm{II}}^r}{k_{\mathrm{I}}^r} \left[ e^{-\frac{\Delta E_{\mathrm{II-I}}}{k_B T_1}} + \frac{\left(\frac{n_{\mathrm{II}}^0}{n_{\mathrm{I}}^0} - e^{-\frac{\Delta E_{\mathrm{II-I}}}{k_B T_1}}\right)\left(k_{\mathrm{I}} + k_{\mathrm{II}}\, e^{-\frac{\Delta E_{\mathrm{II-I}}}{k_B T_1}}\right)}{\left(\frac{n_{\mathrm{II}}^0}{n_{\mathrm{I}}^0} + 1\right) k_{\mathrm{II-I}}^{\mathrm{SLR}}(T_1)} \right] & \frac{1}{I_{\mathrm{tot}}(\mathrm{T}_1)} \cdot \frac{k_{\mathrm{III}}^r}{k_{\mathrm{I}}^r} \cdot \mathrm{e}^{-\frac{\Delta E_{\mathrm{III-I}}}{k_{\mathrm{B}}^r T_1}} \\ \frac{1}{I_{\mathrm{tot}}(\mathrm{T}_2)} & \frac{1}{I_{\mathrm{tot}}(\mathrm{T}_2)} \cdot \frac{k_{\mathrm{II}}^r}{k_{\mathrm{I}}^r} \left[ e^{-\frac{\Delta E_{\mathrm{II-I}}}{k_B T_2}} + \frac{\left(\frac{n_{\mathrm{II}}^0}{n_{\mathrm{I}}^0} - e^{-\frac{\Delta E_{\mathrm{II-I}}}{k_B T_2}}\right)\left(k_{\mathrm{I}} + k_{\mathrm{II}}\, e^{-\frac{\Delta E_{\mathrm{II-I}}}{k_B T_2}}\right)}{\left(\frac{n_{\mathrm{II}}^0}{n_{\mathrm{I}}^0} + 1\right) k_{\mathrm{II-I}}^{\mathrm{SLR}}(T_2)} \right] & \frac{1}{I_{\mathrm{tot}}(\mathrm{T}_2)} \cdot \frac{k_{\mathrm{III}}^r}{k_{\mathrm{I}}^r} \cdot \mathrm{e}^{-\frac{\Delta E_{\mathrm{III-I}}}{k_{\mathrm{B}}^r T_2}} \\ \frac{1}{I_{\mathrm{tot}}(\mathrm{T}_3)} & \frac{1}{I_{\mathrm{tot}}(\mathrm{T}_3)} \cdot \frac{k_{\mathrm{II}}^r}{k_{\mathrm{I}}^r} \cdot \mathrm{e}^{-\frac{\Delta E_{\mathrm{II-I}}}{k_{\mathrm{B}}^r T_3}} & \frac{1}{I_{\mathrm{tot}}(\mathrm{T}_3)} \cdot \frac{k_{\mathrm{III}}^r}{k_{\mathrm{I}}^r} \cdot \mathrm{e}^{-\frac{\Delta E_{\mathrm{III-I}}}{k_{\mathrm{B}}^r T_3}} \end{pmatrix} \quad (47)$$

Now the sought after matrix $\boldsymbol{S}$ of the independent (orthogonal) emissions from the substates **I**, **II**, and **III** can be calculated by inversion of the obviously regular matrix $\boldsymbol{K}$ and multiplication of Eq. 43 by the inverted matrix $\boldsymbol{K^{-1}}$ from the left hand side.

$$\boldsymbol{S} = \boldsymbol{K^{-1}}\boldsymbol{D} \quad (48)$$

This method was applied to the emission spectra of $Ir(btp)_2(acac)$ in $CH_2Cl_2$ (site **H**), registered at the three temperatures $T_1$ =1.5 K, $T_2$ = 4.2 K, and $T_3$ =10 K as given in Fig. 37. The calculations were performed using Maple™ 9. For the parameters $\Delta E$, the values $\Delta E_{\mathrm{II-I}}$ =2.9 $\mathrm{cm}^{-1}$ and $\Delta E_{\mathrm{III-I}}$ =25 $\mathrm{cm}^{-1}$ obtained from highly resolved spectra were used (compare Sect. 4.2). The rate constants $k_i^r$ were specified according to the decay times determined in Sect. 5.1 as $k_{\mathrm{I}}^r = \phi_{PL} \cdot \frac{1}{\tau_{\mathrm{I}}} = \phi_{PL}/150\,\mu\mathrm{s}$, $k_{\mathrm{II}}^r = \phi_{PL} \cdot \frac{1}{\tau_{\mathrm{II}}} = \phi_{PL}/58\,\mu\mathrm{s}$, and $k_{\mathrm{III}}^r = \phi_{PL} \cdot \frac{1}{\tau_{\mathrm{III}}} = \phi_{PL}/1.5\,\mu\mathrm{s}$.[27] Therein, the quantum efficiencies of the emissions from all three substates are assumed to be the same with a value $\phi_{PL}$. This is justified, since for site **H** of $Ir(btp)_2(acac)$ in $CH_2Cl_2$ the quantum efficiency is constant in the temperature range from 1.5 K to 10 K, as indicated by the successful fit presented in Fig. 20. It turns out that the exact value of $\phi_{PL}$ in the radiative rate constants is not critical for the calculation, as long as the ratios between the $k_i^r$ values of the different substates are correct. Thus, for example, a rough estimation of $\phi_{PL} = 0.5$ according to the value measured for $Ir(btp)_2(acac)$ in CBP in Ref. [74] (see also Sect. 5.4) leads to reasonable results. For the spin-lattice

[27] Note that the decay times $\tau_{\mathrm{I}}$, $\tau_{\mathrm{II}}$, and $\tau_{\mathrm{III}}$ represent measured values which are determined by radiative and non-radiative deactivation of the respective state to the ground state.

relaxation rates $k^{SLR}_{\mathrm{II-I}}(\mathrm{T})$ the values $k^{SLR}_{\mathrm{II-I}}(1.5\,\mathrm{K}) = 22.1\,\mu\mathrm{s}$ and $k^{SLR}_{\mathrm{II-I}}(4.2\,\mathrm{K}) = 0.8\,\mu\mathrm{s}$, determined in Sect. 5.3, were used. The population ratio $\frac{n^0_{\mathrm{II}}}{n^0_{\mathrm{I}}}$ was obtained by variation of this parameter. Therefore, the quality of the resulting spectra was evaluated with respect to the occurrence of artifacts, such as negative intensities. It was found that the substates **I** and **II** are equally populated by relaxation from the excited vibrational level of substate **III** with $\frac{n^0_{\mathrm{II}}}{n^0_{\mathrm{I}}} = 1 \pm 0.1$. Interestingly, immaculate results were only obtained applying the above given values (despite of the $\phi_{PL}$ value) within a tolerance of at most 10%. This indicates that the determined energy separations, decay times, and spin-lattice relaxation times are quite reasonable. The obtained spectra are presented and discussed in the next section.

## 6.5 Assignment of vibrational satellites

The described calculations were carried out for the region of the electronic origins of the emission spectra of $Ir(btp)_2(acac)$ in $CH_2Cl_2$ (site **H**), and for the vibrational satellite structure. The resulting spectra from the individual triplet substates **I**, **II**, and **III** are depicted in Fig. 38.

The intensities of the spectra are comparable, if the given scaling factors are kept in mind. A comparison of the calculated spectra with the measured spectra of Fig. 37 reveals distinct differences: Clearly, in the calculated spectra a significantly lower number of lines is observed. This is especially evident when inspecting the region of the electronic origins. There, only one origin line is found in each of the spectra. For example, in (c) only the line at $16293\,\mathrm{cm}^{-1}$, corresponding to the origin transition of **III** $\rightarrow$ **0**, is recognized. The line corresponding to the origin transition **II** $\rightarrow$ **0** (0-0), which was observed in the measured spectrum recorded at $T = 10\,\mathrm{K}$, is not found anymore. (A small peak at $16273\,\mathrm{cm}^{-1}$ is assigned as a phonon satellite of transition **III** $\rightarrow$ **0** (0-0).) This proves that the calculated spectra indeed represent the pure emissions from the individual $\mathbf{T_1}$ substates **I**, **II**, and **III**, which are not anymore corrupted by superposition of emissions from different substates. The situation is also manifested in the vibrational satellite structures. In spectrum (c) ascribed to transition **III** $\rightarrow$ **0**, a doublet structure is not anymore recognized, indicating that the emission stemming from substate **III** has been thoroughly isolated from the emissions stemming from **II** and **I** by the calculation. Similarly, in the emission from the substates **II** and **I**, no features due to transitions from the respective other substates are observed. Only for very few features, especially for the remaining line in spectrum (b) at $15518\,\mathrm{cm}^{-1}$, it is not evident, from which substate

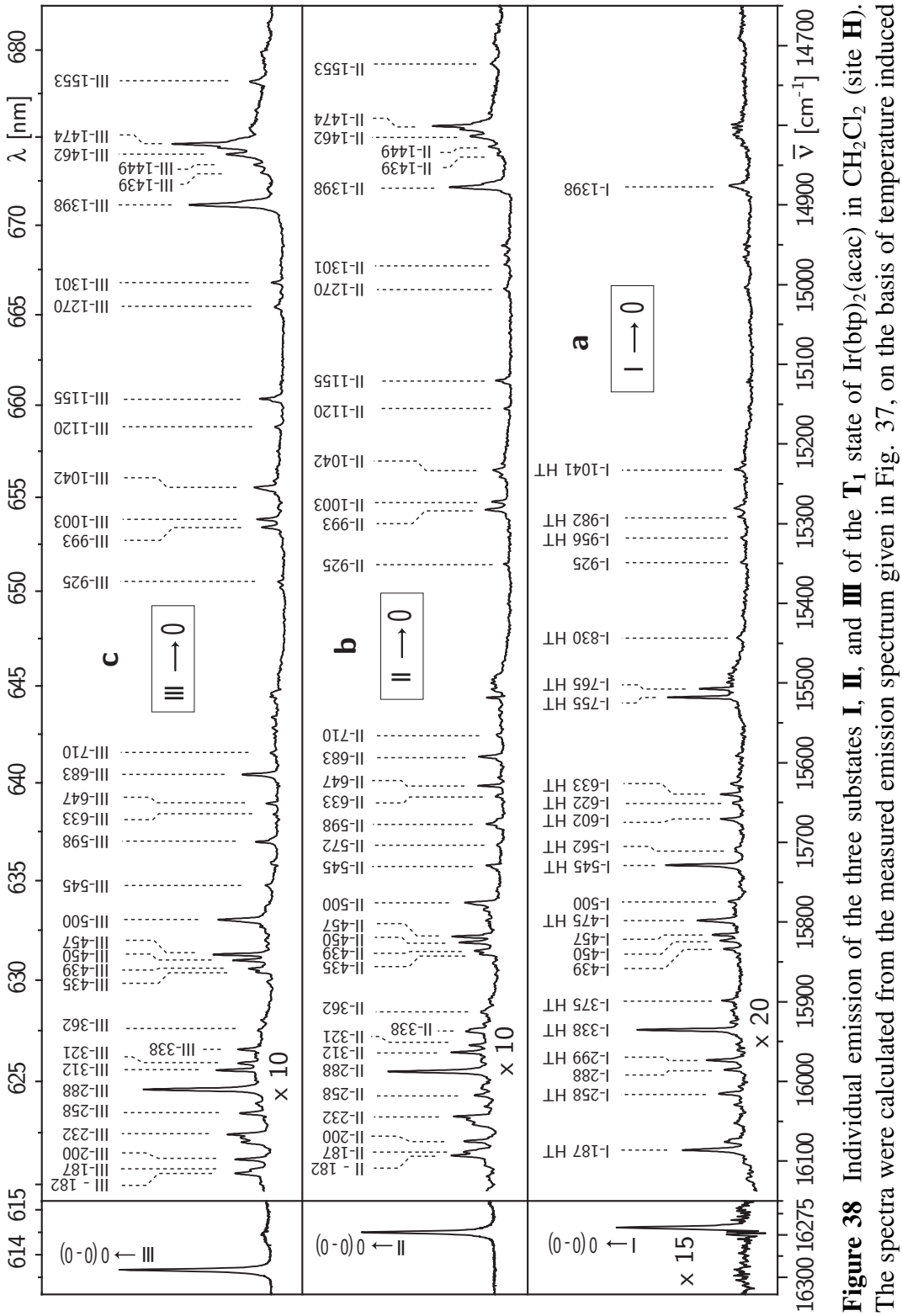


**Figure 38** Individual emission of the three substates **I**, **II**, and **III** of the $\mathbf{T}_1$ state of $Ir(btp)_2(acac)$ in $CH_2Cl_2$ (site **H**). The spectra were calculated from the measured emission spectrum given in Fig. 37, on the basis of temperature induced changes from 1.5 K to 4.2 K and to 10 K. Details of the calculation are explicated in the text (Sect. 6.4).

the emission originates. This line may possibly be regarded as an artifact of the calculation, taking into account that the original spectra are not ideal. For example, a limited wavenumber reproducibility of the spectrograph can cause a slight shift of the respective line between the measured spectra at 1.5 K and 4.2 K.

Interestingly, the vibrational satellite structures of the emission spectra from the substates **II** and **III** are the very same. Hence, the same vibrational modes of the electronic ground state are involved in emission stemming from substate **II** and substate **III**. In the emission from substate **I**, on the other hand, a distinctly different vibrational satellite structure is observed. An explanation is possible, when taking into account that the transitions **III** $\rightarrow$ **0** and **II** $\rightarrow$ **0** are electronically significantly allowed, while the transition **I** $\rightarrow$ **0** is largely forbidden. This is indicated by the corresponding emission decay times $\tau_{III}$ =1.5 µs, $\tau_{II}$ = 58 µs, and $\tau_{I}$ = 150 µs (compare Sect. 5.1) and by the weak 0-0 line of the **I** $\rightarrow$ **0** transition (see Sect. 4.2). Accordingly, satellites occurring *dominantly* with the emission from substate **I**, such as for example the I-338 $cm^{-1}$ satellite, are assigned to be vibronically induced by Herzberg-Teller (HT) vibronic coupling. Indeed, a significant number of these satellites, especially the intensive ones, represent so called 'false origins' (see Appendix B and Fig. 39). In contrast, emission from the substates **II** and **III** is regarded to involve totally symmetric Franck-Condon (FC) activated vibrational modes as, at least in part, progressions are observed (Appendix B, Table 5). On the basis of this consideration, the Herzberg-Teller activated satellites are labeled as HT in Fig. 38. All other satellites (not labeled) are regarded to be Franck-Condon active. These assignments are supported by additional experiments under high magnetic field and by time-resolved measurements, which are discussed below in the Sections 6.7 and 6.8. A detailed list of vibrational energies with assignments of the corresponding modes is given in Appendix B.

Nearly all of the lines observed in the emission from substate **I** represent HT induced vibrational modes. However, also a few week satellites are recognized, which also occur in the emissions from **II** and **III** with similar or even higher intensity. This is especially the case for those modes, which are represented by the most intense satellites in the emission from the substates **II** and **III**. Examples are the 288 $cm^{-1}$, the 1398 $cm^{-1}$ or the 457 $cm^{-1}$ mode. (Note that these satellites of I occur indeed 3 $cm^{-1}$ red shifted to the corresponding ones of II.) Obviously, these are FC activated also when occurring with transition **I** $\rightarrow$ **0**. This is possible, since the electronic origin transition **I** $\rightarrow$ **0** (0-0) carries at least some oscillator strength at all. On the other hand, in the emission stemming from substate **II** and **III** one finds evidence of modes, which exhibit the same vibrational energy as a corresponding HT

mode coupling to transition **I** → **0**. Some of these modes, such as the 338 $cm^{-1}$ and the 258 $cm^{-1}$ mode, seem to be HT (**I** → **0**) *and* FC (**II** → **0**) active. Just as well, these modes may also represent FC active modes having coincidentally the same energy as the corresponding HT active modes involved in transition **I** → **0**. Other modes, such as the 545 $cm^{-1}$ and the 755 $cm^{-1}$ mode, possibly represent strongly HT vibronically induced modes, which couple also to **II** and even to **III**, since their intensity decreases from the spectrum of **II** → **0** to the one of **III** → **0**. However, the occurrence of a HT activated vibrational satellite with the transitions **II** → **0** and **III** → **0** seems unlikely due to the significant electronic allowedness of these transitions.

The vibrational satellites observed in the given spectral range of Fig. 38 correspond to fundamentals, since progressions are generally not found in this range. The only exception is the II/III-572 $cm^{-1}$ satellite, which possibly represents the second member of a progression ($2 \times 288\ cm^{-1}$). As already stated in Sect. 6.3, the fundamentals with energies higher than ≈600 $cm^{-1}$ represent ligand internal vibrations.[45, 120] Satellites in Fig. 38 with energies below ≈600 $cm^{-1}$, on the other hand, involve metal-ligand (M-L) vibrational character.[45] Therefore, the satellites in this energy range which are assigned to be HT activated are probably induced by spin-vibronic coupling. (Compare Sect. 6.2.) HT activated satellites of higher energy, such as the I-755 $cm^{-1}$ satellite or the I-1041 $cm^{-1}$ satellite, may be induced by vibronic coupling of state **I** to a higher lying triplet substate that experiences on its part effective spin-orbit coupling.

In the emission spectrum resulting from substate **I**, no progressions are observed. This underlines the vibronically induced nature of the intense satellites assigned as 'HT'. In contrast, for several vibrational satellites which are attributed to the emission from the substates **II** and **III**, the second members of Franck-Condon progressions are found, for example for the 1398 $cm^{-1}$, 1462 $cm^{-1}$, and 1474 $cm^{-1}$ modes and possibly also for the 288 $cm^{-1}$, mode (not depicted in Fig. 38). However, such a prove of the assignment to FC modes, and therefore to totally symmetric modes, is only possible for the most intense satellites. For all other satellites assigned as 'FC', overtone satellites cannot be identified, but these may be hidden in the noise of the respective spectrum. The largest Huang-Rhys parameter for the observed progressions is estimated by use of Eq. 33 to $S = 0.08$. A similar value has also been reported for other complexes with emitting states of significant MLCT character.[45, 46, 120, 144] From the small value of $S$, it can be concluded that the shifts of the equilibrium positions in the respective vibrational coordinates are small. In other words, the geometry rearrangement upon transitions

**II**,**III** $\leftrightarrow$ **0** is very small. This goes together with the significant MLCT character in the emitting triplet state of $Ir(btp)_2(acac)$. Complexes with larger MLCT character are supposed to feature a larger extension of the electronic wavefunctions. Therefore, the influence of an excitation on the specific binding properties is less pronounced.[45, 46, 144] The progression forming satellites identified in the emissions **II** $\rightarrow$ **0** and **III** $\rightarrow$ **0** occur also as satellites to false origins represented by Herzberg-Teller induced satellites to line I. As shown in Fig. 39, several such combinations due to coupling of FC modes to HT modes are identified, e.g. (338+1398) $cm^{-1}$, (338+1474) $cm^{-1}$, or (545+1474) $cm^{-1}$. The Figure depicts the emission spectrum of site **H** of $Ir(btp)_2(acac)$ in $CH_2Cl_2$, recorded at $T = 1.5$ K in the corresponding energy range. This gives further evidence for the assignment of the FC modes. Finally, combinations of modes assigned as FC active are also observed, e.g. as (288+1398) $cm^{-1}$, (288+1474) $cm^{-1}$, (683+1398) $cm^{-1}$, and (1398+1474) $cm^{-1}$ satellites to II. A detailed list of vibrational energies, also regarding progressions and combinations, is given in Appendix B.

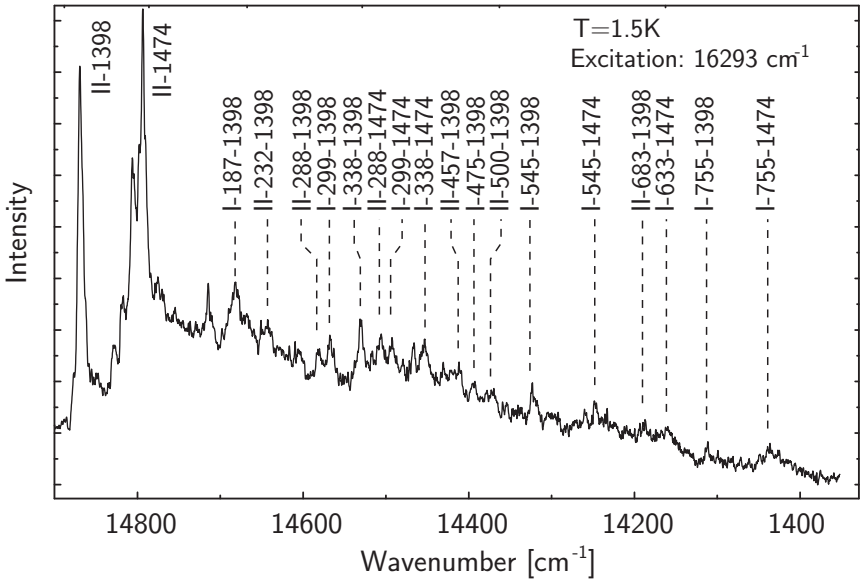


**Figure 39** Emission spectrum of $Ir(btp)_2(acac)$ in $CH_2Cl_2$ (site **H**) recorded at $T = 1.5$ K in the energy region, where combinations of totally symmetric Franck-Condon modes with each other or with Herzberg-Teller modes (false origins) occur.

## 6.6 Considerations on the electronic allowedness of the transition $\mathbf{I} \rightarrow \mathbf{0}$

Interestingly, the spectra depicted in Fig. 38 and obtained according the algebraic method described in Sect. 6.4 reveal another important information. The calculated intensity of the origin line I is by a factor of about 15 smaller than that of line II or III, while the calculated intensities of the lines II and III are roughly the same. The comparable intensities of the origin lines II and III are easily interpreted, taking into account that the emissions from these substates involve the same vibrational satellites. Moreover, these satellites represent Franck-Condon active modes. Thus, the total emission intensity from one substate is proportional to the intensity of the respective electronic origin transition. The factor of proportionality is even the same for the emissions from the substates **II** and **III**, if the Franck-Condon factors of corresponding modes involved in the transitions $\mathbf{II} \rightarrow \mathbf{0}$ and $\mathbf{III} \rightarrow \mathbf{0}$ are the same. In this case, the intensity ratio of the lines II and III directly reflects the ratio of the electronic allowednesses of the transitions $\mathbf{II} \rightarrow \mathbf{0}$ and $\mathbf{III} \rightarrow \mathbf{0}$. Further, this ratio of the electronic allowednesses is given by the ratio of the radiative rate constants $k^r_{\mathrm{II}}$ and $k^r_{\mathrm{III}}$, which can be determined experimentally.[28] In other words, the radiative allowednesses of the transitions $\mathbf{II} \rightarrow \mathbf{0}$ and $\mathbf{III} \rightarrow \mathbf{0}$ can be *compared* on the basis of the intensities of the electronic origin lines and also on the basis of the radiative rate constants. For the calculation of the independent emission spectra according to Sect. 6.4 this means that, if the correct rate constants are applied, the calculated intensities of corresponding emissions lines stemming from the substates **II** and **III** are just the same. This follows with Eq. 43 and is a consequence of the fact that the electronic allowednesses are connected with the radiative rate constants in the same way for both transitions $\mathbf{II} \rightarrow \mathbf{0}$ and $\mathbf{III} \rightarrow \mathbf{0}$.

However, the allowedness and the radiative rate constant of the transition $\mathbf{I} \rightarrow \mathbf{0}$ can not be included in the considerations presented above. For this transition, Herzberg-Teller vibronic coupling is of significant importance, while the electronic allowedness is obviously comparatively weak. Therefore, the total emission intensity corresponding to transition $\mathbf{I} \rightarrow \mathbf{0}$ is more dominantly carried by the vibrational satellites as compared to the transitions $\mathbf{II} \rightarrow \mathbf{0}$ and $\mathbf{III} \rightarrow \mathbf{0}$. Similarly, the radiative rate $k^r_{\mathrm{I}}$ is more dominantly governed by deactivation involving excited vibrational modes of the ground state. This leads to the important consequence that the elec-

[28] Since for the emissions from the substates **I**, **II**, **III** different quantum efficiencies are not indicated, the rate constants $k^r_i$ may also be replaced by the measured rates $k_i$ in the following discussion.

tronic allowedness of transition **I** → **0** cannot be compared to those of the transitions **II** → **0** and **III** → **0** on the basis of the radiative rate constants. The radiative rate of transition **I** → **0** is significantly larger than 'indicated' by the intensity of the electronic origin transition **I** → **0** (0-0). This means also that the electronic origin line is considerably weaker than suspected, if the radiative rate $k_{\mathrm{I}}^{r}$ is compared to the rates $k_{\mathrm{II}}^{r}$ and $k_{\mathrm{III}}^{r}$. Exactly this bahavior is observed. The calculated intensity of the electronic origin line II is by a factor of ≈15 smaller than the intensities of the origin lines **II** and **III**, respectively. This intensity of line **I** represents the intensity, which would be expected to be found, if the vibronic coupling of substate **I** would be neglected and only 'direct' spin-orbit coupling as given for the substates **II** and **III** would occur. If the rate constant $k_{\mathrm{I}}^{r}$ would reflect this intensity only, the calculation according to Sect. 6.4 would yield roughly equal intensities of the electronic origin transitions of **I** → **0**, **II** → **0**, and **III** → **0**. Obviously, the real electronic allowedness of transition **I** → **0** is by a factor of ≈15 smaller than indicated by $k_{\mathrm{I}}^{r}$.[29]

This represents an important result. A comparison of the radiative rate $k_{\mathrm{I}}^{r}$ with $k_{\mathrm{II}}^{r}$, and $k_{\mathrm{III}}^{r}$, which is often carried out to assess the electronic allowednesses of the respective transition, is not reasonable and leads to an overestimation of the electronic allowedness of transition **I** → **0**. However, to obtain a value which may be compared with the rate constants $k_{\mathrm{II}}^{r}$ and $k_{\mathrm{III}}^{r}$, for $Ir(btp)_2(acac)$ in $CH_2Cl_2$ (site **H**) an effective rate constant $k_{\mathrm{I}}^{eff} = k_{\mathrm{I}}^{r}/15$ can be calculated. This $k_{\mathrm{I}}^{eff}$ corresponds to an effective decay time $\tau_{\mathrm{I}}^{eff} \approx 2.3\,\mathrm{ms}$. Obviously, the electronic allowedness of transition **I** → **0** is effectively by a factor of ≈1500 smaller than that of the transition **III** → **0** – not only by a factor of 100, as assumed from the ratio of the decay times $\tau_{\mathrm{I}} = 150\,\mu\mathrm{s}$ and $\tau_{\mathrm{III}} = 1.5\,\mu\mathrm{s}$.

## 6.7 Magnetic field effect

The assignment of the vibrational satellites can be further substantiated by investigation of the emission spectrum under high magnetic fields. Fig. 40 shows emission spectra of $Ir(btp)_2(acac)$ in $CH_2Cl_2$ (site **H**) recorded at $T = 1.5\,\mathrm{K}$. For excitation, the energy of $16293\,\mathrm{cm}^{-1}$ corresponding to transition **0** → **III** was chosen. The lower spectrum is the same as the one given in Fig. 37 and was recorded in the absence of a magnetic field. This spectrum is compared to the corresponding spectrum

[29] In this consideration, the vibrational satellite structure occurring with transition **I** → **0** is implicitly assumed to be the same as those occurring with the transitions **II** → **0** and **III** → **0**. Therefore, the given factor of 15 represents only a rough estimate.

recorded under an external magnetic field of 10 T strength (upper spectrum).

In Sect. 4.3, it has already been shown that application of a magnetic field induces a mixing of the $\mathbf{T_1}$ substates **I**, **II**, and **III**. In particular, the wavefunction of substate **I** experiences an admixture of the wavefunctions of the higher lying substates **II** and **III**. Therefore, the transition $\mathbf{I} \rightarrow \mathbf{0}$, which is electronically largely forbidden in the absence of a magnetic field, gains allowedness. Moreover, magnetically induced shifts of the substates occur and lead to a further separation of these states, in addition to the zero-field splitting. This affects, for example, the spin-lattice relaxation rate $k_{\mathrm{II-I}}^{\mathrm{SLR}}$ from substate **II** to substate **I**, which is strongly increased. As a consequence of these Zeeman effects, the emission spectrum is altered drastically. While in the absence of a magnetic field and at $T = 1.5\,\mathrm{K}$ both substates **I** and **II** emit, under a magnetic field of $B = 10\,\mathrm{T}$ only emission from the magnetically perturbed substate **I** ($\mathbf{I_B}$) is observed. This is recognized, when inspecting the region of the electronic origins of the spectra depicted in Fig. 40. (Compare also Fig. 22.)

Obviously, for the vibrational satellite structure of the emission, a corresponding behavior must apply. At $B = 0\,\mathrm{T}$, satellites of the transitions $\mathbf{I} \rightarrow \mathbf{0}$ and $\mathbf{II} \rightarrow \mathbf{0}$ are observed for $T = 1.5\,\mathrm{K}$ (compare Sect. 6.3). When a magnetic field of $B = 10\,\mathrm{T}$ is applied, the vibrational satellite structure at $T = 1.5\,\mathrm{K}$ is expected to be exclusively comprised of satellites of the $\mathbf{I_B} \rightarrow \mathbf{0}$ transition. This is, in fact, the case. Specific satellites observed at $B = 0\,\mathrm{T}$, such as the I-545 $\mathrm{cm}^{-1}$ or the I-755 $\mathrm{cm}^{-1}$ and I-765 $\mathrm{cm}^{-1}$ satellites, do not occur in the spectrum recorded at $B = 10\,\mathrm{T}$. These satellites are exactly all those satellites which are assigned as HT induced satellites of transition $\mathbf{I} \rightarrow \mathbf{0}$. In contrast, satellites assigned in Sect. 6.5 to represent FC active modes (e.g. II-288 $\mathrm{cm}^{-1}$, II-457 $\mathrm{cm}^{-1}$, II-1398 $\mathrm{cm}^{-1}$) are also found in the 10 T spectrum. Due to the significantly higher allowedness of $\mathbf{II} \rightarrow \mathbf{0}$, the FC satellites in the 0 T spectrum stem from this transition. Therefore the corresponding satellites in the spectrum recorded at $B = 10\,\mathrm{T}$, now occurring with the $\mathbf{I_B} \rightarrow \mathbf{0}$ transition, are red-shifted by $\approx 3\,\mathrm{cm}^{-1}$. Precisely, all FC modes, which are represented in the emissions from the substates **II** and **III** are also identified in the emission from the perturbed substate $\mathbf{I_B}$. Other satellites, especially vibronically induced satellites, are not observed at all at $B = 10\,\mathrm{T}$. Obviously, this dominance of the FC vibrational satellite structure is a consequence of a high electronic allowedness of transition $\mathbf{I_B} \rightarrow \mathbf{0}$ brought about by the magnetic field induced mixing of substate **I** with the higher lying states **II** and **III**.

The striking correspondence between the emission from the perturbed state $\mathbf{I_B}$ and the emissions from the unperturbed states **II** and **III** (Fig. 38) proves that the calculation carried out in Sect. 6.4 to separate the superimposed spectra of **I**, **II**,

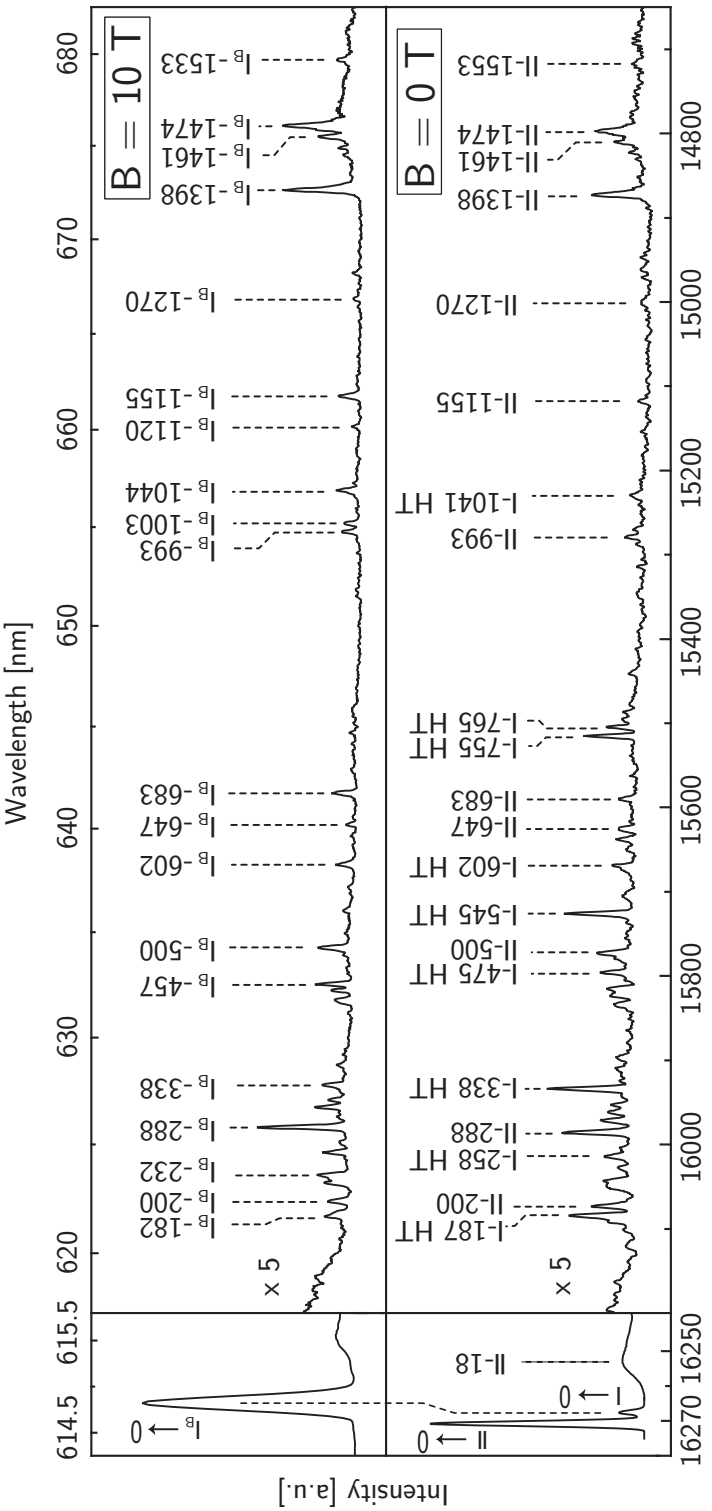


**Figure 40** Emission spectrum of site **H** of $Ir(btp)_2(acac)$ in $CH_2Cl_2$ under an applied magnetic field of $B = 10\,T$ strength. For comparison, also the emission in the absence of a magnetic field ($B = 0\,T$) is given (compare Fig. 37). The spectra were recorded at 1.5 K under excitation of triplet substate **III** at 16293 $cm^{-1}$ ($B = 0\,T$) and 16295 $cm^{-1}$ ($B = 10\,T$), respectively. Note that in the region between 16240 $cm^{-1}$ and 16200 $cm^{-1}$, which is not depicted, no further lines are found.

and **III** provides very reasonable results. Further, the assignments with respect to Herzberg-Teller activity and Franck-Condon activity given in Fig. 38 are substantiated, since vibronically induced satellites are expected to become less important, if the electronic transition gains allowedness. Exactly this behavior is observed for $Ir(btp)_2(acac)$ in $CH_2Cl_2$ under magnetic field. A difference between the emissions stemming from $\mathbf{I_B}$ (Fig. 40) and **II**/**III** (Fig. 38) is only observed for the 755 $cm^{-1}$ mode. This mode is only represented in the emission from the unperturbed substates **II**, but not in the emission from the perturbed substate $\mathbf{I_B}$ at $B = 10$ T. This fits to the explanation that the 755 $cm^{-1}$ mode is strongly vibronically induced and therefore occurs not only with transition $\mathbf{I} \rightarrow \mathbf{0}$, but also with $\mathbf{II} \rightarrow \mathbf{0}$, in the absence of a magnetic field. However, the discussed mode does not occur with transition $\mathbf{III} \rightarrow \mathbf{0}$ at $B = 0$ T. Such a mode is not expected to persist at $B = 10$ T.

The involvement of the same FC modes in the emission from $\mathbf{I_B}$ as from **II** and **III** indicates that these modes are only not observed in the emission at $B = 0$ T, since the electronic allowedness of transition $\mathbf{I} \rightarrow \mathbf{0}$ is very small. As shown in the previous section, the lifetime of state **I** would correspond to an effective time of 2.3 ms, if only the FC activated vibrational satellite structure was taken into account and neglecting deactivation by vibronically induced processes. The fact that the FC activated vibrational satellite structure occurring with transition $\mathbf{I_B} \rightarrow \mathbf{0}$ is the same as the one occurring with $\mathbf{II} \rightarrow \mathbf{0}$ and $\mathbf{III} \rightarrow \mathbf{0}$ means also that the Franck-Condon factors and Huang-Rhys parameters corresponding to the individual modes are largely the same. Therefore, the nuclear configuration in the states **I**, **II**, and **III** is similar.

## 6.8 Time-resolved emission

Evidence for the correct assignment of the vibrational satellites occurring in the emission of $Ir(btp)_2(acac)$ in $CH_2Cl_2$ can also be found on the basis of time-resolved emission spectra. Fig. 41 shows the emission spectrum in the region of the vibrational satellites of site **H** recorded at $T = 1.5$ K in two time windows after the exciting laser pulse ($\bar{\nu}_{exc}$ =16293 $cm^{-1}$). Spectrum (a) was recorded with no delay from the laser pulse and a gate width of 20 µs, while spectrum (b) was registered in the time window from 150 µs to 450 µs after the laser pulse (see insets of Fig. 41).

Indeed the emission spectrum changes significantly with the time window of the detection. The long time spectrum (b) shows a line structure which is very similar

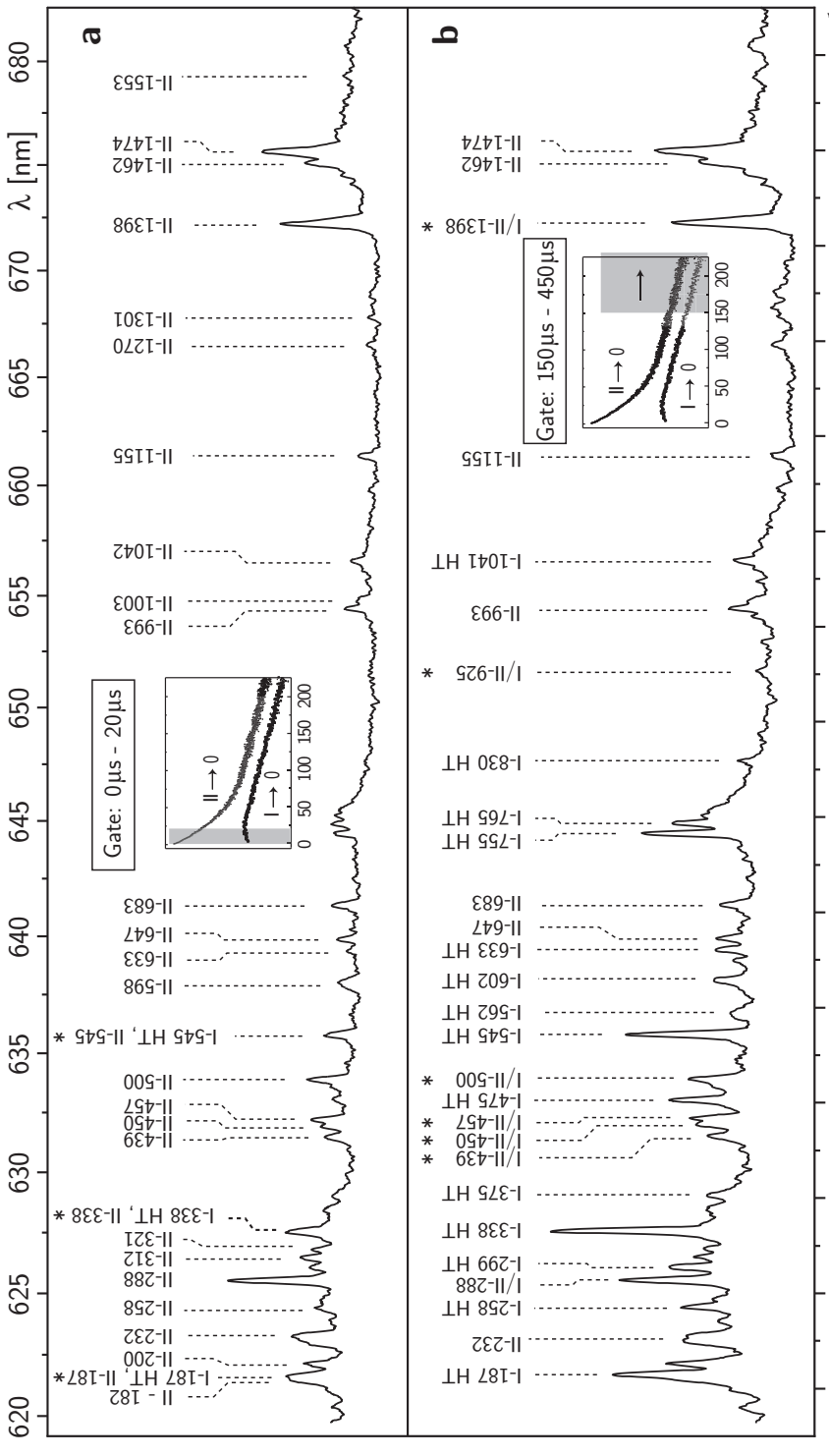


**Figure 41** Time-resolved emission of $Ir(btp)_2(acac)$ in $CH_2Cl_2$ (site **H**) in the region of the vibrational satellites. The spectra were recorded at $T = 1.5$ K and after pulsed excitation of substate **III** at the electronic origin ($\bar{\nu}_{exc} = 16293\,cm^{-1}$). (a) Emission registered in the first 20 µs after the exciting laser pulse. (b) Emission detected in the time window from 150 µs to 450 µs after the excitation. The insets illustrate the detection windows on the basis of the decay curves of the emissions from the substates **II** and **I**. Note that the spectral resolution is lower than for the above given spectra of Figs. 37 and 38. Therefore, emission lines marked with an asterisk represent unresolved emissions from the substates **I** and **II**.

to the one of the time integrated spectrum recorded at $T = 1.5\,\mathrm{K}$ and given in Fig. 37. Again, those satellites assigned to vibronically induced modes occur (e.g. I-338 $\mathrm{cm}^{-1}$ or I-545 $\mathrm{cm}^{-1}$), but also strong Franck-Condon satellites, such as the II-1398 $\mathrm{cm}^{-1}$ or the II-1474 $\mathrm{cm}^{-1}$ satellite, are observed. This is easily understood on the basis of the emission decay curves given in the inset of Fig. 41 (see also Fig. 30). In a time regime later than 150 µs delay from the laser pulse on, the substates **I** and **II** are in thermal equilibrium and the emission from both decays with a time of $\tau_{\mathrm{I}} = \tau_{\mathrm{II}} = 135\,\mu\mathrm{s}$ (see Sect. 5.3) at 1.5 K. Therefore, the spectrum is comprised of emissions from both substates **I** and **II**. It looks similar to the time integrated spectrum, as the regime of the thermalized decay dominates the total intensity of emission. The satellites of the transitions $\mathbf{I} \rightarrow \mathbf{0}$ and $\mathbf{II} \rightarrow \mathbf{0}$ are of comparable importance in this spectrum, since the higher allowedness of transition $\mathbf{II} \rightarrow \mathbf{0}$ compensates the low Boltzmann factor of 0.06 for population of substate **II** at $T = 1.5\,\mathrm{K}$. However, when the detection window is set to 0 - 20 µs, the spectrum is changed significantly. Most of the satellites assigned to stem from substate **I** in spectrum (b) are not observed anymore. The intensities of the strongest satellites such as the I-338 $\mathrm{cm}^{-1}$, the I-545, or the I-755 satellite are drastically decreased. On the other hand, the intensities of satellites assigned to occur with emission from **II** are significantly enhanced. Thus, the spectrum closely resembles the time integrated spectrum recorded at 4.2 K (Fig. 37). Such a behavior is consistent with the emission decay curves given in the inset of Fig. 41b. As shown in Sect. 6.4, the substates **I** and **II** become roughly equally populated by SLR from substate **III**, after this substate is excited by the laser pulse. Taking also into account the higher allowedness of transition $\mathbf{II} \rightarrow \mathbf{0}$, immediately after the excitation, the emission intensity from substate **II** is expected to be significantly higher than that of substate **I**. Therefore, in the time frame 0-20 µs, mainly vibrational satellites due to emission from substate **II** are recognized.

The fact that the satellites that are growing in upon change of the detection window from 150 µs-450 µs to 0 µs-20 µs indeed correspond to those satellites assigned to stem from $\mathbf{II} \rightarrow \mathbf{0}$ in Sect. 6.5, and the satellites which become less intense are those assigned to $\mathbf{I} \rightarrow \mathbf{0}$, proves that the assignment of the satellites given in Sect. 6.5 is consistent also under consideration of the emission decay behavior.

## 6.9 Satellite structure in other sites

Since $\mathrm{Ir(btp)_2(acac)}$ has proven to show distinctly different triplet state properties in different sites of a $\mathrm{CH_2Cl_2}$ matrix (compare the Chapters 4 and 5), it is interesting

also to compare the vibrational satellite structure of the emission for different sites. Figure 42 reproduces the spectrum of the emission resulting from triplet substate **III** of $Ir(btp)_2(acac)$ in the two sites **H** and **I**, respectively, in $CH_2Cl_2$. Corresponding spectra of the emission from substate **I** are given in Fig. 43. All spectra were calculated according to the method described in Sect. 6.4 from emission spectra registered at the three different temperatures 1.5 K, 4.2 K, and 10 K. These original spectra are depicted in Fig. 37 for site **H** and in Fig. 55 (see Appendix C) for site **I**. They were recorded under excitation into triplet substate **III** of each site with excitation energies of 16293 $cm^{-1}$ and 16247 $cm^{-1}$ for the sites **H** and **I**, respectively. The two particular sites were chosen, as they are well-suited for selective investigations. Emission spectra of these sites recorded under selective excitation are largely pure emissions of the respective sites. For higher energy sites such as site **E**, this is not the case in the whole spectral range of the emission and, in addition, a strong inhomogeneous background is found for these sites. For a better comparison of vibrational energies, the spectra of Fig. 42 and 43 are given in relative wavenumbers, which represent the energy differences to the corresponding electronic origin line III and I, respectively. The vibrational energies are also listed in Appendix B (Table 5), where additionally the corresponding vibrational energies of $Ir(btp)_2(acac)$ in an *n*-octane matrix and as a single crystal are given.

As seen in Fig. 42, the vibrational satellite structure of the emission spectrum originating from substate **III** is very similar for the investigated sites **H** (Fig. 42a) and **I** (Fig. 42b). The majority of vibrational satellite lines occurring in the spectrum of site **I**, such as the III-288 $cm^{-1}$, the III-502 $cm^{-1}$, and the III-683 $cm^{-1}$ line, can be identified with corresponding lines in the spectrum of site **H** (Fig. 42a). This is possible, since these lines are found at the same (relative) energy for both sites, if an experimental uncertainty of $\pm 1$ $cm^{-1}$ for site **H** and $\pm 3$ $cm^{-1}$ for site **I** is accounted for. In accordance to the interpretations given for the emission of $Ir(btp)_2(acac)$ in site **H** of $CH_2Cl_2$ (Sect. 6.5), the discussed satellite lines of site **I** are also assigned to correspond to fundamentals of Franck-Condon active vibrational modes. However, the correlation between the vibrational satellites of the spectra (a) and (b) is not a strict one. Specific lines such as the lines between 1390 $cm^{-1}$ and 1500 $cm^{-1}$ are found at slightly different energies for the two sites, although the structure is quite similar. Thus, for example, a mode involved in the transition **III** $\rightarrow$ **0** of site **I** of 1406 $cm^{-1}$ energy seems to correspond to the 1398 $cm^{-1}$ mode represented in the emission from substate **III** in site **H**. The energy shift of the lines is definitely larger than the experimental error. Two explanations are possible. First of all, the modes may be nearly the same though with slightly different energies

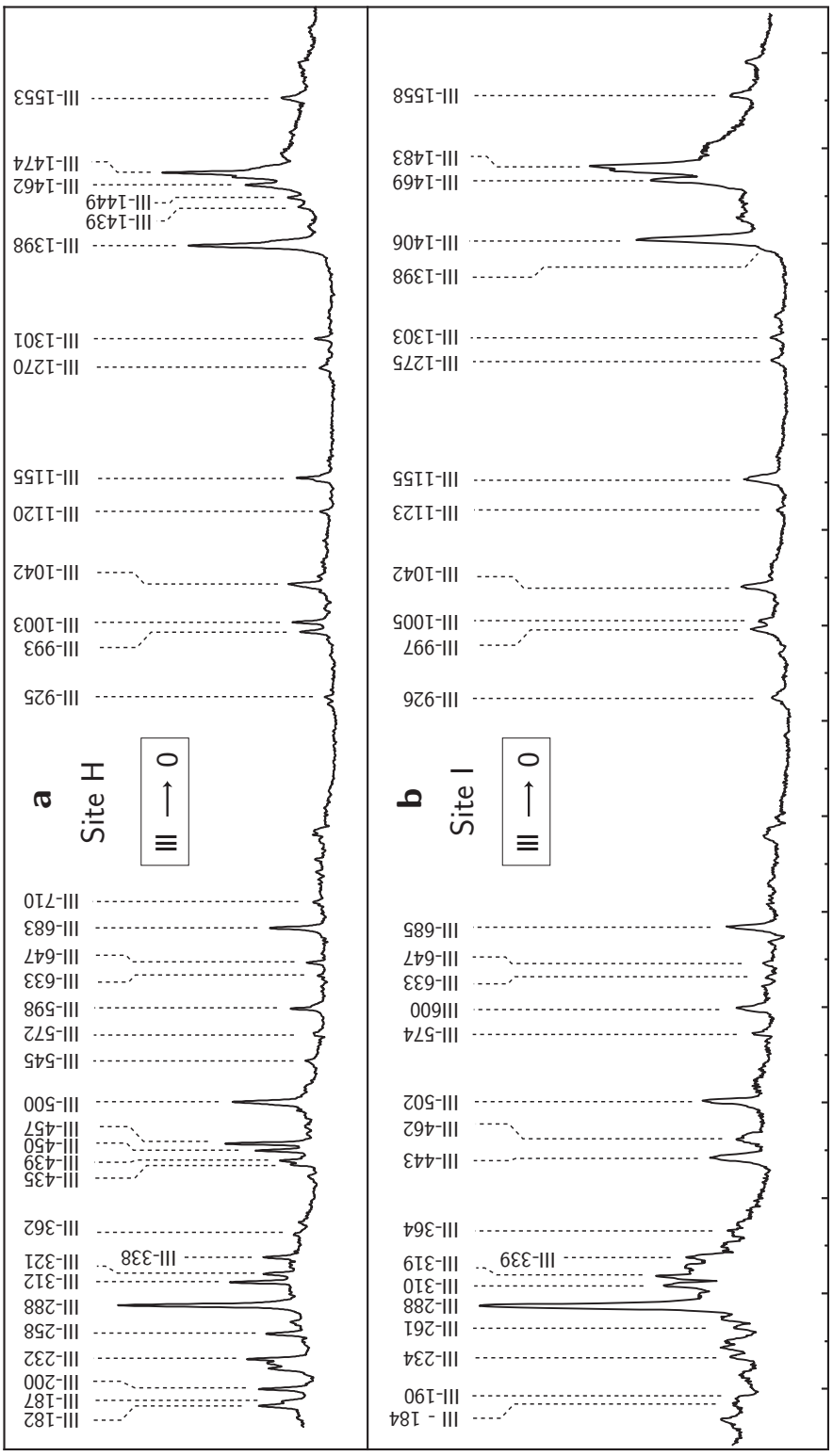


**Figure 42** Emission in the region of the vibrational satellites from substate **III** of the $\mathbf{T_1}$ state of $Ir(btp)_2(acac)$ in two different sites **H** and **I** in a $CH_2Cl_2$ matrix. The spectra were obtained according to the computational procedure described in Sect. 6.4, on the basis of emission spectra recorded at three different temperatures 1.5 K, 4.2 K, and 10 K. The excitation energy was 16293 $cm^{-1}$ and 16247 $cm^{-1}$, respectively, for site **H** and site **E** corresponding to transition $\mathbf{0} \rightarrow \mathbf{III}$. Note that the line-widths in spectrum (b) are slightly larger than those in spectrum (a) due to a lower spectral resolution used for the registration of spectrum (b).

in the two sites. The energy difference in this case may be explained by different widths/shapes of the respective potential curves (different force constants) due to a different influence of the host lattice. This explanation fits to the observation that the intensity distributions of the lines between 1398 $cm^{-1}$ and 1483 $cm^{-1}$ in the two sites are quite similar. However, an energy shift of a vibrational mode of as large as 8 $cm^{-1}$, as discussed for the lines III-1406 $cm^{-1}$ and III-1398 $cm^{-1}$, seems quite unlikely. On the other hand, the two observed lines may as well correspond to different vibrational modes, each one dominating in the spectrum of $Ir(btp)_2(acac)$ in one of the two sites **H** and **I** in $CH_2Cl_2$. This would mean that the intensity of each of these lines differs substantially from one site to the other, for example, due to strongly different Franck-Condon factors of the transitions. Such a behavior would be found, in case for the two sites the equilibrium position of the potential curve of each mode experiences a different shift upon the transition from the excited state to the ground state. A corresponding situation might be indicated in the vibrational satellite structures of Fig. 42, since in the spectrum of site **H** a shoulder at an energy of ≈1406 $cm^{-1}$ is observed, while in the emission of $Ir(btp)_2(acac)$ in site **I** a shoulder – though only a weak one – is observed at ≈1398 $cm^{-1}$. However, a stringent interpretation cannot be given on the basis of the given data. An even more complex situation is found for vibrational modes in the energy range below 400 $cm^{-1}$, and in particular, between 180 $cm^{-1}$ and 290 $cm^{-1}$. The differences in the spectra of the two sites in this range, however, are supposed to result from similar effects as discussed above.

If a comparison is carried out for the vibrational satellites occurring with the transition $\mathbf{I} \rightarrow \mathbf{0}$ of $Ir(btp)_2(acac)$ in the two sites **H** and **I** in $CH_2Cl_2$, drastic differences are found. The situation is illustrated by the spectra of Fig. 43, which were obtained in the same manner as those depicted in Fig. 42. At first sight, the corresponding spectra are only coarsely similar. A clear correspondence of both vibrational satellite structures is not apparent. However, several lines in the spectrum of site **I** can be identified, which represent modes of similar energies as involved in transition $\mathbf{I} \rightarrow \mathbf{0}$ of site **H**. Examples are the lines at I-198 (198) $cm^{-1}$, I-288 (288) $cm^{-1}$, I-299 (299) $cm^{-1}$ I-542 (545) $cm^{-1}$, I-646 (646) $cm^{-1}$, and at I-765 (765) $cm^{-1}$. Although it seems likely, there is no evidence that each of these lines really corresponds to the respective line of similar energy in the emission from site **H** (given in brackets). This is the case, since the discussed lines exhibit, in part, strongly different intensities for the two sites. Structures which are completely different in the two investigated sites are also found. For example the lines corresponding to the 166 $cm^{-1}$, and 776 $cm^{-1}$ vibrational modes are only observed in the emission from

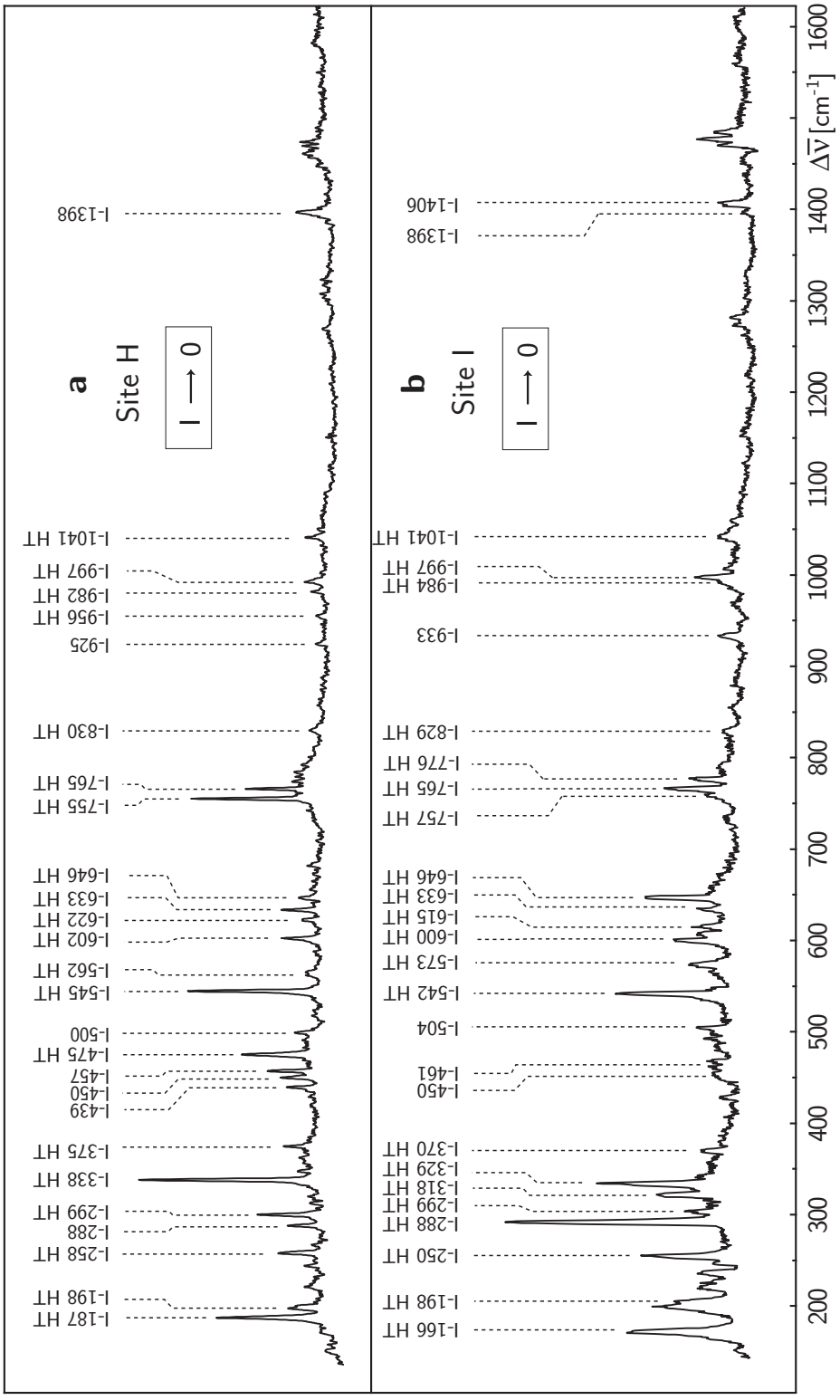


**Figure 43** Emission in the region of the vibrational satellites from substate **I** of the $\mathbf{T_1}$ state of $Ir(btp)_2(acac)$ in two different sites **H** and **I** in a $CH_2Cl_2$ matrix. The spectra were obtained according to the computational procedure described in Sect. 6.4, on the basis of emission spectra recorded at three different temperatures 1.5 K, 4.2 K, and 10 K. The excitation energy was 16293 $cm^{-1}$ and 16247 $cm^{-1}$, respectively, for site **H** and site **E** corresponding to transition $\mathbf{0} \rightarrow \mathbf{III}$.

site **I**, while the modes of 187 $cm^{-1}$ and 338 $cm^{-1}$ energy are only represented in the spectrum of site **H**. Generally, the energies of the vibrational modes represented in the two spectra (a) and (b) in Fig. 43 seem to be correlated stronger than the intensities of the corresponding lines.

Obviously, the intensity differences are much more pronounced between the vibrational satellites structures of the emission from substate **I** of $Ir(btp)_2(acac)$ in the two sites in $CH_2Cl_2$ than those stemming from substate **III**. Since the modes involved in the transitions $\mathbf{I} \rightarrow \mathbf{0}$ are mostly vibronically induced, it seems that vibronically activated modes are influenced stronger by the site situation than Franck-Condon modes. Indeed, an influence of the matrix on the vibronic coupling seems possible, since the state mixing in case of vibronic coupling is a consequence of the Q-dependence of the Hamiltonian (see Sect. 6.2) and is induced by a nuclear displacement. The mixing situation will change no matter whether this nuclear displacement is caused dynamically by a vibration or statically by a change of the molecular geometry due to a different interaction with the host environment.

To conclude, the investigation of the vibrational satellite structures of the emission of $Ir(btp)_2(acac)$ in $CH_2Cl_2$ reveals surprising differences between the two sites **H** and **I**. These differences are not yet understood. However, it is pointed out that the observations cannot be explained by the experimental error of measuring or/and analysis of the data. The energies of vibrational modes coupling to a specific transition have been determined as energy differences within a single spectrum. The accuracy of these energies is better than $\pm 1\,cm^{-1}$ for site **H**. For site **I**, the uncertainty is slightly larger with $\pm 2\,cm^{-1}$, since the corresponding spectra exhibit a lower resolution. The relative intensities of different lines within a spectrum are regarded to be represented in the corresponding spectra with an error of <10%. All spectra have been reproduced several times and with two independent experimental setups.

## 6.10 Vibrational satellite structures – Conclusions

Selective excitation of a single site (site **H**) of $Ir(btp)_2(acac)$ in $CH_2Cl_2$ allows to record well-resolved emission spectra at low temperature also in the region of the vibrational satellites. By an algebraic calculation, it is possible to separate the emissions from the substates **I**, **II**, and **III**, which are otherwise (partly) superimposed. Therefore, important information on the radiative decay paths of the three triplet substates is obtained. The transition from the lowest substate **I** to the $\mathbf{S_0}$ ground

state is largely forbidden at the electronic origin. Deactivation of this state is to a large extent induced by Herzberg-Teller vibronic coupling. Correspondingly, false origins occur. On the other hand, the emission spectra from the two higher lying triplet substates **II** and **III** exhibit a different vibrational satellite structure due to Franck-Condon activity. Experiments under magnetic field prove that this satellite structure occurs also with emission from the perturbed substate $\mathbf{I_B}$. In the absence of a magnetic field, however, only a few weak satellites corresponding to Franck-Condon modes are observed in the emission from substate **I**.

Deactivation of substate **I** due to vibronic activity has an important effect on the emission decay time $\tau_{\mathrm{I}}$. In particular, the emission decay time $\tau_{\mathrm{I}}$ is shorter than would be expected in the absence of vibronic activity. Hence, it is not possible to draw conclusions on the purely electronic allowedness of transition $\mathbf{I} \rightarrow \mathbf{0}$ on basis of the value of $\tau_{\mathrm{I}}$. However, from the calculation described in Sect. 6.4, an effective decay time $\tau_{\mathrm{I}}^{eff}$ can be estimated (see Sect. 6.6), which reflects only the electronic allowedness of transition $\mathbf{I} \rightarrow \mathbf{0}$ and excludes deactivation paths due to vibronic coupling. The estimation yields a value of $\tau_{\mathrm{I}}^{eff} \approx 2.3\,\mathrm{ms}$, which is ≈1500 longer than the decay time $\tau_{\mathrm{III}}$. This underlines the electronically forbidden character of transition $\mathbf{I} \rightarrow \mathbf{0}$.

The occurrence of vibrational satellites of metal-ligand character is consistent with a significant MLCT admixture to the ligand-centered transition as suggested in Sect. 4.5.

Satellites corresponding to fundamentals of ligand-internal vibrational modes occur at least up to $\approx 1550\,\mathrm{cm}^{-1}$ red-shifted to the respective electronic origins. Strong satellites are found from II/III-$1398\,\mathrm{cm}^{-1}$ to II/III-$1474\,\mathrm{cm}^{-1}$ (site **H**). When looking at Fig. 36, it becomes clear that these modes are especially those which contribute to a broad tail of the emission when smeared out by inhomogeneous broadening at $T = 300\,\mathrm{K}$. To be able to minimize the contributions of corresponding vibrations by chemical variations, a normal coordinate analysis should be carried out for $\mathrm{Ir(btp)_2(acac)}$.

Importantly, only small Huang-Rhys parameters occur, indicating that the geometry rearrangements upon the transitions from the electronically excited triplet substates to the ground state are small. Therefore, the width of the emission spectra, i.e. the color purity of the emission is only marginally influenced by higher members of progressions, but is dominated by, in part, intense fundamentals.

Unexpectedly, the vibrational satellite structure of the emission of $\mathrm{Ir(btp)_2(acac)}$ is not exactly the same, if compared for the complex in the two sites **H** and **I** in $\mathrm{CH_2Cl_2}$. Intensities and spectral positions of a significant number of lines vary

significantly between these sites and, in part, a correlation of satellite lines of the two sites is even not apparent. The differences are tentatively ascribed to changes of the Franck-Condon factors of the respective modes or/and changes of the vibronic coupling, both regarded as a consequence of differently distorted geometries of the complex in the two sites.

# 7 Spectral Hole Burning of Ir(btp)$_2$(acac)

## 7.1 Motivation

In the previous chapters, photophysical properties of the $\mathbf{T_1}$ state of Ir(btp)$_2$(acac) were investigated in Shpol'skii or Shpol'skii-like matrices. Although these investigations provide valuable information on the emission character of the complex in these matrices, it is not clear from the first that the obtained results also describe the behavior of the complex in OLED matrices. Therefore, it makes sense to extend the investigations to OLED relevant hosts. As mentioned already in Chapter 1, host materials used for OLEDs can be of small molecular or of polymeric nature – yet they are usually amorphous. This is an important difference to matrices such as $CH_2Cl_2$ or octane, which are polycrystalline. In amorphous hosts, site-selective spectroscopy is not possible, since no discrete sites occur.[30] Therefore, other approaches have to be considered. In principle, it is possible to determine especially the important zero-field splitting by investigation of the temperature dependence of the thermalized emission decay time (compare Sect. 5.1). However, this method has several drawbacks. For example, to obtain reliable results, the required measurements and the evaluation of the data are very time consuming. Further, the method is not a direct one. Influences of non-radiative processes can severely impair the results.

On the other hand, luminescence line narrowing [205] and persistent spectral hole-burning (PSHB) [206] represent methods which allow for high resolution spectroscopy of dye molecules doped into amorphous host. Most of the work published so far concerns singlet-singlet transitions (e.g. see Refs. [206–208]), but also singlet-triplet transitions [209–211] and transitions between levels of higher multiplicity [212–214] have been investigated. However, these methods have not yet been applied to OLED relevant emitter/matrix systems.

In this chapter, persistent spectral hole-burning is studied for Ir(btp)$_2$(acac) doped into the polymer PVB (polyvinylbutyral) and the two polymers PVK (poly-N-

[30] Note that the technique of luminescence line-narrowing does strictly speaking not involve single sites

vinylcarbazol) and PFO (poly(9,9-dioctylfluoren-2,7-diyl) which are frequently applied in OLEDs. It was the aim to develop a method to assess the ZFS and its inhomogeneous distribution, which is generally applicable in different types of matrices, but especially in OLED relevant amorphous hosts. In particular, it is interesting how the ZFS data obtained in Shpol'skii and Shpol'skii-like matrices relate to the properties of a complex in an amorphous environment. The investigations were carried out in cooperation with Dr. U. Bogner and Dr. R. Bauer (Universität Regensburg).

## 7.2 Phosphorescence line narrowing of Ir(btp)$_2$(acac)

The emission spectrum of Ir(btp)$_2$(acac) doped into PFO strongly depends on the excitation energy. When a narrow-line excitation is chosen at a high energy, for example at 19436 cm$^{-1}$ (514.5 nm), which lies in the region of the *homogeneously* broadened $\mathbf{S_0} \rightarrow {}^{\mathbf{1}}\mathbf{MLCT}/{}^{\mathbf{3}}\mathbf{MLCT}$ transitions (compare Figs. 16 and 17), the usual and well-known broad-band emission spectrum is obtained, even at $T = 1.2$ K. (Fig. 44a)

However, upon narrow-line excitation within the *inhomogeneously* broadened $\mathbf{S_0} \rightarrow \mathbf{T_1}$ transition range between about 16100 and 16500 cm$^{-1}$ (shaded bar in Fig. 44a), for example at 16405 cm$^{-1}$, a well-resolved emission spectrum can be recorded, even in this amorphous polymer host. (Fig. 44b) In this case, the laser excites dominantly just those specific sites of Ir(btp)$_2$(acac) in PFO, which have an electronic (0-0) transition precisely at the chosen excitation energy. More exactly, due to the zero-field splitting of the $\mathbf{T_1}$ term into the substates **I**, **II**, and **III** and due to the much higher transition probability of transition $\mathbf{0} \rightarrow$ **III** compared to $\mathbf{0} \rightarrow$ **II** and to $\mathbf{0} \rightarrow$ **I**, specifically those sites will be excited with preference, which have their $\mathbf{0} \rightarrow$ **III** transition at the laser energy. (The $\mathbf{0} \rightarrow$ **III** transition probability is by one and three orders of magnitude larger than that of the transitions $\mathbf{0} \rightarrow$ **II** and $\mathbf{0} \rightarrow$ **I**, respectively (see Chapt. 5 and Sect. 6.6).) The structure displayed in Fig. 44b represents part of a resolved vibrational satellite structure (compare Chapt. 6), which stems from a triplet substate. Although substate **III** is excited selectively, emission from this state is not observed at low temperature. This is due to fast relaxation, i.e. fast spin-lattice relaxation (SLR), from this state to the two lower lying substates (compare Sect. 5.3). (Fig. 44c) On the other hand, SLR between substates **II** and **I** is very slow (Sect. 5.3). Thus, these two triplet sub-

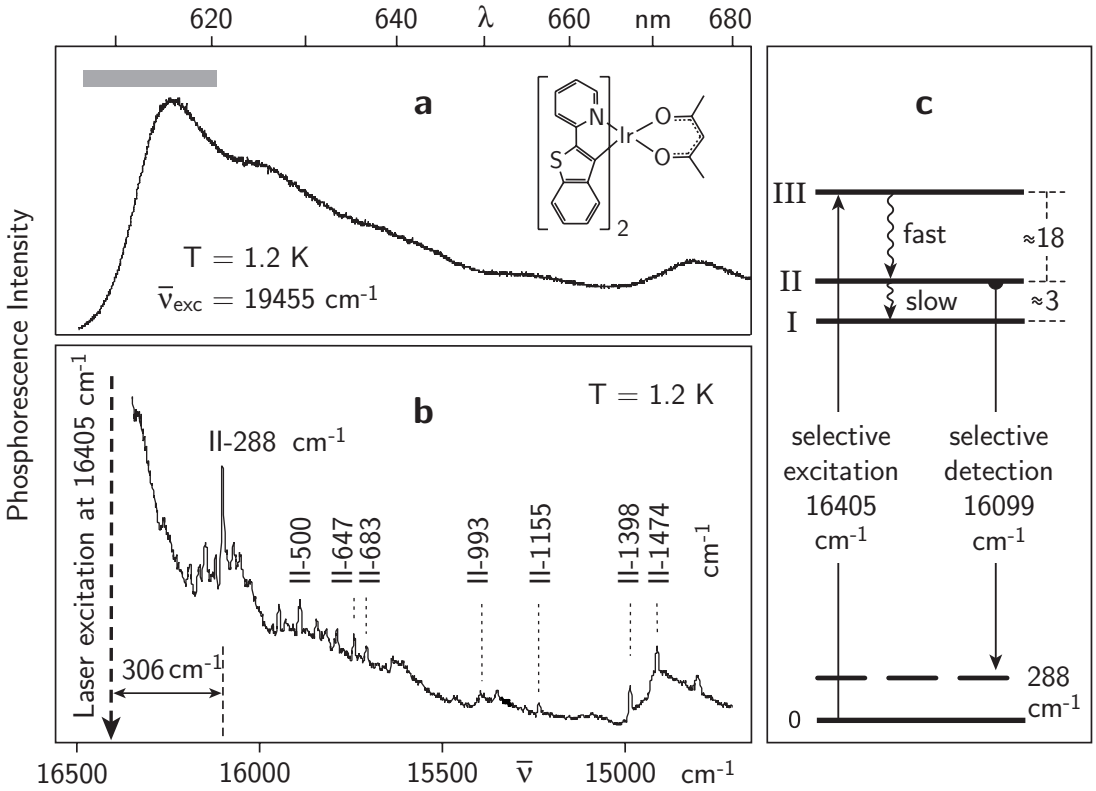


**Figure 44** Emission spectra of Ir(btp)$_2$(acac) in PFO upon excitation at (a) 19455 cm$^{-1}$ and at (b) 16405 cm$^{-1}$. Phosphorescence line-narrowing can be obtained by excitation in the region between about 16100 cm$^{-1}$ and 16500 cm$^{-1}$ (shaded bar in (a)). The intensity of the vibrational zero-phonon line (ZPL) at a spectral distance of 306 cm$^{-1}$ from the exciting laser energy was used for probing of the spectral holes (see Fig. 45). Both spectra were measured in superfluid Helium at 1.2 K. The inset in (a) shows the chemical structure of Ir(btp)$_2$(acac). (c) reproduces the energy level diagram for the triplet substates and depicts radiative and radiationless deactivation paths. The dashed line represents the vibrational level of the 288 cm$^{-1}$ ground state mode.

states emit both, even at $T = 1.2$ K. Analysis of the vibrational satellite structure of Ir(btp)$_2$(acac) doped into a crystalline $CH_2Cl_2$ matrix, as carried out in Chapter 6, allows to identify most of the satellites, which appear in the line-narrowed spectrum. The dominant line represents a vibrational satellite stemming from substate **II** and is induced by a 288 cm$^{-1}$ Franck-Condon active mode. (Fig. 44c) It is found 306 cm below the excitation energy. This value fits well, if it is assumed

that substate **III** lies $18\,\mathrm{cm}^{-1}$ above substate **II** ($288\,\mathrm{cm}^{-1} + 18\,\mathrm{cm}^{-1} = 306\,\mathrm{cm}^{-1}$). The separation of $18\,\mathrm{cm}^{-1}$ lies just in the range of $\Delta E_{\mathrm{III-II}}$ values as determined in Chapt. 4. An independent confirmation of this splitting energy is given below. The $288\,\mathrm{cm}^{-1}$ vibrational satellite line – a so-called vibrational zero-phonon line (ZPL) – is accompanied by a phonon sideband at the low-energy side. This band results from couplings of low-energy vibrational modes of the complex in its matrix cage to the electronic structure/transition. These modes, often called (pseudo-)local phonon modes (hindered rotational motions of the emitter molecule in its matrix cage), have energies in the range of 15 to $30\,\mathrm{cm}^{-1}$ and frequently occur together with purely electronic (0-0) transitions and – as shown in Fig. 44b – also together with vibrational ZPLs.[45, 120]

As characteristic for phosphorescence line narrowing, the spectral shift between the exciting laser energy and the specific vibrational satellite line is almost independent of the excitation energy, when it lies within the inhomogeneously broadened absorption band. However, the absorption in the region of the electronic (0-0) transition depends on the excitation energy due to a varying spectral density of resonantly absorbing molecules. For the investigations presented in this study, the vibrational satellite with a shift of $306\,\mathrm{cm}^{-1}$ relative to the exciting laser is selected for the detection of the spectral holes by a specific synchronous scanning method. This method will be described in Sect. 7.4. The specific vibrational satellite **II** $\rightarrow$ **0** $+ 288\,\mathrm{cm}^{-1}$ (representing a vibrational zero-phonon line) can be observed in the phosphorescence line-narrowed spectra of the $\mathrm{Ir(btp)_2(acac)}$ complex for all three matrices. The width of this line is about $7\,\mathrm{cm}^{-1}$ in PFO and PVB, while it is about $18\,\mathrm{cm}^{-1}$ in PVK. The vibrational ZPL in the PFO matrix has the highest intensity relative to the background, compared to the other matrices.

## 7.3 Persistent spectral hole burning

By narrow-line and intense excitation within an inhomogeneously broadened electronic transition of a light absorbing species, e.g. an organo-transition metal compound in a polymer, the absorption of the sample is reduced at the excitation (laser) energy. The reduced absorption is represented by a spectral hole in the absorption or luminescence excitation spectrum. The formation of a spectral hole is a consequence of a photophysical or a photochemical burning mechanism. In addition to the reduced absorptions (holes), areas of weakly increased absorptions occur (anti-holes). If the anti-holes lie in proximity to the burning energy, i.e. in the spec-

tral range of the inhomogeneously broadened electronic transition, a photophysical hole burning mechanism is indicated. This mechanism can be explained by phonon-induced barrier crossings within asymmetric double well potentials[31] characteristic for disordered systems.[215] Such a barrier crossing corresponds, for example, to a rearrangement of the light absorbing species in its matrix cage – or of any atom, ion or molecule in the immediate neighborhood (compare e.g. Ref. [216]). The transfer from one potential minimum to another one during the hole burning process results in a different absorption energy of the light absorbing species. At low temperature, this new position can be stable and a persistent spectral hole results. Persistent photophysical hole burning can occur in all systems with at least local disorder – in particular in amorphous materials.[207, 215–217] Photochemical hole burning, on the other hand, is usually related to anti-holes which occur in more distant energy regions relative to the burning (laser) energy, since in this case the molecular structure is changed. Especially in the absorption range of the purely electronic transition, persistent spectral holes can provide spectral structures, which are several orders of magnitude narrower than the inhomogeneously broadened band. As a consequence, high-resolution spectroscopy is possible, if the absorption can be scanned over the range of the burnt hole. Since the existence of zero-phonon lines is required, most hole-burning experiments are carried out at liquid He temperatures. Note that the intensity of zero-phonon lines is usually strongly temperature dependent. (See, for example, the Refs. [120] and [206].)

## 7.4 Detection of spectral holes by a synchronous excitation-detection scan technique

As the intensity of a vibrational satellite (vibrational ZPL) depends linearly on the number of resonantly absorbing emitter molecules, it gives information about the inhomogeneous distribution. Using this relation, persistent spectral holes – after having been burnt (compare Sect. 7.3) – are probed in a luminescence excitation technique as schematically depicted in Fig. 45. Hereby, a narrow-line light source of relatively weak intensity excites a subset of molecules within the range of the

[31] A more precise description requires the knowledge of the potential hypersurface. However, for the treatment of a hole burning process by a phonon induced crossing of a barrier between two minima of the potential hypersurface, it is usually sufficient to replace this hypersurface by asymmetric double well potentials. Thereby, only the knowledge of the asymmetry and the barrier height are necessary.

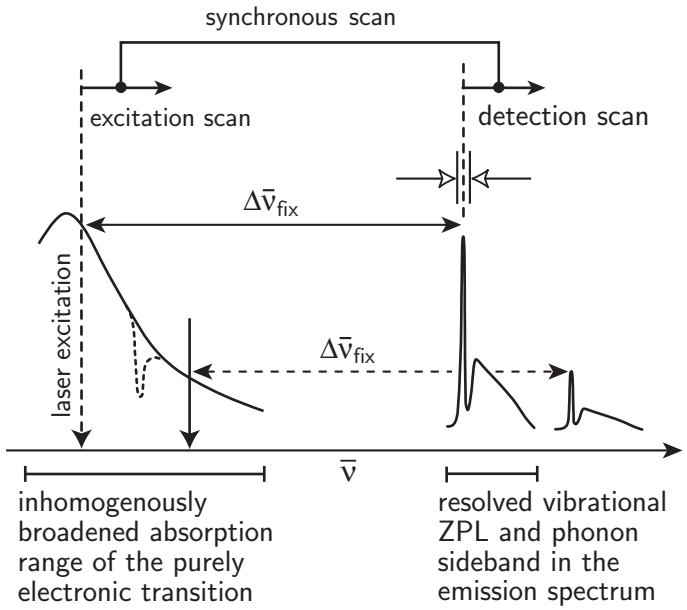


**Figure 45** Schematic diagram to illustrate the synchronous scan technique for the detection of spectral holes. The tunable narrow-line laser light (vertical arrow) excites preferentially a strongly absorbing subset of emitter molecules within its inhomogeneously broadened, purely electronic absorption range. At low temperature, a spectrum results, which usually consists of several vibrational zero-phonon satellite lines (ZPL, vibrational satellites) and the corresponding phonon sidebands, as explained in Sect. 7.2 (Fig. 44). In this diagram, only one ZPL with its phonon sideband is displayed. The inhomogeneous distribution of the purely electronic transitions is obtained by tuning the detection wavelength synchronously with a fixed energy separation $\bar{\nu}_{fix}$ relative to the excitation energy. For detection, a vibrational ZPL is chosen, which occurs with high intensity. The amplitude of the signal in emission is almost proportional to the number of resonantly excited molecules. The dotted spectral structure shows the modified band after burning of a persistent spectral hole (see Sect. 7.3).

inhomogeneously broadened band of the purely electronic transition. The detection energy is chosen selectively at the maximum of a specific (resolved) vibrational satellite. Now scanning the excitation energy, while keeping the energy difference between detection and excitation constant, reproduces the inhomogeneous distribution function. If a persistent spectral hole has been burnt into this distribution (compare Sect. 7.3), the reduced density of resonantly absorbing molecules at the

burning energy is directly displayed in the excitation spectrum (dashed structure in Fig. 45).

For the experiments described in this investigation, the vibrational ZPL with a shift of 306 cm$^{-1}$ was used (see Sect. 7.2, Fig. 44b) primarily because of the high intensity of this satellite relative to the background intensity. According to the discussion presented in Sect. 7.2, the resonant absorption of $\mathbf{T_1}$ substate **III** is by far the strongest among the three triplet substates of Ir(btp)$_2$(acac). (Compare also Sects. 4.2 and 5.1.) Therefore, it can be inferred that this synchronous scanning technique maps dominantly the inhomogeneous distribution function (absorption) of the $\mathbf{0} \rightarrow$ **III** transition, as long as no vibrational levels (e.g. $\mathbf{0} \rightarrow$ **III** $+ \bar{\nu}_0$) of lower lying emitters are involved in the excitation process. In order to avoid complications due to the excitation of such vibrational levels, the hole-burning experiments were performed at the long-wavelength side of the inhomogeneous distribution. It is remarked that this synchronous scan technique is presented here for the first time.

## 7.5 Triplet substates of Ir(btp)$_2$(acac) in different amorphous hosts – Analysis of persistent spectral hole components

With Ir(btp)$_2$(acac) embedded in the amorphous polymer PVB, persistent spectral hole burning was observed at 1.2 K (Fig. 46). After a short burning time, e.g. of 130 s, a spectral hole is recognized only at the energy of the burning laser (hole A in Fig. 46). With increasing burning time, the spectrum changes. Successively, an additional narrow hole component emerges at the high energy side and a broad hole appears at the low energy side of the laser energy. The left part of Fig. 46 shows the spectral hole structure in PVB after three different burning times $t_b$ with a burning intensity of about 10 W/cm$^2$ at 16500 cm$^{-1}$. The width (FWHM) of the resonant hole A increases from 1.7 cm$^{-1}$ after 130 s to 2.4 cm$^{-1}$ after 2480 s. Since the width of the resonant hole depends only on the duration of the hole burning and not on the power density of the burning laser, local heating is not expected to be responsible for the increase of the width. This increase rather is attributed to dynamical processes in the double well potentials in the course of the burning, which lead to slight spectral line shifts and, as a consequence, to a line broadening.[214] The side hole shifted by about 18 cm$^{-1}$ from the resonant hole to the high-energy side has a width of 6.4 cm$^{-1}$. The relatively broad asymmetric hole which appears

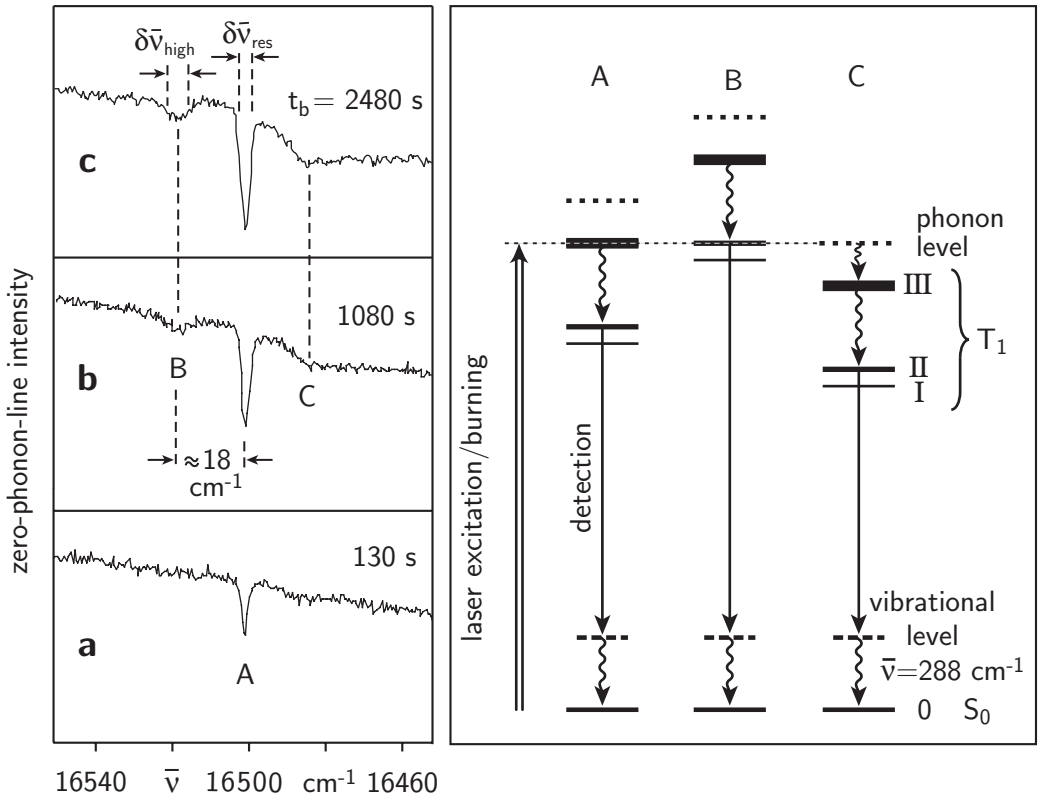


**Figure 46** Persistent spectral holes burnt at 16500 cm$^{-1}$ in the guest/host system Ir(btp)$_2$(acac)/PVB after different burning times $t_b$. The spectral holes were probed by recording the intensity of the strong vibrational ZPL shifted by 306 cm$^{-1}$ relative to the exciting laser energy. The emission stems from substate **II** and is detected at the 288 cm$^{-1}$ vibrational satellite. The diagram on the right hand side displays energy level schemes of three different subsets 'A', 'B', and 'C' of molecules which lie within the inhomogeneous distribution. At a fixed laser energy, the laser burns at different levels with different absorption strengths of the doped molecules. Thus, three hole components A, B, and C result. The differences of the absorption cross sections are indicated by the thicknesses of the levels representing the triplet substates **I**, **II**, and **III** and a local phonon of substate **III**, respectively. The evolution of the hole components A and B allows us to determine the relative absorption cross sections of the transitions to the $\mathbf{T_1}$ substates **II** and **III**, the amount of energy splitting and, in particular, the distribution of this splitting ($T$ = 1.2 K).

at the low-energy side is shifted by about 17 cm$^{-1}$. While the central component is almost saturated after 1080 s, the side components still deepen with further burning.

Quantitative analysis by fitting with Gaussian line shapes indicates that the central hole component has about the same area after 130 s burning time as the high-energy component after 1080 s.

After sufficient burning time, all measured hole spectra show a triple structure with a central hole, which is resonant with the burning laser energy, and two side holes, one low-energy and one high-energy component. Taking into account that probing displays the inhomogeneous distribution of the $\mathbf{T_1}$ substate **III** (see Sect. 7.4), it can be concluded that with increasing burning time different subsets of emitter molecules are involved. Burning is most efficient for molecules with highest absorption cross section, i.e. for those molecules with the energy of their substate **III** at the laser energy. Thus, the central component can be attributed to burning of molecules absorbing the laser by their $\mathbf{0} \rightarrow$ **III** transition (compare subset 'A' in Fig. 46).

Ir(btp)$_2$(acac) molecules with their $\mathbf{T_1}$ substate **II** in resonance with the burning laser have their substate **III** blue shifted by the corresponding ZFS value of $\Delta E_{\mathrm{III-II}}$. Therefore, the high-energy hole component can be attributed to the burning of Ir(btp)$_2$(acac) complexes which absorb at the burning laser energy with their $\mathbf{0} \rightarrow$ **II** transition. (Compare subset 'B' in Fig. 46.) The measured energy difference of both hole components represents the energy difference $\Delta E_{\mathrm{III-II}}$. It lies at about 18 cm$^{-1}$. A similar value of ZFS is found also for Ir(btp)$_2$(acac) doped into polycrystalline $CH_2Cl_2$ and octane, respectively (compare Sect. 4.4).

The hole component shifted by 17 cm$^{-1}$ to the red originates from molecules, which are burnt by absorption of energy levels above the $\mathbf{T_1}$ substate **III**. The most probable explanation is an absorption (burning) into a localized phonon of the excited substate **III** (compare subset 'C' in Fig. 46), since spectral shape and energy of this low energy side hole resemble those of typical phonon side bands [45].

From the longer formation time of the high-energy hole component relative to the central component the ratio of the absorption cross sections for the transitions to the involved triplet substates **II** and **III** can be estimated. The hole area of the central component in PVB after 130 s burning time is in good approximation the same as the area of the blue shifted component after 1080 s. Assuming the same hole burning quantum yields for both subsets of molecules, the difference of burning times can be attributed to the different absorption cross sections. Accordingly, the absorption cross section of the transition from the singlet ground state $\mathbf{S_0}$ to substate **III** can be estimated to be by a factor of about 8 higher than that of the transition to substate **II**. This value lies in the range found for the ratios of decay times measured for different sites of Ir(btp)$_2$(acac) in $CH_2Cl_2$ (Sect. 5.4).

The absorption cross section of the **0** → **I** transition of Ir(btp)$_2$(acac) is several times lower than those of the transitions to the substates **II** and **III** and even to phonon levels of these states. Therefore, the observation of the corresponding side holes would require substantially longer burning times, which was not feasible with the available experimental equipment. Consequently, substate **I** is not displayed in the hole burning spectra.

For completeness it is remarked that anti-hole areas were observed within the inhomogeneous distribution of the electronic transition of the emitter molecule in the matrix. This indicates a photophysical hole-burning mechanism. For example, an anti-hole is manifested in the small intensity increase in the spectral range between hole A and hole B in Fig. 46 (curve for 2480 s). This intensity increase (representing an increase of the absorption) is enhanced with further burning, i.e. the anti-hole becomes more distinct.

Spectral hole burning was also observed with Ir(btp)$_2$(acac) embedded in PFO and PVK, respectively. Figure 47 compares hole spectra for the three matrices, whereby the spectrum depicted in Fig. 47a is the same as the one shown in Fig. 46 after 2480 s burning time. The hole in PFO was burnt with an intensity of about 100 W/cm$^2$ for 600 s resulting in a width of 2.6 cm$^{-1}$ of the resonant component. (Fig. 47b) Here, the high energy component is also shifted by about 18 cm$^{-1}$ and has a width of about 8 cm$^{-1}$. The separation of the hole components is practically identical to the one of Ir(btp)$_2$(acac) doped into the PVB matrix. The low energy component, however, has its minimum shifted by about 15 cm$^{-1}$ and is the least pronounced one in all matrices investigated. This is in accordance with a comparatively weak electron-phonon coupling, which is also supported by the observation that the line-narrowed spectra of Ir(btp)$_2$(acac) in PFO show well resolvable vibrational satellite lines (Fig. 44).

In the PVK matrix, Ir(btp)$_2$(acac) showed significantly less burning efficiency than doped into PVB and PFO. (Fig. 47c) After 4200 s of burning with a strongly focused laser beam of about 1000 W/cm$^2$, the resulting central hole exhibits a width of about 4.5 cm$^{-1}$. In this case, a factor of about 170 more photons per unit area compared to PFO were necessary to burn the hole in PVK. These differences can be attributed to different potential landscapes of the double well potentials in the dissimilar hosts.[214] Concerning the side holes, differences of PVK to both other matrices can be observed. For the high energy part, the minimum is also blue-shifted by about 18 cm$^{-1}$ relative to the central component, but its width of about 15 cm$^{-1}$, as determined by a fit of a Gaussian line shape, is about twice as large as in PFO or PVB. Local heating during burning cannot be responsible for this width as

it is also observed with a less intense burning laser. The low energy contribution has its minimum at about 14 cm$^{-1}$ red shifted relative to the central component, which is similar to the corresponding shift in PFO.

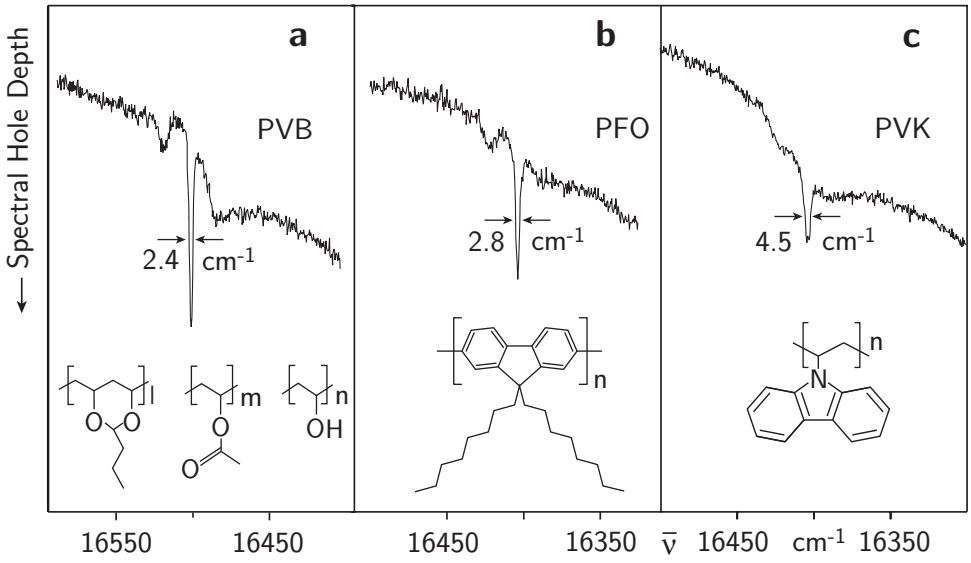


**Figure 47** Persistent spectral holes of Ir(btp)$_2$(acac) in three amorphous polymeric matrices (a) PVB, (b) PFO, and (c) PVK at $T = 1.2$ K. The holes, burnt at 16500 cm$^{-1}$ (PVB) and 16400 cm$^{-1}$ (PFO and PVK) were probed by recording the intensity of an emission peak which lies 306 cm$^{-1}$ below the energy of the probing laser. The insets show the chemical structures of the polymers. PFO and PVK are homopolymers, while PVB is built-up by three constitutional units, which are statistically distributed along the polymer chain with $l > n > m$.

Aside from the hole components discussed so far, in the spectra of Ir(btp)$_2$(acac) in PVK an additional features occurs. The absorption in the comparatively wide range between the high energy side hole and the low energy side hole is significantly reduced additionally to the resonant hole. This is, for example, expressed in the onset of the resonant hole, which is found well below the absorption at the corresponding energy before the burning. As a consequence, the individual hole components are not separated as clearly as in the other two hosts. The reduced absorption is a result of the higher intensity and longer duration of the hole burning in PVK as compared to PVB and PFO. As illustrated in Fig. 48, in PVK not only burning as described in Fig. 46 (see also Fig. 48a) occurs, but probably also the (weaker) absorption of those subsets of molecules is reduced, for which a phonon

satellite of transition **0** → **II** lies within the bandwidth of the burning laser. Since energies of 15 to 20 cm$^{-1}$ are quite typical for phonon satellites of organo-transition metal complexes such as Ir(btp)$_2$(acac), corresponding subsets of molecules can be concerned, which have their transition **0** → **III** slightly above (Fig. 46b) or below (Fig. 46c) the energy of the burning laser. Thus, the absorption at either side of the resonant hole is reduced at a width which is connected to the width of the corresponding phonon sideband.

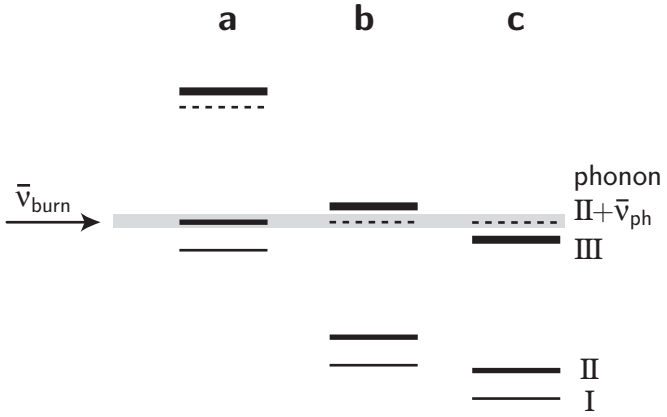


**Figure 48** Illustration of additional burning paths occurring for Ir(btp)$_2$(acac) in PVK. For comparison, burning as given in (a) of the subset (subset 'B' in Fig. 46) which has the transition into substate **II** at the burning energy occurs in all three hosts PVB, PFO, and PVK. In PVK, due to intense and long burning, also burning of subsets of molecules occurs for which the transition energy to a phonon level of substate **II** lies at the energy of the burning laser ((b) and (c)). For such subsets, the energy of the transition to substate **III**, which is registered by the detection of the hole spectra, can lie above (b) or below (c) the energy of the burning laser. Thus, the absorption at both sides of the resonant hole is additionally reduced.

Interestingly, in the present study, the widths of the high-energy hole components – determined in good approximation as FWHM widths of a Gaussian hole shape – reveal that the ZFSs values between the $\mathbf{T_1}$ substates **II** and **III** ($\Delta E_{\mathrm{III-II}}$) are distributed over significant ranges. For a coarse quantification of this distribution, a convolution of Gaussian distributions and line shapes is assumed. In this case, the half width (FWHM) $\delta\bar{\nu}_{high}$ of the high energy hole is given by the half width (FWHM) $\delta\bar{\nu}_{res}$ of the resonant hole and the half width $\delta(\Delta E_{\mathrm{III-II}})$ of the distribution

of the ZFS between the substates **II** and **III** according to [218]

$$(\delta\bar{\nu}_{high})^2 = (\delta\bar{\nu}_{res})^2 + (\delta(\Delta E_{\mathrm{III,II}}))^2 \quad . \tag{49}$$

Thus, the width of the distribution of ZFS values $\Delta E_{\mathrm{III-II}}$ is obtained by [218]

$$\delta\left(\Delta E_{\mathrm{III,II}}\right) = \sqrt{(\delta\bar{\nu}_{high})^2 - (\delta\bar{\nu}_{res})^2} \quad . \tag{50}$$

The analysis yields values for $\delta(\Delta E_{\mathrm{III-II}})$ of approximately $6\,\mathrm{cm}^{-1}$ and $7\,\mathrm{cm}^{-1}$ for PVB and PFO, respectively, and of about $15\,\mathrm{cm}^{-1}$ for PVK. This situation demonstrates that the inhomogeneous distribution of $\Delta E_{\mathrm{III-II}}$ is broader for PVK than for the other two hosts. Obviously, Ir(btp)$_2$(acac) exhibits a more pronounced interaction with PVK than with the two other matrices. This is possibly due to $\pi$-interactions of the (btp) ligand of the Ir complex with the carbazole ring system of PVK. A corresponding interaction is not present in PVB and would also be absent in PFO, if Ir(btp)$_2$(acac) is hosted near the alkyl chains.

Interestingly, the values $\delta(\Delta E_{\mathrm{III-II}})$ obtained by spectral hole burning correspond roughly also to the width (FHWM) of the vibrational satellite line used for detection, which is $7\,\mathrm{cm}^{-1}$ for PVB and PFO, and $18\,\mathrm{cm}^{-1}$ in PVK. Since the line width of the excitation laser is below $1\,\mathrm{cm}^{-1}$ and homogeneous broadening of the ZPL due to electron-phonon coupling is not significant at $T \leq 4.2\,\mathrm{K}$, the line width of the vibrational satellite(s) seems to be dominantly determined by the inhomogeneous distribution of ZFS values. This can be explained as illustrated in Fig. 49: After narrow band excitation, which most probably leads to the excitation of molecules with their strongest absorbing substate **III** at the laser energy, spin-lattice relaxation to substate **II** takes place. If the splitting $\Delta E_{\mathrm{III-II}}$ varies, the subsequent emission from substate **II** exhibits slightly different energies for different molecules, and a broadening of lines in the emission spectrum results. This effect obviously dominates over other effects of line broadening, since in all three matrices the width of the resonant hole is significantly smaller than the obtained width of the ZFS distribution. As a result, it might be sufficient in future investigations to simply analyze the line widths observed in line-narrowed emission spectra to assess the width of the ZFS-distribution of $\Delta E_{\mathrm{III-II}}$ for a complex in a specific host material. The mean value of $\Delta E_{\mathrm{III-II}}$, however, might not be accessible by the method of luminescence line narrowing, in particular, if the line broadening due to the described effect and/or due to electron-phonon coupling is too large.

In this context, it is remarked that the electron-phonon coupling is weakest in the

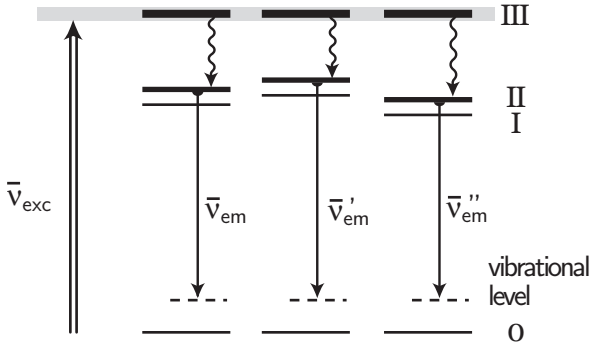


**Figure 49** Broadening of an emission line in a spectrum which is luminescence line-narrowed by narrow-band laser excitation. After excitation of triplet substate **III** of a subset of molecules and subsequent spin-lattice relaxation to substate **II**, the radiative transition from this state to a specific vibrational level of the ground state may exhibit slightly different energies for the different molecules of the excited subset, if the value $\Delta E_{\mathrm{III-II}}$ of ZFS between **III** and **II** is not the same for these molecules.

PFO matrix. This is indicated by the observation that the low-energy hole component is shallowest in PFO, among the three investigated matrices Further it is in accordance with the fact that the line-narrowed spectra of $Ir(btp)_2(acac)$ in PFO show well resolved vibrational satellite lines (Sect. 7.2). This result is important for future investigations of other organo-transition metal complexes, if highly resolved spectra are to be achieved in amorphous matrices.

## 7.6 Evaluation of the synchronous scan technique of hole detection

The synchronous scan technique used for detection of the spectral holes is a very specific method. It had to be applied in connection with the hole burning experiments of $Ir(btp)_2(acac)$, since excitation spectra recorded with detection at a fixed energy did not reveal the desired information on the triplet substate splitting. This is explained in the following. A simple method is described in Fig. 50a. Upon excitation ($\bar{\nu}_{exc}$) within the inhomogeneously broadened $\mathbf{S_0} \rightarrow \mathbf{T_1}$ transition range, a resolved emission spectrum can be recorded. Since, for $Ir(btp)_2(acac)$, the absorption cross section of triplet substate **III** is markedly larger than that of the other

two substates, the resolved emission will mainly result from that specific subset of molecules, which have their **III** states at the excitation energy $\bar{\nu}_{exc}$ (subset 'A' in Fig. 50a). In the emission spectrum, a specific resolved vibrational satellite can be

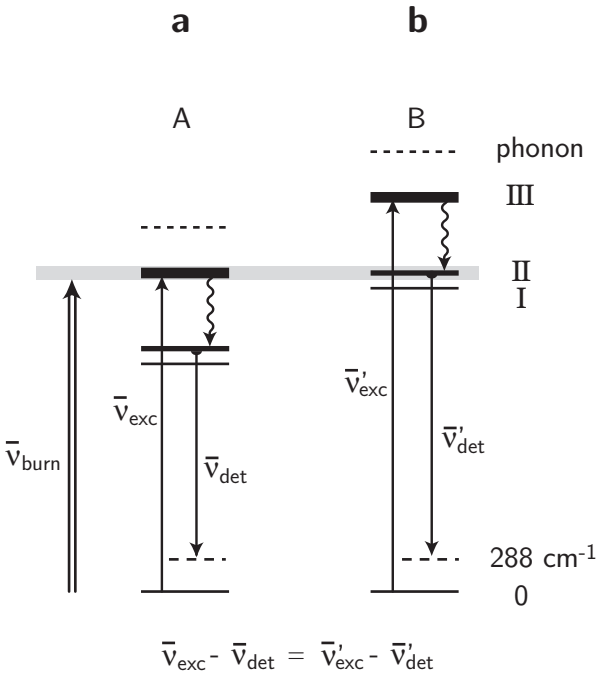


**Figure 50** Illustration of hole detection by a synchronous scan technique with a fixed energy separation between the excitation $\bar{\nu}_{exc}(\bar{\nu}'_{exc})$ and the detection $\bar{\nu}_{det}(\bar{\nu}'_{det})$. Note, that with this method those spectral holes are revealed, which correspond to the absorptions into triplet substate **III** of *different subsets* A (a) and B (b) of molecules within the inhomogeneous distribution. The emission of the different subsets is detected at the same vibrational satellite. Recording an excitation spectrum with a fixed absolute detection energy, in contrast, would gain spectral holes corresponding to the different triplet substates of *one subset*. However, this is not possible in practice (see text).

chosen, which may be used later for detection of an excitation spectrum. At this stage, only the energy difference between the excitation energy and the detection energy of the vibrational satellite is known. Neither the vibrational energy of the corresponding mode, nor the ZFS between the emitting substate (here **II**) and the excited substate **III** is known. Therefore, it makes sense to use the energy of the excitation of subset 'A' into substate **III** also for hole burning. After burning at this energy ($\bar{\nu}_{burn}$ in Fig. 50), among others, the absorption into all three substates

of subet 'A' will be reduced. Recording an excitation spectrum with fixed detection at the chosen vibrational satellite is therefore expected to result in a resonant hole at the burning energy and, theoretically, two electronic low energy side holes corresponding to the triplet substates **I** and **II** of site 'A'.

However, carrying out this experiment for $Ir(btp)_2(acac)$ doped into PVB did not lead to the observation of any side hole. Only the resonant hole was found. Obviously, this is a consequence of the significantly lower probability of the transitions $\mathbf{0} \rightarrow \mathbf{I}$ and $\mathbf{0} \rightarrow \mathbf{II}$ compared to that of transition $\mathbf{0} \rightarrow \mathbf{III}$ (see Chapt. 5). This problem is circumvented, if the spectral hole structure of a different subset of molecules is investigated. As seen in Fig. 50 and described in the last section, burning with an energy $\bar{\nu}_{\mathrm{burn}}$ concerns also the subset of molecules (subset 'B' in Fig. 50), which have their $\mathbf{0} \rightarrow \mathbf{II}$ transitions at the burning energy. The absorption of this subset 'B' can be reduced to the same extent as the one of subset 'A', if the time of burning is sufficiently long. Therefore, it will be possible to observe a resonant hole. Moreover, in this case a high energy side hole exists, which should now be detectable, since it represents the missing (strong) absorption into substate $\mathbf{0} \rightarrow \mathbf{III}$. Thus, in principle, two spectral holes of subset 'B' will be found, if the excitation spectrum is registered, while the detection energy is kept fixed. In reality, however, the corresponding detection energy can not be specified, since the ZFSs between the substates **II** and **III** is unknown for both subsets 'A' and 'B'. The only solution to this problem is to record the hole spectra by tuning the detection energy synchronously with the excitation energy. For this purpose, the energy difference to use is $\bar{\nu}_{\mathrm{exc}} - \bar{\nu}_{\mathrm{det}}$ as given in Fig. 50a. It is important to note that, with this technique, the obtained holes correspond to reduced absorptions only into the triplet substates **III** of the involved subsets of molecules. This is favorable, since these are exactly those spectral holes, which are most probably detectable. The separation of the holes gives information about the ZFS of the $\mathbf{T_1}$ state, in particular about the splitting $\Delta E_{\mathrm{III-II}}$. On the other hand, scanning with a fixed energy difference $\bar{\nu}_{\mathrm{exc}} - \bar{\nu}_{\mathrm{det}}$ implies an equal zero-field splitting $\Delta E_{\mathrm{III-II}}$ of the different subsets, which is obviously not given. Thus, to account for the distribution of ZFS values $\Delta E_{\mathrm{III-II}}$ the detection bandwidth has to be chosen sufficiently large.

## 7.7 Persistent spectral hole burning – Outcomes

The study shows that persistent spectral hole burning and phosphorescence line narrowing provide powerful tools to gain insight into the splitting structure of the

emitting triplet state $\mathbf{T_1}$ of $Ir(btp)_2(acac)$ into substates, even when the compound is doped into amorphous matrices, as is the case in OLED applications. The obtained results are in line with the findings of investigations in Shpol'skii and Shpol'skii-like hosts. (Compare the previous chapters.) In these studies, the total ZFS $\Delta E_{\mathrm{III-I}}$ was found to lie between 15 and 27 $cm^{-1}$ for different discrete sites of $Ir(btp)_2(acac)$ in $CH_2Cl_2$. By persistent spectral hole burning, mean values of 18 $cm^{-1}$ have been found for the splitting between the substates **II** and **III**. The weakly absorbing substate **I** could not be identified by this technique. However, the separation between substate **I** and the next higher lying substate **II** is assumed to be roughly the same as in Shpol'skii-like matrices, where it amounts to about 3 $cm^{-1}$ (Chapt. 4). In this case, the (mean) total ZFS can be estimated to about 21 $cm^{-1}$ for all three matrices. Indeed, these values lie well within the range found in the polycrystalline matrices. This detailed information has not yet been obtained for triplet emitters embedded in amorphous hosts.

In the three amorphous polymer matrices, the ZFS, in particular the value $\Delta E_{\mathrm{III-II}}$, is again distributed over significant ranges. This information is obtained by analysis of spectral hole widths. The amount of $\Delta E$(ZFS) is correlated with the extent of MLCT character, which is mixed into the emitting triplet term via configuration interaction and spin-orbit coupling.[132] Thus, a variation of $\Delta E$(ZFS) in dependence of the matrix environment (or site) indicates a significant interaction of the host with the electronic structure of the dopant and significantly different photophysical properties of the subsets' triplet states. Among the different matrices studied, PVK induces the strongest inhomogeneous distribution of the splitting between the substates **II** and **III**. The width of the distribution amounts to 15 $cm^{-1}$, whereas it is only 6 $cm^{-1}$ and 7 $cm^{-1}$ for PVB and PFO, respectively. As a consequence, a substantial fraction of the $Ir(btp)_2(acac)$ molecules doped into PVK have only small splittings around 10 $cm^{-1}$. Such values might already be too small to enable efficient luminescence properties, as required for OLED applications. This is indicated, since for emitter compounds with small ZFS values, spin-orbit coupling is relatively weak and thus, the important mixing of singlet character into the tiplet states is not effective. Therefore, such complexes exhibit comparatively small radiative decay rates and often also small quantum yields.[120]

As remarked already in Sect. 4.5, efficient OLED triplet emitters hitherto studied exhibit significant or even large zero-field splittings of the $\mathbf{T_1}$ parent term (compare Fig. 11). In this context, a value of 10 $cm^{-1}$ may already be considered as critical.

We suppose that the results obtained for the compound in amorphous matrices at low temperature hold also at ambient temperature, if the matrices are considered to

be rigid enough. This seems to be valid for host materials with a glass transition temperature $T_g$ being significantly larger than 300 K.

Interestingly, the spectral hole widths carry also another message. In each host, the width of the resonant hole is significantly smaller than the width of the high-energy side hole and the width of the vibrational satellite line used for detection of the hole spectra, respectively. This allows to conclude that the line widths in the line-narrowed emission spectra are dominantly governed by the ZFS distribution and only to a significantly lesser extent by other effects. Thus, it is expected that luminescence line narrowing is more difficult to achieve for complexes with a significant or large ZFS ('$^3$**MLCT** emitters'), for which the distribution of splittings may be comparatively large, than for complexes with only small splittings in the order of 1 cm$^{-1}$ ('$^3$**LC** emitters').

In future investigations, persistent spectral hole burning can be used as a sensitive probing technique for the effects of external electric fields [217] on optical transitions in OLED emitter materials. It is expected that the analysis of electric field induced shifts of the electronic levels will provide more detailed information on the emitter complex and the interaction with its closest environment, particularly with regard to the fact that emitters in OLEDs are exposed to high electric fields.

# 8 Experimental

## 8.1 Sample preparation and cooling

Investigations of $Ir(btp)_2(acac)$ in the poly-crystalline matrices dichlormethane ($CH_2Cl_2$) and *n*-octane ($C_8H_{18}$) were carried out at a concentration of $\approx 2.5 \cdot 10^{-5}$ mol/l. The used solvents were of spectroscopic grade. $CH_2Cl_2$ was purchased from Sigma-Aldrich ('Spectranal' grade) and *n*-octane was obtained from Fluka (p.a. quality).

For the low temperature experiments, mainly a Cryovac Konti-IT Helium-cryostat was used. This cryostat is a vacuum- and nitrogen-shielded continuous flow cryostat with integrated liquid helium tank. It can be operated either as a bath cryostat or as an evaporator. In operation, (liquid or gaseous) Helium is transferred from the reservoir to the sample chamber by a pick-up tube. The Helium enters the sample chamber through a sintered diffusor and via a heat exchanger, and directly floods the sample. Controlling the He-stream and the heating allows to measure at temperatures in the range from 4.2 K to 300 K. Lower temperatures down to ≈1.5 K are achieved by reducing the He-vapor pressure by pumping with a rotary pump. Experiments under magnetic field were carried out in an Oxford Instruments MD10 cryostat. This cryostat is of the same type as the Cryovac cryostat. It allows to work in the same temperature range but is additionally equipped with NbTi superconductive magnets in solenoid coil construction which allow for highly homogeneous magnetic fields of up to 12 T flux density at 4.2 K and up to 14 T at 2.2 K. Cooling of the magnetic field coils below 4.2 K is possible by use of an integrated lambda plate. Due to the solenoid magnet design, the sample chamber is optically accessible for light in- and out-coupling only from the bottom side. Both described cryostats are equipped with optical windows made of fused silica (Spectrosil B).

The samples were inserted into the cryostat in a fused silica tube of $4 \times 10$ mm size, which had been closed at the bottom by melting it off from a longer tube. The samples were cooled down to reach the solid state in about 3 minutes, resulting in a favorable site situation, as given in Fig. 18 (Sect. 4.1). The cooling rate was adjusted by pre-cooling the sample chamber of the cryostat to ≈100 K and further

cooling by a controlled He- gas stream from the He-reservoir via the pick-up tube.

The polymeric samples of polyvinylbutyral (PVB, Hoechst), poly-*N*-vinylcarbazol (PVK, Acros) and poly(9,9-dioctylfluoren-2,7-diyl) (PFO, Aldrich) were prepared as polymer films of about 100 µm thickness from solution, using ethanol (PVB) or $CH_2Cl_2$ as solvents. While PVK and PFO are homopolymers, PVB consists of three constitutional units (see inset of Fig. 47), which are statistically distributed in the chain: acetal groups (62%), acetyl groups (4%) and hydroxyl groups (34%). The doping concentration of the polymer films was in the order of $10^{-3}$ mol/l. For spectral hole burning, these samples were immersed in an on-site made optical Helium bath cryostat (glass cryostat), which could be cooled down to 1.2 K by pumping off the He vapor by a rotary/roots pump system.

## 8.2 Standard optical equipment

Absorption measurements were carried out with a commercial absorption spectrometer Varian Cary 300. The device is a UV-Vis double beam spectrometer with a maximum resolution of 0.193 nm and a spectral range from 190 nm to 900 nm. It employs a tungsten halogen bulb lamp and a deuterium arc lamp as light sources, which are filtered by a Czerny-Turner monochromator and an additional pre-monochromator. Thus, absorbances of up to ≈5 can be registered. For detection of the transmitted light, a Hamamatsu R928 photomultiplier tube is used.

Emission and excitation spectra and emission decay curves at 300 K and 77 K were measured using a commercial steady-state fluorescence spectrometer Jobin Yvon Fluorolog 3 (FL 3-2). It uses a 450 W Xenon short arc lamp (Ushio UXL-450S-0) for excitation and a Hamamatsu R928P photon counting photomultiplier tube for detection. Excitation spectra can be recorded by tuning an excitation double monochromator (Czerny-Turner type) in the range from 240 nm to 600 nm. The emission is dispersed by a double monochromator with a range from 300 nm to 850 nm and a maximum spectral resolution of 0.2 nm. The recorded spectra are corrected with regard to the spectral intensity dependence of the excitation and emission unit, respectively. Experiments at ambient temperature were carried out with the solution in a fused silica cuvette or a thin polymeric film on a fused silica substrate. For 77 K measurements, a liquid $N_2$ dewar was used (fused silica), where the sample was inserted in a fused silica tube.

Experiments at lower temperature were carried out by use of the cryostats described in the previous section. For non-selective excitation, a UV diode laser

Toptica Photonics iBeam (373 nm) or an $Ar^+$ laser Coherent Innova 90 was used, if emission spectra were recorded. Emission decay time measurements after non-selective excitation were performed with a diode pumped frequency tripled Nd:YAG laser Industrielaser Berlin Diny PQ (355 nm), featuring a pulse duration of ≈5 ns and a variable repetition rate of up to 1 KHz. For site-selective excitation, a pulsed dye laser Lambdaphysik Scanmate 2C was operated using Rhodamine B and Rhodamine 101, respectively. This laser exhibits a spectral band width of 0.1 $cm^{-1}$ and it was pumped by a frequency doubled Nd:YAG laser Quantel Brilliant LPY 150-20 with a pulse duration of ≈4 ns and a repetition rate of 20 Hz. Spectral holes were burnt and detected with a Spectra-Physics Model 380 dye ring laser with a spectral band width of ≈0.1 $cm^{-1}$. The laser wavelength was scanned by turning a birefringent filter by means of a DC motor and recorded by a wavemeter Burleigh WA20-VIS. For pumping of this laser, the 514 nm line of an $Ar^+$ laser Spectra-Physics 2045 was used.

The phosphorescence was dispersed by a double monochromator Spex 1401 and detected with a Joule-Thomson cooled photomultiplier (RCA C7164R) in case of the spectral hole burning experiments, the measurements under magnetic field, and the measurements of $Ir(btp)_2(acac)$ in *n*-octane. All other spectra were recorded with an intensified CCD camera (Princeton PIMAX) or a cooled photomultiplier (RCA C7164R), both attached to a triple spectrograph (S&I Trivista TR555). The corresponding setup was built in the frame of this work and is therefore described in more detail in the next section. Photomultipliers were always operated in photon counting mode. Emission decay curves were registered using a Fast Comtech P7887 multichannel scaler card with a minimum bin width (time-resolution) of 250 ps.

## 8.3 Setting-up of a new spectrometer

To reduce measuring times as compared to the hitherto used scanning spectrometers featuring single channel detectors, a new spectrometer was set up, which uses a multichannel device (ICCD-camera) for detection. This setup is schematically sketched in Fig. 51.

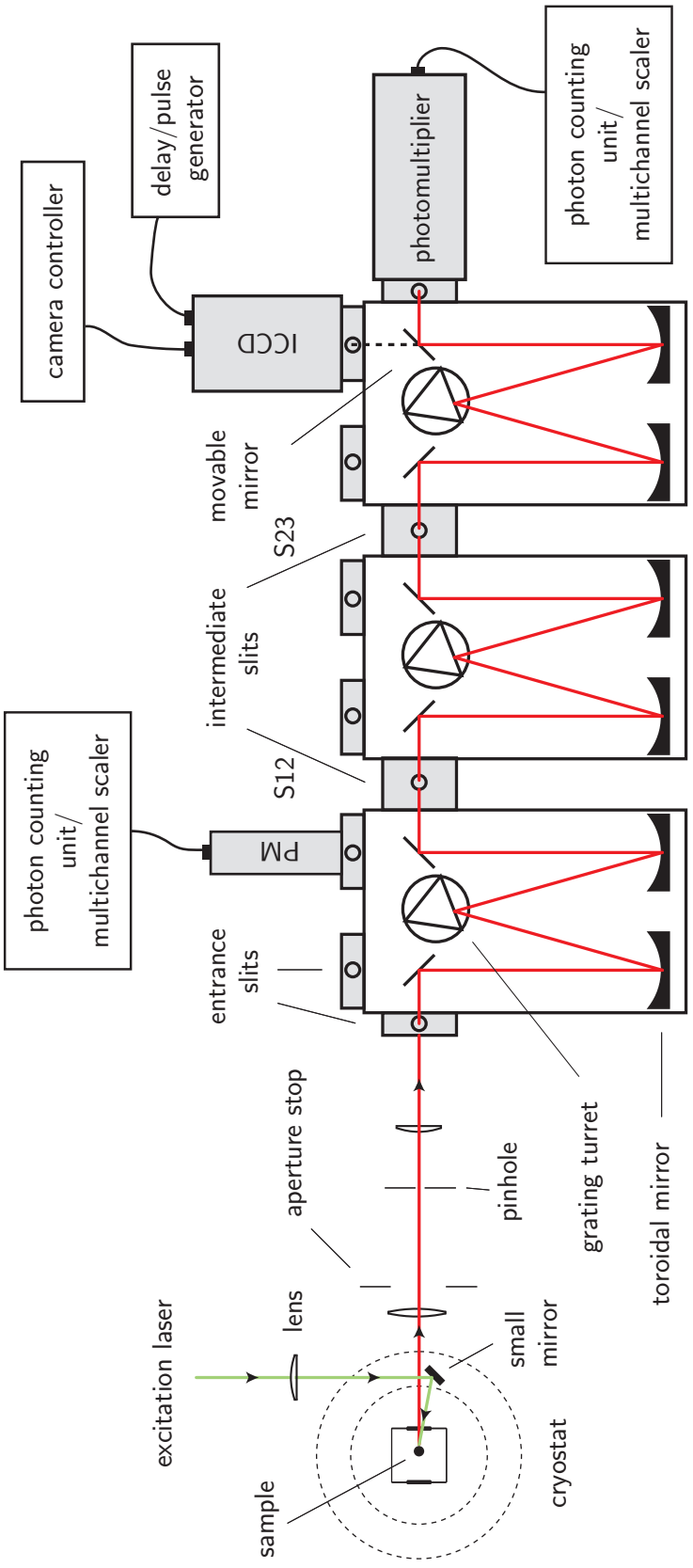


**Figure 51** Experimental setup used for high-resolution emission and excitation spectroscopy. Most spectra of $Ir(btp)_2$-(acac) were measured using this setup. The individual components are described in the text. The optical setup and the ICCD camera are illustrated in detail in Fig. 52 and Figs. 53, and 54, respectively.

The exciting laser light is focused by a lens and directed to the sample by a small tilted mirror. The luminescence of the sample is imaged onto the entrance slit of a triple spectrograph (see below) via a two-lens optics and a pinhole as depicted in Fig. 52. The lens setup (fused silica lenses) is optimized to match the aperture of the spectrograph (aperture ratio F/6.5). A pinhole is used to reject stray light and reflexes.

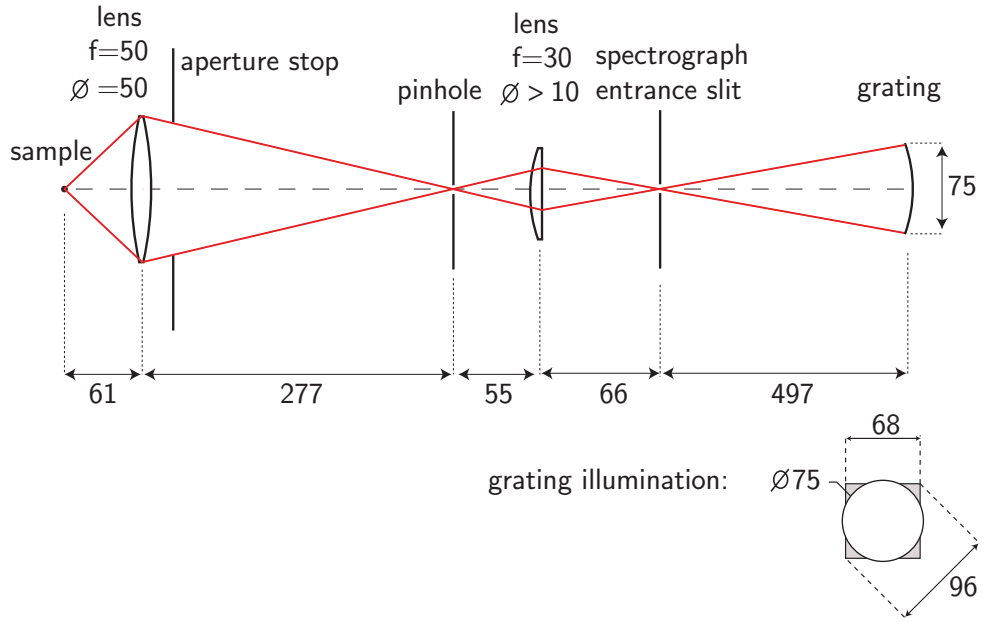


**Figure 52** Optical setup for incoupling of the phosphorescence light into the triple spectrograph. For the (fused silica) lenses, the focal length (f) and the diameter are given. All dimensions are given in mm. The resulting aperture ratio is F/6.6 and the magnification of the image of the sample at the spectrograph slit is about 5.

The triple spectrograph (Spectroscopy & Imaging, Warstein, Germany, Trivista 555) is based on three independent Acton Research SpectraPro-2500i imaging Czerny-Turner spectrographs, which are mounted on a common base plate. These spectrographs incorporate cylindrical field correction introduced by aspheric optics to remove astigmatism. Each stage is equipped with a triple grating turret to switch between two ruled gratings of 150 g/mm and 900 g/mm, and a holographic grating of 1800 g/mm all blazed at a wavelength of 500 nm. The stages exhibit each a focal length of 497 mm and an aperture ratio of F/6.5 (68×84 mm gratings). They scan linearly with respect to wavelength (direct drive) with a nominal drive step size of

0.002 nm and a repeatability of ±0.005 nm.[32] The first stage features two entrance slits (lateral and axial) which are manually adjustable from 10 µm to 3 mm. Light incoupling can be switched between the slits by a motorized tilted mirror. Similarly, at the last stage, the outcoupling of dispersed light can proceed through a manually adjusted slit as described above to a laterally attached photomultiplier or axially via a CCD port to an ICCD camera (see below). Between each two individual stages, motorized slits can be adjusted by software control from 10 µm to 12 mm

The triple spectrograph system is fully software controlled through a USB interface. Especially the grating drives are not hardware-coupled, but synchronized in software. This allows not only for easy adjustment of the system but also for a high flexibility for different means of application. For example, the system can be operated with all stages in an additive mode, where the dispersions of all stages add to give a total focal length of 1500 mm and a maximum linear dispersion of 0.30 nm/mm, if in all stages the 1800 g/mm gratings are used. This mode is especially suited for measurements of highest resolution with the photomultiplier or, if stray-light rejection is not critical, with the ICCD camera. On the other hand, the system can easily be switched to subtractive mode by software. In this case, the grating of the second stage is positioned in a way to completely cancel the dispersion of the first stage. Therefore, the gratings of the first two stages must match in grove density. These stages then act as a very sharp bandpass filter depending on the opening of the intermediate slit S12 (Fig. 51). The dispersion of the whole setup is entirely defined by the dispersion of the last stage, in this mode. With the typical grating configuration 900/900/1800 for the three stages in subtractive mode, a nominal linear dispersion of 0.90 nm/mm is obtained. Since in this configuration the emission light is recombined at the intermediate slit S23 (ideally) to the shape of the original image, this slit can be very narrow and thus a very high level of stray light rejection can be reached. This is especially important for detection with the ICCD camera, as in this case a comparatively large bandwidth must be allowed to pass through the system to illuminate the whole width of the multichannel detector all at once. Therefore, the bandwidth-limiting intermediate slit S12 has to be relatively wide for detection with the ICCD camera (typically 8 mm). A comparable stray light rejection for ICCD measurements would not be possible with a double spectrograph. High stray light rejection was especially important in the presented work, since the matrices doped with the organometallic complexes were often highly scattering polycrystalline media at low temperatures. In addition to the

[32] The given values apply, if the 1800 g/mm gratings are used in all stages (in additive mode).

described features, the spectrograph system offers a high flexibility for measurements with different resolution and, importantly, also with different CCD coverage. For example, the triple additive configuration with three 1800 gr/mm gratings offers a high resolution, but a CCD coverage of only a few $cm^{-1}$. On the other hand, also a configuration is possible, where the first two stages are operated with the gratings in zeroth order and with a 150 g/mm grating set in the last stage. Thus, a whole emission spectrum ranging over several hundred $cm^{-1}$ can be registered all at once, if a low resolution can be tolerated. To apply the different settings, the additive or subtractive operation mode, the widths of the intermediate slits, the positions of the tilted mirrors and the grating, and the order in which to use each grating can be specified in the software and configurations can be saved and set as a whole. The throughput of the whole system is of the order of 15%.

For detection of the dispersed emission, different detectors are attached to the spectrograph system. Measurements of emission decay curves with high sensitivity can be carried out with a photomultiplier (Hamamatsu H5783P-01) directly attached to the (axial) output slit of the first stage. (Each stage can also be used individually.) For highly-resolving measurements, a photomultiplier RCA 7164R is mounted at the (lateral) exit slit of the last stage. This detector is Joule-Thompson cooled to $-40°C$ and is operated in photon counting mode. The data are registered with a Stanford Research SR400 gated photon counter (500 ns pulse pair resolution) or a Fast Comtec P7887 multichannel scaler PC card (250 ps pulse pair resolution/binwidth). The latter is used also for emission decay time measurements.

For registration of emission spectra with high sensitivity and yet in a short time, an intensified CCD camera (ICCD camera, Princeton Instruments) is attached to the (axial) exit port of the triple spectrograph. The principle of this detection system is illustrated in Fig. 53. The main component is an image intensifier tube which amplifies the intensity of the incident light and is very sensitive at low light levels. The working principle is seen from Fig. 54. After passing an input window, the incident light strikes a photocathode, which is provided with a high voltage. Due to the photoelectric effect, electrons are released from the photocathode. These electrons are accelerated and enter a micro-channel plate (MCP), where small channels each act as a continuous-dynode electron multiplier. The micro-channels are oriented at an angle relative to the incident electrons to guarantee that the electrons hit the wall and release secondary electrons. The impact starts a cascade of electrons that propagates through the channel due to an applied electric field. Thus, the original signal can be amplified by several orders of magnitude. The use of many small channels for amplification is necessary to conserve the spatial resolution of

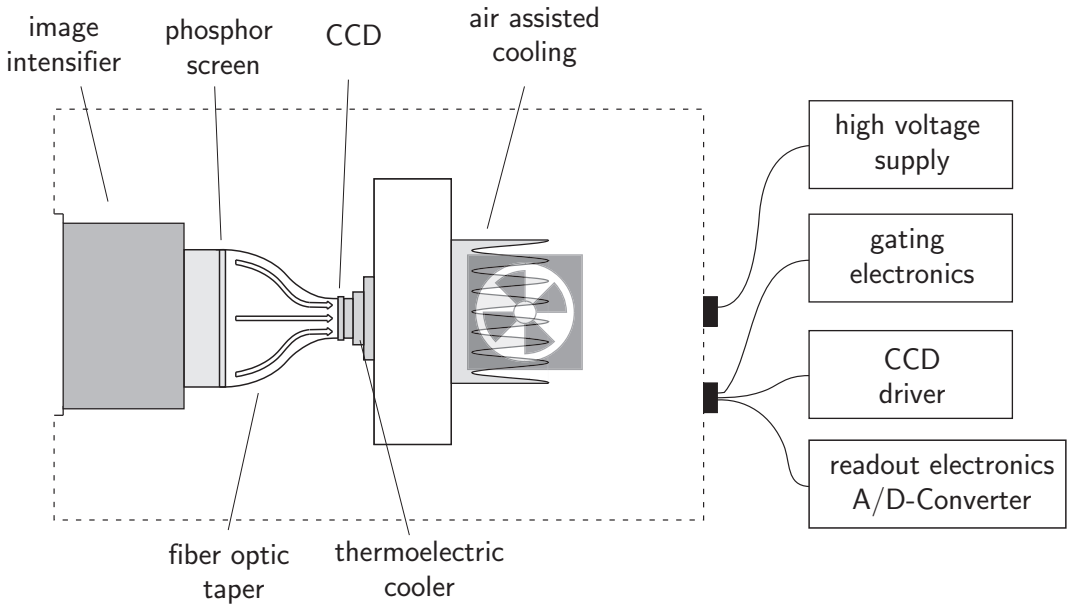


**Figure 53** Schematic drawing of a CCD camera with image intensifier (ICCD camera).

the image. After leaving a channel of the MCP, the electrons are accelerated by a high voltage towards a phosphor screen, where they are converted into light. The resulting intensified image is recorded by a CCD camera, which is connected to the phosphor screen by a fiber optic taper to conserve the spatial resolution. Since the high-voltage of the photocathode can be switched on and off very fast, such an ICCD system can be used for time-resolving measurements. The possibility of gated operation is the major benefit compared to CCD sensors.

The ICCD camera used in this work (PI-MAX 1024 HB-18 unigen) is equipped with a 18 mm diameter high resolution intensifier ((ITT Industries FS9900 Series) with a GaAs photocathode (Gen III). This intensifier is modified with an additional UV-downconversion coating ('unichrome' coating) in front of the photocathode and is sensitive in the wavelength range from 150 to 900 nm. It is capable of gating with a gate width down to 5 ns (fastgate version) and a maximum pulse rate of 5 KHz. The CCD used for detection is a Marconi EEV 30-11 full frame CCD with 26×26 µm pixel size, 1024×256 pixels and a full well capacity of each pixel of 500 000 electrons. It supports vertical binning and subregion readout modes. The 16 bit 100 KHz A/D-converter allows readout times of <20 ms (in binning mode) and is therefore well compatible with the used 20 Hz lasers to principally allow for

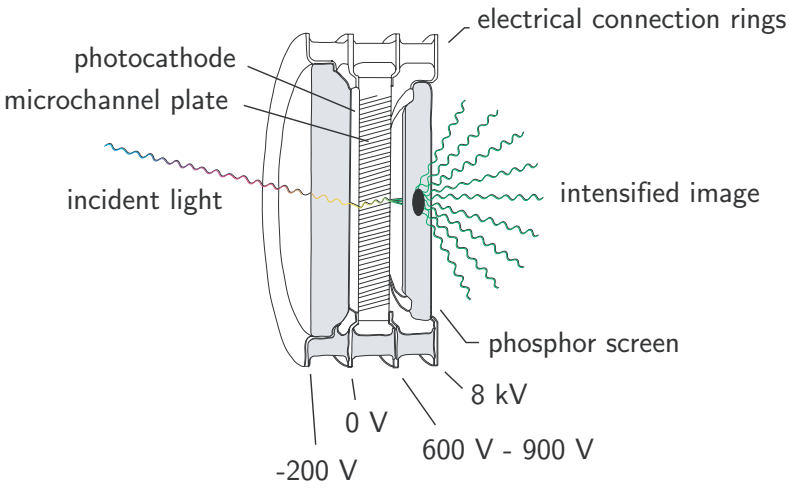


**Figure 54** Elements of an image intensifier used for ICCD cameras as depicted in Fig. 53. All parts are bonded together and sealed in vacuum. Drawing adapted from Princeton Instruments.

readout of the CCD after each laser pulse. The ICCD system can be operated with internal (continuous mode) or external (gate mode) gating. Gate pulses are supplied to the intensifier by an integrated programmable pulse/delay generator (PTG). For time-resolving measurements, the ICCD and the excitation laser (Lambdaphysik dye laser) were synchronized by triggering the PTG by a (preponed) laser Q-switch output signal.

All spectra, which were registered using this experimental setup, have been corrected for the wavelength dependent sensitivity of the spectrograph/detector system. This was achieved by recording the emission of an Osram Wi-14 calibration lamp with the same settings as used for the measurements of the respective samples.

# Summary

*The phosphorescent organo-transition metal complex Ir(btp)$_2$(acac) represents an efficient red emitter for organic light-emitting devices (OLEDs). Photophysical properties of Ir(btp)$_2$(acac) were studied by highly-resolving optical spectroscopy in different matrices. The complex was investigated in the poly-crystalline matrices $CH_2Cl_2$ and n-octane, respectively, and as a single crystal. These investigations were carried out using site-selective emission and excitation spectroscopy under variation of temperature or magnetic flux density, time-resolving emission spectroscopy, and emission decay time measurements. Most of the measurements were performed using a new experimental setup, which was built in the frame of this work. Further, the investigations were extended to emitter/dopant combinations as used in OLEDs. In particular, Ir(btp)$_2$(acac) doped into the polymeric host materials PVB, PFO, and PVK was studied. For this purpose, the technique of persistent spectral hole burning (PSHB) was applied and refined.*

In organic light emitting devices, electrical excitation leads to population not only of singlet states of the emitting species, but to a large extent (75%) also of triplet states. To obtain highly efficient devices, both excited singlet and triplet states (singlet and triplet excitons) have to be utilized for light emission. This is achieved by application of highly phosphorescent organo-transition metal complexes as emitter materials. Due to strong spin-orbit coupling induced by the Ir(III) center, these complexes exhibit a high rate of intersystem crossing from the lowest excited singlet states to the lowest excited triplet state $\mathbf{T_1}$. Therefore, all excitations of the complex, no matter whether they are initially created as singlet or triplet excited states, end up as excitation of the molecules in the lowest excited triplet state $\mathbf{T_1}$. The $\mathbf{T_1}$ state, in turn, can decay to the ground state under emission of light. For OLED applications, phosphorescent organo-transition metal with highest possible quantum efficiencies and decay rates of this phosphorescence are desired. Favorable properties like these, however, are usually only given, if sufficient singlet character is mixed into the emitting triplet $\mathbf{T_1}$, i.e. spin-orbit coupling is effective. This is the case particularly for states which involve sufficient d-orbital parentage, i.e. for states which result from metal-to-ligand charge transfer (MLCT) excitations. How-

ever, since the emitting triplet state of typical organo-transition metal complexes is often a mainly ligand-centered $\boldsymbol{\pi\pi^*}$ state, SOC is only enabled, if MLCT character is introduced into this state by mixing with a higher lying state of high MLCT parentage – for example by configurational interaction. In other words, the degree of MLCT admixture to the emitting $\mathbf{T_1}$ state is a crucial precondition for effective SOC and, thus, indirectly also for favorable photophysical properties of a complex. The extent of MLCT admixture to the $\mathbf{T_1}$ state is reflected in the zero-field splitting (ZFS) of this state into substates. Thus a parameter is at hand, which allows for an assessment of the important MLCT character of a complex by spectroscopic means. This parameter was addressed in the experimental part of this work.

Detailed spectroscopic measurements of $Ir(btp)_2(acac)$ were carried out in different matrices and were presented mainly on the example of the complex doped into a $CH_2Cl_2$ host. $CH_2Cl_2$ seems to be a well-suited matrix for Ir-complexes, which is reported here for the first time. By site-selective emission and excitation spectra of a specific site (site **H**) at different temperatures, the individual substates **I**, **II**, and **III** of the $\mathbf{T_1}$ state were identified. Zeeman effects observed at high magnetic fields provided additional evidence for the triplet nature of the emitting substates and prove directly that these substates result from a $\mathbf{T_1}$ parent term of one specific site. For the preferentially investigated site of $Ir(btp)_2(acac)$ in $CH_2Cl_2$ (site **H**), a total ZFS ($\Delta E_{\mathrm{III-I}}$) of the $\mathbf{T_1}$ state of $25\,cm^{-1}$ was found. On the basis of this zero-field splitting, the MLCT character of the $\mathbf{T_1}$ state of $Ir(btp)_2(acac)$ was classified in the context of other complexes using an ordering scheme developed by Yersin.[45, 46] Thereby, the emitting state was assigned as a ligand-centered ($^3$**LC**) $(btp)^3\boldsymbol{\pi\pi^*}$ state with significant admixtures of MLCT ($\mathbf{d\pi^*}$) character.

Remarkably, the magnitude of ZFS varies with the matrix environment of the $Ir(btp)_2(acac)$ complex. Other sites of the complex in $CH_2Cl_2$ exhibit zero-field splittings from $\approx 15\,cm^{-1}$ to $\approx 27\,cm^{-1}$. In an *n*-octane matrix, the ZFS amounts to $25\,cm^{-1}$ for the main site. Moreover, for the complex as a single crystal, a value of $\approx 19\,cm^{-1}$ is obtained. The results indicate a variation of the MLCT character of $Ir(btp)_2(acac)$ molecules with the host environment. This variation can be interpreted in terms of different relative energy shifts of the emitting $^3$**LC** state and mixing $^{1,3}$**MLCT** states for different environments of the complex. Such relative shifts can, for example, be caused by charge density shifts due to polar groups of the host molecules, which in general may have a different effect on **MLCT** states as on **LC** states.

The variation of the MLCT character seems to be reflected also in the decay times of phosphorescence. By site-selective decay time measurements under variation of

temperature, the individual decay times of the triplet substates **I**, **II**, and **III** could be determined for two spectroscopic sites of $Ir(btp)_2(acac)$ in $CH_2Cl_2$ (sites **E** and **H**). For site **H**, decay times of $\tau_I$ =150 µs, $\tau_{II}$ =58 µs, and $\tau_{III}$ =1.5 µs were found, while for site **E**, distinctly different values of $\tau_I$ =62 µs, $\tau_{II}$ =19 µs, and $\tau_{III}$ ≈3 µs were determined. Especially the $\tau_{III}$ value is shorter for the site which also exhibits a higher ZFS and MLCT character. This fits to the general trend saying that tiplet emitters with a higher MLCT character of the $\mathbf{T_1}$ state can exhibit higher radiative rates (see e.g. Ref. [120]). The results indicate that this trend applies not only to *different complexes*, but also to *one complex*, for which the MLCT character varies with the matrix environment. A variation of the emission decay time, especially of the radiative decay time, with the specific matrix environment of a complex also represents a reasonable explanation for the non-monoexponential decay behavior, which is often observed for Ir(III)-complexes and also for $Ir(btp)_2(acac)$ after UV-excitation at low temperature. The variations, in particular, of the comparatively long decay times $\tau_I$ and $\tau_{II}$, however, may as well be due to contributions of radiationless deactivation processes, which cannot be fully excluded even in the temperature range below about 5 K.

The spin-lattice relaxation (SLR) from substate **II** to substate **I** was also investigated. At low temperatures (e.g. up to 2.0 K for site **E**) the *direct* process of SLR dominates, while at higher temperatures, the *Orbach* process takes effect and is mainly responsible for the relaxation. Interestingly, the relaxation time $\tau_{II-I}^{SLR}$ at 1.5 K, which is due to the *direct* process, is significantly shorter for site **E** (≈4 µs) than for site **H** (≈22 µs). This explains, for example, why in the emission spectra of site **E** at 1.5 K, the emission mainly originates from substate **I**, while in the spectra of site **H** at this temperature, the emission from substate **II** dominates. The differences of the SLR times in the two sites can be explained by a possible anisotropy of the sound velocity in $CH_2Cl_2$ or/and differences of electron-phonon coupling. SLR from triplet substate **III** to the substates **II** and **I** was found to be very effective at any temperature.

Well-resolved emission spectra of $Ir(btp)_2(acac)$ in $CH_2Cl_2$ in the region of the vibrational satellites were also presented and were recorded by selective excitation of a single site (site **H**) at different low temperatures. By an algebraic calculation, it was possible to separate the emissions from the substates **I**, **II**, and **III**, which are otherwise (partly) superimposed. Therefore, important information on the radiative decay paths of the three triplet substates was obtained. The transition from the lowest substate **I** to the $\mathbf{S_0}$ ground state is largely forbidden at the electronic origin. Deactivation of this state is to a large extent induced by Herzberg-Teller vibronic

coupling, which is manifested in the occurrence of false origins. On the other hand, the emission spectra from the two higher lying triplet substates **II** and **III** exhibit a different vibrational satellite structure, which is probably due to Franck-Condon activity. This satellites structure is the same for the emissions from substate **II** and substate **III**. The described observations are independently confirmed by investigations under magnetic field and by time-resolved experiments.

Deactivation of substate **I** due to vibronic activity leads to incorrect interpretations, if the electronic allowednesses of the transitions from the three triplet substates to the ground state are assessed and compared on the basis of the respective emission decay times. This is often not accounted for in discussions of the emission decay times of organo-transition metal complexes. In fact, when neglecting deactivation through vibronic pathways, for site **H** of $Ir(btp)_2(acac)$ in $CH_2Cl_2$, the emission decay time of substate **I** can be estimated to ≈2.3 ms. This estimation reveals that the purely electronic allowedness of the transition $\mathbf{I} \rightarrow \mathbf{0}$ is by a factor of ≈40 smaller than the one of transition $\mathbf{II} \rightarrow \mathbf{0}$, and by a factor of even ≈1500 smaller than the one of transition $\mathbf{III} \rightarrow \mathbf{0}$.

In the spectra, a large number of vibrational satellites of metal-ligand character is observed. This is consistent with a significant MLCT admixture to the $\mathbf{T_1}$ state. Further, comparatively small intensities of Franck-Condon satellites relative to the corresponding electronic origins or to false origins, respectively (small Huang-Rhys parameters S<0.08), indicate only small geometry rearrangements upon the transitions from the electronically excited triplet substates to the ground state. Therefore, the width of the emission spectra, i.e. the color purity of the emission, is only marginally influenced by higher members of progressions, but is dominated by fundamentals.

Unexpectedly, the host environment of the complex seems to exert a significant influence on the vibrational satellite structure of the emission. For the two sites **H** and **I** in $CH_2Cl_2$, vibrational energies and, especially, intensities of vibrational satellites are in part significantly different. This is tentatively ascribed to different force constants, Franck-Condon factors, and/or vibronic couplings.

The $CH_2Cl_2$ matrix, in which most of the investigations on $Ir(btp)_2(acac)$ were carried out, represents a poly-crystalline host. Therefore, it was not clear, in how far the results obtained for $Ir(btp)_2(acac)$ in $CH_2Cl_2$ are also relevant for the complexes behavior in amorphous host environments as applied in OLEDs, in particular, since spectroscopic parameters such as the ZFS were found to significantly depend on the host. Consequently, $Ir(btp)_2(acac)$ was also investigated in the OLED relevant

amorphous host materials PVB, PFO, and PVK.[33] For this purpose, persistent spectral hole-burning (PSHB) and luminescence line narrowing were tested with regard to their applicability to organo-transition metal complexes in amorphous matrices. The study showed on the example of $Ir(btp)_2(acac)$ that these methods provide useful tools to gain insight into the splitting structure of the emitting triplet state $\mathbf{T_1}$ into substates. Due to the triplet nature of the lowest excited state, hole-burning with a narrow-band laser in the energy region of the inhomogeneously broadened electronic origin transition leads to the formation not only of a resonant hole, but also of different types of (electronic) satellite holes. The satellite holes could only be detected by application of a newly developed synchronous scan detection technique. An analysis of hole separations gave direct information on the ZFS of the $\mathbf{T_1}$ state into substates. The obtained results are in line with the findings of the previous investigations in Shpol'skii and Shpol'skii-like hosts. For $Ir(btp)_2(acac)$ in all three matrices PVB, PFO, and PVK, mean values of $18\,cm^{-1}$ were found for the splitting between the substates **II** and **III**. Information on the weakly absorbing substate **I** could not be obtained by PSHB.

Interestingly, PSHB allowed not only to assess the mean value of ZFS, but also the distribution of ZFS values. This distribution could be evaluated on the basis of the widths of specific satellite holes. Among the different matrices studied, PVK induces the strongest inhomogeneous distribution of the splitting between the substates **II** and **III**. The width of the distribution in PVK amounts to $15\,cm^{-1}$ and, thus, is largely consistent with the spread of $\Delta E_{\mathrm{III-II}}$ found in $CH_2Cl_2$ from $12\,cm^{-1}$ to $24\,cm^{-1}$. In PVB and PFO, the distribution widths are smaller and amount to only $6\,cm^{-1}$ and $7\,cm^{-1}$, respectively. A thorough explanation of this behavior requires information on the detailed interactions of $Ir(btp)_2(acac)$ with the host environments. Such information may be obtained by future PSHB experiments under application of electrical fields. Nevertheless, the results show that the important MLCT character in the $\mathbf{T_1}$ state of $Ir(btp)_2(acac)$ molecules obviously varies significantly also in typical OLED matrices. Further, the variation of ZFS values in amorphous matrices seems to be one of the reasons of why luminescence line narrowing is difficult to achieve for complexes with a strong MLCT character of the emitting triplet state.

[33] Chemical notations and structures of the three polymers are given in Sect. 7.1 and Fig. 47, respectively.

# Conclusion

The frequently used red OLED emitter $Ir(btp)_2(acac)$ could be classified to emit from a ligand-centered state with significant admixtures of metal-to-ligand charge transfer character. This finding is not only valid for the complex doped into polycrystalline hosts such as $CH_2Cl_2$ or n-octane, but could also be verified for the complex doped into amorphous matrices such as the polymers PVB, PFO, and PVK. The MLCT character manifests itself in several respects in the photophysical behavior of the complex. In particular, it is reflected in the emission decay times and in the vibrational satellite structures of the emission, respectively. The results fit to the general trend that phosphorescent organo-transition metal emitters being successfully applied in OLEDs exhibit a high MLCT character. In this context it should be noted that all good OLED emitters investigated so far feature a zero-field splitting of at least about $10\,cm^{-1}$. Therefore it is suggested that – as a rule of thumb – organo-transition metal complexes should feature a ZFS of their emitting triplet of at least about $10\,cm^{-1}$ to be applicable in OLEDs. However it is remarked that this criterion is regarded to be necessary, but certainly is not sufficient.

For $Ir(btp)_2(acac)$, however, a serious variation of ZFS values and thus of the MLCT character, depending on the specific host environment, i.e. on the specific spectroscopic site or on the host material, could be demonstrated. Since molecules of the distribution with less MLCT character may exhibit poorer emission properties such as a longer emission decay time or/and a lower quantum efficiency than the average, this may represent a limitation to the complexes' overall emission properties in OLEDs. Especially those types of $Ir(btp)_2(acac)$ molecules may be concerned, which feature only moderate ZFS values near the estimated limit of $10\,cm^{-1}$. An optimization of emitter-dopant systems for OLEDs therefore has to account for this circumstance.

Carrying out a comparison of $Ir(btp)_2(acac)$ with other representatives of the group of organo-transition metal complexes regarding the ZFS (compare Table 11), an interesting detail strikes the attention. Among complexes with a high ZFS/MLCT character, quasi-octahedral complexes seem to be represented in a significantly larger number than quasi-planar complexes. Especially, the largest ZFS of a quasi-octahedral complex is significantly larger than the largest ZFS of a quasi-planar complex. In fact, the most frequently used complexes applied as emitters in OLEDs are Ir-complexes, e.g. $Ir(ppy)_3$, $Ir(btp)_2(acac)$, $Ir(piq)_3$, and FIrpic.[34] An

[34]For the structures, see Sect. 1, Fig. 8.

approach towards an explanation of this phenomenon may be given by the theoretical considerations presented in Chapter 2. In these considerations, differences between both types of complexes are traced back to the ligand-field splitting pattern of the metal d-orbitals. Due to peculiarities of the specific ligand-field splitting of quasi-octahedral complexes (energy proximity of the highest occupied d-orbitals), spin-orbit coupling may be especially effective in these compounds. In the future, further investigations on organo-transition metal complexes will have to be carried out to bring about the desired clarification.

# Appendix

## A Intensity ratios

The intensity $I_i(t)$ of the emission from a specific triplet substate $i$ at one moment $t$ can be calculated, if the radiative rate $k_i^r$ and the population density $n_i(t)$ of state $i$ are known.

$$I_i(t) = k_i^r n_i(t) \tag{51}$$

The time dependence of the population density $k_i^r$, however, is not in any case given by a simple exponential law as might be expected. Especially for site **H** of $Ir(btp)_2$-(acac) doped into $CH_2Cl_2$, the spin-lattice relaxation from triplet substate **II** to substate **I** is comparatively slow at temperatures below about 5 K. The characteristic time $\tau_{\mathrm{II-I}}^{\mathrm{SLR}}$ is of the same order of magnitude as the deactivation of state **II** to the ground state. Therefore, when emitting, the two substates are not in thermal equilibrium for a significant time range of the emission decay. Hence, to be able to calculate the intensity ratio $\frac{I_{\mathrm{II}}}{I_{\mathrm{I}}}$ of the time-integrated emissions from the substates **II** and **I** (see Sect. 6.4, Eq. 46), not only the relaxation to the ground state is to be considered, but the relaxation dynamics between these states is to be accounted for as well. The dynamics of the system can be described by the following differential equations:

$$\frac{\mathrm{d}n_{\mathrm{II}}}{\mathrm{d}t} = -\left(k_{\mathrm{II}} + k_{21}\right) \cdot n_{\mathrm{II}} + k_{12} \cdot n_{\mathrm{I}} \tag{52}$$

$$\frac{\mathrm{d}n_{\mathrm{I}}}{\mathrm{d}t} = -\left(k_{\mathrm{I}} + k_{12}\right) \cdot n_{\mathrm{I}} + k_{21} \cdot n_{\mathrm{II}} \tag{53}$$

Therein, $n_{\mathrm{I}}$ and $n_{\mathrm{II}}$ are the population densities of the substates **I** and **II**, respectively, at time $t$. $k_{\mathrm{I}}$ and $k_{\mathrm{II}}$ denote the deactivation rates to the electronic ground state. $k_{21}$ is the net rate of the relaxation **II** $\rightarrow$ **I** and $k_{12}$ the one of relaxation **I** $\rightarrow$ **II**. Under the approximation $k_{\mathrm{II-I}}^{\mathrm{SLR}} = k_{21} + k_{12} \gg k_{\mathrm{II}}, k_{\mathrm{I}}$ and by use of the condition $k_{12} = k_{21}\, \mathrm{e}^{-\Delta E_{\mathrm{II-I}}/k_{\mathrm{B}}T}$, the explicit time-dependence of the population densities $n_{\mathrm{I}}$ and

$n_{\mathrm{II}}$ is given by [139, 172]

$$n_{\mathrm{II}}(t) = \frac{n_{\mathrm{I}}^0 + n_{\mathrm{II}}^0}{1 + \mathrm{e}^{\Delta E_{\mathrm{II-I}}/k_{\mathrm{B}}T}} \cdot \mathrm{e}^{-k_{\mathrm{therm}}t} + \frac{n_{\mathrm{II}}^0 - n_{\mathrm{I}}^0\,\mathrm{e}^{-\Delta E_{\mathrm{II-I}}/k_{\mathrm{B}}T}}{1 + \mathrm{e}^{-\Delta E_{\mathrm{II-I}}/k_{\mathrm{B}}T}} \cdot \mathrm{e}^{-k_{\mathrm{II-I}}^{\mathrm{SLR}}t} \tag{54}$$

$$n_{\mathrm{I}}(t) = \frac{n_{\mathrm{I}}^0 + n_{\mathrm{II}}^0}{1 + \mathrm{e}^{-\Delta E_{\mathrm{II-I}}/k_{\mathrm{B}}T}} \cdot \mathrm{e}^{-k_{\mathrm{therm}}t} - \frac{n_{\mathrm{II}}^0 - n_{\mathrm{I}}^0\,\mathrm{e}^{-\Delta E_{\mathrm{II-I}}/k_{\mathrm{B}}T}}{1 + \mathrm{e}^{-\Delta E_{\mathrm{II-I}}/k_{\mathrm{B}}T}} \cdot \mathrm{e}^{-k_{\mathrm{II-I}}^{\mathrm{SLR}}t} \tag{55}$$

$\Delta E_{\mathrm{II-I}}$ is the energy separation of the substates **I** and **II**, and $k_{\mathrm{therm}}$ corresponds to the thermalized decay time $\tau_{\mathrm{therm}}$, which is given by (compare Eq. 17)

$$k_{\mathrm{therm}} = k_{\mathrm{I}} + k_{\mathrm{II}}\,\mathrm{e}^{-\Delta E_{\mathrm{II-I}}/k_{\mathrm{B}}T} \quad , \tag{56}$$

With the Equations 54 and 55, the intensity ratio $I_{\mathrm{II}}/I_{\mathrm{I}}$ is obtained by integration of Eq. 51 over the whole time of the emission.[139, 172]

$$\frac{I_{\mathrm{II}}}{I_{\mathrm{I}}} = \frac{\int_0^\infty I_{\mathrm{II}}(t)\mathrm{d}t}{\int_0^\infty I_{\mathrm{I}}(t)\mathrm{d}t} = \frac{k_{\mathrm{II}}^r}{k_{\mathrm{I}}^r}\left[e^{-\frac{\Delta E_{\mathrm{II-I}}}{k_{\mathrm{B}}T}} + \frac{\left(\frac{n_{\mathrm{II}}^0}{n_{\mathrm{I}}^0} - e^{-\frac{\Delta E_{\mathrm{II-I}}}{k_{\mathrm{B}}T}}\right)\left(k_{\mathrm{I}} + k_{\mathrm{II}}\,e^{-\frac{\Delta E_{\mathrm{II-I}}}{k_{\mathrm{B}}T}}\right)}{\left(\frac{n_{\mathrm{II}}^0}{n_{\mathrm{I}}^0} + 1\right) k_{\mathrm{II-I}}^{\mathrm{SLR}}(\mathrm{T})}\right] \tag{57}$$

# B Vibrational energies

**Table 5** Energies of vibrational modes involved in the emission of $Ir(btp)_2(acac)$ in different sites in $CH_2Cl_2$/matrices – in part with assignments to the specific $\mathbf{T_1}$ substates. Reliable assignments were only possible for site **H** in $CH_2Cl_2$ (relative uncertainty $\pm 1\,cm^{-1}$) and, with less accuracy, also for site **I** (uncertainty $\pm 2\,cm^{-1}$). For these two sites, also tentative assignments to Franck-Condon (FC) and Herzberg-Teller activity (HT), according to the discussion in Sect. 6.5, are given. For the *n*-octane matrix and the single crystal, only the vibrational energies are given (uncertainty $\pm 3\,cm^{-1}$), since reasonable assignments were not possible on the basis of the available data. Progressions and combinations were safely identified only for site **H** in $CH_2Cl_2$. Therefore the given values are related only to this site. Energies of IR active modes (determined in KBr) are also given.

| $CH_2Cl_2$ | | | | Octane | Crystal | IR | Assignment |
|---|---|---|---|---|---|---|---|
| Site H | | Site I | | Site A | | | |
| $\mathbf{III/II} \rightarrow \mathbf{0}$ | $\mathbf{I} \rightarrow \mathbf{0}$ | $\mathbf{III/II} \rightarrow \mathbf{0}$ | $\mathbf{I} \rightarrow \mathbf{0}$ | | | | |
| - | - | - | 166 | - | - | | HT |
| 182 | - | 184 | - | - | - | | FC |
| 187 | 187 | 190 | - | - | - | | FC/HT[a,b] |
| - | 198 | - | 198 | 199 | 199 | | HT |
| 200 | - | - | - | 199 | 199 | | FC |
| 232 | - | 234 | - | 232 | 234 | | FC |
| 258 | 258 | 261 | - | 258 | 256[d] | | FC/HT[b] |
| - | - | - | 250 | - | - | | HT |
| 288 | 288 | 288 | 288 | - | 288 | | FC[c] |
| - | 299 | - | 299 | 299 | 295[d] | | HT[a] |
| 312 | - | 310 | - | 312 | 315[d] | | FC |
| 321 | - | 319 | 318 | - | - | | FC/HT[b] |
| 338 | 338 | 339 | - | 335 | 336 | | FC/HT[a,b] |
| - | - | - | 329 | - | - | | HT |
| 362 | - | 364 | - | 362 | 362 | | FC |
| - | 375 | - | 370[d] | - | - | | HT |
| 439 | 439 | 443 | - | 436[d] | 441 | [e] | FC |

*continued on the next page*

| $CH_2Cl_2$ | | | | Octane | Crystal | IR | Assignment |
|---|---|---|---|---|---|---|---|
| Site H | | Site I | | Site A | | | |
| III/II → 0 | I → 0 | III/II → 0 | I → 0 | | | | |
| 450 | 450 | - | 450 | - | - | - | FC |
| 457 | 457 | 462 | 461 | - | - | - | FC |
| - | 475 | - | - | - | - | 476 | HT[a] |
| 500 | 500 | 502 | 504 | 497 | 502 | 504 | FC/HT[b] |
| 545 | 545 | - | 542 | 542 | 543 | 538[d] | HT[a] |
| 572 | - | 574 | - | - | - | - | 2 x 288 |
| - | - | - | 573 | - | - | - | HT |
| 598 | - | 600 | | 599 | 601 | 599 | FC[f] |
| - | 602 | - | 600 | 599 | 601 | 603 | HT[g] |
| - | - | - | 615 | - | - | - | HT |
| - | 622 | - | - | - | - | 624 | HT |
| 633 | 633 | 633 | 633 | - | - | 630 | FC/HT[a,b] |
| 647 | 646 | 646 | 646 | - | - | 644 | FC/HT[b] |
| 683 | - | 685 | - | 685 | 683 | - | FC |
| 710 | - | - | - | - | 710 | 710 | FC |
| - | 755 | - | 757 | 754[d] | 760 | 758 | HT[a] |
| - | 765 | - | 765 | 766 | - | 768 | HT |
| 777 | - | 780 | 776 | 776 | 780 | - | FC/HT[b] |
| - | 830 | - | 829 | - | - | 825[d] | HT |
| 925 | 925 | 926 | - | 926 | 927 | - | FC |
| - | - | - | 933 | - | - | 932 | HT |
| - | 956 | - | - | - | - | 956 | HT |
| - | 982 | - | 984 | 984 | - | - | HT |
| 993 | 993 | 997[d] | 993 | 993 | 993 | 994 | FC/HT[b] |
| 1003 | 1003 | 1005 | 1003 | 1003 | 1002 | - | FC |
| 1042 | 1041 | 1042 | 1041 | 1041 | 1041 | - | FC/HT[b] |
| 1120 | - | 1123 | - | 1122 | - | 1117[d] | FC |
| 1155 | - | 1155 | - | 1155 | 1164[d] | 1158 | FC |
| 1270[d] | - | 1275 | - | 1275 | 1279[d] | 1265[d] | FC |
| 1301 | - | 1303 | - | 1305[d] | 1307[d] | - | FC |
| 1312 | - | 1314 | - | 1313 | 1312 | - | FC |
| 1326 | - | 1326 | - | 1325 | 1328 | - | FC |
| 1398 | 1398 | - | - | - | - | 1398 | FC[c] |

*continued on the next page*

| $CH_2Cl_2$ | | | | Octane | Crystal | IR | Assignment |
|---|---|---|---|---|---|---|---|
| Site H | | Site I | | Site A | | | |
| **III/II → 0** | **I → 0** | **III/II → 0** | **I → 0** | | | | |
| - | - | 1406 | - | 1406 | 1406 | - | FC |
| 1462 | - | - | - | - | - | - | FC |
| - | - | 1469 | - | 1470 | 1470 | - | FC |
| 1470 | - | - | - | - | - | 1473 | FC |
| - | - | 1479 | - | 1481 | - | - | FC |
| 1474 | - | - | - | - | 1476 | 1473 | FC[c] |
| - | - | 1483 | - | 1481 | - | - | FC |
| 1553[d] | - | 1558 | - | 1557 | - | 1555 | FC |
| - | 1585 | - | - | - | - | - | 187+1398 (HT+FC) |
| 1630 | - | - | - | - | - | - | 232+1398 (FC+FC) |
| 1685 | - | - | - | - | - | - | 288+1398 (FC+FC) |
| - | 1697 | - | - | - | - | - | 299+1398 (HT+FC) |
| - | 1661 | - | - | - | - | - | 187+1474 (HT+FC) |
| - | 1736 | - | - | - | - | - | 338+1398 (HT+FC) |
| 1762 | - | - | - | - | - | - | 288+1474 (FC+FC) |
| - | 1773 | - | - | - | - | - | 299+1474 (HT+FC) |
| - | 1812 | - | - | - | - | - | 338+1474 (HT+FC) |
| 1855 | - | - | - | - | - | - | 457+1398 (FC+FC) |
| - | 1873 | - | - | - | - | - | 475+1398 (HT+FC) |
| 1898 | - | - | - | - | - | - | 500+1398 (FC+FC) |
| - | 1943 | - | - | - | - | - | 545+1398 (HT+FC) |
| - | 1974 | - | - | - | - | - | 500+1474 (HT+FC) |
| - | 2019 | - | - | - | - | - | 545+1474 (HT+FC) |
| 2081 | - | - | - | - | - | - | 683+1398 (FC+FC) |
| - | 2107 | - | - | - | - | - | 633+1474 (HT+FC) |
| - | 2153 | - | - | - | - | - | 755+1398 (HT+FC) |
| - | 2229 | - | - | - | - | - | 755+1474 (HT+FC) |
| 2796 | - | - | - | - | - | - | 2x1398 |
| 2860 | - | - | - | - | - | - | 1398+1462(FC+FC) |
| 2872 | - | - | - | - | - | - | 1398+1474 (FC+FC) |
| 2948 | - | - | - | - | - | - | 2x1474 |

[a] Herzberg-Teller (HT) active mode, for which combinations occur.

[b] Mode, which is tentatively assigned to be HT *and* FC active.

[c] Franck-Condon (FC) active modes, for which higher members of progressions are observed.
[d] A correspondence to modes of similar energy in the other sites/matrices is not clear, since the energy differences are large.
[e] Energies of IR active modes are only available for $\geq$450 $cm^{-1}$.
[f] Energies lower than $\approx$600 $cm^{-1}$ largely repesent modes of metal-ligand vibrational character.
[g] Modes of energies larger than $\approx$600 $cm^{-1}$ are assumed to be ligand-centered.

# C Emission spectra of $Ir(btp)_2(acac)$ in $CH_2Cl_2$ (site I) – Vibrational satellite structure

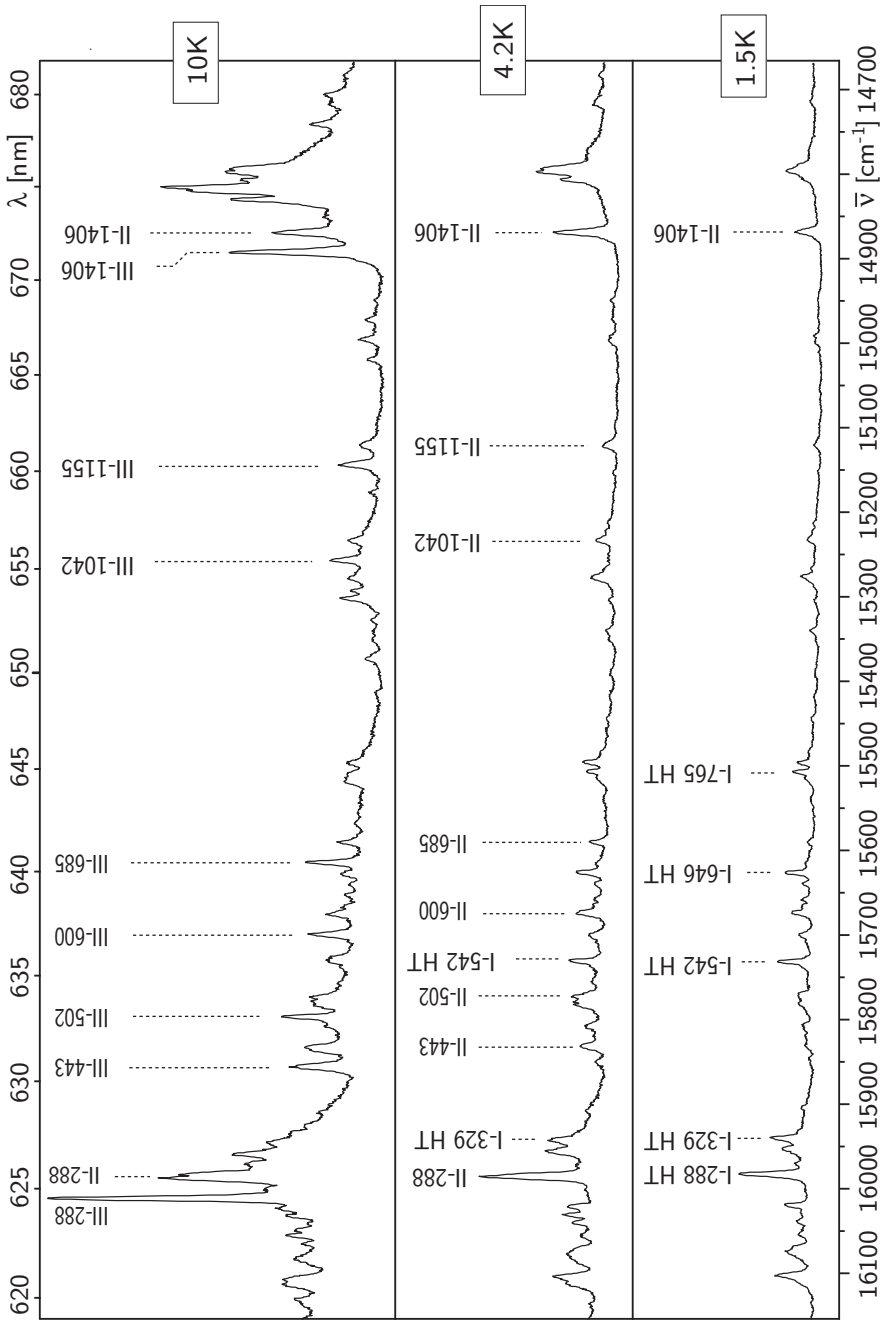


**Figure 55** Emission of $Ir(btp)_2(acac)$ in $CH_2Cl_2$ (site **I**) in the region of the vibrational satellites, recorded at 1.5 K, 4.2 K, and 10 K, respectively. For excitation, the energy of the electronic origin of the $\mathbf{0} \rightarrow \mathbf{III}$ transition ($\bar{\nu}_{exc} = 16247\,cm^{-1}$) was chosen. The vibrational satellite lines are, in part, labeled according to the respective origins $I_{0-0}$, $II_{0-0}$, and $III_{0-0}$, and tentatively assigned with respect to the Herzberg-Teller (HT) and Franck-Condon (FC) activity. A detailed list of vibrational energies and tentative assignments of the corresponding modes is given in Table 5 of Appendix B.

# References


[1] Medina-Castillo, A. L.; Fernandez-Sanchez, J. F.; Klein, C.; Nazeeruddin, M. K.; Segura-Carretero, A.; Fernandez-Gutierrez, A.; Graetzel, M.; Spichiger-Keller, U. E. *Analyst (Cambridge, United Kingdom)* **2007,** *132*, 929.

[2] Drew, S. M.; Janzen, D. E.; Buss, C. E.; MacEwan, D. I.; Dublin, K. M.; Mann, K. R. *Journal of the American Chemical Society* **2001,** *123*, 8414.

[3] Buss, C. E.; Mann, K. R. *Journal of the American Chemical Society* **2002,** *124*, 1031.

[4] Daws, C. A.; Exstrom, C. L.; Sowa, John R., J.; Mann, K. R. *Chemistry of Materials* **1997,** *9*, 363.

[5] Choudhury, B.; Shinar, R.; Shinar, J. *Journal of Applied Physics* **2004,** *96*, 2949.

[6] Holmlin, R. E.; Barton, J. K. *Inorganic Chemistry* **1995,** *34*, 7.

[7] Heumann, A.; Jens, K.-J.; Reglier, M. *Progress in Inorganic Chemistry* **1994,** *42*, 483.

[8] Kuninobu, Y.; Kawata, A.; Takai, K. *Journal of the American Chemical Society* **2006,** *128*, 11368.

[9] Kuninobu, Y.; Nishina, Y.; Nakagawa, C.; Takai, K. *Journal of the American Chemical Society* **2006,** *128*, 12376.

[10] Beletskaya, I.; Moberg, C. *Chemical Reviews (Washington, DC, United States)* **2006,** *106*, 2320.

[11] Gao, R.; Hernandez, B.; Hunt, P. L.; Selke, M.; Djurovich, P. I.; Murphy, D. L.; Thompson, M. E. *Abstracts of Papers, 229th ACS National Meeting, San Diego, CA, United States, March 13-17, **2005**, INOR-931* .

[12] Nazeeruddin, M. K.; Pechy, P.; Renouard, T.; Zakeeruddin, S. M.; Humphry-Baker, R.; Comte, P.; Liska, P.; Cevey, L.; Costa, E.; Shklover, V.; Spiccia, L.; Deacon, G. B.; Bignozzi, C. A.; Gratzel, M. *Journal of the American Chemical Society* **2001,** *123,* 1613.

[13] Mayo, E. I.; Kilsa, K.; Tirrell, T.; Djurovich, P. I.; Tamayo, A.; Thompson, M. E.; Lewis, N. S.; Gray, H. B. *Photochemical & Photobiological Sciences* **2006,** *5,* 871.

[14] Renouard, T.; Fallahpour, R. A.; Nazeeruddin, M. K.; Humphry-Baker, R.; Gorelsky, S. I.; Lever, A. B. P.; Graetzel, M. *Inorganic Chemistry* **2002,** *41,* 367.

[15] Wang, P.; Klein, C.; Humphry-Baker, R.; Zakeeruddin, S. M.; Gratzel, M. *Applied Physics Letters* **2005,** *86,* 123508/1.

[16] Graetzel, M.; Kalyanasundaram, K. *Catalysis by Metal Complexes* **1993,** *14,* 247.

[17] Lee, C.; Yum, J.-H.; Choi, H.; Kang, S. O.; Ko, J.; Humphry-Baker, R.; Graetzel, M.; Nazeeruddin, M. K. *Inorganic Chemistry (Washington, DC, United States)* ACS ASAP.

[18] Ege, D.; Becker, W. G.; Bard, A. J. *Analytical Chemistry* **1984,** *56,* 2413.

[19] Sasso, M. G.; Quina, F. H.; Bechara, E. J. H. *Analytical Biochemistry* **1986,** *156,* 239.

[20] Gorner, H.; Tossi, A. B.; Stradowski, C.; Schulte-Frohlinde, D. *J Photochem Photobiol B* **1988,** *2,* 67.

[21] Gallhuber, E.; Hensler, G.; Yersin, H. *Journal of the American Chemical Society* **1987,** *109,* 4818.

[22] Humbs, W.; Strasser, J.; Yersin, H. *Journal of Luminescence* **1997,** *72-74,* 677.

[23] Lee, K. W.; Slinker, J. D.; Gorodetsky, A. A.; Flores-Torres, S.; Abruna, H. D.; Houston, P. L.; Malliaras, G. G. *Physical Chemistry Chemical Physics* **2003,** *5,* 2706.

[24] Yersin, H., Ed.; *Highly Efficient OLEDs with Phosphorecent Materials;* Wiley-VCH, 2007.

[25] Müllen, K.; Scherf, U., Eds.; *Organic Light-Emitting Devices - Synthesis, Properties, and Applications;* Wiley-VCH: Weinheim, 2006.

[26] Shinar, J., Ed.; *Organic Light-Emitting Devices;* Springer, AIP Press: Berlin, 2004.

[27] Kafafi, Z. H., Ed.; *Organic Electroluminescence;* Taylor and Francis: Boca Raton, 2005.

[28] Kalinowski, J., Ed.; *Organic Light-Emitting Diodes: Principles, Characteristics and Processes;* Marcel Dekker: New York, 2005.

[29] Li, Z.; Meng, H., Eds.; *Organic Light-Emitting Materials and Devices;* CRC/Taylor & Francis: Boca Raton, 2007.

[30] Pope, M.; Kallmann, H. P.; Magnante, P. *Journal of Chemical Physics* **1963,** *38,* 2042.

[31] Tang, C. W.; VanSlyke, S. A. *Applied Physics Letters* **1987,** *51,* 913.

[32] U.S. Department of Energy, *Energy Savings Potential of Solid State Lighting in General Illumination Applications, Final Report;* Navigant Consulting Inc.: Washington, DC, 2006.

[33] D'Andrade, B.; Alleyne, B.; Hack, M.; Hewitt, R.; Brown, J. J. *Proceedings of SPIE-The International Society for Optical Engineering* **2006,** *6333,* 63330N/1.

[34] Tanaka, D.; Sasabe, H.; Li, Y.-J.; Su, S.-J.; Takeda, T.; Kido, J. *Japanese Journal of Applied Physics, Part 2: Letters & Express Letters* **2007,** *46,* L10.

[35] Watanabe, S.; Ide, N.; Kido, J. *Japanese Journal of Applied Physics, Part 1: Regular Papers, Brief Communications & Review Papers* **2007,** *46,* 1186.

[36] Birnstock, J.; Lux, A.; Amman, M.; Wellmann, P.; Hofmann, M.; Stübinger, T. *SID 06 DIGEST* **2006,** 1866.

[37] He, G.; Walzer, K.; Pfeiffer, M. P.; Leo, K.; Pudzich, R.; Salbeck, J. *Proceedings of SPIE-The International Society for Optical Engineering* **2004,** *5519,* 42.

[38] Ide, N.; Komoda, T.; Kido, J. *Proceedings of SPIE-The International Society for Optical Engineering* **2006,** *6333,* 63330M/1.

[39] Tanaka, D.; Agata, Y.; Takeda, T.; Watanabe, S.; Kido, J. *Japanese Journal of Applied Physics, Part 2: Letters & Express Letters* **2007,** *46,* L117.

[40] Adachi, C.; Baldo, M. A.; Forrest, S. R.; Lamansky, S.; Thompson, M. E.; Kwong, R. C. *Applied Physics Letters* **2001,** *78,* 1622.

[41] Adachi, C.; Baldo, M. A.; Thompson, M. E.; Forrest, S. R. *Journal of Applied Physics* **2001,** *90,* 5048.

[42] Chen, F.-C.; Yang, Y.; Thompson, M. E.; Kido, J. *Applied Physics Letters* **2002,** *80,* 2308.

[43] Meerheim, R.; Walzer, K.; Pfeiffer, M.; Leo, K. *Applied Physics Letters* **2006,** *89,* 061111/1.

[44] Yang, X. H.; Neher, D. *Applied Physics Letters* **2004,** *84,* 2476.

[45] Yersin, H.; Donges, D. *Topics in Current Chemistry* **2001,** *214,* 81.

[46] Yersin, H.; Humbs, W.; Strasser, J. *Topics in Current Chemistry* **1997,** *191,* 153.

[47] Yersin, H.; Vogler, A., Eds.; *Photochemistry and Photophysics of Coordination Compounds;* Springer Verlag: Berlin, 1987.

[48] Finkenzeller, W. J.; Yersin, H. *Chemical Physics Letters* **2003,** *377,* 299.

[49] Marchetti, A. P.; Deaton, J. C.; Young, R. H. *Journal of Physical Chemistry A* **2006,** *110,* 9828.

[50] Namdas, E. B.; Ruseckas, A.; Samuel, I. D. W.; Lo, S.-C.; Burn, P. L. *Journal of Physical Chemistry B* **2004,** *108,* 1570.

[51] Hay, P. J. *Journal of Physical Chemistry A* **2002,** *106,* 1634.

[52] Nozaki, K. *Journal of the Chinese Chemical Society* **2006,** *53,* 101.

[53] Schlaf, R.; Parkinson, B. A.; Lee, P. A.; Nebesny, K. W.; Jabbour, G.; Kippelen, B.; Peyghambarian, N.; Armstrong., N. A. *J. Appl. Phys.* **1998,** *84,* 6729.

[54] Mori, T.; Fujikawa, H.; Tokito, S.; Taga, Y. *Appl. Phys. Lett.* **1998,** *73,* 2763.

[55] Thompson, M. private communication.

[56] Yang, X.; Neher, D.; Hertel, D.; Daeubler, T. K. *Advanced Materials* **2004,** *16,* 161.

[57] He, G.; Pfeiffer, M.; Leo, K.; Hofmann, M.; Birnstock, J.; Pudzich, R.; Salbeck, J. *Applied Physics Letters* **2004,** *85,* 3911.

[58] Lu, H.-T.; Tsou, C.-C.; Yokoyama, M. *Journal of Crystal Growth* **2005,** *277,* 388.

[59] Park, J. H.; Oh, S. S.; Kim, S. W.; Choi, E. H.; Hong, B. H.; Seo, Y. H.; Cho, G. S.; Park, B.; Lim, J.; Yoon, S. C.; Lee, C. *Applied Physics Letters* **2007,** *90,* 153508/1.

[60] Greenham, N. C.; Friend, R. H.; Bradley, D. D. C. *Advanced Materials* **1994,** *6,* 491.

[61] Shiga, T.; Fujikawa, H.; Taga, Y. *Journal of Applied Physics* **2003,** *93,* 19.

[62] Mulder, C. L.; Celebi, K.; Milaninia, K. M.; Baldo, M. A. *Applied Physics Letters* **2007,** *90,* 211109/1.

[63] Tsutsui, T.; Yahiro, M.; Yokogawa, H.; Kawano, K.; Yokoyama, M. *Advanced Materials* **2001,** *13,* 1149.

[64] Lupton, J. M.; Matterson, B. J.; Samuel, I. D. W.; Jory, M. J.; Barnes, W. L. *Applied Physics Letters* **2000,** *77,* 3340.

[65] Matterson, B. J.; Lupton, J. M.; Safonov, A. F.; Salt, M. G.; Barnes, W. L.; Samuel, I. D. W. *Advanced Materials* **2001,** *13,* 123.

[66] Safonov, A. N.; Jory, M.; Matterson, B. J.; Lupton, J. M.; Salt, M. G.; Wasey, J. A. E.; Barnes, W. L.; Samuel, I. D. W. *Synthetic Metals* **2001,** *116,* 145.

[67] Huang, Q.; Walzer, K.; Pfeiffer, M.; Leo, K.; Hofmann, M.; Stubinger, T. *Journal of Applied Physics* **2006,** *100,* 064507/1.

[68] Sun, Y.; Forrest, S. R. *Journal of Applied Physics* **2006,** *100,* 073106/1.

[69] Walzer, K.; Maennig, B.; Pfeiffer, M.; Leo, K. *Chemical Reviews* **2007,** *107,* 1233.

[70] Baldo, M. A.; Forrest, S. R. *Physical Review B: Condensed Matter and Materials Physics* **2000,** *62,* 10958.

[71] Baldo, M. A.; Adachi, C.; Forrest, S. R. *Physical Review B: Condensed Matter and Materials Physics* **2000,** *62,* 10967.

[72] Staroske, W.; Pfeiffer, M.; Leo, K.; Hoffmann, M. *Physical Review Letters* **2007,** *98,* 197402/1.

[73] Blochwitz, J. *Organic light-emitting diodes with doped charge transport layers,* Thesis, Technische Universität Dresden, 2001.

[74] Kawamura, Y.; Goushi, K.; Brooks, J.; Brown, J. J.; Sasabe, H.; Adachi, C. *Applied Physics Letters* **2005,** *86,* 071104/1.

[75] Sajoto, T.; Djurovich, P. I.; Tamayo, A.; Yousufuddin, M.; Bau, R.; Thompson, M. E.; Holmes, R. J.; Forrest, S. R. *Inorganic Chemistry* **2005,** *44,* 7992.

[76] Yang, C.-H.; Cheng, Y.-M.; Chi, Y.; Hsu, C.-J.; Fang, F.-C.; Wong, K.-T.; Chou, P.-T.; Chang, C.-H.; Tsai, M.-H.; Wu, C.-C. *Angewandte Chemie, International Edition* **2007,** *46,* 2418.

[77] D'Andrade, B. W.; Baldo, M. A.; Adachi, C.; Brooks, J.; Thompson, M. E.; Forrest, S. R. *Applied Physics Letters* **2001,** *79,* 1045.

[78] Shim, H. Y.; Kim, S. Y.; Kim, Y. K.; Kim, J. H.; Lee, K. H.; Yoon, S. S. *Molecular Crystals and Liquid Crystals* **2007,** *462,* 233.

[79] Peng, H. J.; Zhu, X. L.; Sun, J. X.; Yu, X. M.; Wong, M.; Kwok, H. S. *Applied Physics Letters* **2006,** *88,* 033509/1.

[80] Borek, C.; Hanson, K.; Djurovich, P. I.; Thompson, M. E.; Aznavour, K.; Bau, R.; Sun, Y.; Forrest, S. R.; Brooks, J.; Michalski, L.; Brown, J. *Angewandte Chemie, International Edition* **2007,** *46,* 1109.

[81] Lo, S.-C.; Burn, P. L. *Chemical Reviews* **2007,** *107,* 1097.

[82] Anthopoulos, T. D.; Markham, J. P. J.; Namdas, E. B.; Samuel, I. D. W.; Lo, S.-C.; Burn, P. L. *Applied Physics Letters* **2003,** *82,* 4824.

[83] Bera, R. N.; Cumpstey, N.; Burn, P. L.; Samuel, I. D. W. *Advanced Functional Materials* **2007,** *17,* 1149.

[84] Liu, C.; Li, J.; Li, B.; Hong, Z.; Zhao, F.; Liu, S.; Li, W. *Applied Physics Letters* **2006,** *89,* 243511/1.

[85] Liu, C. B.; Li, J.; Li, B.; Hong, Z. R.; Zhao, F. F.; Liu, S. Y.; Li, W. L. *Chemical Physics Letters* **2007,** *435,* 54.

[86] Evans, N. R.; Devi, L. S.; Mak, C. S. K.; Watkins, S. E.; Pascu, S. I.; Koehler, A.; Friend, R. H.; Williams, C. K.; Holmes, A. B. *Journal of the American Chemical Society* **2006,** *128,* 6647.

[87] Chen, X.; Liao, J.-L.; Liang, Y.; Ahmed, M.; Tseng, H.-E.; Chen, S.-A. *Journal of the American Chemical Society* **2003,** *125,* 636.

[88] Tokito, S.; Suzuki, M.; Sato, F. *Thin Solid Films* **2003,** *445,* 353.

[89] Xia, H.; Zhang, C.; Qiu, S.; Lu, P.; Zhang, J.; Ma, Y. *Applied Physics Letters* **2004,** *84,* 290.

[90] Chou, P.-T.; Chi, Y. *European Journal of Inorganic Chemistry* **2006,** 3319.

[91] Li, Y.; Liu, Y.; Guo, J.; Wu, F.; Tian, W.; Li, B.; Wang, Y. *Synthetic Metals* **2001,** *118,* 175.

[92] Si, Z.; Li, J.; Li, B.; Hong, Z.; Lu, S.; Liu, S.; Li, W. *Applied Physics A: Materials Science & Processing* **2007,** *88,* 643.

[93] Li, F.; Zhang, M.; Cheng, G.; Feng, J.; Zhao, Y.; Ma, Y.; Liu, S.; Shen, J. *Applied Physics Letters* **2004,** *84,* 148.

[94] Carlson, B.; Phelan, G. D.; Kim, J. H.; Jen, A. K.-Y.; Dalton, L. *Materials Research Society Symposium Proceedings* **2003,** *771,* 363.

[95] Chen, Y.-L.; Lee, S.-W.; Chi, Y.; Hwang, K.-C.; Kumar, S. B.; Hu, Y.-H.; Cheng, Y.-M.; Chou, P.-T.; Peng, S.-M.; Lee, G.-H.; Yeh, S.-J.; Chen, C.-T. *Inorganic Chemistry* **2005,** *44,* 4287.

[96] Chou, P.-T.; Chi, Y. *Chemistry–A European Journal* **2007,** *13,* 380.

[97] Lamansky, S.; Kwong, R. C.; Nugent, M.; Djurovich, P. I.; Thompson, M. E. *Organic Electronics* **2001,** *2,* 53.

[98] He, Z.; Wong, W.-Y.; Yu, X.; Kwok, H.-S.; Lin, Z. *Inorganic Chemistry* **2006,** *45,* 10922.

[99] Hirani, B.; Li, J.; Djurovich, P. I.; Yousufuddin, M.; Oxgaard, J.; Persson, P.; Wilson, S. R.; Bau, R.; Goddard, William A., I.; Thompson, M. E. *Inorganic Chemistry* **2007,** *46,* 3865.

[100] Xiang, H.-F.; Lai, S.-W.; Lai, P.-T.; Che, C.-M. In *Highly Efficient OLEDs with Phosphorescent Materials*; Yersin, H., Ed.; Wiley-VCH: Weinheim, 2007.

[101] Choy, W. C. H.; Tao, D. *Solid State Chemistry Research Trends* **2007,** 23.

[102] Bian, Z.-Q.; Huang, C.-H. In *Highly Efficient OLEDs with Phosphorescent Materials*; Yersin, H., Ed.; Wiley-VCH: Weinheim, 2007.

[103] Huang, Q.; Walzer, K.; Pfeiffer, M.; Lyssenko, V.; He, G.; Leo, K. *Applied Physics Letters* **2006,** *88,* 113515/1.

[104] Okumoto, K.; Kanno, H.; Hamaa, Y.; Takahashi, H.; Shibata, K. *Applied Physics Letters* **2006,** *89,* 063504/1.

[105] Kim, S. W.; Park, J. H.; Oh, S. S.; Kim, D. Y.; Choi, E. H.; Cho, G. S.; Seo, Y. H.; Kang, S. O.; Park, B.; Saito, Y.; Watanabe, N.; Takezoe, H.; Watanabe, J. *Applied Physics Letters* **2006,** *89,* 213511/1.

[106] Kang, J.-W.; Jeong, W.-I.; Kim, J.-J.; Kim, H.-K.; Kim, D.-G.; Lee, G.-H. *Electrochemical and Solid-State Letters* **2007,** *10,* J75.

[107] "http://www.ge.com/research/grc_7_1_9.html", 2004.

[108] Nakayama, T.; Hiyama, K.; Furukawa, K.; Ohtani, H. *Digest of Technical Papers - Society for Information Display International Symposium* **2007,** *38*, 1018.

[109] "http://www.universaldisplay.com/pholed.htm", 2007.

[110] "OLLA-Project, Press Release", 14.05.2007.

[111] Jurran, N. *c't Magazin für Computertechnik* **2008,** *3*, 18.

[112] Wilson, J. S.; Dhoot, A. S.; Seeley, A. J. A. B.; Khan, M. S.; Köhler, A.; Friend, R. H. *Nature* **2001,** *413*, 828.

[113] Baldo, M. A.; O'Brien, D. F.; Thompson, M. E.; Forrest, S. R. *Phys. Rev. B* **1999,** *60*, 14422.

[114] Wohlgenannt, M.; Jiang, X. M.; Vardeny, Z. V. *Synthetic Metals* **2003,** *137*, 1069.

[115] Holmes, R. J.; Forrest, S. R.; Tung, Y.-J.; Kwong, R. C.; Brown, J. J.; Garon, S.; Thompson, M. E. *Applied Physics Letters* **2003,** *82*, 2422.

[116] Gong, X.; Ma, W.; Ostrowski, J. C.; Bazan, G. C.; Moses, D.; Heeger, A. J. *Advanced Materials* **2004,** *16*, 615.

[117] Lane, P. A.; Palilis, L. C.; O'Brien, D. F.; Giebeler, C.; Cadby, A. J.; Lidzey, D. G.; Campbell, A. J.; Blau, W.; Bradley, D. D. C. *Physical Review B: Condensed Matter and Materials Physics* **2001,** *63*, 235206/1.

[118] Holmes, R. J.; D'Andrade, B. W.; Forrest, S. R.; Ren, X.; Li, J.; Thompson, M. E. *Applied Physics Letters* **2003,** *83*, 3818.

[119] Yersin, H. *Topics in Current Chemistry* **2004,** *241*, 1.

[120] Yersin, H.; Finkenzeller, W. J. In *Highly Efficient OLEDs with Phosphorescent Materials*; Yersin, H., Ed.; Wiley-VCH: Weinheim, 2007.

[121] Hellwege, K.-H., Ed.; *Einführung in die Festkörperphysik;* Springer-Verlag: Berlin, 1976.

[122] Yersin, H. *Displays and Vacuum Electronics, Proceedings, 10th, Garmisch-Partenkirchen, Germany, May 3-4, 2004* **2004,** 287.

[123] Reufer, M.; Walter, M. J.; Lagoudakis, P. G.; Hummel, A. B.; Kolb, J. S.; Roskos, H. G.; Scherf, U.; Lupton, J. M. *Nature Materials* **2005,** *4,* 340.

[124] Yersin, H. *Proceedings of SPIE-The International Society for Optical Engineering* **2004,** *5214,* 124.

[125] Donges, D.; Nagle, J. K.; Yersin, H. *Inorganic Chemistry* **1997,** *36,* 3040.

[126] Tang, K.-C.; Liu, K. L.; Chen, I.-C. *Chemical Physics Letters* **2004,** *386,* 437.

[127] Klessinger, M., Ed.; *Elektronenstruktur organischer Moleküle;* Verlag Chemie: Weinheim, 1982.

[128] Turro, N. J. *Modern Molecular Photochemistry;* Benjamin/Cummings Publ.: Menlo Park, California, 1978.

[129] Fraga, S.; Saxena, K. M. S.; Karwowski, J. *Handbook of Atomic Data. Physical Sciences Data Vol. 5;* Elsevier: Amsterdam, The Netherlands, 1976.

[130] Obara, S.; Itabashi, M.; Okuda, F.; Tamaki, S.; Tanabe, Y.; Ishii, Y.; Nozaki, K.; Haga, M.-a. *Inorganic Chemistry* **2006,** *45,* 8907.

[131] Vlcek, A.; Zalis, S. *Coordination Chemistry Reviews* **2007,** *251,* 258.

[132] Rausch, A. F.; Homeier, H. H. H.; Djurovich, P. I.; Thompson, M. E.; Yersin, H. *Proceedings of SPIE-The International Society for Optical Engineering* **2007,** *6655,* 66550F/1.

[133] McGlynn, S. P.; Azumi, T.; Kinoshita, M. *Molecular Spectroscopy of the Triplet State;* Prentice-Hall: Englewood Cliffs, New Jersey, 1969.

[134] Abedin-Siddique, Z.; Ohno, T.; Nozaki, K.; Tsubomura, T. *Inorganic Chemistry* **2004,** *43,* 663.

[135] Finkenzeller, W. J.; Stoessel, P.; Yersin, H. *Chemical Physics Letters* **2004,** *397,* 289.

[136] Glasbeek, M.; Sitters, R.; Van Veldhoven, E.; Von Zelewsky, A.; Humbs, W.; Yersin, H. *Inorganic Chemistry* **1998,** *37,* 5159.

[137] Yersin, H.; Donges, D.; Nagle, J. K.; Sitters, R.; Glasbeek, M. *Inorganic Chemistry* **2000,** *39,* 770.

[138] Yersin, H.; Humbs, W.; Strasser, J. *Coordination Chemistry Reviews* **1997,** *159,* 325.

[139] Yersin, H.; Strasser, J. *Coordination Chemistry Reviews* **2000,** *208,* 331.

[140] Finkenzeller, W.; Stößel, P.; Kulikova, M.; Yersin, H. *Proceedings of SPIE-The International Society for Optical Engineering* **2003,** *5214,* 356.

[141] Yersin, H.; Strasser, J. *Journal of Luminescence* **1997,** *72-74,* 462.

[142] Lai, S. W.; Che, C. M.; Rausch, A. F.; Finkenzeller, W. J.; Yersin, H. page submitted.

[143] Yersin, H.; Humbs, W. *Inorganic Chemistry* **1999,** *38,* 5820.

[144] Yersin, H.; Huber, P.; Wiedenhofer, H. *Coordination Chemistry Reviews* **1994,** *132,* 35.

[145] Schläfer, H. L.; Gliemann, G. *Einführung in die Ligandenfeldtheorie;* Akademische Verlagsgesellschaft: Frankfurt am Main, 1967.

[146] Yersin, H.; Donges, D.; Humbs, W.; Strasser, J.; Sitters, R.; Glasbeek, M. *Inorganic Chemistry* **2002,** *41,* 4915.

[147] Nozaki, K.; Takamori, K.; Nakatsugawa, Y.; Ohno, T. *Inorganic Chemistry* **2006,** *45,* 6161.

[148] Minaev, B.; Jansson, E.; Agren, H.; Schrader, S. *Journal of Chemical Physics* **2006,** *125,* 234704/1.

[149] Tsuboi, T.; Aljaroudi, N. *Physical Review B: Condensed Matter and Materials Physics* **2005,** *72,* 125109/1.

[150] Lamansky, S.; Djurovich, P.; Murphy, D.; Abdel-Razzaq, F.; Lee, H.-E.; Adachi, C.; Burrows, P. E.; Forrest, S. R.; Thompson, M. E. *Journal of the American Chemical Society* **2001,** *123,* 4304.

[151] Lamansky, S.; Djurovich, P. I.; Abdel-Razzaq, F.; Garon, S.; Murphy, D. L.; Thompson, M. E. *Journal of Applied Physics* **2002,** *92,* 1570.

[152] Moon, D. G.; Pode, R. B.; Lee, C. J.; Han, J. I. *Materials Science & Engineering, B: Solid-State Materials for Advanced Technology* **2005,** *B121,* 232.

[153] Tokito, S.; Suzuki, M.; Sato, F.; Kamachi, M.; Shirane, K. *Organic Electronics* **2003,** *4,* 105.

[154] Chen, F.-C.; Chang, S.-C.; He, G.; Pyo, S.; Yang, Y.; Kurotaki, M.; Kido, J. *Journal of Polymer Science, Part B: Polymer Physics* **2003,** *41,* 2681.

[155] Sandee, A. J.; Williams, C. K.; Evans, N. R.; Davies, J. E.; Boothby, C. E.; Koehler, A.; Friend, R. H.; Holmes, A. B. *Journal of the American Chemical Society* **2004,** *126,* 7041.

[156] Chen, F.-C.; Yang, Y.; Pei, Q. *Applied Physics Letters* **2002,** *81,* 4278.

[157] Muegge, B. D.; Richter, M. M. *Analytical Chemistry* **2004,** *76,* 73.

[158] Muegge, B. D.; Richter, M. M. *Luminescence* **2005,** *20,* 76.

[159] Kapturkiewicz, A.; Nowacki, J.; Borowicz, P. *Electrochimica Acta* **2005,** *50,* 3395.

[160] Maiorano, V.; Perrone, E.; Carallo, S.; Biasco, A.; Pompa, P. P.; Cingolani, R.; Croce, A.; Blyth, R. I. R.; Thompson, J. *Synthetic Metals* **2005,** *151,* 147.

[161] Echigo, T.; Naka, S.; Okada, H.; Onnagawa, H. *Japanese Journal of Applied Physics, Part 1: Regular Papers, Short Notes & Review Papers* **2002,** *41,* 6219.

[162] Echigo, T.; Naka, S.; Okada, H.; Onnagawa, H. *Japanese Journal of Applied Physics, Part 1: Regular Papers, Short Notes & Review Papers* **2005,** *44,* 626.

[163] Thompson, J.; Arima, V.; Matino, F.; Berkebile, S.; Koller, G.; Netzer, F. P.; Ramsey, M. G.; Cingolani, R.; Blyth, R. I. R. *Synthetic Metals* **2005,** *153,* 233.

[164] Matsusue, N.; Suzuki, Y.; Naito, H. *Japanese Journal of Applied Physics, Part 1: Regular Papers, Brief Communications & Review Papers* **2005,** *44,* 3691.

[165] Lamansky, S.; Djurovich, P.; Murphy, D.; Abdel-Razzaq, F.; Kwong, R.; Tsyba, I.; Bortz, M.; Mui, B.; Bau, R.; Thompson, M. E. *Inorganic Chemistry* **2001,** *40,* 1704.

[166] King, K. A.; Spellane, P. J.; Watts, R. J. *Journal of the American Chemical Society* **1985,** *107,* 1431.

[167] Colombo, M. G.; Guedel, H. U. *Inorganic Chemistry* **1993,** *32,* 3081.

[168] Rebane, K. K. In *Zero-Phonon Lines and Spectral Hole Burning in Spectroscopy and Photochemistry*; Sild, O.; Haller, K., Eds.; Springer: Berlin, 1988.

[169] Harrigan, R. W.; Crosby, G. A. *Journal of Chemical Physics* **1973,** *59,* 3468.

[170] Azumi, T.; O'Donnell, C. M.; McGlynn, S. P. *Journal of Chemical Physics* **1966,** *45,* 2735.

[171] Strasser, J.; Homeier, H. H. H.; Yersin, H. *Chemical Physics* **2000,** *255,* 301.

[172] Strasser, J. *Dynamik der Desaktivierung angeregter Zustände in Übergangsmetallkomplexen. Spin Gitter Relaxation und Energietransfer,* Thesis, Universität Regensburg, 1999.

[173] Wiedenhofer, H.; Schützenmeier, S.; von Zelewsky, A.; Yersin, H. *J. Phys. Chem.* **1995,** *99,* 13385.

[174] Becker, D.; Yersin, H.; von Zelewsky, A. *Chemical Physics Letters* **1995,** *235,* 490.

[175] Braun, D.; Yersin, H. *Inorganic Chemistry* **1995,** *34,* 1967.

[176] Yersin, H.; Kratzer, C. *Coordination Chemistry Reviews* **2002,** *229,* 75.

[177] Striplin, D. R.; Crosby, G. A. *Coordination Chemistry Reviews* **2001,** *211,* 163.

[178] Kalyanasundaram, K. *Journal of the Chemical Society, Faraday Transactions 2: Molecular and Chemical Physics* **1986,** *82,* 2401.

[179] Fleischhauer, H. C.; Kryschi, C.; Wagner, B.; Kupka, H. *Journal of Chemical Physics* **1992,** *97,* 1742.

[180] Striplin, D. R.; Crosby, G. A. *Chem. Phys. Lett.* **1994,** *221,* 426.

[181] Pentlehner, D.; Grau, I.; Yersin, H. *Chemical Physics Letters* **2008,** in press.

[182] Henderson, B.; Imbusch, G. F. *Optical Spectroscopy of Inorganic Solids;* Clarendon Press: Walton Street, Oxford, UK, 1989.

[183] Waller, I. *Z. f. Physik* **1932,** *79,* 370.

[184] de Kronig, R. L. *Physica* **1939,** *6,* 33.

[185] Van Vleck, J. H. *Physical Review* **1940,** *57,* 426.

[186] Manenkov, A. A.; Orbach, R. *Spin-Lattice-Relaxation in Ionic Solids;* Harper & Row: New York, 1966.

[187] Abragam, A.; Bleaney, B. *Electron Paramagnetic Resonance of Transition Ions;* Clarendon Press: Oxford, 1970.

[188] Walker, M. B. *Physical Review Letters* **1967,** *162,* 199.

[189] Walker, M. B. *Canadian Journal of Physics* **1968,** *46,* 1347.

[190] Orbach, R.; Blume, M. *Physical Review Letters* **1962,** *8,* 478.

[191] Homeier, H. H. H.; Strasser, J.; Yersin, H. *Chemical Physics Letters* **2000,** *316,* 280.

[192] Schmidt, J.; Strasser, J.; Yersin, H. *Inorganic Chemistry* **1997,** *36,* 3957.

[193] Hofbeck, T.; Yersin, H. *submitted* .

[194] Fischer, T. Thesis, Universität Regensburg, in preparation.

[195] Finkenzeller, W.; Hofbeck, T.; Pentlehner, D.; Yersin, H. *submitted* .

[196] Rausch, A. Diplomarbeit, 2006.

[197] Pentlehner, D. Diplomarbeit, 2006.

[198] Kawamura, Y.; Brooks, J.; Brown, J. J.; Sasabe, H.; Adachi, C. *Physical Review Letters* **2006,** *96,* 017404/1.

[199] Veerman, J. A.; Garcia-Parajo, M. F.; Kuipers, L.; van Hulst, N. F. *Physical Review Letters* **1999,** *83,* 2155.

[200] Endo, A.; Suzuki, K.; Yoshihara, T.; Tobita, S.; Adachi, C. *Chemical Physics Letters, submitted* .

[201] Fischer, G. *Vibronic Coupling;* Academic Press: London, 1984.

[202] Herzberg, G.; Teller, E. Z. *Zeitschrift für Physikalische Chemie* **1933,** *B21,* 410.

[203] Albrecht, A. C. *Journal of Chemical Physics* **1963,** *38,* 354.

[204] Braun, D.; Hensler, G.; Gallhuber, E.; Yersin, H. *Journal of Physical Chemistry* **1991,** *95,* 1067.

[205] Personov, R. I. In *Spectroscopy and excitation dynamics of condensed molecular systems*; Agranovich, V.; Hochstrasser, R. M., Eds.; North-Holland Publishing Co.: Amsterdam, 1983.

[206] Moerner, W. E., Ed.; *Persistent spectral hole-burning: science and applications;* Springer: Berlin, 1988.

[207] Bogner, U.; Schwarz, R. *Physical Review B: Condensed Matter and Materials Physics* **1981,** *24,* 2846.

[208] Attenberger, T.; Bogner, U.; Maier, M. *Chemical Physics Letters* **1991,** *180,* 207.

[209] Lin, S.; Fuenfschilling, J.; Zschokke-Graenacher, I. *Journal of Luminescence* **1988,** *40-41,* 513.

[210] Riesen, H.; Krausz, E. *Chemical Physics Letters* **1991,** *182,* 266.

[211] Riesen, H.; Krausz, E.; Wallace, L. *Journal of Physical Chemistry* **1992,** *96,* 3621.

[212] Kozankiewicz, B.; Bernard, J.; Migirdicyan, E.; Orrit, M.; Platz, M. S. *Chemical Physics Letters* **1995,** *245,* 549.

[213] Kozankiewicz, B.; Gudmundsdottir, A. D.; Orrit, M.; Platz, M. S.; Tamarat, P. *Journal of Luminescence* **2000,** *86,* 261.

[214] Riesen, H. *Coordination Chemistry Reviews* **2006,** *250,* 1737.

[215] Bogner, U. *Physical Review Letters* **1976,** *37,* 909.

[216] Attenberger, T.; Bogner, U.; Jones, G. D.; Murdoch, K. M. *Journal of Physics and Chemistry of Solids* **1997,** *58,* 1513.

[217] Bogner, U. In *Molecular Electronics: Properties, Dynamics, and Applications*; Schreiber, M.; May, V.; G., M., Eds.; Marcel Dekker Inc.: New York, 1996.

[218] Cramér, H. *Mathematische Zeitschrift* **1936,** *41*, 405.

# Acknowledgment

*First of all, I thank my supervisor Prof. Dr. Hartmut Yersin for his constant help in scientific questions and in any other concern throughout the whole work. The success of this work is due in large part to his experience and foresight. The unconstrained and humorous atmosphere Prof. Dr. Yersin provides, makes it a pleasure to work in his group.*

*Just as well, I thank Prof. Dr. Bernhard Dick for the nice and pleasant working atmosphere at the Institut für Physikalische und Theoretische Chemie. Surely, I'm indebted to Prof. Dr. Dick also for providing infrastructural facilities and operating supplies, without which my work would not have been possible.*

*The German Federal Ministry of Education and Research (Bundesministerium für Bildung und Forschung, BMBF) is acknowledged for the financial support of our project "Entwicklung neuer Triplett-Emitter-Materialien für die OLED-Display-Technik". A special thank goes to our contact person Dr. Gerd Warmer for his very obliging support and the confidence he has shown our group.*

*Further, I thank Prof. Dr. Mark E. Thompson and Dr. Peter Djurovich (University of Southern California, Ca, USA) for the faithful cooperation and, especially, for making available a significant amount of the $Ir(btp)_2(acac)$ complex for investigation. Moreover, I thank Prof. Dr. Thompson and his group for the hospitality – it was a great pleasure to visit the likable group in Los Angeles and join the interesting discussions.*

*The Bavaria California Technology Center (BaCaTeC) is kindly acknowledged for the funding of the exchange program of our group with the group of Prof. M.E. Thompson.*

*My sincere thank goes also to Dr. Udo Bogner and Dr. Reinhard Bauer for their fruitful cooperation in the interesting field of persistent spectral hole burning.*

*I wish to express my gratitude to all members of the institute, no matter in which position, who supported me in scientific, technical, or organizational matters. In particular, I'd like to mention my colleagues Dr. Reinhard Bauer, Dr. Rafal Czerwieniec, Tobias Fischer, Thomas Hofbeck, Ralph Huber, Dr. Uwe Monkowius, Dominik Pentlehner, Andreas Rausch, Dr. Alexander Starukhin, and Dr. Andreas*

*Strasser. Especially, I'd like to thank also Dr. Uwe Kensy for his technical support and Mrs. Ulrike Berg and Mrs. Madlene von Sanden-Flohe for their qualified and motivated assistance.*

*Thanks also to anybody I might have forgot to mention.*

*Last but not least, my scientific work would not have been possible without the constant backing of my family. Therefore, my parents and my wife deserve my kindest thanks.*